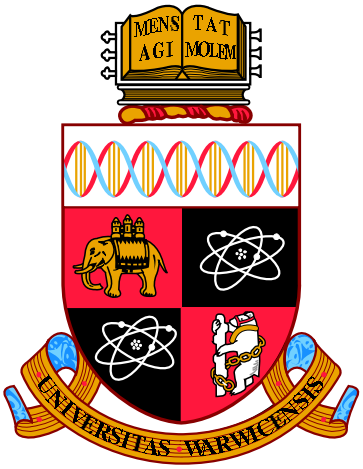

Design and Mechanism of Action of Novel Organoiridium(III) Azopyridine Anticancer Complexes

by

George Marc Hughes

Thesis

Submitted to the University of Warwick

for the degree of

Doctor of Philosophy

MOAC

January 2018

THE UNIVERSITY OF WARWICK

Contents

Acknowledgments

First, I must thank my Mum, Paula, who has battled cancer head on and won, and inspired me to do the same in the best way I can, through research. I also thank my Dad, Marc, for always being there to support and encourage me when I needed it. Without both of them I would never have made it this far.

I thank Prof. Peter Sadler for the 3 amazing years I have spent working in his group. Peter has been an excellent supervisor and I could not have wished for more. His guidance, encouragement, and dedication to his students and his research is truly remarkable and I am glad to have been a part of it. I have learned so much here and have thoroughly enjoyed every minute.

I thank Prof. Lawrence Young for our stimulating discussions. His sheer enthusiasm for the research always left me feeling inspired and rearing to get back to the lab and push myself to do more.

I thank Dr. Abraha Habtemariam, for making chemistry truly enjoyable. His perpetual smile and love of chemistry is truly infectious, and it has been an absolute pleasure to work alongside him. I have now well and truly developed a love for drug synthesis and hope to make a career out of it. Hopefully I can one day become as great a role-model to someone else one day as you were to me.

I thank Dr. Isolda Romero-Canelón, for approximately a million different things. Teaching me proper cell work, taking me to ESRF, supporting me through our trip to Guangzhou and ICBIC, her enormous amount of help with publication and this thesis, and her patience with me most of all. Her incredible professionalism, drive, and work ethic will always keep me pushing myself to do better.

I thank every member of Sadler group, past and present. There are too many to name here but they have all inspired me and helped me succeed. I give special thanks to those who have, at some point, shared an office with me, and been there for the ups and the downs. I thank Dr. Adam Millett for being my desk buddy all the way back when I was a first-year PhD, and for helping me with the most basic of the basics while I was still finding my feet. I thank Dr. Russell Needham for all his help in the lab and for teaching me how to run up walls. I thank Dr. Prinessa Chellan for the chocolate and the laughs that she always brought to the office. I thank Dr. Carlos Sanchez-Cano for helping with HPLC and for the amazing trip to Grenoble, I thank Hannah for the zebrafish and biology work and for being an always-smiling presence in the bio lab, and I thank Carolina Gonçalves-Oliveira for being an amazing friend, desk buddy, and for giving me someone to talk to endlessly about food. I truly cannot thank all of you enough.

I thank Prof. Alison Rodger, Dr. Nikola Chmel, Dr. Hugo Van den Berg, Naomi Grew, and everyone at MOAC DTC and MAS CDT for the fantastic masters year that lead me to this PhD, and all the support, conferences, lunches, and memorable moments throughout the past 4 years.

Last, but absolutely not least, I would like to thank Steph. Thank you for being my other (better) half, my partner in crime, my constant source of love and support. But the thing I must thank you for most of all, the greatest

and most harrowing thing you have ever done for me. I thank you, Steph, for proofreading this thesis.

Declarations

I hereby declare that the work contained in this thesis is the original work of the author, except where specific reference is made to other sources, with the nature and extent of the author's contribution indicated (as appropriate) where work was based on collaborative research. This thesis is submitted to the University of Warwick in support of my application for the degree of Doctor of Philosophy. It has been composed by myself and has not been submitted in any previous application for any degree.

List of publications including submitted papers:

George M. Hughes, Jessica M. Hearn, Isolda Romero-Canelón, Alison F. Munro, Belén Rubio-Ruiz, Zhe Liu, Neil O. Carragher, and Peter J. Sadler. Pharmaco-genomic investigations of organo-iridium anticancer complexes reveal novel mechanism of action. Metallomics, 2017, DOI: 10.1039/c7mt00242d.

George Hughes

January 2018

Abstract

This thesis is concerned with the synthesis, characterisation, and purification of 19 organoiridium(III) complexes, seventeen of which are novel. The complexes are of the general structure [Cp^{X}Ir(azopyridine)Z]A, where the iridium centre is coordinated to either a pentamethyl-cyclopentadienyl (Cp*) ligand, a tetramethyl(phenyl)-cyclopentadienyl Cp^{xph} ligand, or a tetramethyl(biphenyl)-cyclopentadienyl Cp^{xbiph} ligand. The azopyridine acts as an N,N-chelated bidentate ligand with a variety of substituents, the chemical and biological effects of which are investigated. Z represents a monodentate halido ligand. In this work, complexes with chlorido and iodido ligands in this position are investigated. A represents the counterion to the cationic organoiridium complex. In this work, complexes bearing the hexafluorophosphate (PF_6^-), Cl^-, and I^- anions are investigated. X-ray crystal structures of eight of the complexes are determined, confirming that the complexes adopt the expected 'piano-stool' configuration. The anticancer properties of these complexes are thoroughly investigated in multiple cancer cell lines, revealing that several are more potent than many clinically-utilised chemotherapeutics including cisplatin (CDDP), as well as many previously reported metal-based anticancer complexes. The mechanism of action (MoA) of this family of complexes has been investigated, revealing an MoA based on the generation of reactive oxygen species (ROS) and superoxide (SO) in addition to mitochondrial membrane depolarisation. Drugs with this MoA hold the potential to selectively kill cancer cells over normal ones as cancer cells have higher levels of basal ROS and are therefore more sensitive to perturbation of their ROS balance. The charge, solubility, hydrophobicity, hydrolytic behaviour, and mechanism of action (MoA) of these complexes can all be modified with small synthetically trivial adjustments, resulting in highly potent complexes. This demonstrates this family of complexes as an effective and versatile platform for drug design.

Abbreviations

5-AMP	5'-Adenosine monophosphate/5'-adenylic acid
5-CMP	5'-Cytidine monophosphate/5'-cytidylic acid
5-GMP	5'-Guanosine monophosphate/5'-guanidylic acid
5-TMP	5'-Thymidine monophosphate/5'-thymidylic acid
9-EtG	9-Ethylguanine
Å	Angstrom
ADP	Adenosine diphosphate
AICDA	Activation-induced cytidine deaminase
AIDS	Acquired immune deficiency syndrome
ATP	Adenosine triphosphate
azpy(OH)$_2$	4-(pyridin-2-yldiazenyl)benzene-1,3-diol
azpy	2-(phenyldiazenyl)pyridine
azpyNMe$_2$	N,N-dimethyl-4-(pyridin-2-yldiazenyl)aniline
azpyOH	4-(pyridin-2-yldiazenyl)phenol
BL	Burkitt's lymphoma

Brazpy(OH)NEt$_2$ 2-((5-bromopyridin-2-yl)diazenyl)-5-(diethylamino)phenol

BRCA Breast cancer susceptibility gene

ca. *circa*

CCCP Carbonyl cyanide m-chlorophenyl hydrazone

CD Circular dichroism

CDDP Cisplatin

Cp cyclopentadienyl

Cp* η^5-C_5Me_5

Cp^{xbiph} η^5-$C_5Me_4C_6H_4C_6H_5$

Cp^{xph} η^5-$C_5Me_4C_6H_5$

ctDNA Calf thymus deoxyribonucleic acid

DCM Dichloromethane

DEA Diethylamine

DFT Density functional theory

DMEM Dulbecco's modified Eagle's medium

DMS Dimethyl sulphate

DMSO Dimethyl sulphoxide

DSB Double-strand break (usually in DNA)

dsDNA Double-stranded deoxyribonucleic acid

ECACC European Collection of Authenticated Cell Cultures

ESI-MS Electrospray ionisation mass spectrometry

EtBr Ethidium Bromide

FCS Foetal calf serum

GDSC Genomics of Drug Sensitivity in Cancer

HIV Human immunodeficiency virus

HL Hodgekin's lymphoma

HOazpyNO$_2$ 6-((4-nitrophenyl)diazenyl)pyridin-3-ol

HPLC High performance liquid chromatography

HPV Human Papillomavirus

HR Homologous recombination

IC$_{50}$ Half maximal inhibitory concentration

ICP-MS Inductively coupled plasma mass spectrometry

ICP-OES Inductively coupled plasma optical emission spectroscopy

IRIM Imidazolium bisimidazoletetrachloroiridate(III)

L-BSO L-buthionine sulphoximine

LC-MS Liquid chromatography mass spectrometry

LD Linear dichroism

lin linear (usually referring to DNA)

Log P Partition coefficient

MALDI Matrix-assisted laser desorption ionisation

MANOVA Multivariate analysis of variance

MoA Mechanism of action

NAC N-acetyl cysteine

NAD^+ Nicotinamide adenine dinucleotide

NADH Nicotinamide adenine dinucleotide (reduced)

NER Nucleotide excision repair

NPC Nasopharyngeal carcinoma

oc open circular (usually referring to DNA)

PARP Poly-(ADP-ribose) polymerase

PBS Phosphate-buffered saline

PMO Precious Metals Online

PTA 1,3,5-triaza-7-phosphatricyclo-[3.3.1.1]decane

RAED Ruthenium arene ethylenediamine

ROS Reactive Oxygen Species

RPMI-1640 Roswell Park Memorial Institute medium

sc supercoiled (usually referring to DNA)

SO Superoxide

SRB Sulforhodamine B

SSB Single-strand break (usually in DNA)

ssDNA Single-stranded deoxyribonucleic acid

TEA Triethylamine

TFA Trifluoroacetic acid

TOF Turnover frequency

TON Turnover number

UV-Vis Ultraviolet-visible

XRC X-ray crystallography

Chapter 1

Introduction

1.1 Cancer

According to Cancer Research UK, one in two people will develop cancer at some point in their lives.[1]

Cancer is a disease characterised by unregulated, abnormal cell growth. Cancerous cells typically continue to grow and replicate, potentially spreading into other parts of the body. These cells often bypass mechanisms of programmed cell death and grow independent of the body's signals. Significant cell replication forms a mass, or tumour. This is the first symptom of cancer.

Cancer cells can spread beyond the primary tumour site via local spread through neighbouring tissues, via the lymphatic system, or via the blood vessels. This is known as metastasis. Invasion of key organs such as the brain, lungs, liver and kidneys can interfere with essential bodily functions, causing death.

1.1.1 Risk Factors

In 2012, there were an estimated 8.2 million cancer-related deaths worldwide. More than half of these occurred in countries with a medium or low human

development index, highlighting low wealth as a risk factor for cancer. Some of the other most prevalent risk factors include tobacco, alcohol consumption, obesity, poor diet, lack of exercise, exposure to carcinogens, exposure to radiation, and oncogenic infection (such as Epstein-Barr virus infection, discussed in Chapter 4).[2,3]

Age is one of the greatest risk factors for developing cancer, and half of all cancers occur in people over the age of 70. As cancer arises from random genetic mutations, the chance of a carcinogenic mutation occurring at some point in one's lifetime is higher the longer one's life is. Another important factor to consider is that as we age, the cells in our body accumulate damage and the body becomes less able to repair effectively. Over time, exposure to environmental carcinogenic factors also accumulate and can lead to the manifestation of cancer later in life.

Genetics also plays a significant part in cancer genesis and progression. In order to facilitate carcinogenesis, the genes that regulate cell growth and division must be altered.[4] Over-expression of oncogenes, which promote cell growth and survival, along with concurrent under-expression of tumour suppressor genes, which inhibit cell replication, are typically required to transform a normal cell into a cancer cell.

Whilst the vast majority of carcinogenic genetic abnormalities are random and sporadic, approximately 3–10% of cancers are hereditary, i.e. caused by an inherited gene or genes that significantly increase cancer risk. Prime examples of this are the breast cancer-associated genes, BRCA1 and BRCA2, which are associated with a >75% breast and ovarian cancer risk.[5]

Certain hormones can also play a part in cancer development. Sex-related cancers in particular, such as breast or prostate cancer, are closely associated with the levels of sex hormones present in the body. High levels of estrogen or progesterone are associated with higher incidence of breast cancer, and high levels of testosterone are associated with prostate cancer. These are associated with other cancer risk factors, as the levels of these hormones are affected by ancestry, obesity, and level of exercise.[6]

1.1.2 Prevention

Unlike most diseases, anyone can develop cancer. There is no way to completely eliminate one's risk of developing it, however there are many ways by which to minimise it. An estimated >75% of cancers could be prevented by avoiding, where possible, the risk factors mentioned previously.[7,8]

Three of the most prevalent and preventable risk factors are diet, tobacco, and infection.

Diet is closely linked to obesity, which is another risk factor in itself. Studies have linked consumption of red meat and processed meats with increased risk of breast, colon, prostate, and pancreatic cancers.[9,10] A possible explanation for this is that carcinogenic heterocyclic amines can be found in cooked meats (Figure 1.1), especially well-done meats. Meats do, however, contain many anticarcinogens, such as omega-3, polyunsaturated fatty acids, and conjugated linoleic acid, as well as important micronutrients such as selenium, and vitamins B6, B12, and D.[11,12]

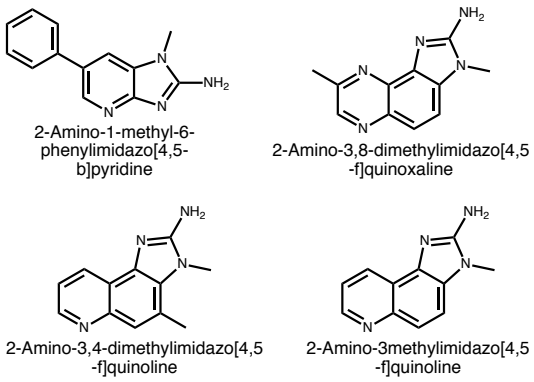

Figure 1.1: Four heterocyclic amines found in cooked ground beef. All four are known carcinogens.[13]

A diet for minimising cancer risk would therefore include more fruits, vegetables, whole grains and fish with less red meat, animal fat, and refined sugar. Maintaining a healthy weight would also contribute to minimising cancer risk.[14]

Exposure to tobacco is one of the most easily avoidable risk factors for cancer,

in particular those of the mouth, larynx, lung, and pancreas. Over 50 of the chemicals in cigarette smoke are carcinogens.[15] Some of the most abundant dangerous chemicals include acetaldehyde, which reacts with deoxyguanine, forming DNA adducts; isoprene, which causes single- and double-strand breaks in DNA; acrolein, which causes DNA-DNA crosslinks, DNA-protein crosslinks, and forms DNA adducts; and 1,3-butadiene, which also forms DNA adducts as well as inducing a global loss of DNA methylation, affecting an organism's epigenetics (Figure 1.2).[16–19]

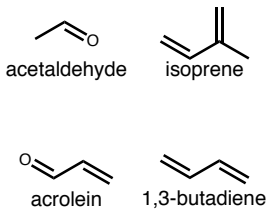

Figure 1.2: Four highly carcinogenic chemicals found in cigarettes at amounts >100 μg per cigarette.[16–19]

Secondary smoke has also been closely linked to lung cancer and contains many known carcinogens.[13] Avoiding tobacco entirely is a highly effective way to lower one's risk of developing cancer.

Some infections agents can contribute to the development of cancer. Infection by human papillomavirus (HPV) is a significant risk factor for cervical cancers[20] and hepatitis B and C infections are associated with liver cancer.[21] There are 200 types of human papilomaviruses and the level of cancer risk associated with infection varies. The E6 and E7 oncoproteins of some of the high-risk HPVs inactivate host p53 and retinoblastoma tumour suppressor genes, as well as inducing centrosome abnormalities leading to aneuploidy (abnormal number of chromosomes) and, consequently, genomic instability.

Hepatitis B and C cause carcinogenic DNA damage and chronic inflammation in the liver by the induction of excessive reactive oxygen species (ROS). This subsequently triggers up-regulation of activation-induced cytidine deaminase (AICDA), which deaminates cytidine bases in DNA, converting them into uracil. This causes DNA mismatches which can further contribute to carcinogenesis.[22]

Epstein-Barr virus (EBV) infects >90% of the global population asymptomatically, however, in most hosts it remains dormant for the duration of their life, only exprssing a small subset of its genes. In some cases, such as in an immunodeficient host, the virus can reactivate and begin expressing more of its genome. Some of these are oncogenes and can lead to Burkitt's lymphoma (BL), Hodgekin's lymphoma (HL), stomach cancer, and nasopharyngeal carcinoma (NPC).[23]

Other prominent viruses linked with cancer include herpesviruses, human T cell lymphotropic virus, Merkel cell polyomavirus, and human immunodeficiency virus (HIV), which leads to acquired immune deficiency syndrome (AIDS). HIV does not cause cancer directly, but is associated with Kaposi's sarcoma, non-Hodgekin's lymphoma, anal cancer, and cervical cancer. As HIV effectively destroys the body's immune system, it cannot fight off the viruses that cause these cancers and so they run rampant, leading to malignancies.[24]

Vaccines against HPV and Hepatitis B are available in many countries, however no vaccines or treatments exist for many others. Avoidance of infection where possible is the most effective way to reduce cancer risk from infectious agents, however this can be difficult for those that are more easily transmissible, such as EBV.

Whilst minimising these risk factors can reduce the risk of cancer, there is no way to completely eliminate one's chances of developing it, as an element of pure chance is involved in cancerous transformation. There are, however, a variety of effective treatments available, and being in good general health increases your short- and long-term survival chance.

1.1.3 Treatments

The long-term survival and quality of life of cancer patients has increased over the recent years due to both improved diagnostics and treatments. The chance of survival is highly dependent on the type of cancer and what stage it has progressed to when diagnosed. Late-stage cancers are comparatively far more difficult to treat. There are over 100 different cancers, typically named after the organ from which the primary tumour arose. Survival varies enormously between them, for example, the one-year net survival % for pancreatic cancer is only 20.8%, whereas for testicular cancer it is as high as 99.1%.[25] Whilst many new and experimental treatments are being developed, most cancers are treated by some form of surgery, radiotherapy, chemotherapy, or combinations thereof.

When a patient is diagnosed with cancer, there are a wide variety of treatments available to either destroy the cancer or to ease the symptoms, depending on the nature of the cancer itself. Many different forms of surgery are utilised to physically remove or destroy cancerous growths. Typically, it is carried out with a scalpel, or similar equipment, however other forms of surgery are sometimes used. Laser surgery can be employed to carry out very precise destruction of cancer tissue, or to preemptively destroy abnormal growths that may develop into cancer. Unfortunately, not all cancers can be treated surgically, and removal of the primary tumour is a significantly less effective treatment if the cancer has already spread through local tissues or metastasised.

Many other treatments exist that can be used instead of, or in conjunction with, surgery. One such treatment is radiotherapy. Radiotherapy uses high doses of radiation to kill tumours, or to shrink them to ease surgical removal. The radiation damages the cancer cells' DNA, causing their growth to dramatically slow. In cases where the damage to the DNA is beyond repair, the cancer cells die and are broken down by the body.

Radiotherapy can be applied either externally or internally. External beam radiotherapy is carried out by a machine that aims a beam at the specific area of the body containing the cancer. Typically, the beam will apply radiation from many directions and angles, their vectors crossing at the point of the

cancer. This maximises the dose of radiation received by the cancer whilst minimising the radiation received by the surrounding healthy tissues. This helps to reduce side-effects.

Internal radiotherapy involves the insertion of a solid or liquid radiation source into the body. Solid source radiotherapy is known as brachytherapy and is used to treat the area harbouring the tumour. It may be used to apply low doses of radiation over a period of days, or high doses over a span of minutes. Liquid source radiotherapy is known as systemic therapy and can travel through the blood, affecting cancerous cells around the body. External beam radiotherapy will not make a patient radioactive, however internal systemic radiotherapy will cause the patient's bodily fluids to give off radiation for some time after treatment.

Radiation therapy often has side effects due to the damage it can cause to healthy cells. The exact nature of these side effects depends on the part of the body being irradiated, however many patients receiving radiotherapy develop significant fatigue. Additionally, there are limits on how much radiation an area of the body can safely receive over a patient's lifetime. Both of these factors can hamper the efficacy of radiotherapy.

Chemotherapy is another highly-utilised form of cancer treatment involving the use of anticancer drugs. It is often used alongside other treatments to kill cancers or ease symptoms. Neoadjuvant chemotherapy is chemotherapy applied before surgery or radiotherapy to reduce the size of a tumour. Chemotherapy used to destroy cancer cells that remain after surgery or radiotherapy is known as adjuvant chemotherapy. Chemotherapy is also an effective way of killing cancer cells that have spread from the primary tumour site to other parts of the body.

Chemotherapy comes in a variety of forms, and the drug, or drugs, used depend on the type and stage of the cancer being treated. Chemotherapeutics may be administered orally, intravenously/intraarterially, by injection directly into tissue, or topically as a cream.

Depending on the type and dose, chemotherapy may cause undesirable side-

effects. Chemotherapy typically targets fast-growing cancer cells, but can also kill or slow the growth of other, healthy, fast-growing cells, such as those in the mouth and intestinal lining, as well as hair follicles. This can lead to mouth sores, nausea, and hair loss, respectively. To minimise side-effects, chemotherapy is often scheduled and carried out in cycles to allow the body time to recover and repair any damage caused by the chemotherapy.

Cancers that were once susceptible can become resistant to some chemotherapeutics, and there is still a great deal of room for improvement in terms of increasing the range of treatable cancers and improving patient prognoses. Clinical trials are regularly carried out to aid the development and assessment of new potential chemotherapeutics. They can also be employed to treat cancers for which there is not yet a highly effective treatment and to ultimately improve the overall understanding of cancer. In this thesis, the anticancer properties of a variety of complexes are investigated to evaluate their potential as possible chemotherapeutics towards entry into clinical trials.

1.2 Precious Metal-based Anticancer Complexes

A significant proportion of chemotherapy treatments utilise drugs containing precious metals. Transition metals possess a number of properties that make them particularly well-suited for the generation of effective chemotherapeutics.[26] These include, but are not limited to, their various accessible redox states, allowing for biological redox catalysis;[27] their wide range of coordination geometry, allowing for three-dimensional design of shaped complexes to fit molecular target sites;[28] and their unique kinetic and thermodynamic properties, opening up avenues of design not accessible to organic compounds.[29] Currently, ca. 40% of chemotherapy regimens utilise platinum drugs. In this section, a selection of relevant platinum-, ruthenium-, osmium-, and iridium-based anticancer therapeutics are described.

1.2.1 Platinum

Platinum-based chemotherapeutics began with the serendipitous discovery of the anticancer properties of cisplatin (CDDP) *cis*-$[Pt(NH_3)_2Cl_2]$. CDDP was, in fact, first discovered by Michael Peyrone in 1844 and was known as Peyrone's chloride. Its anticancer properties went undiscovered until 1965. Barnett Rosenberg, whilst studying the effects of electric fields on bacterial growth, found that the platinum electrodes he was using were corroding in the test solution, yielding the platinum(IV) complex $[PtCl_6]^{2-}$. This complex inhibited cell growth. Furthermore, exposure to light caused this complex to exchange ligands, forming a mixture of *cis* and *trans* isomers of $[PtCl_4(NH_3)_2]$. Interestingly, the cis isomer induced filamentous growth of the bacteria, the result of replication defects that typically occur when bacteria respond to stress, such as that which arises from DNA damage. The trans isomer, however, did not induce filamentous growth. In the process of synthesising this salt, CDDP was also synthesised and tested. This revealed that CDDP was even more effective at inducing filamentous growth in the bacteria than the platinum(IV) salt was.[30] Rosenberg proceeded to show that CDDP could cure tumours in mice,

leading to the discovery of a new class of antitumour agents.[31]

Since then, platinum-based anticancer complexes have become a key component of chemotherapy. CDDP remains highly utilised in clinics even today, as are its derivatives, carboplatin, oxaliplatin (Figure 1.3), and others. CDDP platinates DNA, crosslinking guanine bases and inducing proapoptotic events. The mechanism of action (MoA) of CDDP is discussed in more detail in Chapter 4.

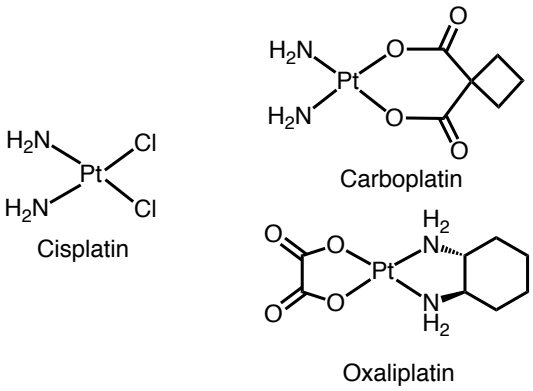

Figure 1.3: Clinically utilised platinum drug cisplatin (CDDP) and its derivatives, carboplatin and oxaliplatin.

CDDP revolutionised cancer therapy. Before its discovery, the cure rate of testicular cancer was only 10%. CDDP-based treatment, combined with early detection, has raised this to almost 100%. However, CDDP-based chemotherapy still has a number of drawbacks, including the need for intravenous injection, severe dose-limiting side-effects, and intrinsic and acquired resistance of some cancers to it. Improvements are being made to circumvent the drawbacks of CDDP, such as the development of lipoplatin, a liposomal form of CDDP able to persist in the body for ca. 120 h and fuse with tumour cell membrane, resulting in greater antitumour activity.[32]

CDDP and its aforementioned derivatives are not the only effective platinum-based anticancer drugs. Many other platinum-based complexes have been developed to overcome the drawbacks of CDDP and to attack cancers in new ways.[33] To generate a more effective platinum anticancer complex, bulky carrier ligands were introduced to reduce the reactivity of platinum drugs to

deactivating cellular molecules. A prominent example of this is picoplatin, which, unlike CDDP, can be administered orally. Additionally, it has been shown to retain cytotoxicity in CDDP- and oxaliplatin-resistant cancer cell lines.[34] Picoplatin (Figure 1.4), however, has been unsuccessful in phase III clinical trials, indicating the need for further research and development in this field.

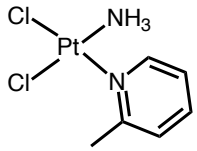

Picoplatin

Figure 1.4: The chemical structure of the orally available CDDP-derivative, picoplatin.

More recently, research into methyl-substituted oxaliplatin analogs has resulted in complexes with improved therapeutic characteristics relative to oxaliplatin itself. KP1537 and KP1691 (Figure 1.5) showed superior cytotoxicity to oxaliplatin in both platinum-sensitive and platinum-resistant cell lines,[35] in addition to increasing the life span of L1210 leukemic mice to a greater extent than oxaliplatin.[36]

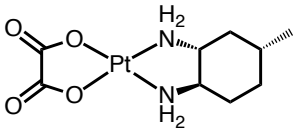

KP1537

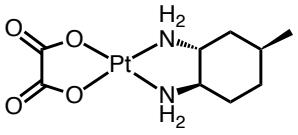

KP1691

Figure 1.5: Oxaliplatin analogues KP1537 and KP1691 with *in vivo* antitumour activity.

1.2.2 Ruthenium

Ruthenium-based complexes offer another avenue for drug discovery. Ruthenium complexes can bear six coordinating ligands, allowing for hexacoordinate and octahedral geometry, in contrast to the square planar geometry typically adopted by platinum anticancer drugs. Two of the most prominent ruthenium anticancer drugs are NAMI-A and KP1019 (Figure 1.6). NAMI-A acts as a pro-drug, taking advantage of ruthenium's capability to be reduced by the acidic environment in cancer cells where the drug is activated.[37] NAMI-A acts as an antimetastatic drug, rather than being directly cytotoxic. The MoA of NAMI-A is currently thought to involve cell cycle disruption.[38] NAMI-A also possesses antiangiogenic activity,[39] as well as selectively inhibiting metastasis, particularly of lung cancers.[40] This is thought to be due to its ability to bind collagen.[41] NAMI-A is the first ruthenium anticancer drug to reach human clinical trials, however studies in patients with non-small cell lung cancer revealed that NAMI-A administered in combination with the clinically-used drug gemcitabine is less active after first line treatment than gemcitabine alone.[42]

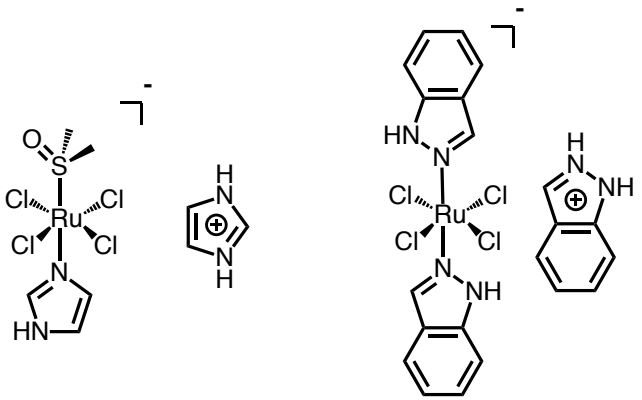

Figure 1.6: Two ruthenium anticancer complexes that have reached human clinical trials NAMI-A and KP1019 exhibiting octahedral geometry.

KP1019 exerts cytotoxicity by inducing apoptosis through disruption of the cellular electron transport chain and depolarisation of the mitochondrial membrane. Additionally, it down-regulates the anti-apoptotic factor bcl-2 whilst activating the apoptotic protein caspase-3, independent of p53 status.[43]

KP1019 has shown potent cytotoxicity against transplanted chemoresistant mouse colon carcinomas. KP1019 induced complete tumour responses in the majority of tumours, whereas 5-fluorouracil produced only partial responses against half the tumours and CDDP produced no responses.[44,45] KP1019 is the second ruthenium anticancer drug to reach human clinical trials. In a phase I clinical trial on six patients with progressive solid tumours, intravenous administration of KP1019 lead to disease stabilisation in five patients with no dose-limiting toxicity.[46]

RAPTA complexes (Figure 1.7) are characterised by their 1,3,5-triaza-7-phosphatricyclo-[3.3.1.1]decane (PTA) ligand, which confers high water solubility.[47] RAPTA complexes, unlike classical antitumour agents, show only low levels of DNA binding. Instead, they interact strongly, and selectively, with proteins, such as the histone core in chromatin, leading to cytoxicity.[48] RAPTA complexes have been demonstrated to interfere with enzymes essential to tumour targeting and drug deactivation to overcome drug resistance. RAPTA complexes, unfortunately, tend to exhibit low *in vivo* cytotoxicities, however they do exert a strong antiangiogenic and antimetastatic effect *in vivo*.[49,50] The antiangiogenic and antimetastatic effects of RAPTA-C are thought to be due to its localisation being primarily on the cell membrane, rather than entering the cell.[51] One of the great strengths of RAPTA complexes is their extremely low toxicity, allowing them to be combined with other antitumour agents without additional toxic side-effects.[52]

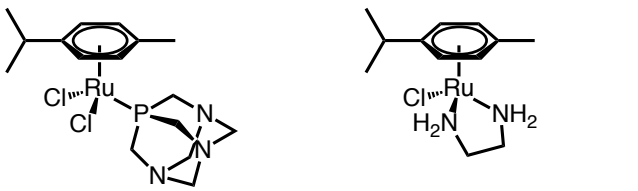

RAPTA-C [(η6-p-cymene)Ru(II)(en)Cl]PF6

Figure 1.7: Two ruthenium anticancer complexes RAPTA-C and [(η^6-p-cymene)Ru(en)Cl]PF_6 exhibiting piano stool geometry.

Another promising ruthenium-based class of potential anticancer therapeutics are ruthenium arene ethylenediamine (RAED) compounds. Like many

platinum-based agents, they form adducts selectively with guanine at N7.[53,54] This site selectivity has been shown to be directed by hydrogen bonding of the NH_2 groups on the diamine ligand to exocyclic oxygens. RAED complexes exhibit cytotoxicity at a similar level to carboplatin[55] and are able to overcome cross-resistance with CDDP in ovarian carcinoma models, as well as being active *in vivo*.[56]

1.2.3 Osmium

The precious heavy metal osmium is often associated with its extremely toxic complex, osmium tetroxide. However, complexes of osmium can also be potent anticancer agents without being overly toxic to healthy cells.[57] Osmium analogues of the ruthenium anticancer complexes NAMI-A and KP1019 have been synthesised (Figure 1.8) and both show anticancer activity,[58] however they exhibit different biological properties to their ruthenium analogues. The osmium analogue of NAMI-A, unlike NAMI-A itself, is inert to hydrolysis, a step thought to be necessary for anticancer activity. It is, however, also more potent than NAMI-A, suggesting that a hydrolysis-independent mechanism contributes to its cytotoxicity.[59]

Osmium(IV) analogues of KP1019 have been synthesised with comparable anticancer activity to KP1019 itself,[60] however in the most similar analogue the indazole ligands are coordinated to osmium at the N1 atom, in contrast to the N2 atom in KP1019.[61]

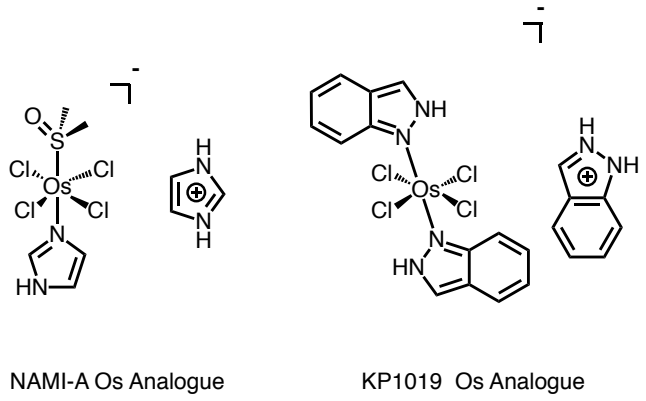

Figure 1.8: Osmium analogues of the two ruthenium anticancer complexes NAMI-A and KP1019 showing anticancer activity.

The osmium analogue of RAPTA-C has been synthesised (Figure 1.9) and shown to have comparable activity to its ruthenium analogue.[62] Unlike ruthenium RAPTA complexes, osmium RAPTA analogues preferentially bind DNA, however some of these are more toxic to healthy cells than cancers.[63]

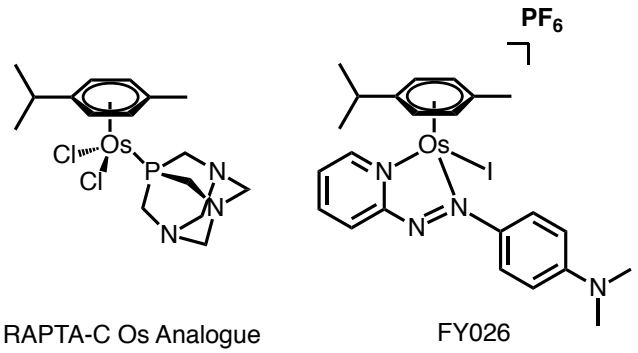

Figure 1.9: Osmium analogue of RAPTA-C and FY026, a potent *in vivo* organoosmium complex.

Osmium-arene complexes have also shown potential as anticancer agents, exhibiting cytotoxicity at the nanomolar level in multiple cell lines including drug-resistant cancers. They have also been shown to delay cancer growth in an *in vivo* colon xenograft in a mouse model with no observable toxic side-effects.[64] Osmium arene complexes bearing azopyridine or iminopyridine ligands can generate reactive oxygen species (ROS) in cells and can be potentiated by co-administration with L-buthionine sulphoximine (L-BSO), which reduces the level of the cellular antioxidant glutathione (GSH). Such complexes have also been reported to induce S-phase cell cycle arrest.[65] This suggests a MoA for osmium arene complexes distinct from classical anticancer agents, involving disruption of the redox balance of cancer cells.[66–68] Osmium arene complexes have been modified to interact with DNA. The incorporation of N,N- or N,O-chelating ligands on osmium-biphenyl systems results in complexes that hydrolyse and bind both adenine and guanine nucleobases, whereas complexes with N,S-chelating ligands can bind histone proteins.[69] This demonstrates that the MoA of organoosmium complexes can be finely tuned by modification of its chelating bidentate ligand.[70–72]

1.2.4 Iridium

In contrast to osmium, the iridium analogue of NAMI-A, and the imidazolium bisimidazole tetrachloro iridate(III) (IRIM) complex, which is the closest iridium analogue to KP1019, are both biologically inactive (Figure 1.10),[73,74] as is the iridium analogue of RAPTA-C.[75] Their lack of cytotoxicity is thought to be due to its kinetic inertness conferred by the iridium centre relative to ruthenium. Iridium complexes do, however, hold great potential as anticancer agents when they break from the conventional drug designs.

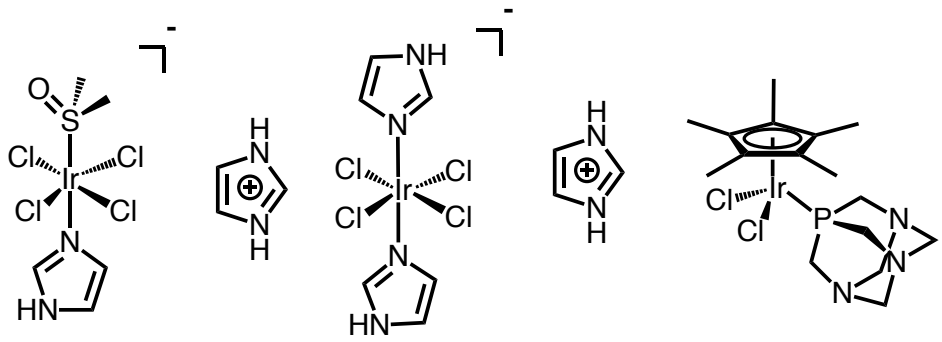

Figure 1.10: Biologically inactive iridium analogues of the ruthenium anticancer complexes NAMI-A and RAPTA-C, and the IRIM complex, which has significant structural similarity to KP1019.

Whilst iridium(I) complexes have been shown to exhibit anticancer activity,[76,77] iridium(III) complexes have shown impressive cytotoxicity in various cancer cell lines, with N,N-chelated polypyridyl complexes exhibiting micromolar potencies.[78] A wide variety of iridium(III) anticancer complexes have been developed in recent years, including Cp* complexes with N,N-, N,O- and O,O-chelating ligands exhibiting micromolar activity.[79] Further research into unconventional iridium(III) complexes has produced complexes with N,N-chelated pyrazole-based ligands with emissive theranostic properties and comparable activity to CDDP,[80] DNA-binding lipophilic steroidal conjugates with ca. 6× the activity of CDDP,[81] and cytotoxic, DNA-binding dinuclear iridium complexes.[82]

Variation of the Cp system, bidentate, and monodentate ligands of iridium(III) complexes has also produced complexes with nanomolar potency (Figure 1.11). Iridium(III) bipyridyl complexes with monodentate hydrosulphide adducts readily oxidise GSH and exhibit nanomolar potency against A2780 ovarian carcinoma.[83] The C,N-chelated complex ZL105 with pyridine as the monodentate ligand displays extremely potent activity, attributed to the slow hydrolysis of the Ir-py bond relative to the rapid hydrolysis of its Ir-Cl analogue, preventing deactivation.[84] Studies on both of these complexes indicate a ROS-based MoA. Iridium(III) complex have also shown activity as biocatalysts. Iridium(III) complexes bearing chlorine as a monodentate ligand have been shown to interfere with the nicotinamide adenine dinucleotide (NAD^+/NADH) hydride transfer reactions in cells as a novel MoA by catalysing oxidation or reduction transfer hydrogenation reactions.[85,86]

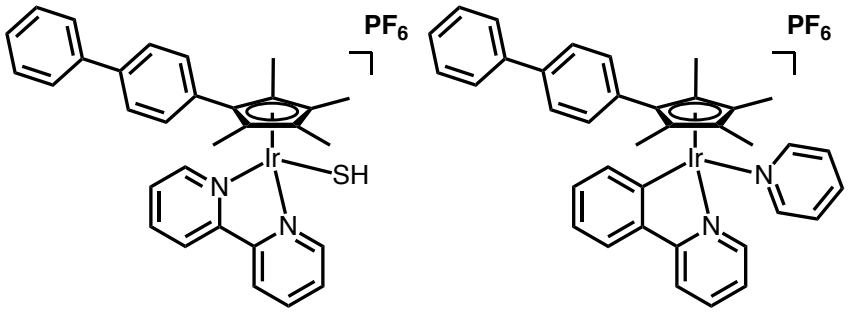

Figure 1.11: Two Cp^{xbiph} iridium(III) half-sandwich complexes with nanomolar potency, bearing unconventional monodentate ligands. Both generate ROS in cancer cells.

Research into new precious metal-based complexes has lead to the discovery of many promising anticancer compounds, yet there is still much more to be explored. Cancer is an extremely heterogeneous disease, and many cancers are still very difficult to treat and can become resistant to current therapeutics. Iridium(III) complexes represent a rich and still relatively untapped area to be explored for the purpose of anticancer drug discovery.

In this work, novel iridium(III) complexes are designed, synthesised, and investigated in order to meet the growing need for effective anticancer therapeutics.

1.3 Aims

1. To synthesise, characterise, and purify a library of highly potent and selective organoiridium(III) anticancer complexes bearing a variety of cyclopentadienyl ligands, bidentate azopyridine ligands, and monodentate halido ligands.

2. To assess the anticancer activity of these complexes against various cancer cell lines, thereby identifying structure-activity relationships which can inform future drug synthesis.

3. To investigate the MoAs of these complexes, in particular their catalytic oxidant activity on NADH, interactions with DNA, the cell cycle, mitochondria, and their ability to generate ROS and SO.

Chapter 2

Experimental Methods

2.1 Instrumentation

2.1.1 Nuclear Magnetic Resonance Spectroscopy (NMR)

NMR data (^{1}H, ^{13}C and 2D experiments) were acquired in 5 mm NMR tubes and carried out in the University of Warwick Department of Chemistry NMR Spectroscopy Facility on either a Bruker Avance 300 MHz, Bruker Avance III HD 300 MHz, Bruker Avance III 400 MHz, Bruker Avance III HD 400 MHz, Bruker Avance III HD 500 MHz, Bruker Avance 500 MHz or a Bruker Avance III 600 MHz instrument. Experiments were carried out at 298 K unless otherwise stated. ^{1}H-NMR chemical shifts were internally referenced to residual hydrogens: CHD$_2$CN (1.94 ppm) for acetonitrile-d_3, C$_3H$D$_5$O (2.05 ppm) for acetone-d_6, (CHD$_2$)(CD$_3$)SO (2.50 ppm) for DMSO-d_6, CHD$_2$OD (3.49 ppm) for methanol-d_4, C$_4H$H$_7$O$_2$ (3.75 ppm) for 1,4-dioxane or CHCl$_3$ (7.26 ppm) for chloroform-d_3. ^{13}C-NMR chemical shifts were internally referenced to C$_3H$D$_5$O (29.84 ppm) for acetone-d$_6$. Spectra were processed using Bruker Topspin 3.2.

2.1.2 Microwave Reactor

Some synthesis was performed using microwave-assisted chemistry to expand the temperature and pressure range at which reactions could take place beyond the limits of standard laboratory conditions. A CEM Discovery-SP microwave reactor was used at conditions specified in the appropriate section.

2.1.3 Elemental Analysis

Elemental analysis of the percentage of carbon, hydrogen and nitrogen in samples was carried out on a CE-440 Exeter Elemental Analyzer by the Warwick Analytical Service.

2.1.4 UV-Vis Absorption Spectroscopy

Absorption spectroscopy data were collected using a Varian Cary 300 UV-Vis spectrometer using 1 cm path-length cuvettes. Experiments were carried out at 298 K unless otherwise stated. The spectrometer was fitted with a PTP1 Peltier temperature controller to maintain or change the desired temperature of the cuvette.

2.1.5 pH Measurements

All pH measurements were taken using a micro combination electrode filled with a 3 M solution of KNO_3 attached to a Mi 150 Bench Meter. The electrode was calibrated using pH calibration solutions of pH 4.00, 7.01, and 10.01 purchased from HANNA Instruments. When not in use the electrode was left to soak in a 3 M solution of KNO_3.

2.1.6 Linear Dichroism (LD)

Spectra were recorded using a Jasco J-815 spectropolarimeter adapted for LD spectroscopy. Measurements were performed using a quartz capillary LD Couette flow cell built by Crystal Precision Optics spinning at 3000 RPM.[87,88]

2.1.7 Circular Dichroism (CD)

Measurements were taken using a Jasco J-1500 Circular Dichroism Spectrometer fitted with a PTC-517 Peltier Thermostatted Single Cell Holder, using 1 cm path-length quartz cuvettes (Starna UK).

2.1.8 Electrospray Ionisation Mass Spectrometry (ESI-MS)

Data were recorded in the University of Warwick Department of Chemistry Mass Spectrometry Facility on a Agilent 6130B single Quad using electrospray ionization on solutions of samples dissolved in 0.5 mL MeOH. The mass spectrometer was operated in electrospray positive ion mode. Scanning range used was either 50 – 500 m/z or 400 – 1000 m/z as appropriate for the sample.

2.1.9 Liquid Chromatography Mass Spectrometry (LC-MS)

LC-MS experiments were carried out in the University of Warwick Department of Chemistry Mass Spectrometry Facility on an amazon X Agilent system coupled to a Bruker HCT-Ultra ETD II PTR PTM mass spectrometer. The mass spectrometer was operated in electrospray positive ion mode with a scan range of 50 – 2,000 m/z. Data were processed using Data Analytics 3.3 (Bruker Daltonics).

2.1.10 Inductively Coupled Plasma Optical Emission Spectroscopy (ICP-OES)

Inductively coupled Plasma Optical Emission Spectroscopy (ICP-OES) experiments were carried out on a PerkinElmer 5300 DV ICP-OES set to detect ^{193}Ir at 224.268 nm. Calibrations carried out using iridium Specupure plasma standards (Alfa Aesar, 1000 pm in 10% HCl) prepared at 0, 50, 100, 200, 300, 400, 500, 600 and 700 ppm in 3.6% nitric acid in double distilled 18.2 MilliQ water purified using a using a Millipore Milli-Q water purification system and a USF Elga UHQ water deionizer. Standards were spiked with NaCl so that the final concentration matched that of the of the samples being analyzed where appropriate.

2.1.11 Flow Cytometry

Flow cytometry experiments were carried out by Dr. Isolda Romero-Canelón on a Becton-Dickinson FACScan flow cytometer. Data processed using Flowjo software. Specific experimental conditions are described in the appropriate section.

2.1.12 X-ray Crystallography (XRC)

X-ray diffraction data were collected and processed by Dr. Guy Clarkson (Department of Chemistry, University of Warwick). An Oxford Diffraction Gemini four circle system with a Ruby CCD area detector using Mo Kα radiation was used to obtain diffraction data. The crystals were mounted in oil and held at either 100 or 150 K with an Oxford Cryosystem Cobra. Data and generation of structural images carried out in Mercury 3.3.

Single crystals of were grown from 1 mg of dissolved complex in MeOH and diethyl ether or DCM and hexane unless stated otherwise in a vial-in-vial system to facilitate vapour diffusion. A suitable crystal was selected and mounted on glass fibre with Fromblin oil and placed on an Xcalibur Gemini diffractometer

with a Ruby CCD area detector. The crystal was kept at 150 K during data collection. Using Olex2,[89] the structure was solved with the ShelXT[90] structure solution program using Direct Methods and refined with the ShelXL[91] refinement package using Least Squares minimisation.

2.2 Materials

Solvents

All solvents used were HPLC-grade and were purchased from commercial sources (Sigma Aldrich, Fischer Scientific).
Trifluoroacetic acid (TFA, 99.99%, spectrophotometric grade) and 1,4-dioxane were purchased from Sigma Aldrich.
Triethylamine (TEA, HPLC-grade) was purchased from Fischer Scientific.

Materials for Ligand Synthesis

Nitrosobenzene, ammonium hexafluorophosphate, 2-aminopyridine, 4-nitroaniline, 2-(5-Bromo-2-pyridylazo)-5-(diethylamino)phenol, 97%, 2-hydrazinopyridine and p-benzoquinone were purchased from Sigma Aldrich.
4-(2-pyridylazo)-N,N-dimethylaniline and 3-hydroxypyridine purchased from Alfa Aesar.
Sodium nitrite was purchased from Scientific Laboratory Supplies Ltd.
Aqueous tetramethylammonium hydroxide (extra pure 25% in water), 60% Perchloric acid and formic acid were purchased from Fischer Scientific.
4-(2'-Pyridylazo)resorcinol, 97% was purchased from Acros Organics.

Materials for Iridium Dimer Synthesis

$IrCl_3 \bullet 3H_2O$ was purchased from Precious Metals Online (PMO pty Ltd, Australia). Supplier confirms 50-56% Ir.
1,2,3,4,5-Pentamethylcyclopentadiene (95%), 2,3,4,5-tetramethyl-2-cyclopentenone (95%), 4-bromobiphenyl (98%), n-butyllithium (1.6 M in hexanes) and phenyllithium (1.6 M in dibutyl ether) were purchased from Sigma-Aldrich (UK).

Materials for Cell Biology

Petri-dish 10 ml (Greiner Bio One)
25 cm^2 CELLSTAR culture flasks (Greiner Bio One)
75 cm^2 CELLSTAR culture flasks (Greiner Bio One)
2 ml serological pipettes (Greiner Bio One)
5 ml serological pipettes (Greiner Bio One)
10 ml serological pipettes (Greiner Bio One)
25 ml serological pipettes (Greiner Bio One)
7 ml Bijoux tubes (Greiner Bio One)
Pipette controller/pipette aid (INTEGRA)
Trypsin-EDTA, 0.25% (Thermo Fisher Scientific, Gibco^{TM})
Dulbeccos Modified Eagle Medium (DMEM) (Thermo Fisher Scientific, Gibco^{TM})
L-glutamine (Thermo Fisher Scientific, Gibco^{TM})

Cell Lines Used

A2780 human ovarian carcinoma (European Collection of Authenticated Cell Cultures (ECACC))
A2780cis human ovarian carcinoma with acquired CDDP resistance (ECACC)
A549 human Caucasian lung carcinoma (ECACC)
MRC-5 normal human fetal lung fibroblasts (ECACC)
EBV-positive and -negative OE19 human Caucasian oesophageal carcinomas, CNE1, CNE2, and SUNE-1 human nasopharyngeal carcinomas provided by Dr. Chris Dawson, University of Birmingham.

Miscellaneous Materials

Deoxyribonucleic acid sodium salt from calf thymus, Type I, fibers (ctDNA) purchased from Sigma Aldrich.
Geneticin (G418 Sulphate) was purchased from Fischer Scientific.
Quantofix peroxides test sticks were purchased from Sigma Aldrich.
Any further materials are specified in the appropriate section.

2.2.1 Synthesis of the Starting Materials

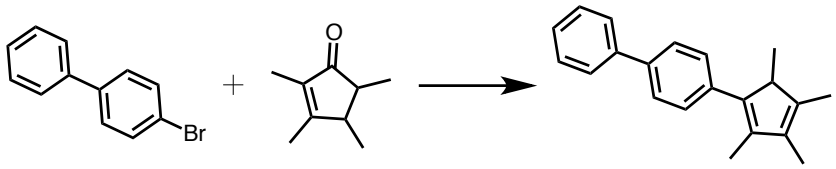

Figure 2.1: Synthesis of 3-biphenyl-1,2,4,5-tetramethyl-1,3-cyclopentadiene ($Cp^{xbiph}H$)

Based on previously reported methods,[92] a solution of 4-bromobiphenyl (18.65 g, 80 mmol) in dry THF (300 mL) was treated dropwise with n-butyl lithium (50 mL, 80 mmol, 1.6 M in hexanes) and stirred at 195 K for 4 h. 2,3,4,5-tetramethyl-2-cyclopentenone (14.31 mL, 96 mmol) was added and the reaction was allowed to warm to ambient temperature whilst stirring over 18 h. The resulting yellow solution was acidified with HCl (36%). The aqueous solution was extracted with diethyl ether (2 x 50 mL), dried over anhydrous $MgSO_4$, filtered, allowed to air dry, the volume reduced under vacuum and the resulting oily substance stored at 277 K for 18 h. The product was washed once with cold hexane and filtered to leave a yellow/orange powder. A second crop was obtained from the filtrate by crystallisation at 277 K. Yield: 15 g (69 %) ^{1}H-NMR (400 MHz, $CDCl_3$) δ_H = 7.67-7.62 (4H, m), 7.48-7.45 (2H, m), 7.37-7.35 (3H, m), 3.30-3.25 (1H, m), 2.12 (3H, s), 1.98 (3H, s), 1.92 (3H, s), 1.04 (2H, d, J = 7.5 Hz).

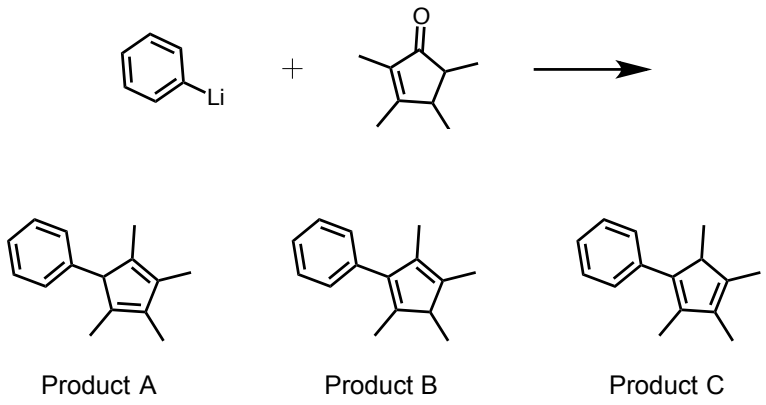

Figure 2.2: Synthesis of 3-phenyl-1,2,4,5-tetramethyl-cyclopentadiene ($Cp^{xph}H$)

Based on previously reported methods,[93] a solution of 2,3,4,5-tetramethyl-2-cyclopentenone (12 mL, 80 mmol) was treated dropwise with a solution of phenyllithium (50 mL, 90 mmol, 1.8 M in dibutyl ether) under nitrogen. The solution was kept at 273 K using ice water and NaCl. The reaction was allowed to warm to ambient temperature whilst stirring over 18 h. The resulting yellow solution was cooled by direct addition of ice and acidified with HCl (36%). The aqueous solution was extracted with diethyl ether (3 x 50 mL) and washed once with brine then the combined organic portions dried over anhydrous $MgSO_4$, filtered and the solvents evaporated to dryness under vacuum. The product was purified by distillation. Yield: 12.2 g (77 %) ^{1}H-NMR (400 MHz, $CDCl_3$) δ_H = 7.60-7.58 (0.17 H, m), 7.45-7.41 (0.17 H, m), 7.38-7.33 (1.5 H, m), 7.27-7.23 (1.6H, m), 7.20-7.14 (1.1 H, m), 6.93-6.91 (0.36 H, m), 3.22-3.17 (0.48 H, m), 2.72-2.66 (0.19 H, m), 2.00 (1.5 H, s), 1.93 (1.4 H, s), 1.89 (0.6 H, s), 1.86 (2.1 H, s), 1.83 (1.17 H, s), 1.73 (0.6 H, s), 1.67 (1.2 H, s), 1.13 (0.7 H, d, J = 7.5 Hz), 0.95 (1.7 H, d, J = 7.5 Hz).

Three products are formed, hence the fractional integrals. The ratio of the products is not 1:1:1 but for the purposes intended this mixture of products is suitable for use in further synthesis as any of them will form the same aromatic tetramethylcyclopentane ring when coordinated to an iridium centre in the ways described in section 2.2.2.

2.2.2 Synthesis of Iridium Dimers

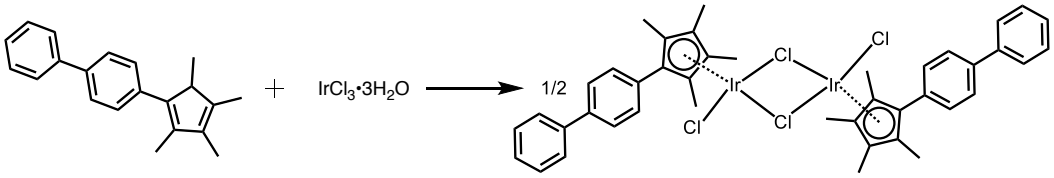

Figure 2.3: Synthesis of $[(Cp^{xbiph})IrCl_2]_2$

Based on previously reported methods,[94] $IrCl_3 \bullet 3H_2O$ (0.8 g, 2.27 mmol) and 3-biphenyl-1,2,4,5-tetramethyl-1,3-cyclopentadiene (1.5 g, 5.46 mmol) were placed in a microwave vial and dissolved in MeOH (10 mL), degassed with N_2 and the solution sonicated at ambient temperature for 5 min. The vial was put in a microwave reactor (438 K, 150 W, 250 psi, 5 min). The reaction was then allowed to reach ambient temperature and *n*-pentane (10 mL) was added and the mixture stirred for 5 min. The contents of the vial were then decanted onto a funnel with a frit filter under suction. The orange/red solid collected on the filter was then placed in a beaker and stirred in diethyl ether for 5 min before filtering again. This was repeated 3 times to yield a bright red residue. (947 mg, 32 %) ^{1}H-NMR (400 MHz d_6-DMSO) δ_H = 7.76-7.66 (12H, m), 7.52-7.46 (4H, m), 7.43-7.37 (2H, m), 1.74 (12H, s), 1.71 (12H, s)

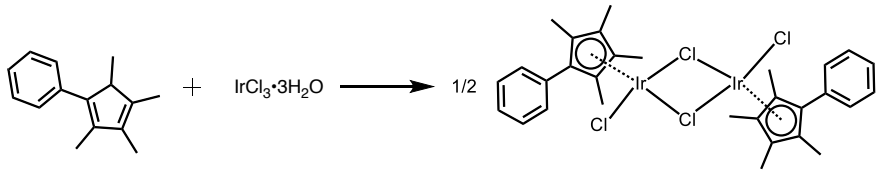

Figure 2.4: Synthesis of $[(Cp^{xph})IrCl_2]_2$

Based on previously reported methods,[92] $IrCl_3 \bullet 3H_2O$ (1.0 g, 2.84 mmol) was placed in a microwave vial and dissolved in MeOH (10 mL), degassed with N_2 and the solution sonicated at ambient temperature for 5 min. 3-phenyl-1,2,4,5-tetramethyl-1,3-cyclopentadiene (1.3 g, 6.70 mmol) was added and the vial put in a microwave reactor (438 K, 150 W, 250 psi, 5 min).

The reaction was then allowed to reach ambient temperature and *n*-pentane (10 mL) was added and the mixture stirred for 5 min. The contents of the vial were then decanted onto a funnel with a frit filter under suction. The orange/red solid collected on the filter was then placed in a beaker and stirred in ether for 5 min before filtering again. This was repeated 3 times to yield a bright red residue. (688 mg, 22 %) ^{1}H-NMR (400 MHz d_6-DMSO) δ_H = 7.62-7.56 (4H, m), 7.43-7.38 (6H, m), 1.72 (12H, s), 1.66 (12H, s)

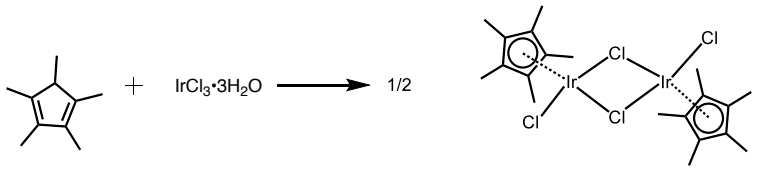

Figure 2.5: Synthesis of $[(Cp^*)IrCl_2]_2$

Based on previously reported methods,[95] $IrCl_3 \bullet 3H_2O$ (1.0 g, 2.84 mmol) was placed in a microwave vial and dissolved in MeOH (10 mL), degassed with N_2 and the solution sonicated at ambient temperature for 5 min. 1,2,3,4,5-Pentamethylcyclopentadiene (2.8 g, 3.2 mL, 20.4 mmol) was added and the vial put in a microwave reactor (438 K, 150 W, 250 psi, 5 min). The reaction was then allowed to reach ambient temperature and *n*-pentane (10 mL) was added and the mixture stirred for 5 min. The contents of the vial were then decanted onto a funnel with a frit filter under suction. The orange/red solid collected on the filter was then placed in a beaker and stirred in ether for 5 min before filtering again. This was repeated 3 times to yield a bright red residue. (1.0 g, 69 %) ^{1}H-NMR (400 MHz d_6-DMSO) δ_H = 1.63 (30H, s)

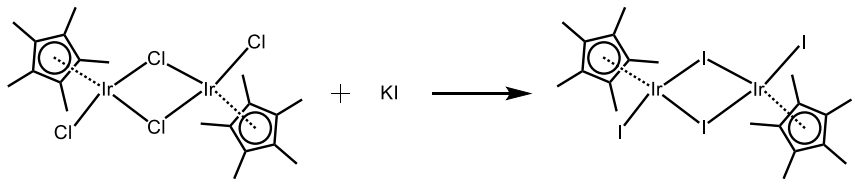

Figure 2.6: Synthesis of $[(Cp^*)IrI_2]_2$

A solution of $[(Cp^*)IrCl_2]_2$ (200 mg, 0.25 mmol) in 20% MeOH:H_2O was heated to 353 K and the temperature maintained for 1 h. KI (4.16 g, 25.10 mmol) was added and the solution changed to a deep, cloudy orange. This was kept overnight at 277 K. This was reduced to dryness under vacuum, redissolved in DCM and filtered. The filtrate was recrystallized overnight at 277 K in DCM:diethyl ether, filtered and washed once with diethyl ether to leave a dark red-orange ppt. (173 mg, 59 %) ^{1}H-NMR (300 MHz, $CDCl_3$) δ_H = 1.83 (30H, s)

2.2.3 Synthesis of Azopyridine Ligands

Where purchase of the desired ligand was either not possible or not financially viable, ligands were instead synthesised from commercially available starting materials as described (Figures 2.7 – 2.9) based on previous literature reports.[96]

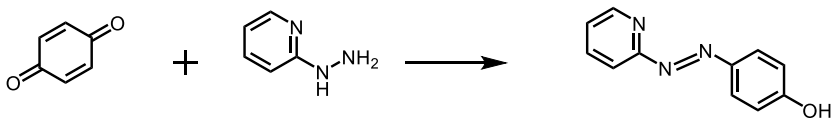

Figure 2.7: Synthesis of 4-(pyridin-2-yldiazenyl)phenol (azpyOH)

Benzoquinone (1.479 g, 13.6 mmol) was dissolved in water (100 mL) and perchloric acid (9 mL). 2-hydrazinopyridine (1.493 g, 13.6 mmol) in water (20 mL) was added dropwise and the solution stirred at ambient temperature for 1 h. The solution turned reddish brown. The solution was filtered and washed quickly with cold water (1 x 10 mL) to leave an orange crystalline ppt. This was dissolved in MeOH (50 mL) and formic acid (5 mL) and ammonia gas was bubbled through the mixture for 1 h. The mixture was left for 72 h and red crystals formed. These were filtered out and dried under vacuum. Yield: 1.106 g (41 %) ^{1}H-NMR (400 MHz 80% CD_3CN:20% D_2O) δ_H = 8.63 (1H, d, J = 6.0 Hz), 8.35 (1H, d, J = 6.0 Hz), 7.92 (2H, d, J = 8.0 Hz), 7.75 (1H, m), 7.49 (1H, m), 7.00 (2H, d, J = 8.0 Hz)

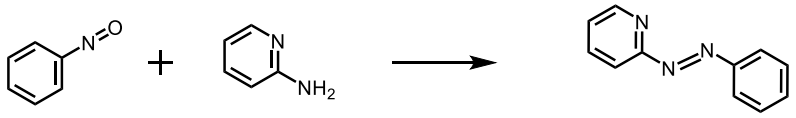

Figure 2.8: Synthesis of 2-(phenyldiazenyl)pyridine (azpy)

2-Aminopyridine (200 mg, 2.13 mmol) and aqueous tetramethylammonium hydroxide solution (2.5 mL) was put in a microwave vial and dissolved in

pyridine (2.5 mL). To this was added nitrosobenzene (300 mg, 2.80 mmol) in pyridine (5.0 mL) and the vial put in a microwave reactor (438 K, 150 W, 250 psi, 5 min). The solution was allowed to cool to 298 K and extracted with toluene (3 x 5 mL). The toluene fraction was washed with brine, dried with $MgSO_4$ and as much solvent as possible was removed under vacuum. The crude product was purified by column chromatography using silica and a 2:1 mixture of cyclohexane/ethyl acetate as eluent (Rf of product = 0.68). The product was clearly visible as a deep red band on the column. The pure compound was dried under vacuum and stored at 277 K. Yield: 216.7 mg (62 %) ^{1}H-NMR (400 MHz d_6-DMSO) δ_H = 8.73 (1H, d, J = 6.0 Hz), 8.01 (1H, t, J = 8.0 Hz), 7.96 (2H, m), 7.74 (1H, d, J = 8.0), 7.65 (3H, m), 7.60 (1H, d, J = 6.0 Hz)

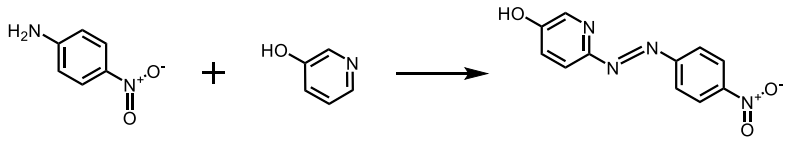

Figure 2.9: Synthesis of 6-((4-nitrophenyl)diazenyl)pyridin-3-ol ($HOazpyNO_2$)

Sodium nitrite (6.8 g, 100 mmol) and 4-nitroaniline (13.8 g, 100 mmol) were added to sterile distilled water (200 mL) and kept at 273 – 274 K in an NaCl and ice-filled dewer. The resulting slurry was stirred vigorously and 35% HCl (39.5 mL) was added slowly. This resulting slurry was added to a solution of 3-hydroxypyridine (9.5 g, 100 mmol) and potassium hydroxide tablets (5.6 g, 100 mmol) dissolved in sterile distilled water (150 mL) and cooled to 273 – 274 K. This yielded a bright orange solution. 2 M potassium hydroxide solution was added until to solution became basic and dark red. The dark red reaction mixture was stirred at 273 – 274 K for 1 h. Acetic acid (25 mL) was added slowly as the reaction was allowed to room temperature and the resulting orange solution filtered under suction to complete dryness. The solid orange precipitate was taken up in ethanol and treated with active carbon. The resulting mixture was left to cool overnight at 277 K. The mixture was then filtered, the volume of the filtrate was reduced under vacuum until the onset of precipitation. The solution was then cooled at 277 K until the product

precipitated out as a dark orange solid. Yield: 2.5 g (10 %) ^{1}H-NMR (400 MHz d_6-DMSO) δ_H = 8.42 (2H, d, J = 9.0 Hz), 8.27 (1H, d, J = 3.0 Hz), 8.06 (2H, d, J = 9.0 Hz), 8.84 (1H, ds, J = 9.0 Hz), 7.38 (1H, dd, J = 9.0, 3.0 Hz)

2.2.4 Synthesis of Ir(III) Half-Sandwich Complexes

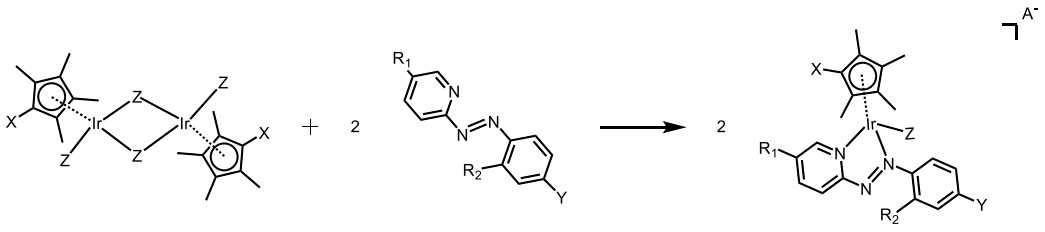

Figure 2.10: General synthesis scheme for Ir(III) complexes in this work

All the complexes in this work can be synthesised with high yields and purity by stirring the appropriate dimer and ligand in commercially available anhydrous organic solvent following the scheme shown (Figure 2.10). The exact conditions required to synthesise each complex are detailed in the corresponding chapter in which they are first introduced.

2.3 Methods

Unless specified otherwise data were processed using R,[97] Origin 9.1[98] or Microsoft Excel.

2.3.1 Aquation Studies

Aquation studies were carried out by 600 MHz ^{1}H-NMR of solutions of complexes over 24 h in 10% d_6-DMSO:D_2O, 0.1% 1,4-dioxane at 310 K. All solutions were pre-warmed to 310 K and spectra were taken approximately 10 min after addition to D_2O. Experiments were carried out in parallel under the same conditions with 120 mM NaCl to simulate the chloride concentration in the cell medium used for *in vitro* cancer cell studies. The concentration of complex used is described in the corresponding section.

2.3.2 LC-MS

Complexes were dissolved in acetonitrile. All LC-MS experiments (purity determination/relative hydrophobicity and nucleotide binding) were carried out in HPLC-grade H_2O with varying percentages of acetonitrile at the gradient shown in Figure 2.11. 0.1% TFA was added to both mobile phases. LC was carried out on an Agilent 1200 equipped with a variable wavelength detector and 100 µL loop using a 250 x 4.6 mm Agilent Zorbax Eclipse Plus C18 column in reverse phase with a 5 µm pore size.

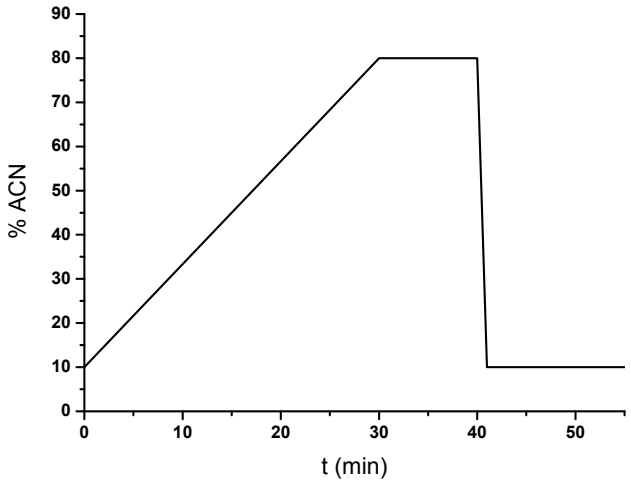

Figure 2.11: Solvent gradient used for LC-MS experiments in this work.

2.3.3 Cancer Cell Studies

Of the cell lines used in this work, A2780 human ovarian carcinoma, A2780cis human ovarian carcinoma with acquired CDDP resistance, A549 human Caucasian lung carcinoma, and MRC-5 normal human fetal lung fibroblasts were obtained from the ECACC. EBV-positive and -negative OE19 human Caucasian oesophageal carcinomas, CNE1, CNE2, and SUNE-1 human nasopharyngeal carcinomas provided by Dr. Chris Dawson, University of Birmingham.

2.3.3.1 Cell Maintenance

Cells grown in Roswell Park Memorial Institute medium (RPMI-1640) or Dulbecco's Modified Eagle Medium (DMEM). Media were supplemented with 10% foetal calf serum (FCS), 1% of 2 mM L-glutamine (20 μM) and 1% of 2 mM penicillin/streptomycin (20 μM). All cell incubation was at 310 K in 5% CO_2 humidified atmosphere. Cells were grown as adherent monolayers in either 25 cm^2, 75 cm^2, 175 cm^2 culture flasks and split when approximately 90% confluence was reached by incubation with 0.25% trypsin/EDTA (0.1 mM trypsin,

0.9 mM EDTA). EBV infected cell lines were subcultured in medium and supplemented with 400 mg/ml Geneticin (G418 Sulphate) 12-24 h after plating.

2.3.3.2 Antiproliferative Activity

To carry out antiproliferative assays, cells were grown to approximately 90% confluence before use. Medium was removed by suction and cells washed twice with phosphate-buffered saline (PBS). Cells were then incubated with trypsin/EDTA for 5 min to create a cell suspension and medium was then added to quench the activity of the trypsin to avoid damage to cells. A single cell suspension was obtained by thorough mixing by pipette and the cell concentration measured by haemocytometer. This suspension was diluted so that 150 μL of cell solution per well resulted in cells seeded in 96-well plates at 5,000 cells per well. Cells were incubated for 48 h then a solution of the complex to be tested was prepared at 100 μM in 5% DMSO, 95% medium. Five further dilutions were prepared at various concentrations from this solution and cells incubated with each concentration for 24 h. CDDP was used as a positive control and prepared in the same way. Medium was used a the negative control. Each concentration of complex was tested on 3 wells of two plates, to check for intra-plate variation. Next, the complex solutions were removed from the plate by aspiration and the plates incubated with 200 μL of fresh medium for 72 h.

To measure cell survival percentages, the sulforhodamine B (SRB) assay was used. The SRB assay is widely employed to investigate drug cytotoxicity against cells *in vitro*.[99] The SRB dye binds to the basic amino acid residues of proteins and is an accurate measure of cell mass, and, by extrapolation, cell survival.[100] Cells were fixed with 50 μL of trifluoroacetic acid (TFA) at 277 K for 1 h. The TFA was then removed by gentle washing with cold tap water and the plates dried in air. Cells were stained with 50 μL of 0.4% SRB dye in 1% acetic acid for 30 min at ambient temperature. The plates were then gently washed with 1% acetic acid to remove excess dye and the plates dried again. To solubilise the bound dye, 200 μL of 10 mM of pH 10.5 Tris base solution was added to each well and the plates left for 1 hr whilst being gently tilted.

Absorbance at 490 nm was measured for each well using a plate reader and cell survival percentages calculated by comparison with the negative controls. IC_{50} values were calculated by plotting the cell survival percentage against the control and fitting a boltzmann sigmoidal curve to determine the midpoint.

In cases where a sigmoidal curve could not be well-fitted to the data points, either the experiment was repeated with complex at different concentrations, the IC_{50} determined to lie within a concentration range, or the data presented in a non-IC_{50} format.

Antiproliferative screenings against A2780, OE19 and SUNE-1 cell lines carried out by Dr. Isolda Romero-Canelón, Ji-Inn Song and Bindy Heer.

2.3.4 Flow Cytometry Experiments

Cells were seeded on 6-well plates at 1 million cells per well in complex-free medium and incubated for 24 h at 310 K. The cells were then exposed to an equipotent (at IC_{50} concentration) solution of complex for 24 h after which the supernantant was removed and the cells washed with PBS. Cells were then harvested using trypsin/EDTA and further treatment and staining carried out as appropriate to the experiment. Finally, cell pellets were resuspended and washed with PBS before analysis in a flow cytometer.

2.3.4.1 ROS and Superoxide Generation

After harvesting, cells were stained using a buffered solution of green/orange fluorescent reagents according to the instructions in the ROS/Superoxide detection kit (Enzo Life Sciences). FL1 channel on the flow cytometer used to measure total ROS. FL2 channel used to measure superoxide.

2.3.4.2 Mitochondrial Membrane Depolarisation

After harvesting, cells were stained using the JC10 mitochondrial membrane potential assay kit according to the manufacturer's instructions. FL2

channel on the flow cytometer used to measure reduction in JC10 fluorescence. For positive controls cells were exposed to 1 μM carbonyl cyanide 3-chlorophenylhydrazone (CCCP) for 15 min. These experiments were carried out at Sun Yat-sen University Cancer Center, Guangzhou, China.

2.3.4.3 Cell Cycle Analysis

After harvesting, cells were fixed using cold 70% EtOH. Propidium iodide (PI)/RNase solution was used to stain cell DNA before flow cytometry. FL2 channel on the flow cytometer used to measure PI fluorescence.

2.3.4.4 Induction of Apoptosis

After harvesting, cells were stained using a buffered solution of annexin V/PI according to the instructions in the annexin V-FITC apoptosis detection kit (Sigma-Aldrich). FL1 channel on the flow cytometer used to measure annexin V fluorescence. FL2 channel used to measure PI fluorescence.

Chapter 3

Anticancer Structure-Activity Relationships

3.1 Introduction

Resistance to current anticancer therapeutics is a major clinical problem, as are the side-effects associated with many current treatments. By generating novel chemotherapeutics we aim to widen the spectrum of treatable cancers, overcome drug-resistance and reduce side-effects, with the ultimate aim of improving patient prognoses and quality of life.

Precious metal-based complexes have been a cornerstone of anticancer drug development since the discovery of cisplatin (CDDP). Since then, other precious metals have been utilised in an effort to explore more chemical space and expand the range of available therapeutics to combat cancer. Complexes of Pt, Ru, Rh, Os and Ir have all been reported to have anticancer properties, however of these metals, Ir is the least explored in publications.[101]

Previous investigations into the properties of organoiridium anticancer drugs have shown promise and potent complexes with a variety of mechanisms of action (MoAs) have been generated. Despite this, an organoiridium anticancer drug has yet to reach the clinics. An organoiridium azopyridine complex

$[Cp^{xph}Ir(azpyNMe_2)Cl]PF_6$ (Complex **2**) has shown impressive cytotoxicity against a panel of 60 cancer cell lines and has been associated with targeting mitochondrial metabolism and increasing redox stress in cancer cells.[102] Its MoA is not yet fully understood, so in this chapter further research into its MoA is carried out towards understanding how this complex kills cancer cells.

In this chapter an extensive and diverse library of a further 18 organoiridium(III) azopyridine complexes are synthesised based on complex **2**.

This library is comprised of families of complexes bearing 6 different bidentate azopyridine ligands differing only in the functional groups on the azopyridine phenyl and pyridine rings. Within most of these families, Cp^{xbiph}, Cp^{xph} and Cp* analogues are synthesised and investigated to test the effect of the Cp system within, and between, families. Additionally, analogues of selected complexes are synthesised bearing different monodentate halido ligands or counterions to assess the effect of these structural features on their chemical and biological properties.

The complexes synthesised were designed in this way so that structure-activity relationships can be drawn between their functional groups and their anticancer activity. By doing so, this research can guide future organoiridium drug development towards generating complexes with greater anticancer potency.

MoA studies are carried out on a subset of these complexes to assess their solution chemistry, capacity to oxidise NADH, induce apoptosis, generate ROS and depolarise the mitochondrial membrane. Finally, a thorough statistical analysis is carried out on data from a large-scale pharmaco-genomic screen of complex **2** against ca. 900 cell lines to further elucidate the MoAs of this family of complexes.

3.2 Experimental Methods

3.2.1 Synthesis and Characterization of Complexes

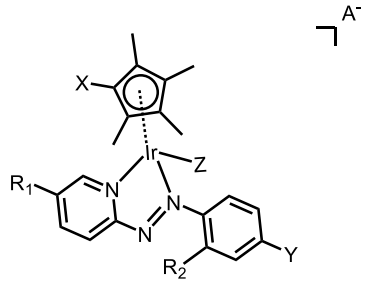

Complex	X	Y	Z	A	R_1	R_2
1	Biph	NMe_2	Cl	PF_6	H	H
2	Ph	NMe_2	Cl	PF_6	H	H
3	Me	NMe_2	Cl	PF_6	H	H
4	Me	NMe_2	I	PF_6	H	H
5	Biph	OH	Cl	PF_6	H	H
6	Ph	OH	Cl	PF_6	H	H
7	Me	OH	Cl	PF_6	H	H
8	Me	OH	Cl	Cl	H	H
9	Me	OH	I	PF_6	H	H
10	Me	OH	I	I	H	H
11	Biph	OH	Cl	PF_6	H	OH
12	Me	OH	Cl	PF_6	H	OH
13	Biph	H	Cl	PF_6	OH	H
14	Ph	H	Cl	PF_6	OH	H
15	Me	H	Cl	PF_6	OH	H
16	Biph	NO_2	Cl	PF_6	H	H
17	Ph	NO_2	Cl	PF_6	H	H
18	Me	NO_2	Cl	PF_6	H	H
19	Biph	NEt_2	Cl	PF_6	Br	OH

Figure 3.1: Overview of all complexes studied in this work. Lines separate complexes of different families by azopyridine ligand.

Complex 1 – $[Cp^{xbiph}Ir(azpyNMe_2)Cl]PF_6$

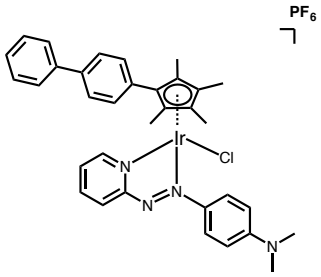

$[(Cp^{xbiph})IrCl_2]_2$ (123 mg, 0.115 mmol, 1 mol. equiv.) and 4-(2-pyridylazo)-N,N-dimethylaniline ($azpyNMe_2$) (51 mg, 0.230 mmol, 2 mol. equiv.) were dissolved in DCM (20 mL) and stirred overnight at ambient temperature. The solvent was completely removed under vacuum in a rotary evaporator and the compound redissolved in the minimum amount of MeOH. NH_4PF_6 (187 mg, 1.147 mmol, 5 mol. equiv.) was added and the solution stirred then stored overnight at 277 K. The resulting mixture was filtered through a frit and washed once quickly with cold MeOH (10 mL), the remaining solid material collected and redissolved in DCM then filtered once more. Diethyl ether was added to the filtrate until the onset of precipitation and the mixture left to crystallise overnight at 277 K. Recrystallisation of 1 mg in the minimum amount of MeOH/acetone and slow addition of diethyl ether by vapours using a small vial with pierced lid in large vial of diethyl ether system over many weeks yielded an x-ray quality crystal. This complex is novel.

Yield: 180 mg (90%)

^{1}H-NMR (400 MHz, CD_3CN): δ_H = 8.50 (1H, d, J = 5.5 Hz), 8.40 (1H, d, J = 8.2 Hz), 8.17 (1H, t, J = 7.9 Hz), 8.07 (2H, d, J = 9.4 Hz), 7.74 – 7.71 (4H, m), 7.58 (1H, t, J = 6.7 Hz), 7.55 – 7.51 (2H, m), 7.47 – 7.43 (3H, m) 6.77 (2H, d, J = 9.5 Hz) 3.25 (6H, s), 1.73 – 1.70 (9H, m), 1.55 (3H, s).

^{13}C-NMR-APT (125 MHz, acetone-d_6): δ_C = 166.76 (s, C), 156.08 (s, C), 149.82 (s, C), 143.74 (s, CH/CH_3), 142.40 (s, C), 141.45 (s, C), 139.71 (C), 130.71 (s, CH/CH_3), 130.53 (s, CH/CH_3), 130.48 (s, CH/CH_3), 129.75 (s, CH/CH_3), 129.11 (s, CH/CH_3), 129.06 (s, CH/CH_3), 128.05 (s, C), 127.96

(s, CH/CH_3), 127.57 (s, CH/CH_3), 127.50 (s, CH/CH_3), 126.87 (s, CH/CH_3), 126.80 (s, CH/CH_3), 126.43 (s, CH/CH_3), 123.80 (s, CH/CH_3), 112.44 (s, CH/CH_3), 101.83 (s, C), 99.53 (s, C), 91.52 (s, C), 90.23 (s, C), 85.66 (s, C), 39.82 (s, CH/CH_3), 9.17 (s, CH_3), 9.08 (s, CH_3), 8.50 (s, CH_3), 7.96 (s, CH_3).

ESI-MS (MeOH): m/z = 727.2 $[M - PF_6]^+$

Elemental Analysis: Calc'd for **1**•MeOH: C: 46.48, H: 4.35, N: 6.20. Found: C: 46.14, H: 3.92, N: 6.38.

Complex 2 – $[Cp^{xph}Ir(azpyNMe_2)Cl]PF_6$

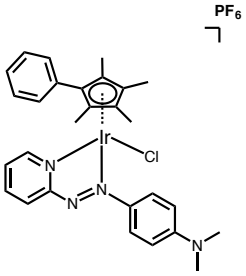

Synthesised as above using $[(Cp^{xph})IrCl_2]_2$ (141 mg, 0.154 mmol, 1 mol. equiv.) and 4-(2-pyridylazo)-N,N-dimethylaniline ($azpyNMe_2$) (69 mg, 0.306 mmol, 2 mol. equiv.). This complex has been previously reported.[102]

Yield: 172 mg (71%)

^{1}H-NMR (400 MHz, CD_3CN): δ_H = 8.46 (1H, d, J = 5.6 Hz), 8.40 (1H, d, J = 8.2 Hz), 8.16 (1H, t, J = 7.8 Hz), 8.07 (2H, d, J = 9.4 Hz), 7.56 (1H, t, J = 6.7 Hz), 7.52 – 7.43 (3H, m), 7.32 (2H, d, J = 7.2 Hz) 6.80 (2H, d, J = 9.5 Hz) 3.29 (6H, s), 1.72 (3H, s), 1.70 (3H, s), 1.68 (3H, s), 1.45 (3H, s)

^{13}C-NMR-APT (125 MHz, acetone-d_6): δ_C = 166.73 (s, C), 156.11 (s, C), 149.78 (s, CH/CH_3), 143.74 (s, C), 142.39 (s, CH/CH_3), 129.87 (s, CH/CH_3), 129.74 (s, CH/CH_3), 129.21 (s, CH/CH_3), 129.08 (s, CH/CH_3), 126.40 (s, CH/CH_3), 123.79 (s, CH/CH_3), 112.47 (s, CH/CH_3), 102.32 (s, C), 99.86 (s, C), 91.32 (s, C), 89.97 (s, C), 85.55 (s, C), 39.85 (s, CH/CH_3), 9.07 (s, CH_3), 8.99 (s, CH_3), 8.50 (s, CH_3), 7.94 (s, CH_3).

ESI-MS (MeOH): m/z = 651.1 $[M - PF_6]^+$

Elemental Analysis: Calc'd: C: 41.97, H: 4.53, N: 6.99 Found: C: 41.87, H: 3.81, N: 7.05.

Complex 3 – $[Cp^*Ir(azpyNMe_2)Cl]PF_6$

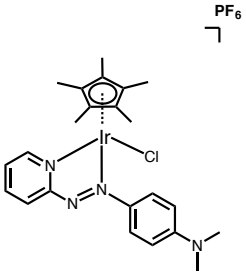

Synthesised as above using $[(Cp^*)IrCl_2]_2$ (135 mg, 0.170 mmol). Recrystallisation of 1 mg in the minimum amount of DCM and slow addition of pentane by vapours using a small vial with pierced lid in large vial of *n*-pentane system over many weeks yielded an x-ray quality crystal. This complex has been previously synthesised.[94]

Yield: 198 mg (79%)

^{1}H-NMR (400 MHz, CD_3CN): δ_H = 8.50 (1H, d, J = 5.5 Hz), 8.40 (1H, d, J = 8.2 Hz), 8.17 (1H, t, J = 7.9 Hz), 8.07 (2H, d, J = 9.4 Hz), 7.69 (1H, t, J = 6.6 Hz) 6.93 (2H, d, J = 9.4) 3.32 (6H, s), 1.73 – 1.70 (9H, m), 1.58 (15H, s)

^{13}C-NMR-APT (125 MHz, acetone-d_6): δ_C = 166.56 (s, C), 156.00 (s, C), 150.12 (s, CH/CH_3), 143.76 (s, C), 142.19 (s, CH/CH_3), 129.51 (s, CH/CH_3), 126.49 (s, CH/CH_3), 123.64 (s, CH/CH_3), 112.35 (s, CH/CH_3), 92.58 (s, C), 39.83 (s, CH/CH_3), 7.95 (s, CH_3).

ESI-MS (MeOH): m/z = 589.1 $[M - PF_6]^+$

Elemental Analysis: Calc'd for **3**•H_2O: C: 36.73, H: 4.15, N: 7.45 Found: C: 36.70 , H: 3.85, N: 7.39.

Complex 4 – $[Cp^*Ir(azpyNMe_2)I]PF_6$

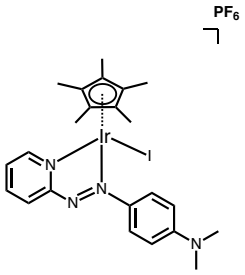

$[(Cp^*)IrI_2]_2$ (70 mg, 0.06 mmol, 1 mol. equiv.) and 4-(2-pyridylazo)-N,N-dimethylaniline ($azpyNMe_2$) (27 mg, 0.12 mmol, 2 mol. equiv.) were dissolved in DCM (20 mL) and stirred overnight at ambient temperature. The solvent was completely removed under vacuum in a rotary evaporator and the compound redissolved in the minimum amount of MeOH. NH_4PF_6 (49 mg, 0.30 mmol, 5 mol. equiv.) was added and the solution stirred then stored overnight at 277 K. The resulting mixture was then filtered through a frit and washed with diethyl ether (3 x 10 mL) and the remaining solid material collected and redissolved in DCM then filtered once more. Diethyl ether was added to the filtrate until the onset of precipitation and the mixture left to crystallise overnight at 277 K. This complex is novel.

Yield: 80 mg (81%)

^{1}H-NMR (500 MHz, CD_3CN): δ_H = 8.70 (1H, d, J = 5.5 Hz), 8.43 (1H, d, J = 8.0 Hz), 8.14 (1H, t, J = 7.5 Hz), 8.09 (2H, d, J = 9.5 Hz), 7.60 (1H, t, J = 7.0 Hz), 6.88 (2H, d, J = 9.0 Hz), 3.31 (6H, s), 1.71 (15H, s).

^{13}C-NMR-APT (125 MHz, CD_3CN): δ_C = 166.85 (s, C), 156.47 (s, C), 151.35 (s, CH_3), 144.76 (s, C), 142.18 (s, CH_3), 130.48 (s, CH_3), 126.01 (s, CH_3), 124.14 (s, CH_3), 112.62 (s, CH_3), 94.18 (s, C), 40.34 (s, CH_3), 9.25 (s, CH_3).

ESI-MS (MeOH): m/z = 681.1 $[M - PF_6]^+$

Elemental Analysis: Calc'd for **4**•$2H_2O$: C: 32.06, H: 3.86, N: 6.50. Found: C: 32.14, H: 3.33, N: 6.31.

Complex 5 – $[Cp^{xbiph}Ir(azpyOH)Cl]PF_6$

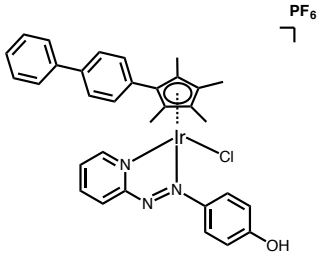

$[(Cp^{xbiph})IrCl_2]_2$ (73 mg, 0.07 mmol, 1 mol. equiv.) and 4-(pyridin-2-yldiazenyl)phenol (azpyOH) (27 mg, 0.14 mmol, 2 mol. equiv.) were dissolved in DCM (20 mL) and stirred overnight at ambient temperature. The solvent was completely removed under vacuum in a rotary evaporator and the compound redissolved in the minimum amount of MeOH. NH_4PF_6 (48 mg, 0.29 mmol, 5 mol. equiv.) was added and the solution stirred then stored overnight at 277 K. The mixture was then filtered through a frit and washed once quickly with cold ether and the remaining solid material collected and redissolved in acetone then filtered once more the same way. The solution was dried under vacuum and the solid material redissolved in MeOH. Diethyl ether was added to the filtrate until the onset of precipitation and the mixture left to crystallise at 277 K. Recrystallisation of 1 mg in the minimum amount of MeOH/acetone and slow addition of diethyl ether by vapours using a small vial with pierced lid in large vial of diethyl ether system over many weeks yielded an x-ray quality crystal. This complex is novel.

Yield: 74 mg (64%)

^{1}H-NMR (400 MHz, CD_3CN): δ_H = 8.66 (1H, d, J = 8.2 Hz), 8.50 (1H, d, J = 5.2 Hz), 8.27 (1H, t, J = 7.8 Hz), 7.97 (2H, d, J = 8.6 Hz), 7.77 – 7.70 (5H, m), 7.55 – 7.52 (2H, m), 7.50 – 7.44 (3H, m), 7.18 (2H, d, J = 8.6 Hz), 1.77 (3H, s), 1.65 (6H, m), 1.50 (3H, s).

^{13}C-NMR-APT (125 MHz, CD_3CN): δ_C = 166.49 (s, C), 165.44 (s, C), 150.40 (s, CH/CH_3), 147.30 (s, C), 143.42 (s, CH/CH_3), 142.16 (s, C), 140.27 (s, C), 131.04 (s, CH/CH_3), 129.71 (s, CH/CH_3), 128.65 (s, CH/CH_3), 128.55

(s, CH/CH_3), 128.25 (s, CH/CH_3), 127.96 (s, C), 127.57 (s, CH/CH_3), 127.48 (s, CH/CH_3), 117.17 (s, CH/CH_3), 104.77 (s, C), 100.45 (s, C), 94.41 (s, C), 91.15 (s, C), 86.73 (s, C), 9.85 (s, CH_3), 9.53 (s, CH_3), 9.02 (s, CH_3), 8.59 (s, CH_3).

ESI-MS (MeOH): m/z = 700.1 $[M - PF_6]^+$

Elemental Analysis: Calc'd for **5**•2H_2O: C: 43.61, H: 3.89, N: 4.77. Found: C: 44.00, H: 3.67, N: 4.85.

Complex 6 – $[Cp^{xph}Ir(azpyOH)Cl]PF_6$

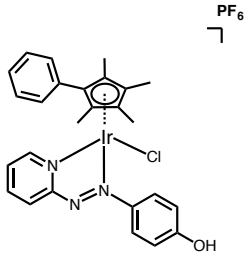

Synthesised as above using $[(Cp^{xph})IrCl_2]_2$ (36.9 mg, 0.040 mmol, 1 mol. equiv.) and 4-(pyridin-2-yldiazenyl)phenol (16.0 mg, 0.080 mmol, 2 mol. equiv.). This complex is novel.

Yield: 39.4 mg (63%)

^{1}H-NMR (400 MHz, $CDCl_3$): δ_H = 8.50 (1H, d, J = 7.9 Hz), 8.26 (1H, d, J = 5.5 Hz), 8.15 (1H, t, J = 7.8 Hz), 7.92 (2H, d, J = 8.6 Hz), 7.56 – 7.46 (4H, m), 7.32 (2H, d J = 7.3 Hz), 7.22 (2H, d, J = 8.4 Hz), 1.79 (3H, s), 1.67 (3H, s), 1.61 (3H, s), 1.43 (3H, s)

^{13}C-NMR-APT (125 MHz, CD_3CN): δ_C = 166.36 (s, C), 164.60 (s, C), 150.47 (s, CH/CH_3), 147.43 (s, C), 143.50 (s, CH/CH_3), 130.45 (s, CH/CH_3), 130.08 (s, CH/CH_3), 129.88 (s, CH/CH_3), 128.83 (s, C), 128.35 (s, CH/CH_3), 127.99 (s, CH/CH_3), 116.86 (s, CH/CH_3), 104.79 (s, C), 100.74 (s, C), 94.24 (s, C), 91.46 (s, C), 87.35 (s, C), 9.74 (s, CH_3), 9.43 (s, CH_3), 9.00 (s, CH_3), 8.57 (s, CH/CH_3).

ESI-MS (MeOH): m/z = 624.0 $[M - PF_6]^+$

Elemental Analysis: Calc'd for **6**•H_2O: C: 46.08, H: 4.17, N: 6.20. Found: C: 45.59, H: 3.91, N: 6.38.

Complex 7 – [Cp*Ir(azpyOH)Cl]PF_6

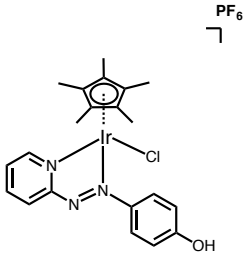

Synthesised as above using $[(Cp^*)IrCl_2]_2$ (56 mg, 0.70 mmol, 1 mol. equiv.). Recrystallisation of 1 mg in the minimum amount of MeOH and slow addition of diethyl ether by vapours using a small vial with pierced lid in large vial of diethyl ether system over 5 weeks at ambient temperature yielded an x-ray quality crystal. This complex is novel.

Yield: 73 mg (73%)

^{1}H-NMR (400 MHz, CD_3CN): δ_H = 8.77 (1H, d, J = 5.5 Hz), 8.66 (1H, d, J = 8.0 Hz), 8.31 (1H, t, J = 7.7 Hz), 7.95 (2H, d, J = 8.8 Hz), 7.87 (1H, t, J = 6.7 Hz), 7.28 (2H, d, J = 8.9 Hz), 1.57 (15H, s).

^{13}C-NMR-APT (125 MHz, CD_3CN): δ_C = 166.27 (s, C), 164.25 (s, C), 150.67 (s, CH/CH_3), 147.63 (s, C), 143.35 (s, CH/CH_3), 129.98 (s, CH/CH_3), 128.17 (s, CH/CH_3), 127.68 (s, CH/CH_3), 116.80 (s, CH/CH_3), 94.63 (s, C), 8.54 (s, CH_3).

ESI-MS (MeOH): m/z = 562.1 $[M - PF_6]^+$

Elemental Analysis: Calc'd: C: 35.67, H: 3.42, N: 5.94. Found: C: 35.67, H: 3.34, N: 5.90.

Complex 8 – [Cp*Ir(azpyOH)Cl]Cl

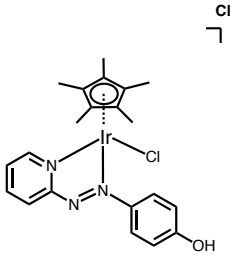

$[(\eta_5\text{-Cp*})IrI_2]_2$ (150 mg, 0.188 mmol, 1 mol. equiv.) and 4-(pyridin-2-yldiazenyl)phenol (azpyOH) (75.0 mg, 0.376 mmol, 2 mol. equiv.) were dissolved in DCM (50 mL) and stirred overnight at 323 K. The solvent was completely removed under vacuum in a rotary evaporator and the compound redissolved in the minimum amount of MeOH. Diethyl ether was added to the filtrate until the onset of precipitation and the mixture left to crystallise at 277 K. The mixture was then filtered through a frit and washed once quickly with cold ether and the remaining solid material collected and redissolved in MeOH then filtered once more the same way. Diethyl ether was added to the filtrate until the onset of precipitation and the mixture left to recrystallise at 277 K. This complex is novel.

Yield: 170 mg (61%)

^{1}H-NMR (400 MHz d_6-DMSO): δ_H = 8.75 (1H, d, J = 5.5 Hz), 8.63 (1H, d, J = 8.0 Hz), 8.29 (1H, t, J = 7.5 Hz), 7.96 (2H, d, J = 8.0 Hz), 7.85 (1H, t, J = 6.0 Hz), 7.20 (2H, d, J = 8.0 Hz), 1.57 (15H, s)

^{13}C-NMR-APT (125 MHz, d_6-DMSO): δ_C = 166.66 (s, C), 151.11 (s, C), 146.26 (s, CH/CH_3), 143.32 (s, C), 129.59 (s, CH/CH_3), 128.37 (s, CH/CH_3), 126.85 (s, CH/CH_3), 117.12 (s, CH/CH_3), 93.86 (s, CH/CH_3), 65.39 (s, C), 8.69 (s, CH_3).

ESI-MS (MeOH): m/z = 562.1 $[M - PF_6 - Cl]^+$

Elemental Analysis: Calc'd for **8**•H_2O: C: 40.97, H: 4.26, N: 6.83. Found: C: 40.91, H: 4.15, N: 6.59.

Complex 9 – [Cp*Ir(azpyOH)I]PF_6

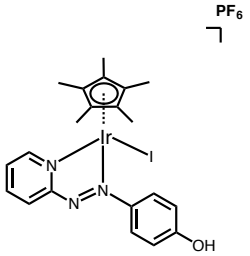

[(η_5-Cp*)IrI_2]$_2$ (88.9 mg, 0.08 mmol, 1 mol. equiv.) and 4-(pyridin-2-yldiazenyl)phenol (azpyOH) (30.5 mg, 0.16 mmol, 2 mol. equiv.) were dissolved in DCM (50 mL) and stirred overnight at 323 K. The solvent was completely removed in a rotary evaporator and the compound redissolved in MeOH (10 mL). 5 mL of this was taken and used to prepare [Cp*Ir(azpyOH)I]I (Complex **10**). NH_4PF_6 (62.3 mg, 0.38 mmol, 5 mol. equiv.) was added and the solution stirred then stored overnight at 277 K. The mixture was then filtered through a frit and washed once quickly with cold ether and the remaining solid material redissolved in acetone then filtered once more the same way. The solution was dried under vacuum and the solid material redissolved in MeOH. Diethyl ether was added to the filtrate until the onset of precipitation and the mixture left to crystallise at 277 K. This complex is novel.

Yield: 39 mg (78%)

^{1}H-NMR (400 MHz d_6-DMSO): δ_H = 8.84 (1H, d, J = 6.0 Hz), 8.77 (1H, d, J = 8.0 Hz), 8.28 (1H, t, J = 8.0 Hz), 7.99 (2H, d, J = 8.0 Hz), 7.81 (1H, t, J = 6.5 Hz), 7.08 (2H, d, J = 8.0 Hz), 1.70 (15H, s)

^{13}C-NMR-APT (125 MHz, CD_3CN): δ_C = 165.52 (s, C), 163.53 (s, C), 151.01 (s, CH/CH_3), 147.54 (s, C), 142.03 (s, CH/CH_3), 128.16 (s, CH/CH_3), 128.04 (s, CH/CH_3), 126.84 (s, CH/CH_3), 115.81 (s, CH/CH_3), 94.88 (s, C), 8.52 (s, CH_3).

ESI-MS (MeOH): m/z = 654.1 $[M - PF_6]^+$

Elemental Analysis: Calc'd for **9**•2MeOH: C: 32.03, H: 3.74, N: 4.87. Found: C: 32.23, H: 2.95, N: 5.28.

Complex 10 – [Cp*Ir(azpyOH)I]I

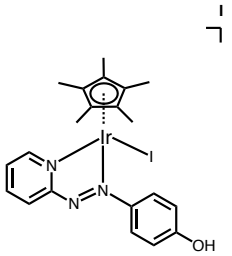

A 5 mL aliquot was taken from the reaction to synthesise complex **9** at the point described. Diethyl ether was added to this until the onset of precipitation and the mixture left to crystallise at 277 K. The mixture was then filtered through a frit and washed once quickly with cold ether and the remaining solid material collected and redissolved in MeOH then filtered once more the same way. Diethyl ether was added to the filtrate until the onset of precipitation and the mixture left to recrystallise at 277 K. This complex is novel.

Yield: 41 mg (82%)

^{1}H-NMR (400 MHz d_6-DMSO): δ_H = 8.85 (1H, d, J = 6.0 Hz), 8.78 (1H, d, J = 8.0 Hz), 8.29 (1H, t, J = 7.5 Hz), 7.99 (2H, d, J = 8.0 Hz), 7.81 (1H, t, J = 6.5 Hz), 7.10 (2H, d, J = 8.0 Hz), 1.70 (15H, s)

^{13}C-NMR-APT (125 MHz, CD_3CN): δ_C = 165.50 (s, C), 163.41 (s, C), 151.01 (s, CH/CH_3), 147.53 (s, C), 142.02 (s, CH/CH_3), 128.12 (s, CH/CH_3), 128.09 (s, CH/CH_3), 126.89 (s, CH/CH_3), 115.76 (s, CH/CH_3), 94.89 (s, C), 8.52 (s, CH_3).

ESI-MS (MeOH): m/z = 654.1 $[M - PF_6 - Cl]^+$

Elemental Analysis: Calc'd: C: 32.11, H: 3.72, N: 5.35. Found: C: 32.30, H: 3.03, N: 5.27.

Complex 11 – $[Cp^{xbiph}Ir(azpy(OH)_2)Cl]PF_6$

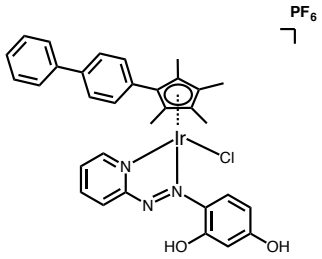

$[(Cp^{xbiph})IrCl_2]_2$ (75.0 mg, 0.070 mmol, 1 mol. equiv.) and 4-(pyridin-2-yldiazenyl)benzene-1,3-diol ($azpy(OH)_2$) (30.1 mg, 0.139 mmol, 2 mol. equiv.) were dissolved in DCM (20 mL) and stirred for 4 h at ambient temperature. The solvent was completely removed under vacuum in a rotary evaporator and the compound redissolved in the minimum amount of MeOH. NH_4PF_6 (57 mg, 0.350 mmol, 5 mol. equiv.) was added and the solution stirred then stored for 4 days at 277 K. The resulting mixture was then filtered through a frit and washed once with diethyl ether (10 mL) and the remaining solid material collected and redissolved in DCM then filtered once more. Diethyl ether was added to the filtrate until the onset of precipitation and the mixture left to crystallise at 277 K. This complex is novel.

Yield: 28 mg (23%)

^{1}H-NMR (400 MHz d_6-acetone): δ_H = 8.86-8.84 (2H, m), 8.45 (1H, t, J = 8.0 Hz), 8.09 (1H, d, J = 9.0 Hz), 7.95-7.91 (1H, m), 7.81-7.74 (4H, m), 7.62-7.60 (2H, m), 7.54-7.51 (2H, m), 7.46-7.42 (1H, m), 6.58 (1H, d, J = 2.0 Hz), 6.53-6.50 (1H, dd, J = 9.0, 2.0 Hz), 1.86 (6H, d, J = 9.0 Hz), 1.79 (3H, s), 1.69 (3H, s).

^{13}C-NMR-APT (125 MHz, d_6-acetone): δ_C = 169.22 (s, C), 165.25 (s, C), 156.08 (s, C), 149.96 (s, CH/CH_3), 142.54 (s, CH/CH_3), 141.57 (s, C), 139.69 (s, C), 135.82 (s, C), 134.80 (s, CH/CH_3), 130.56 (s, CH/CH_3), 129.08 (s, CH/CH_3), 128.00 (s, CH/CH_3), 127.85 (s, C), 127.53 (s, CH/CH_3), 126.83 (s, CH/CH_3), 123.72 (s, CH/CH_3), 112.70 (s, CH/CH_3), 104.03 (s, CH/CH_3), 102.64 (s, C), 99.87 (s, C), 92.61 (s, C), 90.28 (s, C), 85.70 (s, C), 40.43 (s, CH/CH_3), 9.23 (s, CH/CH_3), 8.96 (s, CH/CH_3), 8.33 (s, CH/CH_3), 7.97 (s,

CH/CH_3).

ESI-MS (MeOH): m/z = 680.2 $[M - PF_6 - Cl - H]^+$ (Most likely corresponding to the complex with the ortho phenyl oxygen coordinated to the iridium after loss of the chloride ligand.)

Elemental Analysis: Calc'd: C: 44.63, H: 3.51, N: 4.88. Found: C: 44.82, H: 3.51, N: 4.72.

Complex 12 – $[Cp^*Ir(azpy(OH)_2)Cl]PF_6$

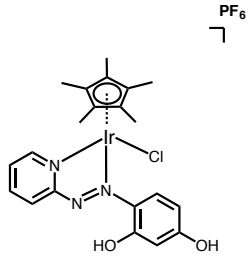

Synthesised as above using $[(Cp^*)IrCl_2]_2$ (55.1 mg, 0.069 mmol). This complex is novel.

Yield: 90 mg (78%)

^{1}H-NMR (400 MHz, d_6-acetone): δ_H = 11.15 (1H, br), 9.03 (1H, d, J = 6.0), 8.77 (1H, d, J = 9.0 Hz), 8.43 (1H, t, J = 9.0 Hz), 8.06 (1H, d, J = 5.0 Hz), 7.98 (1H, t, J = 6.0), 6.80 (1H, d, J = 9.0), 6.56 (1H, s), 1.72 (15H, s)

^{13}C-NMR-APT (125 MHz, d_6-acetone): δ_C = 165.97 (s, C), 151.27 (s, CH/CH_3), 143.39 (s, CH/CH_3), 134.95 (s, CH/CH_3), 128.35 (s, CH/CH_3), 124.95 (s, CH/CH_3), 124.95 (s, CH/CH_3), 104.83 (s, CH/CH_3), 94.21 (s, C), 8.79 (s, CH_3).

ESI-MS (MeOH): m/z = 600.1 $[M - PF_6 - H + Na]^+$

Elemental Analysis: Calc'd for **12**•H_2O: C: 34.04, H: 3.54, N: 5.67. Found: C: 34.38, H: 3.27, N: 5.70.

Complex 13 – $[Cp^{xbiph}Ir(azpy)Cl]PF_6$

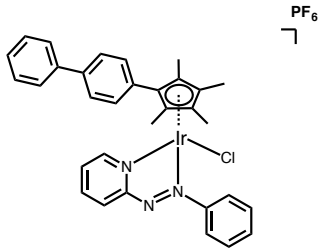

$[(Cp^{xbiph})IrCl_2]_2$ (74.6 mg, 0.070 mmol) and 2-(phenyldiazenyl)pyridine (azpy) (25.6 mg, 0.14 mmol, 2 mol. equiv.) were dissolved in DCM (20 mL) and stirred for 4 hr at ambient temperature. The solvent was completely removed under vacuum in a rotary evaporator and the compound redissolved in the minimum amount of MeOH. NH_4PF_6 (63.6 mg, 0.390 mmol, 5 mol. equiv.) was added and the solution stirred then stored overnight at 277 K. The mixture was then filtered through a frit and washed once quickly with cold MeOH (10 mL), the remaining solid material collected and redissolved in acetone then filtered once more the same way. Next, *n*-hexane was added to the filtrate until the onset of precipitation and the mixture left to crystallise overnight at 277 K. Recrystallisation of 1 mg in the minimum amount of MeOH/acetone and slow addition of diethyl ether by vapours using a small vial with pierced lid in large vial of diethyl ether system over many weeks yielded an x-ray quality crystal. This complex is novel.

Yield: 76 mg (76%)

^{1}H-NMR (400 MHz, 80% CD_3CN:20% D_2O): δ_H = 8.90 (1H, d, J = 8.0 Hz), 8.60 (1H, d, J = 5.0 Hz), 8.40 (1H, t, J = 8.0 Hz), 7.91 (2H, d, J = 7.0), 7.75 – 7.68 (5H, m), 7.63 – 7.60 (2H, m), 7.53 – 7.49 (2H, m), 7.43 (2H, d, J = 7.0 Hz), 1.71 (3H, s), 1.61 (3H, s), 1.54 (3H, s), 1.46 (3H, s).

^{13}C-NMR (500 MHz, CD_3CN): δ_C = 166.07 (s, C), 154.20 (s, C), 150.69 (s, CH/CH_3), 143.88 (s, CH/CH_3), 142.21 (s, C), 140.12 (s, C), 134.68 (s, CH/CH_3), 131.45 (s, CH/CH_3), 131.03 (s, CH/CH_3), 130.19 (s, CH/CH_3), 129.73 (s, CH/CH_3), 129.66 (s, CH/CH_3), 128.71 (s, CH/CH_3), 128.21 (s,

CH/CH_3), 127.55 (s, C), 127.44 (s, CH/CH_3), 124.73 (s, CH/CH_3), 105.64 (s, C), 100.85 (s, C), 95.73 (s, C), 91.47 (s, C), 87.86 (s, C), 9.80 (s, CH_3), 9.36 (s, CH_3), 8.70 (s, CH_3), 8.55 (s, CH_3).

ESI-MS (MeOH): m/z = 680.2 $[M - PF_6 - Cl + MeO]^+$

Elemental Analysis: Calc'd: C: 46.07, H: 4.23, N: 5.04. Found: C: 46.24, H: 3.54, N: 5.04.

Complex 14 – $[Cp^{xph}Ir(azpy)Cl]PF_6$

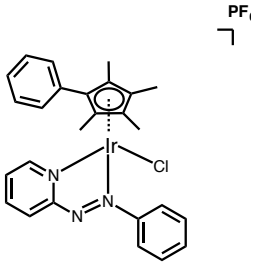

Synthesised as above using. $[(Cp^{xph})IrCl_2]_2$ (71.5 mg, 0.078 mmol, 1 mol. equiv.) and 2-(phenyldiazenyl)pyridine (28.4 mg, 0.156 mmol, 2 mol. equiv.) Recrystallisation of 1 mg in the minimum amount of MeOH/acetone and slow addition of diethyl ether by vapours using a small vial with pierced lid in large vial of diethyl ether system over many weeks yielded an enantiomerically pure x-ray quality crystal. This complex is novel.

Yield: 65 mg (65%)

^{1}H-NMR (400 MHz 80% CD_3CN:20% D_2O): δ_H = 8.90 (1H, d, J = 8.0 Hz), 8.57 (1H, d, J = 5.0 Hz), 8.39 (1H, t, J = 8.0 Hz), 7.90-7.87 (3H, m), 7.72 – 7.69 (1H, m), 7.63 – 7.60 (2H, m), 7.53 – 7.44 (3H, m), 7.31 (2H, d, J = 8.0 Hz), 1.67 (3H, s), 1.60 (3H, s), 1.53 (3H, s), 1.38 (3H, s)

^{13}C-NMR (500 MHz, CD_3CN): δ_C = 166.03 (s, C), 154.20 (s, C), 150.69 (s, CH/CH_3), 143.86 (s, CH/CH_3), 134.67 (s, CH/CH_3), 131.43 (s, CH/CH_3), 130.43 (s, CH/CH_3), 130.19 (s, CH/CH_3), 130.02 (s, CH/CH_3), 129.89 (s, CH/CH_3), 129.66 (s, CH/CH_3), 128.46 (s, C), 124.70 (s, CH/CH_3), 105.58 (s, C), 100.96 (s, C), 95.44 (s, C), 91.59 (s, C), 88.35 (s, C), 9.69 (s, CH_3), 9.26 (s, CH_3), 8.70 (s, CH_3), 8.53 (s, CH_3).

ESI-MS (MeOH): m/z = 608.0 $[M - PF_6]^+$

Elemental Analysis: Calc'd: C: 41.19, H: 4.12, N: 5.54. Found: C: 40.87, H: 3.41, N: 5.46.

Complex 15 – [Cp*Ir(azpy)Cl]PF_6

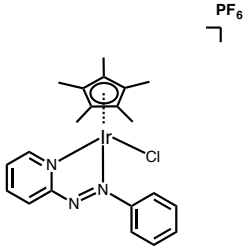

Synthesised as above using $[(Cp^*)IrCl_2]_2$ (69.6 mg, 0.87 mmol, 1 mol. equiv.). This complex is novel.

Yield: 57 mg (57%)

^{1}H-NMR (400 MHz 80% CD_3CN:20% D_2O): δ_H = 8.86 (1H, d, J = 7.0 Hz), 8.40 (1H, t, J = 7.5 Hz), 8.01 (1H, t, J = 7.0 Hz), 7.91 (2H, d, J = 7.5 Hz), 7.77 – 7.70 (5H, m), 1.51 (15H, s)

^{13}C-NMR (500 MHz, CD_3CN): δ_C = = 165.99 (s, C), 154.39 (s, C), 150.85 (s, CH/CH_3), 143.66 (s, CH/CH_3), 134.60 (s, CH/CH_3), 131.24 (s, CH/CH_3), 130.24 (s, CH/CH_3), 129.19 (s, CH/CH_3), 124.68 (s, CH/CH_3), 95.32 (s, C), 8.42 (s, CH_3).

ESI-MS (MeOH): m/z = 540.0 $[M - PF_6 - Cl + MeO]^+$

Elemental Analysis: Calc'd: C: 36.23, H: 4.20, N: 6.04. Found: C: 36.16, H: 3.35, N: 6.02.

Complex 16 – $[Cp^{xbiph}Ir(HOazpyNO_2)Cl]PF_6$

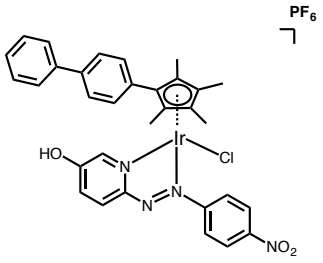

$[(Cp^{xbiph})IrCl_2]_2$ (60.3 mg, 0.056 mmol) and 6-((4-nitrophenyl)diazenyl)pyridine-3-ol ($HOazpyNO_2$) (27.4 mg, 0.112 mmol, 2 mol. equiv.) were dissolved in DCM (20 mL) and stirred for 4 hr at ambient temperature. The solvent was completely removed under vacuum in a rotary evaporator and the compound redissolved in the minimum amount of MeOH. NH_4PF_6 (40.7 mg, 0.280 mmol, 5 mol. equiv.) was added and the solution stirred then stored overnight at 277 K. The mixture was then filtered through a frit and washed once quickly with cold MeOH (10 mL) and the remaining solid material collected and redissolved in DCM then filtered once more the same way. Next, *n*-hexane was added to the filtrate until the onset of precipitation and the mixture left to crystallise at 277 K. This complex is novel.

Yield: 64 mg (64%)

^{1}H-NMR (400 MHz d_6-acetone): δ_H = 8.28 (2H, d, J = 9.0 Hz), 7.97 (2H, d, J = 9.0 Hz), 7.78 (1H, d, J = 5.0 Hz), 7.76 – 7.72 (4H, m), 7.55 – 7.43 (6H, m), 7.39 (1H, d, J = 9.0 Hz), 1.73 (3H, s), 1.61 (3H, s), 1.56 (3H, s), 1.46 (3H, s).

^{13}C-NMR-APT (125 MHz, CD_3CN): δ_C =166.13 (s, C), 157.34 (s, C), 155.50 (s, C), 149.11 (s, C), 142.00 (s, C), 141.66 (s, CH/CH_3), 140.32 (s, C), 135.83 (s, CH/CH_3), 133.56 (s, CH/CH_3), 131.84 (s, CH/CH_3), 131.10 (s, CH/CH_3), 129.68 (s, CH/CH_3), 128.59 (s, CH/CH_3), 128.19 (s, CH/CH_3), 127.47 (s, CH/CH_3), 125.42 (s, CH/CH_3), 103.96 (s, C), 98.76 (s, C), 93.72 (s, C), 89.15 (s, C), 86.58 (s, C), 9.65 (s, CH_3), 9.37 (s, CH_3), 8.66 (s, CH_3), 8.63

(s, CH_3).

ESI-MS (MeOH): m/z = 745.1 $[M - PF_6]^+$

Elemental Analysis: Calc'd for **16**•3$(CH_3)_2CO$: C: 46.26, H: 4.45, N: 5.26. Found: C: 46.52, H: 3.41, N: 6.17.

Complex 17 – $[Cp^{xph}Ir(HOazpyNO_2)Cl]PF_6$

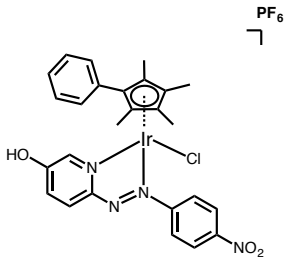

Synthesised as above using. $[(Cp^{xph})IrCl_2]_2$ (30.2 mg, 0.033 mmol, 1 mol. equiv.) and 6-((4-nitrophenyl)diazenyl)pyridine-3-ol ($HOazpyNO_2$) (16.0 mg, 0.066 mmol, 2 mol. equiv.). This complex is novel.

Yield: 35 mg (66%)

^{1}H-NMR (500 MHz, CD_3CN): δ_H = 8.28 (2H, d, J = 9.0 Hz), 7.95 (2H, d, J = 9.0 Hz), 7.76 (1H, d, J = 5.0 Hz), 7.53 – 7.45 (4H, m), 7.41 (0.6H, d, J = 1.0 Hz), 7.40 (0.4H, d, J = 1.0 Hz), 7.37 – 7.34 (2H, m), 1.69 (3H, s), 1.60 (3H, s), 1.55 (3H, s), 1.39 (3H, s)

^{13}C-NMR-APT (125 MHz, d_6-acetone): δ_C = 168.56 (s, C), 156.75 (s, C), 153.52 (s, C), 148.11 (s, C), 144.51 (s, CH/CH_3), 132.03 (s, CH/CH_3), 130.15 (s, CH/CH_3), 129.27 (s, CH/CH_3), 129.19 (s, CH/CH_3), 128.76 (s, C), 126.99 (s, CH/CH_3), 124.83 (s, CH/CH_3), 124.61 (s, CH/CH_3), 103.40 (s, C), 98.12 (s, C), 92.41 (s, C), 88.39 (s, C), 86.04 (s, C), 8.92 (s, CH_3), 8.71 (s, CH_3), 8.12 (s, CH_3), 7.99 (s, CH_3).

ESI-MS (MeOH): m/z = 669.1 $[M - PF_6]^+$

Elemental Analysis: Calc'd for **17**•2$(CH_3)_2CO$: C: 41.31, H: 4.01, N: 6.02. Found: C: 41.13, H: 3.08, N: 7.23.

Complex 18 – $[Cp^*Ir(HOazpyNO_2)Cl]PF_6$

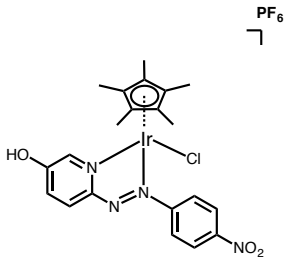

Synthesised as above using. $[(Cp^*)IrCl_2]_2$ (25.2 mg, 0.033 mmol, 1 mol. equiv.) and 6-((4-nitrophenyl)diazenyl)pyridine-3-ol ($HOazpyNO_2$) (16.0 mg, 0.066 mmol, 2 mol. equiv.). This complex is novel.

Yield: 33 mg (66%)

^{1}H-NMR (500 MHz, CD_3CN): δ_H = 8.44 (2H, d, J = 9.0 Hz), 8.28 (1H, dd, J = 5.0, 1.0 Hz), 8.04 (2H, d, J = 9.0 Hz), 7.84 (0.4, d, J = 5.0 Hz), 7.82 (0.6H, d, J = 5.0 Hz), 7.73 (0.6, d, J = 1.0 Hz), 7.71 (0.4H, d, J = 1.0 Hz), 1.54 (15H, s).

^{13}C-NMR-APT (125 MHz, d_6-acetone): δ_C = 168.38 (s, C), 157.01 (s, C), 153.80 (s, C), 148.24 (s, C), 144.10 (s, CH/CH_3), 131.79 (s, CH/CH_3), 126.85 (s, CH/CH_3), 124.86 (s, CH/CH_3), 124.67 (s, CH/CH_3), 92.50 (s, C), 7.80 (s, CH_3).

ESI-MS (MeOH): m/z = 607.1 $[M - PF_6]^+$

Elemental Analysis: Calc'd for **18•**$(CH_3)_2CO$: C: 35.58, H: 3.61, N: 6.92. Found: C: 35.90, H: 3.16, N: 7.66.

Complex 19 – [Cp^{xbiph}Ir(Brazpy(OH)NEt$_2$)Cl]PF$_6$

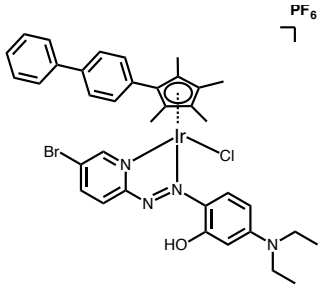

[(Cp^{xbiph})IrCl$_2$]$_2$ (63.2 mg, 0.059 mmol, 1 mol. equiv.) and 2-((5-bromopyridin-2-yl)diazenyl)-5-(diethylamino)phenol (Brazpy(OH)NEt$_2$) (41.1 mg, 0.118 mmol, 2 mol. equiv.) were dissolved in DCM (20 mL) and stirred at ambient temperature for 5 h. The solvent was completely removed under vacuum in a rotary evaporator and the compound redissolved in the minimum amount of MeOH. NH_4PF_6 (48 mg, 0.294 mmol, 5 mol. equiv.) was added and the solution stirred then stored overnight at 277 K. The resulting mixture was then filtered through a frit and washed once quickly with cold MeOH (10 mL) then with diethyl ether (3 x 10 mL) and the remaining solid material collected and redissolved in DCM then filtered once more. Diethyl ether was added to the filtrate until the onset of precipitation and the mixture left to crystallise overnight at 277 K. This complex is novel.

Yield: 87 mg (74%)

^{1}H-NMR (500 MHz d$_6$-acetone): δ_H = 13.32 (0.6H, br), 8.63 (1H, d, J = 2.0), 8.34 (0.4H, d, J = 2.0 Hz), 8.32 (0.6H, d, J = 2.0 Hz), 8.27 (0.6H, s), 8.25 (0.4H, s), 8.89 (1H, d, J = 10 Hz), 7.83-7.81 (2H, m), 7.77 (2H, m), 7.65-7.63 (2H, m), 7.55-7.52 (2H, m), 7.47-7.44 (1H, m), 6.52 (1H, dd, J = 10.0, 2.0 Hz), 6.31 (1H, d, J = 2.0 Hz), 2.84-2.81 (10H, m), 1.95 (3H, s), 1.87 (3H, s), 1.84 (3H, s), 1.83 (3H, s).

^{13}C-NMR-APT (125 MHz, d$_6$-acetone): δ_C = 164.09 (s, C/CH), 159.33 (s, C/CH$_2$), 156.45 (s, C/CH$_2$), 149.18 (s, CH/CH$_3$), 144.27 (s, CH/CH$_3$), 141.61 (s, C/CH$_2$), 139.71 (s, C/CH$_2$), 137.46 (s, CH/CH$_3$), 135.48 (s, C/CH$_2$), 130.61 (s, CH/CH$_3$), 129.09 (s, CH/CH$_3$), 128.04 (s, CH/CH$_3$), 127.85 (s, C/CH$_2$), 127.53 (s, CH/CH$_3$), 126.83 (s, CH/CH$_3$), 119.64 (s, CH/CH$_3$),

116.46 (s, C/CH_2), 111.69 (s, CH/CH_3), 99.44 (s, C/CH_2), 97.88 (s, CH/CH_3), 97.18 (s, C/CH_2), 91.81 (s, C/CH_2), 89.96 (s, C/CH_2), 86.62 (s, C/CH_2), 46.06 (s, C/CH_2), 12.62 (s, CH/CH_3), 9.26 (s, CH/CH_3), 9.25 (s, CH/CH_3), 8.42 (s, CH/CH_3), 7.99 (s, CH/CH_3).

ESI-MS (MeOH): m/z = 849.1 $[M - PF_6]^+$

Elemental Analysis: Calc'd: C: 43.23, H: 4.33, N: 5.60. Found: C: 43.61, H: 3.71, N: 5.41.

3.2.2 Chiral Separation Studies

All initial samples were dissolved in HPLC-grade EtOH at 1 mg/ml, sonicated for 15 minutes at ambient temperature, and filtered through glass microfibre filter paper and celite. Chiral separation studies were carried out on an Agilent 1200 series HPLC system equipped with a binary pump, a variable wavelength detector, and fitted with a 100 μL loop. The column used was a CHIRALPAK IC column (250 mm x 4.6 mm) in normal phase composed of cellulose-based packing with tris(3,5-dichlorophenylcarbamate) immobilized on 5 μM silica-gel from Chiral Technologies Europe with an isocratic gradient of heptane:ethanol 0.5% triethylamine (TEA), 0.3% trifluoroacetic acid (TFA) (v/v), flow-rate 1.00 mL/min, wavelength of detection 254 nm. Initial method development for the separation of similar complexes on CHIRALPAK IC was carried out previously[103] based on protocols developed by Chiral Technologies Europe (Figure 3.2).

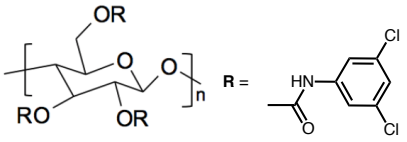

Figure 3.2: Composition of the CHIRALPAK IC column used for separation of chiral enanatiomers: Cellulose-based packing with tris(3,5-dichlorophenylcarbamate) immobilized on 5 μM silica-gel.

Injection size was initially 25 μL and was increased to 100 μL if it was possible to do so without compromising separation in order to collect more sample per run. Separated peaks were collected, combined and dried under vacuum at ambient temperature then stored at 193 K for 20 h. The same procedure was then run on the separated peak fractions to determine their stability.

3.2.3 Genomics of Drug Sensitivity in Cancer (GDSC) Pharmaco-genomic Screen

Cells were grown in medium supplemented with penicillin/streptomycin and 10% FBS to approximately 15% confluency then seeded in 384-well plates and left to incubate for 24 h at 310 K, 5% CO_2, 95% air and 100% humidity until approximately 85% confluency was reached. For adherent cell lines, cells were treated with nine concentrations of each compound in a 2-fold dilution series over a 256-fold concentration range and incubated for 72 h. Cells then fixed with 4% formaldehyde for 30 min then stained with 1 μM Syto60 for 1 h. Fluorescent signal intensity was measured using a plate reader at excitation/emission wavelengths of 630/695 nm. For cell lines in suspension, cells were treated with compound immediately after plating, then incubated for 72 h. Cells stained with 55 μg/mL Resazurin in glutathione-free medium for 4 h. Fluorescent signal intensity measured using a plate reader at excitation/emission wavelengths of 535/595 nm. MANOVA analysis was performed by the Sanger Bioinformatics Institute. Data were processed in R.[97]

3.3 Results

3.3.1 Synthesis, Characterisation and Purity Determination

Nineteen organoiridium azopyridine complexes containing six different azopyridine ligands were synthesised, characterised, and purified (Figure 3.3). Seventeen of these are novel. X-ray crystal structures were obtained for eight complexes, all of which exhibit the expected half-sandwich pseudooctahedral structure with bond angles and lengths in the expected range. The complexes differ in either their bidentate azopyridine ligand, their monodentate halido ligand, their Cp system, or their counterion. In most cases each complex has an analogue with only one difference in functional group. This allows any differences in anticancer activity or MoA to be attributed to the presence or absence of that group. In this way, meaningful conclusions can be drawn about their activity from their structural differences.

Seventeen complexes bear the PF_6 counterion and these have poor aqueous solubility (<100 μM). Complex **8** instead bears a chloride counterion and complex **10** bears an iodide counterion. Both of these complexes have >100 μM solubility in aqueous solution. Complex purity was determined by a combination of ^{1}H-NMR, ^{13}C-NMR, CHN elemental analysis and LC-MS. For some complexes, CHN elemental analysis shows some solvent present in the complex sample. The presence of these solvents is supported by their corresponding peaks in the NMR spectra. Peaks in LC-MS were shown to be either complex, hydrolysed complex, products of complex breakdown in column, or peaks present in the blank LC run, further demonstrating that molecules of solvent are the only possible impurities. LC-MS data for complexes can be found in Appendix Figures S2 – S19, pg. 273 – 290.

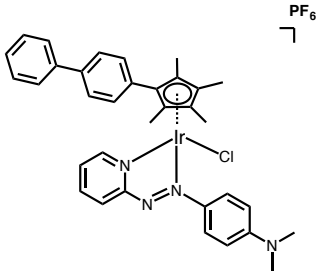

Complex **1***

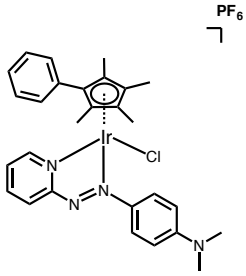

Complex **2**

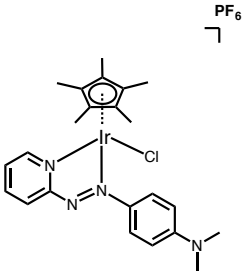

Complex **3***

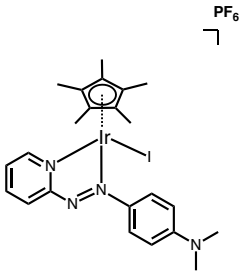

Complex **4**

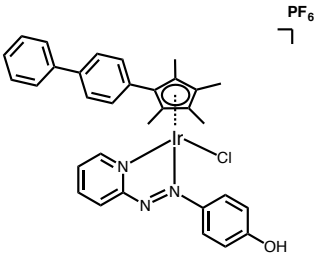

Complex **5***

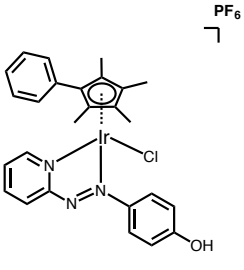

Complex **6***

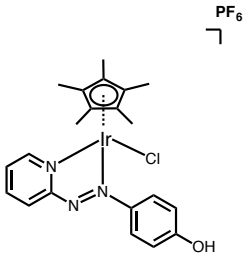

Complex **7**

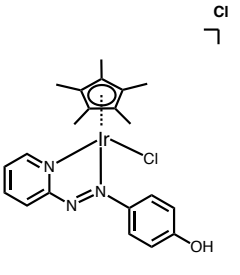

Complex **8***

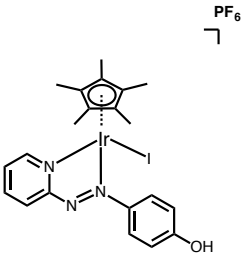

Complex **9**

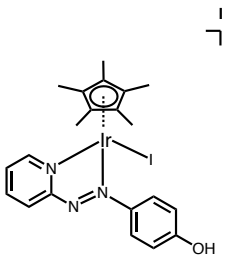

Complex **10***

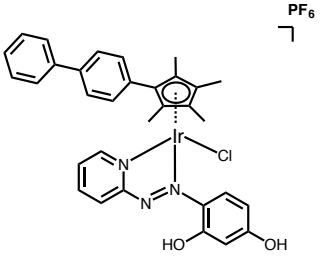

Complex **11**

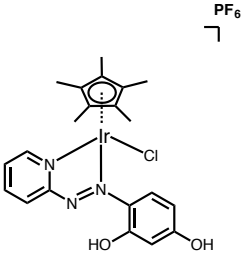

Complex **12**

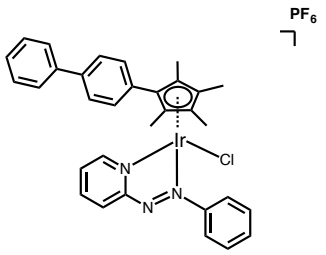

Complex **13***

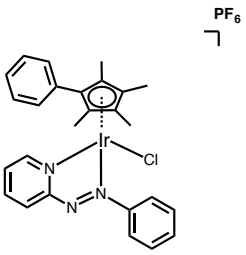

Complex **14***

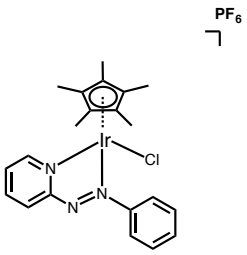

Complex **15**

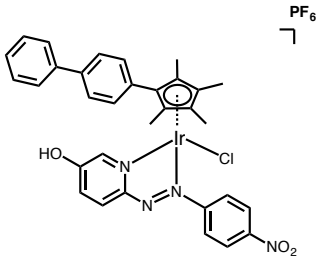

Complex **16**

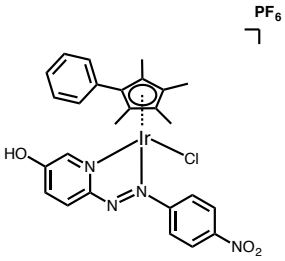

Complex **17**

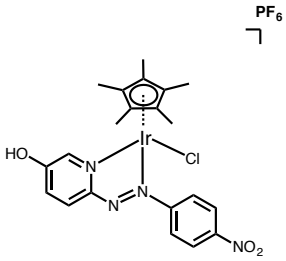

Complex **18**

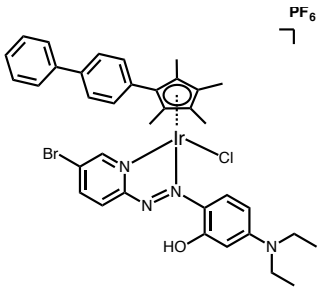

Complex **19**

Figure 3.3: Structures of complexes **1** − **19** studied in this work. A crystal structure was obtained for complexes marked with an asterisk (*) Families of complexes grouped by bidentate azopyridine ligand. The azpyNMe_2 family consists of complexes **1** − **4**, the azpyOH family of complexes **5** − **10**, the azpy$(OH)_2$ family of complexes **11** and **12**, the azpy family of complexes **13** − **15**, the HOazpyNO_2 family of complexes **16** − **18**, and the single Brazpy(OH)NEt_2 complex **19**.

3.3.2 X-ray Crystal Structures

For the complexes for which an x-ray crystal structure was determined, the 3D structures and data are presented here (Figures 3.4 – 3.11 and Tables 3.1 – 3.9).

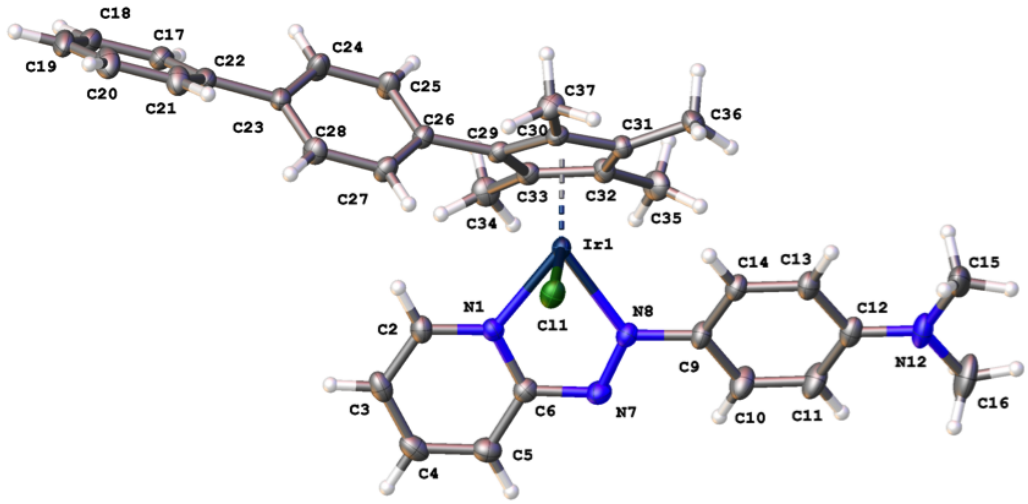

Figure 3.4: Solid state structure of complex **1** with atom labelling and thermal parameters at 50% probability level. Hydrogens placed at geometrically calculated positions. The asymmetric unit contains the complex and there are two in the unit cell. Disordered solvent and counter ion have been removed for clarity.

Table 3.1: Crystallographic and structure refinement data for complex **1**

Complex	**1**
Empirical formula	$C_{34}H_{35}ClF_6IrN_4P$
Formula weight	872.28
Temperature (K)	150(2)
Crystal system	triclinic
Space group	P-1
a (Å)	8.65951(14)
b (Å)	12.50429(16)
c (Å)	15.80665(15)
α (°)	85.2790(9)
β (°)	86.2334(10)
γ (°)	78.4092(12)
Volume (Å^3)	1668.85(4)
Z	2
ρ_{calc} (g/cm^3)	1.736
μ (mm^{-1})	4.193
F(000)	860.0
Crystal size (mm^3)	0.24 × 0.18 × 0.08 brown block
Radiation	MoKα (λ = 0.71073)
2Θ range for data collection (°)	4.808 to 62.08
Index ranges	-12 ≤ h ≤ 12, -17 ≤ k ≤ 18, -22 ≤ l ≤ 21
Reflections collected	97326
Independent reflections	10164 [R_{int} = 0.0669, R_{sigma} = 0.0338]
Data/restraints/parameters	10164/0/430
Goodness-of-fit on F^2	1.021

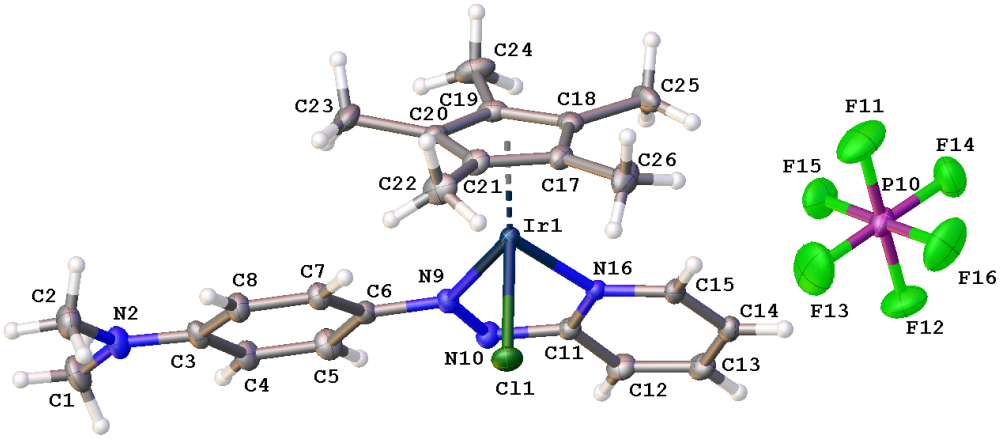

Figure 3.5: Solid state structure of complex **3** with atom labelling and thermal ellipsoids drawn at 50% probability level. Hydrogens placed at geometrically calculated positions. The asymmetric unit contains the complex with a PF_6 counter ion. Four times all this in the unit cell. No disorder or unusual features to report.

Table 3.2: Crystallographic and structure refinement data for complex **3**

Complex	**3**
Empirical formula	$C_{23}H_{29}ClF_6IrN_4P$
Formula weight	734.12
Temperature (K)	150(2)
Crystal system	monoclinic
Space group	$P2_1/n$
a (Å)	8.2820(3)
b (Å)	14.8766(6)
c (Å)	21.0325(8)
α (°)	90
β (°)	96.921(4)
γ (°)	90
Volume (Å^3)	2572.49(17)
Z	4
ρ_{calc} (g/cm^3)	1.895
μ (mm^{-1})	5.420
F(000)	1432.0
Crystal size (mm^3)	0.42 × 0.24 × 0.08
Radiation	MoKα (λ = 0.71073)
2Θ range for data collection (°)	5.476 to 63.506
Index ranges	-12 ≤ h ≤ 11, -21 ≤ k ≤ 20, -30 ≤ l ≤ 29
Reflections collected	38144
Independent reflections	8161 [R_{int} = 0.0471, R_{sigma} = 0.0378]
Data/restraints/parameters	8161/0/332
Goodness-of-fit on F^2	1.131

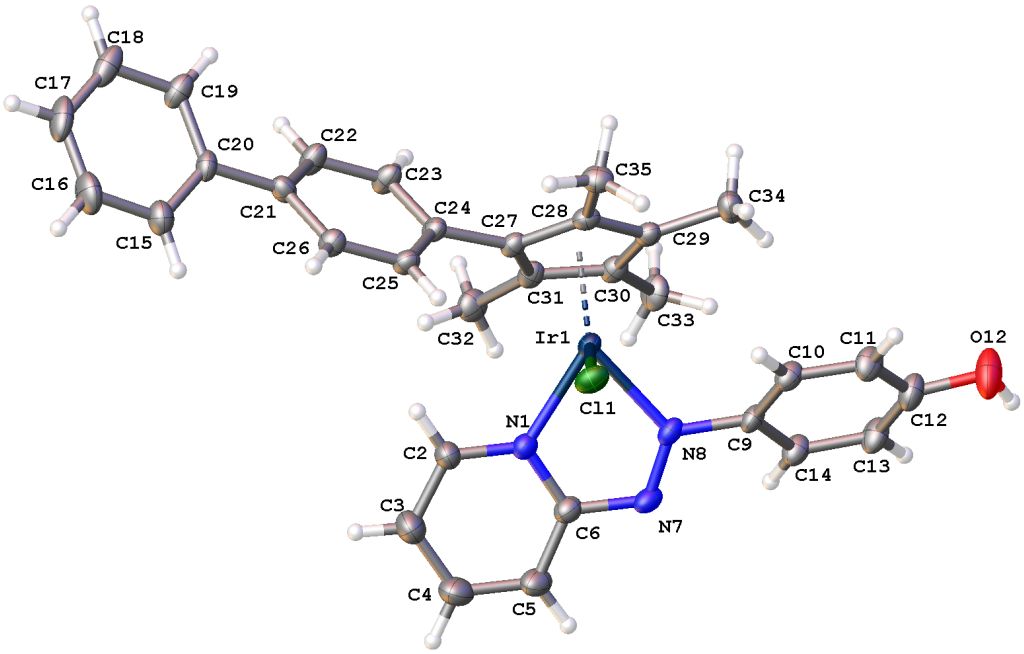

Figure 3.6: Solid state structure of the complex **5** with atom labelling and thermal parameters at 50% probability level. Hydrogens placed at geometrically calculated positions. The asymmetric unit contains an Ir complex, two PF_6 counter ions at half occupancy, and a disordered molecule of methanol.

Table 3.3: Crystallographic and structure refinement data for complex **5**

Complex	**5**
Empirical formula	$C_{33}H_{30}ClF_6IrN_3O_2P$
Formula weight	873.22
Temperature (K)	150(2)
Crystal system	monoclinic
Space group	$P2_1/n$
a (Å)	19.5364(5)
b (Å)	8.82093(19)
c (Å)	23.1386(8)
α (°)	90
β (°)	114.633(4)
γ (°)	90
Volume (Å^3)	3624.6(2)
Z	4
ρ_{calc} (g/cm^3)	1.600
μ (mm^{-1})	3.865
F(000)	1712.0
Crystal size (mm^3)	0.2 × 0.2 × 0.02 brown plate
Radiation	MoKα (λ = 0.71073)
2Θ range for data collection (°)	5.156 to 64.85
Index ranges	-17 ≤ h ≤ 28, -13 ≤ k ≤ 12, -33 ≤ l ≤ 31
Reflections collected	58453
Independent reflections	12175 [R_{int} = 0.0551, R_{sigma} = 0.0501]
Data/restraints/parameters	12175/7/473
Goodness-of-fit on F^2	1.042

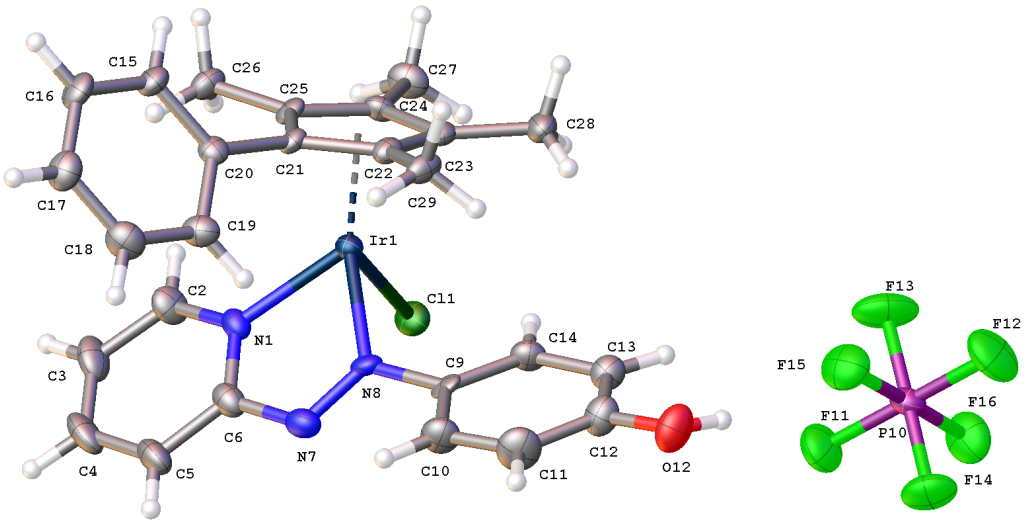

Figure 3.7: Solid state structure of complex **6** with atom labelling and thermal ellipsoids drawn at 50% probability level. Hydrogens placed at geometrically calculated positions. The asymmetric unit contains an Ir complex formed from a C-metallated phenyl azopyridine ligand and a phenyl tetra methyl Cp with a chloride and a PF_6 counter ion. Twice all this in the unit cell.

Table 3.4: Crystallographic and structure refinement data for complex **6**

Complex	**6**
Empirical formula	$C_{26}H_{26}ClF_6IrN_3OP$
Formula weight	769.12
Temperature (K)	150(2)
Crystal system	triclinic
Space group	P-1
a (Å)	8.71914(18)
b (Å)	9.9018(2)
c (Å)	15.7288(3)
α (°)	89.3248(16)
β (°)	78.0376(16)
γ (°)	88.7062(17)
Volume (Å^3)	1328.08(5)
Z	2
ρ_{calc} (g/cm^3)	1.923
μ (mm^{-1})	5.256
F(000)	748.0
Crystal size (mm^3)	0.35 × 0.16 × 0.06
Radiation	MoKα (λ = 0.71073)
2Θ range for data collection (°)	5.294 to 75.372
Index ranges	-14 ≤ h ≤ 14, -16 ≤ k ≤ 16, -26 ≤ l ≤ 26
Reflections collected	66113
Independent reflections	13636 [R_{int} = 0.0501, R_{sigma} = 0.0370]
Data/restraints/parameters	13636/0/357
Goodness-of-fit on F^2	1.059

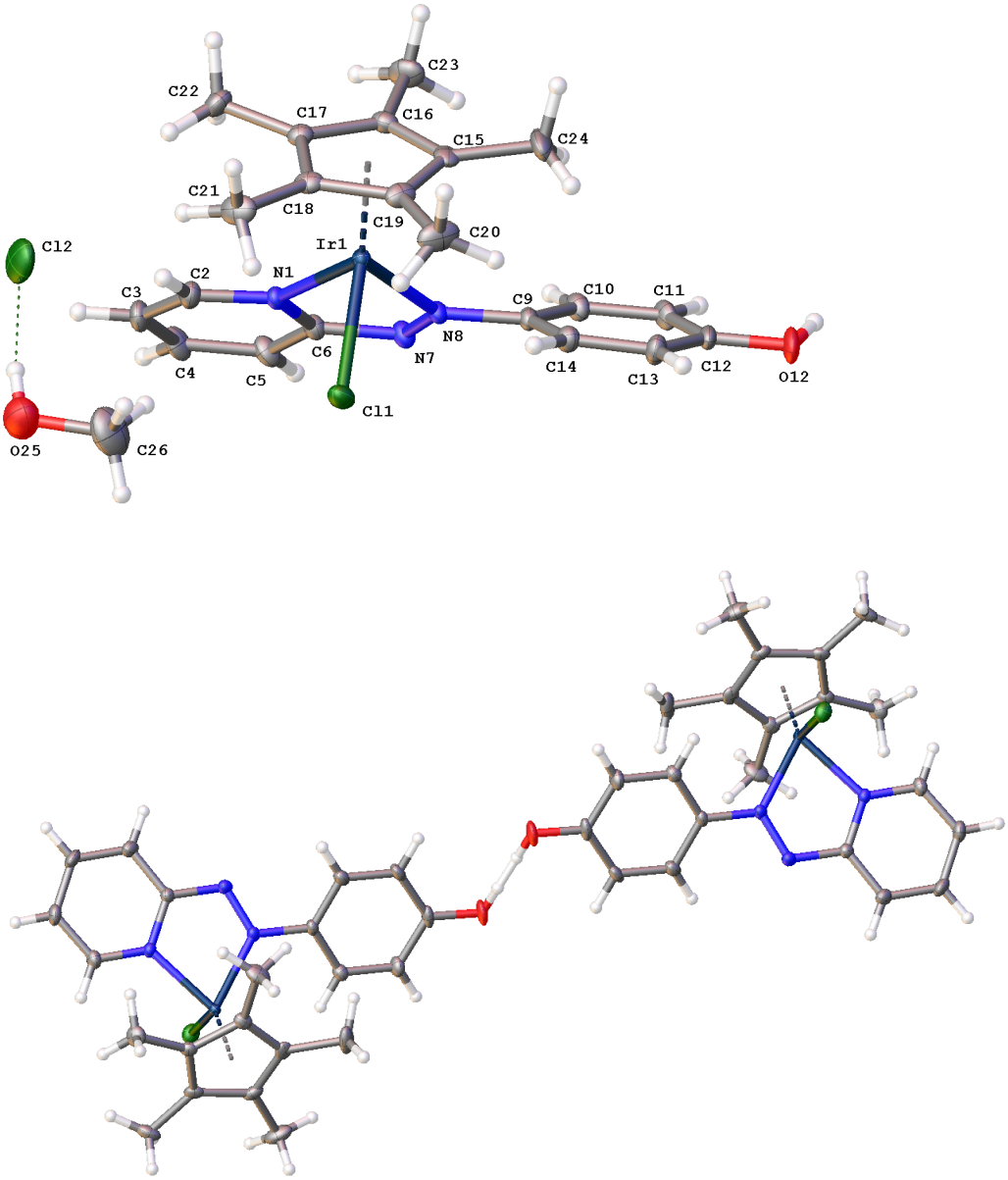

Figure 3.8: Solid state structures of complex **8** with atom labelling and thermal ellipsoids drawn at 50% probability level. Hydrogens placed at geometrically calculated positions. The asymmetric unit contains the Ir complex and a molecule of methanol and a chloride counter ion. The chloride counter ion sits on an inversion centre (so is at half occupancy), four times all this in the unit cell.

In the generation of the crystal structures of complex **8**, the hydroxyl group

hydrogens on the methanol and the phenol were not located but placed at calculated positions. Problems arise as there is only half a chloride counter ion per Ir complex and the phenol OH forms a hydrogen bond to a symmetry related phenol so there is a clash of the phenolic OHs. This is because there is only one proton shared between the two phenol oxygens. This has been observed in organoosmium complexes bearing the same azpyOH ligand.[104] This means that there are two complexes with (2 x Ir(+3) balanced by two pentamethylcyclopentadienyls, two metal bound chlorides and a single chloride (Cl2) and two phenoxides sharing H12). In reality the hydrogen shuttles between the phenol oxygen O12 and the symmetry related O12 represented by Figure 3.8 but this situation cannot be resolved by this X-ray experiment.

Table 3.5: Crystallographic and structure refinement data for complex **8**

Complex	**8**
Empirical formula	$C_{22}H_{27.5}Cl_{1.5}IrN_3O_2$
Formula weight	611.34
Temperature (K)	150(2)
Crystal system	monoclinic
Space group	$P2_1/n$
a (Å)	8.93939(15)
b (Å)	18.6768(3)
c (Å)	13.4520(2)
α (°)	90
β (°)	94.0660(14)
γ (°)	90
Volume (Å^3)	2240.28(6)
Z	4
ρ_{calc} (g/cm^3)	1.813
μ (mm^{-1})	6.162
F(000)	1196.0
Crystal size (mm^3)	0.5 × 0.35 × 0.28 (purple block)
Radiation	MoKα (λ = 0.71073)
2Θ range for data collection (°)	5.062 to 65.382
Index ranges	-12 ≤ h ≤ 13, -28 ≤ k ≤ 28, -19 ≤ l ≤ 19
Reflections collected	36123
Independent reflections	7716 [R_{int} = 0.0360, R_{sigma} = 0.0316]
Data/restraints/parameters	7716/0/276
Goodness-of-fit on F^2	1.297

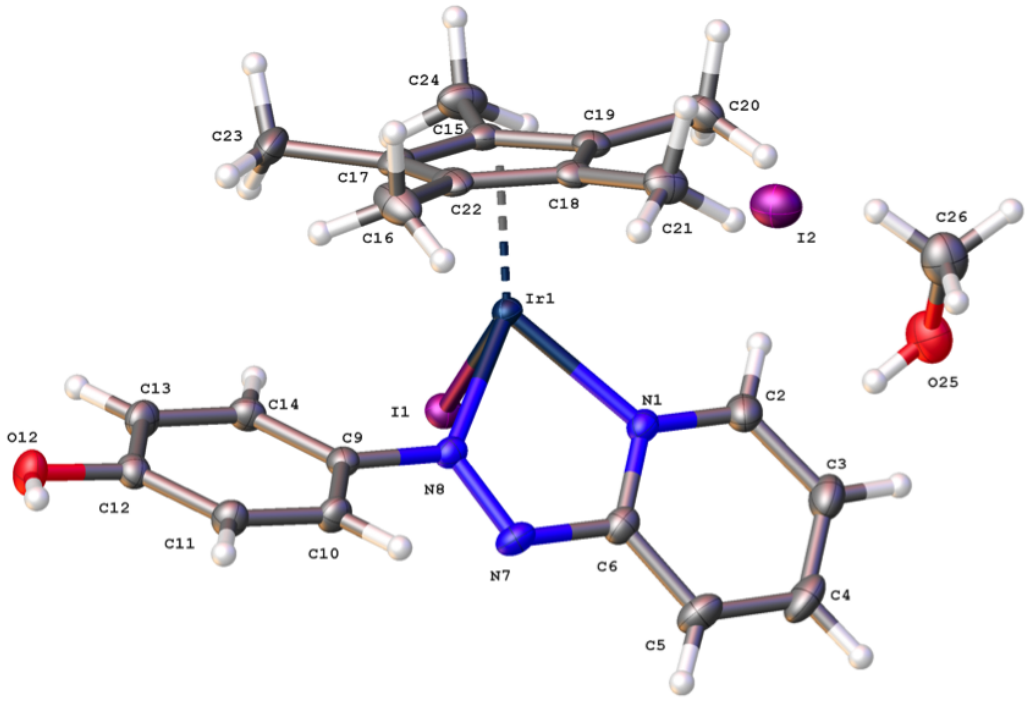

Figure 3.9: Solid state structure of complex **10** with atom labelling and thermal parameters drawn at 50% probability level. Hydrogens placed at geometrically calculated positions. The asymmetric unit contains the complex, an iodide and a solvent methanol. Four times all this in the unit cell.

Table 3.6: Crystallographic and structure refinement data for complex **10**

Complex	**10**
Empirical formula	$C_{22}H_{28}I_2IrN_3O_2$
Formula weight	812.47
Temperature (K)	150(2)
Crystal system	monoclinic
Space group	$P2_1/n$
a (Å)	9.29339(12)
b (Å)	13.27724(15)
c (Å)	20.1881(3)
α (°)	90
β (°)	91.3644(12)
γ (°)	90
Volume (Å^3)	2490.31(6)
Z	4
ρ_{calc} (g/cm^3)	2.167
μ (mm^{-1})	7.863
F(000)	1520.0
Crystal size (mm^3)	0.16 × 0.08 × 0.08 brown block
Radiation	MoKα (λ = 0.71073)
2Θ range for data collection (°)	4.87 to 62.262
Index ranges	-13 ≤ h ≤ 13, -18 ≤ k ≤ 18, -28 ≤ l ≤ 28
Reflections collected	64660
Independent reflections	7479 [R_{int} = 0.0416, R_{sigma} = 0.0254]
Data/restraints/parameters	7479/0/279
Goodness-of-fit on F^2	1.093

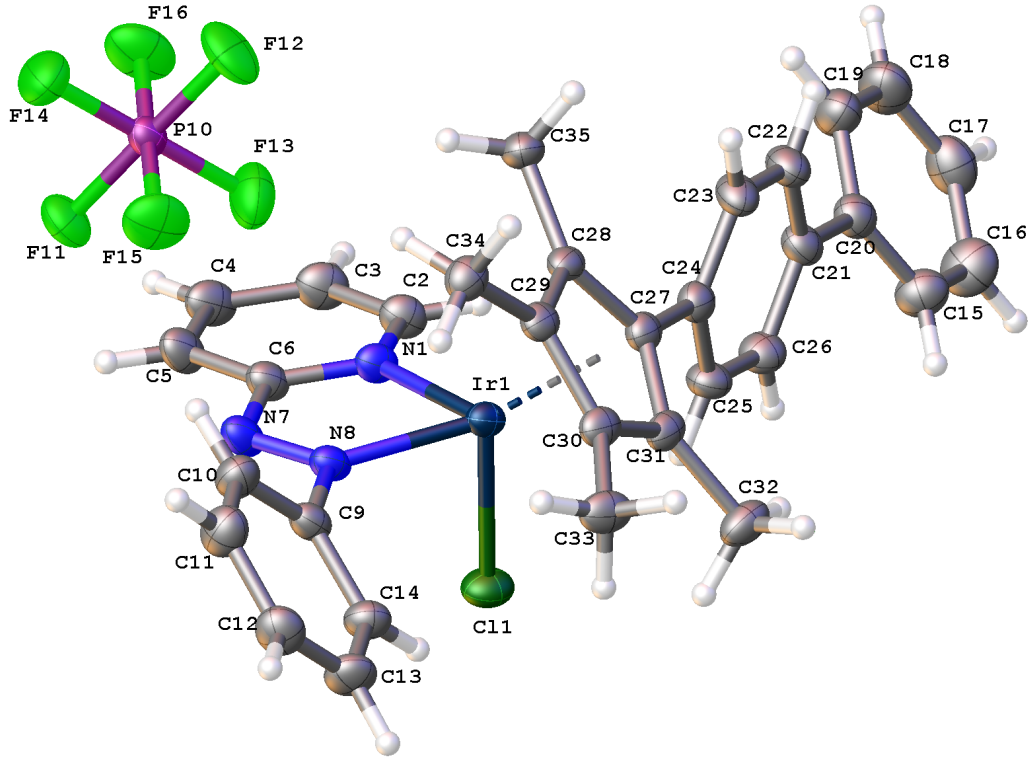

Figure 3.10: Solid state structure of complex **13** with atom labelling and thermal ellipsoids drawn at 50% probability level. Hydrogens placed at geometrically calculated positions. The asymmetric unit contains the complex and a PF_6 counter ion, four times all this in the unit cell.

Table 3.7: Crystallographic and structure refinement data for complex **13**

Complex	**13**
Empirical formula	$C_{32}H_{30}ClF_6IrN_3P$
Formula weight	829.21
Temperature (K)	150(2)
Crystal system	monoclinic
Space group	$P2_1/n$
a (Å)	9.13036(14)
b (Å)	30.6604(4)
c (Å)	11.18445(15)
α (°)	90
β (°)	94.2735(13)
γ (°)	90
Volume (Å^3)	3122.27(8)
Z	4
ρ_{calc} (g/cm^3)	1.764
μ (mm^{-1})	4.477
F(000)	1624.0
Crystal size (mm^3)	0.4 × 0.3 × 0.3 brown block
Radiation	MoKα (λ = 0.71073)
2Θ range for data collection (°)	5.204 to 64.802
Index ranges	-13 ≤ h ≤ 13, -46 ≤ k ≤ 45, -16 ≤ l ≤ 16
Reflections collected	94866
Independent reflections	10712 [R_{int} = 0.0444, R_{sigma} = 0.0260]
Data/restraints/parameters	10712/0/401
Goodness-of-fit on F^2	1.141

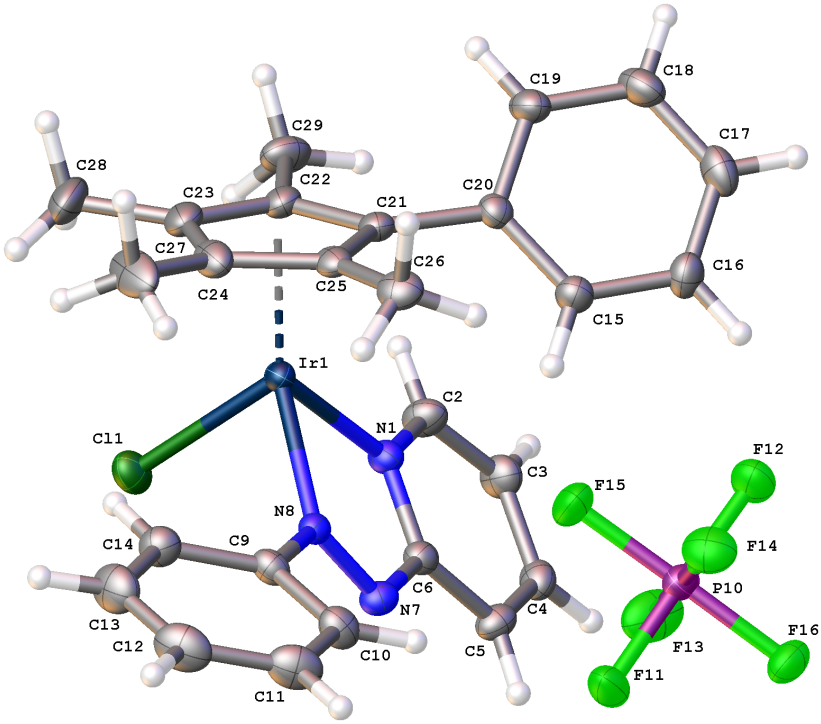

Figure 3.11: Solid state structure of complex **14** with atom labelling and thermal ellipsoids drawn at 50% probability level. Hydrogens placed at geometrically calculated positions. The asymmetric unit contains the complex and a PF_6 counter ion, four times all this in the unit cell. The molecule has crystallised in a chiral space group [(P2(1)2(1)2(1)] so is associated with a Flack (and Hooft) parameter that give a confidence in the assignment of the appropriate handedness of the crystal chosen.

Table 3.8: Crystallographic and structure refinement data for complex **14**

Complex	**14**
Empirical formula	$C_{26}H_{26}ClF_6IrN_3P$
Formula weight	753.12
Temperature (K)	150(2)
Crystal system	orthorhombic
Space group	$P2_12_12_1$
a (Å)	9.68478(19)
b (Å)	14.1744(2)
c (Å)	19.6375(3)
α (°)	90
β (°)	90
γ (°)	90
Volume (Å^3)	2695.76(8)
Z	4
ρ_{calc} (g/cm^3)	1.856
μ (mm^{-1})	5.174
F(000)	1464.0
Crystal size (mm^3)	0.6 × 0.2 × 0.18 brown block
Radiation	MoKα (λ = 0.71073)
2Θ range for data collection (°)	5.046 to 64.752
Index ranges	-14 ≤ h ≤ 14, -21 ≤ k ≤ 21, -29 ≤ l ≤ 29
Reflections collected	41771
Independent reflections	9081 [R_{int} = 0.0366, R_{sigma} = 0.0317]
Data/restraints/parameters	9081/0/347
Goodness-of-fit on F^2	1.039
Flack parameter	-0.017(2)

Table 3.9: Bond lengths of iridium-halide bonds for eight complexes determined by x-ray experiments. Estimated standard deviation shown in brackets.

Complex	Atom 1	Atom 2	Length/Å
1	Ir	Cl	2.3857(5)
3	Ir	Cl	2.3771(11)
5	Ir	Cl	2.3803(9)
6	Ir	Cl	2.3719(5)
8	Ir	Cl	2.3888(8)
10	Ir	I	2.68371(16)
13	Ir	Cl	2.3791(6)
14	Ir	Cl	2.3796(10)

Bond lengths lie within the expected range for complexes of this structure.[94,104] The Ir-I bond of complex **10** is significantly longer than the Ir-Cl bonds of the other complexes for which crystal structure data were obtained.

3.3.3 Effect of Structure on Hydrophobicity

Hydrophobicity is a key component in drug design, and there is a general perception that very hydrophobic complexes are unlikely to progress to commercial drugs, due to factors such as difficulty in solubilisation and formulation. Low hydrophobicity is typically desirable as high water-solubility correlates with high oral availability and easier formulation, although such complexes are sometimes harder to purify. A desirable feature of the chemotherapeutic oxaliplatin is that it can be orally administered, and, as such, is more favourable for administration to patients.[105] Liplinski's rule of five[106] encourages drug development to be focussed on small, moderately hydrophobic/lipophilic molecules. Moderate lipophilicity is a desirable drug feature, as, to be intracellularly active, a drug needs to be able to permeate the lipid bilayer of cell membranes. Hence, a balance must be struck between hydrophobicity and hydrophilicity in order to maximise solubility for formulation without impeding the drug's ability to permeate cell membranes and reach intracellular target sites. For non-orally deliverable drugs, there are a variety of other delivery systems that can be utilised, such as the delivery of the anticancer drugs paclitaxel or doxorubicin by encapsulation in liposomes.[107,108] The effect of modulation of functional groups of organoiridium complexes **1** − **19** on their relative hydrophobicity was measured by LC-MS (Figure 3.12). LC-MS carried out under the conditions described in Chapter 2.

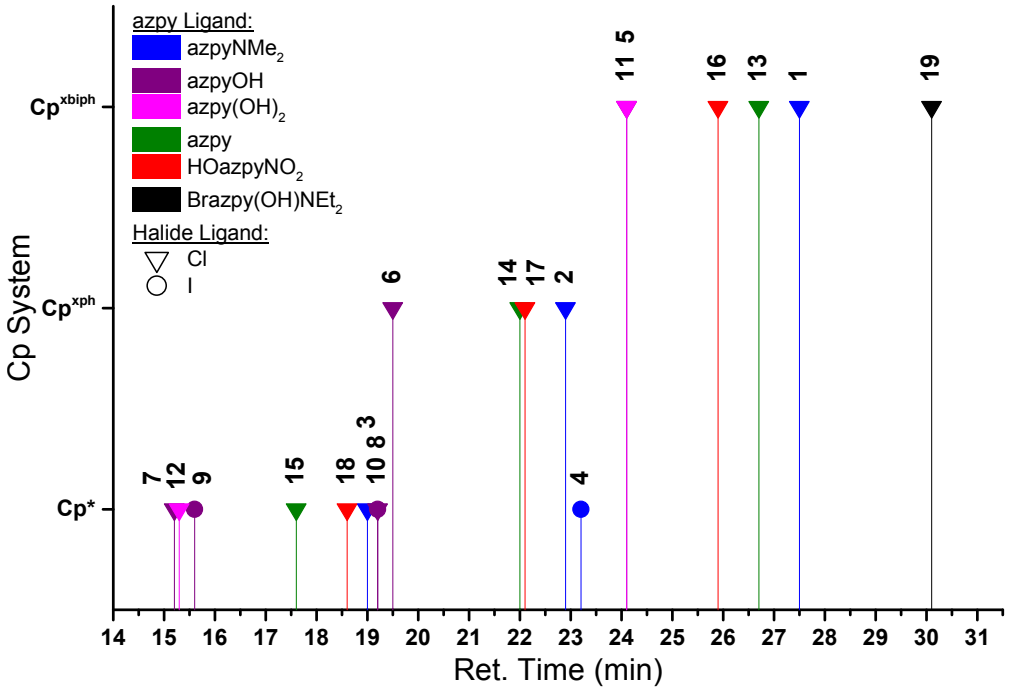

Figure 3.12: Relative hydrophobicity measured by LC-MS retention times for complexes **1** − **19** colour-coded by bidentate azopyridine ligand and shape-coded by halido ligand.

When comparing structurally similar complexes, the level of hydrophobicity vs. Y group generally follows the trend: $NEt_2 > NMe_2 > H > NO_2 > OH > (OH)_2$. The extension of the Cp system system by the addition of phenyl rings increases hydrophobicity as evidenced by retention times being highest for Cp^{xbiph} complexes **1**, **5**, **11**, **13**, **16** and **19**, followed by Cp^{xph} complexes **2**, **14** and **17**, then the remaining Cp* complexes. A notable exception is the one Cp* azpyNMe$_2$ iodido complex **4**, which has higher hydrophobicity than all other Cp* and Cp^{xph} complexes. Two other Cp* complexes bearing the azpyOH ligand, complexes **9** and **10**, also bear the iodido ligand. Whilst they are considerably less hydrophobic than complex **4**, both are far more hydrophobic than their otherwise identical chlorido analogues.

3.3.4 Relationships Between Hydrophobicity and Antiproliferative Activity

Previous literature on the antiproliferative activity of C'N-chelated organoiridium complexes revealed a correlation between LC retention time, cellular uptake of complex, and anticancer potency. Complexes which were more hydrophobic had higher retention times, greater uptake and superior cytotoxicity against cancer cells.[86] To determine if this was the case for N'N-chelated azopyridine ligands, IC_{50} values were determined in A2780 and compared to their LC-MS retention times (Table 3.10 and Figure 3.13). A compilation of IC_{50} values for complexes **1** − **19** in all cell lines in all chapters of this work can be found in Appendix Tables S1 and S2, pg. 269 – 270. Antiproliferative screenings against A2780 carried out by Dr. Isolda Romero-Canelón, Ji-Inn Song and Bindy Heer.

Table 3.10: IC_{50} values (in μM) in A2780 cells for complexes **1** − **19** and CDDP. Values and standard deviations obtained from duplicates of triplicate experiments. LC-MS retention times for complexes **1** − **19** carried out under identical separation conditions. Lines separate complexes of different families by azopyridine ligand (*n.d.* = not determined).

Complex	Structure	A2780 IC_{50} (μM)	Ret. Time. (min)
1	$[(Cp^{xbiph})Ir(azpyNMe_2)Cl]PF_6$	0.095 ± 0.006	27.5
2	$[(Cp^{xph})Ir(azpyNMe_2)Cl]PF_6$	0.101 ± 0.001	22.9
3	$[(Cp^*)Ir(azpyNMe_2)Cl]PF_6$	1.59 ± 0.03	19
4	$[(Cp^*)Ir(azpyNMe_2)I]PF_6$	*n.d.*	23.2
5	$[(Cp^{xbiph})Ir(azpyOH)Cl]PF_6$	0.14 ± 0.09	24.1
6	$[(Cp^{xph})Ir(azpyOH)Cl]PF_6$	0.108 ± 0.009	19.5
7	$[(Cp^*)Ir(azpyOH)Cl]PF_6$	0.12 ± 0.04	15.2
8	$[(Cp^*)Ir(azpyOH)Cl]Cl$	0.17 ± 0.07	19.2
9	$[(Cp^*)Ir(azpyOH)I]PF_6$	0.25 ± 0.02	15.6
10	$[(Cp^*)Ir(azpyOH)I]I$	0.34 ± 0.02	19.2
11	$[(Cp^{xbiph})Ir(azpy(OH)_2)Cl]PF_6$	5.0 ± 0.5	24.1
12	$[(Cp^*)Ir(azpy(OH)_2)Cl]PF_6$	0.776 ± 0.002	15.3
13	$[(Cp^{xbiph})Ir(azpy)Cl]PF_6$	0.126 ± 0.002	26.7
14	$[(Cp^{xph})Ir(azpy)Cl]PF_6$	0.22 ± 0.02	22
15	$[(Cp^*)Ir(azpy)Cl]PF_6$	1.5 ± 0.2	17.6
16	$[(Cp^{xbiph})Ir(HOazpyNO_2)Cl]PF_6$	0.4 ± 0.1	25.9
17	$[(Cp^{xph})Ir(HOazpyNO_2)Cl]PF_6$	0.184 ± 0.002	22.1
18	$[(Cp^*)Ir(HOazpyNO_2)Cl]PF_6$	0.43 ± 0.04	18.6
19	$[(Cp^{biph})Ir(Brazpy(OH)NEt_2)Cl]PF_6$	16 ± 6	30.1
CDDP	*cis*-$[Pt(NH_3)_2Cl_2]$	1.2 ± 0.2	*n.d.*

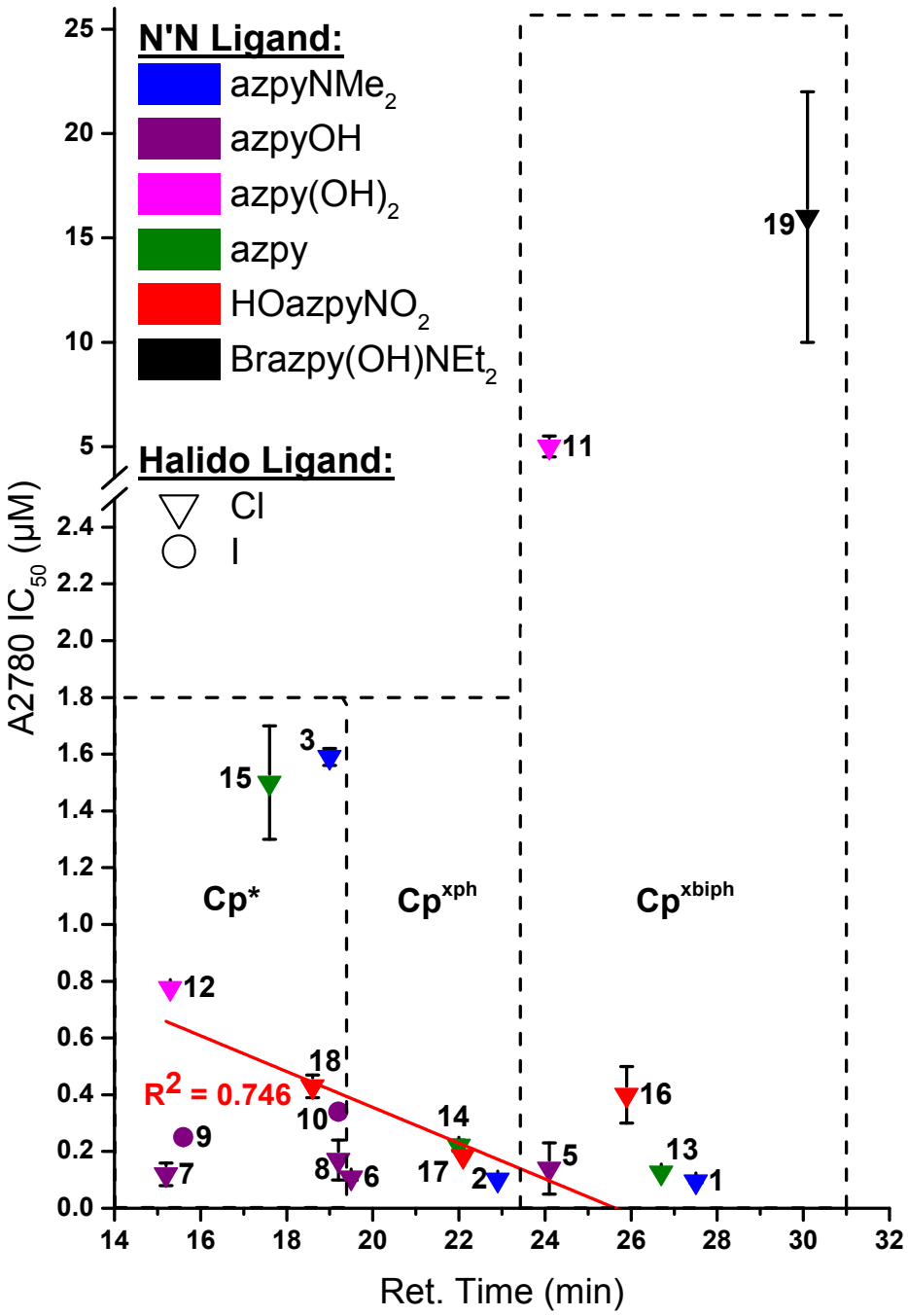

Figure 3.13: Plot of IC_{50} values (in μM) in A2780 cells vs. LC-MS retention times for complexes **1** – **19**. Points colour-coded by bidentate azopyridine ligand, shape-coded by halido ligand and Cp system shown for comparison. Error bars obtained from IC_{50} standard deviations. Correlation between IC_{50} and retention time fitted by weighted linear regression and a line of best fit plotted (red). Adjusted r-squared value = 0.746.

There is a weak correlation between retention time and anticancer potency in agreement with trends observed in previous literature.[86] However, there are multiple significant outliers which are mostly ignored by the weighted line fitting algorithm, in particular the Cp^{xbiph} Brazpy(OH)NEt_2 complex **19**, with the highest retention time, has the least potency, with an IC_{50} value ca. 1 – 2 orders of magnitude greater than most of the other complexes. However, complex **19** does have many structural differences to the rest of the complex families in this work. Conversely, complex **7**, which has the lowest retention time, is one of the most potent.

Further interesting trends can be observed within families of complexes bearing the same azopyridine ligand. These families of complexes are grouped together in Tables 3.1 and 3.10. Structures can be found in Figure 3.3.

Complexes **1** − **4** bear the azpyNMe_2 ligand. Within this family of complexes, extension of the Cp system by a phenyl ring imparts an large increase in potency, however the addition of a second phenyl ring only increases potency by a negligible amount.

Complexes **5** − **10** which bear the azpyOH bidentate ligand (azpyOH pK_a values investigated in Chapter 5) all have comparatively low retention times, yet retain potent activity. Of further interest is the almost identical potencies of complexes **5** − **7**, as they bear differing Cp systems. This usually leads to dramatic differences in activity, however, this is not observed for this family of complexes.

Another interesting comparison can be made between the Cp* azpyOH chlorido complexes **7** and **8** and their iodido analogues **9** and **10**. Unlike the case for the azpyNMe_2 complexes **3** and **4** there is not a large difference in retention times between the azpyOH chlorido and iodido analogues, however both iodido complexes are slightly less potent. The azpyOH family of complexes is investigated further in Chapter 5.

Complexes **11** and **12** bear the azpy$(OH)_2$ ligand. In stark contrast, the Cp^{xbiph} complex **11** of azpy$(OH)_2$ family is significantly less active than its Cp* analogue, complex **12**. A Cp^{xph} azpy$(OH)_2$ complex was not synthesised

in this work.

Complexes **13** − **15** bear the azpy ligand. Within this family of complexes the same relationship between the Cp system and potency is observed as for the azpyNMe$_2$ complexes.

Complexes **16** − **18** bear the HOazpyNO$_2$ ligand. The HOazpyNO$_2$ family shows little difference in potency between the Cp* and Cp^{xbiph} complexes, whereas the Cp^{xph} is the most potent.

3.3.5 Catalysis of NADH Oxidation

The results shown in this chapter thus far have focused on the characterisation of the chemical properties of several organoiridium complexes and their level of antiproliferative activity against cancer cells. However, understanding how these complexes exert their cytotoxic effect on cancer cells is of great importance. Therefore, investigations into the MoA of eleven of these complexes were carried out, beginning with their ability to oxidise the cellular coenzyme nicotinamide adenine dinucleotide (NAD^+). NAD^+ has been of recent interest as a potential target for anticancer complexes[86,94,104] and transfer hydrogenation has been shown to be an effective way of selectively killing cancer cells.[57]

NAD^+ and its reduced form NADH play essential roles in cellular metabolism. The complex accepts or donates electrons in redox reactions (Figure 3.14).[109] One of the most important roles of NAD^+ is the acceptance of electrons from the citric acid cycle that occurs in the mitochondrial matrix to generate NADH. Subsequent oxidation of this NADH releases energy used to pump protons from the mitochondrial matrix into the intermembrane space. The higher concentration of protons in the intermembrane space relative to the mitochondrial matrix generates potential energy in the form of a proton gradient. Protons flow back into the mitochondrial matrix through the transmembrane enzyme adenosine triphosphate (ATP) synthase, providing the energy required for oxidative phosphorylation, generating the universal energy carrier ATP, from adenosine diphosphate (ADP) and phosphate.[110]

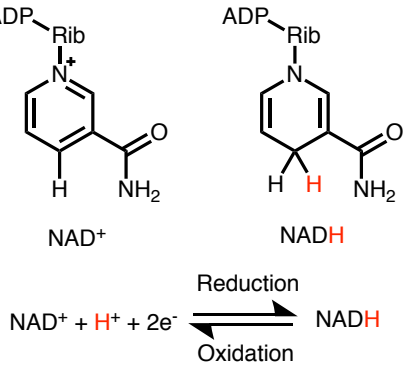

Figure 3.14: The structures and oxidation/reduction reactions of $NADH/NAD^+$.

NADH is known to be involved in the production of mitochondrial reactive oxygen species (ROS), and the primary mitochondrial ROS is superoxide (SO).[111,112] Perturbation of cellular redox balance has proven to be an effective way to kill cancer cells.[113] The ratio of coenzyme NADH and its oxidised form NAD^+ therefore has implications to biological function. A highly potent and selective organoiridium complex has been shown to catalyse the oxidiation of NADH by hydride transfer to molecular oxygen to generate H_2O_2.[84] To investigate whether any of the organoiridium complexes in this work have the capability to catalyse the oxidation of NADH, UV studies were carried out on NADH incubated with each of 11 organoiridium complexes for 24 h at 310 K and the solutions tested for H_2O_2 (Figure 3.15). ^{1}H-NMR spectra of the reaction mixtures of complexes **1** and **13** were examined 10 min after NADH addition in an attempt to observe an Ir-H intermediate, however, no corresponding peaks were observed. Turnover number (TON) corresponds to the μM of NADH oxidised over 24 h, calculated from the known molar extinction coefficient of NADH at 340 nm (6220 $M^{-1}cm^{-1}$). Turnover frequency (TOF) calculated as the gradient of TON vs. time in the first 2 h.

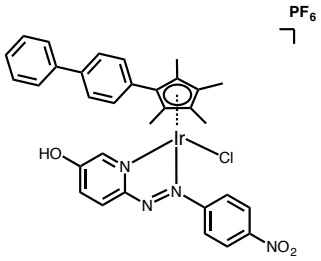

Complex **16**

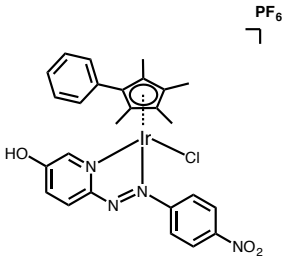

Complex **17**

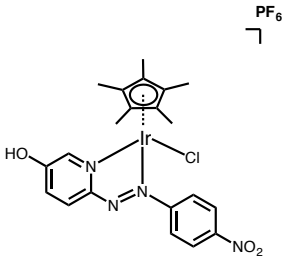

Complex **18**

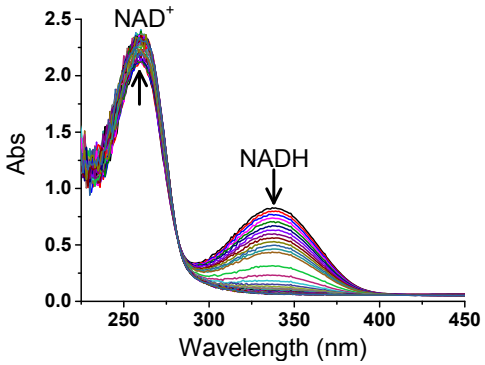

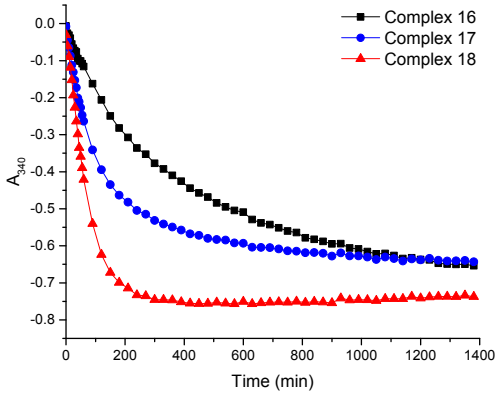

Complex 18
Slight blue colour
indicates peroxide

MeOH Control
White indicates
no peroxide

Complex	TON (μM)	TOF (h^{-1})	H_2O_2
1	3	1	N
3	6	1	N
4	4	1	N
12	25	2	N
13	14	4	N
14	53	6	N
15	17	1	N
16	105	16	N
17	103	31	N
18	119	48	Y
19	119	18	N

Figure 3.15: Catalytic oxidation of 150 μM NADH to NAD^+ by 11 complexes. (Top Left) UV spectra of 2.5 μM of complex **18** in 0.5% MeOH/99.5% (v/v) 5 mM Na_2HPO_4/NaH_2PO_4 buffer pH 7.4 at 310 K. (Top Right) Comparison of changes in NADH absorbance at 340 nm relative to 0.5% MeOH-buffer control for $HOazpyNO_2$ complexes **16** – **18**. (Bottom Left) Test for H_2O_2 generation by complex **18** after 24 h using Quantofix peroxide test sticks, which turn from white to blue in the presence of H_2O_2. (Bottom Right) Calculated TONs after 24 h and TOF values for the 11 complexes tested.

All complexes tested showed some level of NADH oxidation relative to the MeOH control with no complex, with a measurable reduction in the UV peak of NADH at 340 nm and a concomitant increase in the peak at 261 nm corresponding to NAD^+. The level of catalytic activity varies significantly, depending greatly on the bound ligands, however further experimental repeats would be required to obtain more accurate data. The azpyNMe$_2$ complexes **1**, **3**, and **4** induce little to no oxidation of NADH, demonstrated by very low TONs, between 3 – 6 μM, compared to the control. The chlorido azpyNMe$_2$ complex **3** shows a slightly higher TON than its iodido analogue, complex **4**. The azpy complexes **13** − **15** have a comparably higher TON. Of these, the Cp^{xph} analogue, complex **14**, displayed significantly higher catalytic activity than its Cp* or Cp^{xbiph} analogues. The azpy(OH)$_2$ complex **12** showed a greater TON and TOF than the azpy and azpyNMe$_2$ complexes, with the exception of complex **14**. The three HOazpyNO$_2$ complexes **16** − **18** all showed significantly higher TONs than previously mentioned complexes ($\geq$ 100 μM) as well as higher TOFs. There is a clear trend in the catalytic activity of the HOazpyNO$_2$ complexes. The TON and TOFs are highest in the Cp* analogue, complex **18**, and follow the trend Cp* >Cp^{xph} >Cp^{xbiph}. Additionally, complex **18** is the only complex tested that generates detectable levels of H_2O_2, generating an amount in the range 0.5 mg/L – 2.5 mg/L. Qualitative assessment of H_2O_2 generation can be found in Appendix Figure S20, pg. 291. Complex **18** and the BrazpyONEt$_2$ complex **19** have equal TONs, whereas complex **18** has 3× the TOF, demonstrating the most rapid NADH oxidisation in the first 2 h of any of the 11 complexes tested.

3.3.6 Effect of Functional Groups on Aquation

The azpyNMe$_2$ complex **1** is the most potent complex against A2780 ovarian carcinoma of the nineteen complexes studied (Table 3.10). However all azpyNMe$_2$ complexes tested have almost no oxidant activity towards NADH (Figure 3.15), indicating that they possess a MoA that does not involve NADH oxidation. The remainder of this chapter details further investigations into possible MoAs of the azpyNMe$_2$ complexes.

To elucidate the MoA of a complex, it is necessary to know what form it takes when in solution. The activation step of CDDP involves the hydrolysis of the metal-Cl bond. Many anticancer complexes of other transition metals share this activation step, in many cases the rate of hydrolysis is dependent on the bound halide.[114] To investigate whether changing the halide bound to the iridium centre affects hydrolysis, solutions of complexes **1** and **4** were monitored over 24 h by ^{1}H-NMR in 10% d$_6$-DMSO:D$_2$O, 0.1% 1,4-dioxane at 310 K (Figure 3.16 and 3.17) and the extent of hydrolysis calculated by the peak integrals (Table 3.11). The presence of DMSO ensured the solubility of the complexes and 1,4-dioxane was used as the reference peak to calibrate the spectra. Further experiments were carried out under the same conditions using 120 mM NaCl to assess whether the presence of excess chloride would suppress hydrolysis of the Cl bond. This concentration of chloride matches that of the cell medium in which antiproliferative screenings were carried out, therefore spectra under these conditions provide an indication of what form the complexes would likely take in solution under biological conditions.

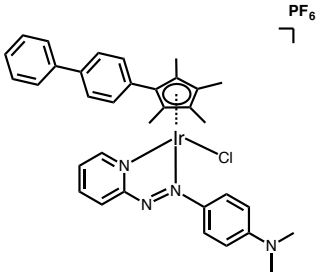

Complex **1**

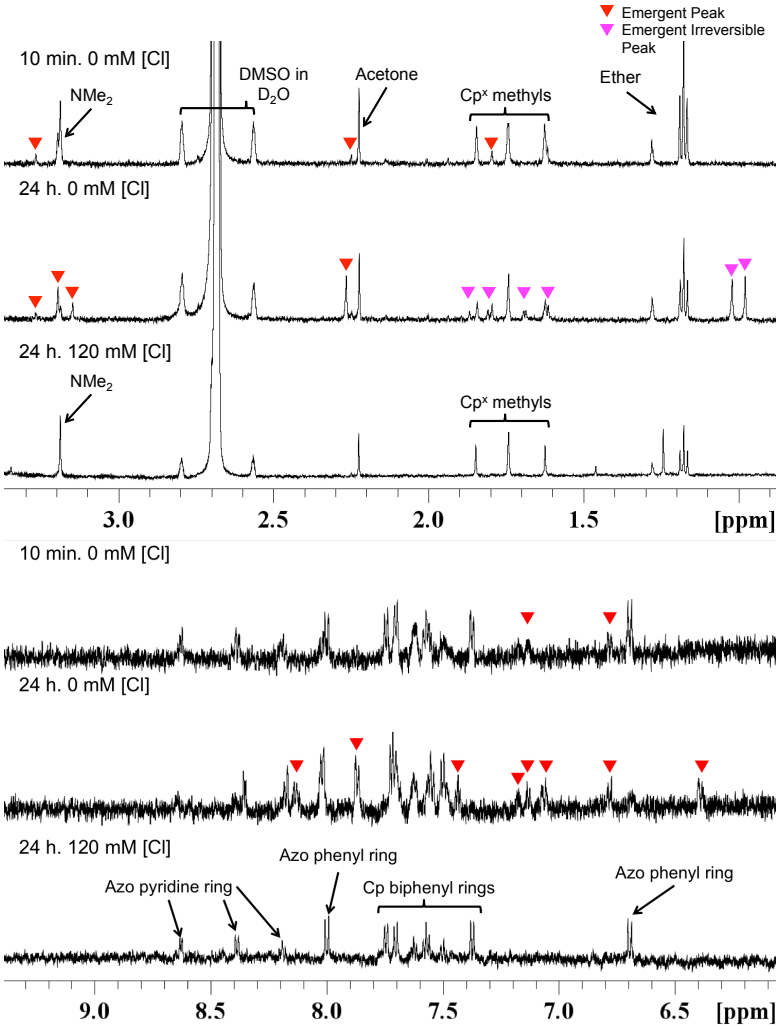

Figure 3.16: Hydrolysis of complex **1** studied by 600 MHz ^{1}H-NMR spectra of a 100 μM solution of complex **1** in 10% d_6-DMSO:D_2O, 0.1% 1,4-dioxane (v/v) at 310 K, unbuffered at pD 8. Aliphatic region shown above, aromatic region shown below. Spectra shown 10 min after sample preparation, 24 h after sample preparation, and 24 h after sample preparation in 120 mM NaCl solution. Emergent peaks not corresponding to original complex denoted by red arrows. Traces of acetone/ether from the NMR tube are visible.

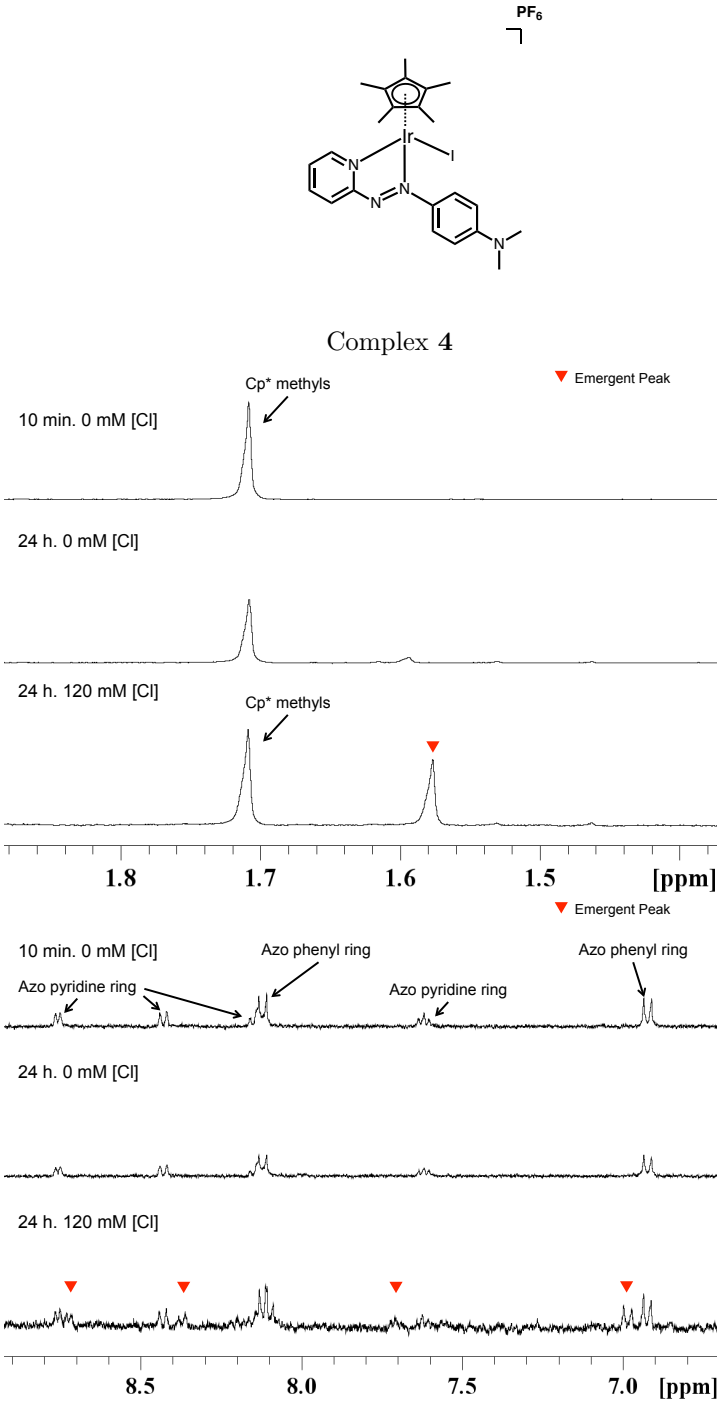

Figure 3.17: Hydrolysis of complex **4** studied by 600 MHz ^{1}H-NMR spectra of a 100 μM solution of complex **1** in 10% d_6-DMSO:D_2O, 0.1% 1,4-dioxane (v/v) at 310 K, unbuffered at pD 8. Spectra shown 10 min after sample preparation, 24 h after sample preparation, and 24 h after sample preparation in 120 mM NaCl solution. Emergent peaks not corresponding to original complex denoted by red arrows.

Table 3.11: Hydrolysis data for complexes **1** and **4** monitored over 24 h by ^{1}H-NMR in 10% d_6-DMSO:D_2O, 0.1% 1,4-dioxane at 310 K. Aliphatic region shown above, aromatic region shown below. Experiments were repeated with the addition of 120 mM NaCl before or after 24 h to assess suppression and reversibility of hydrolysis by chloride.

Complex	Structure	% Extent of Hydrolysis (0 mM [Cl])	% Extent of Hydrolysis (120 mM [Cl])
1	$[Cp^{xbiph}Ir(azpyNMe_2)Cl]PF_6$	79%	0%
4	$[Cp^{*}Ir(azpyNMe_2)I]PF_6$	0%	40%*

*Complex **4** did not hydrolyse in the presence on 120 mM [Cl], instead 40% of the complex exchanged its iodido ligand for a chlorido one.

To determine whether the hydrolysis of complex **1** was reversible by post-hydrolysis addition of chloride, the experiment was repeated without chloride then 120 mM chloride was subsequently added after 24 h incubation as solid NaCl, and another spectrum was taken 10 min thereafter.

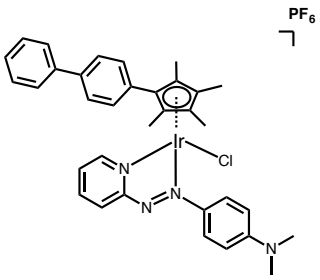

Complex **1**

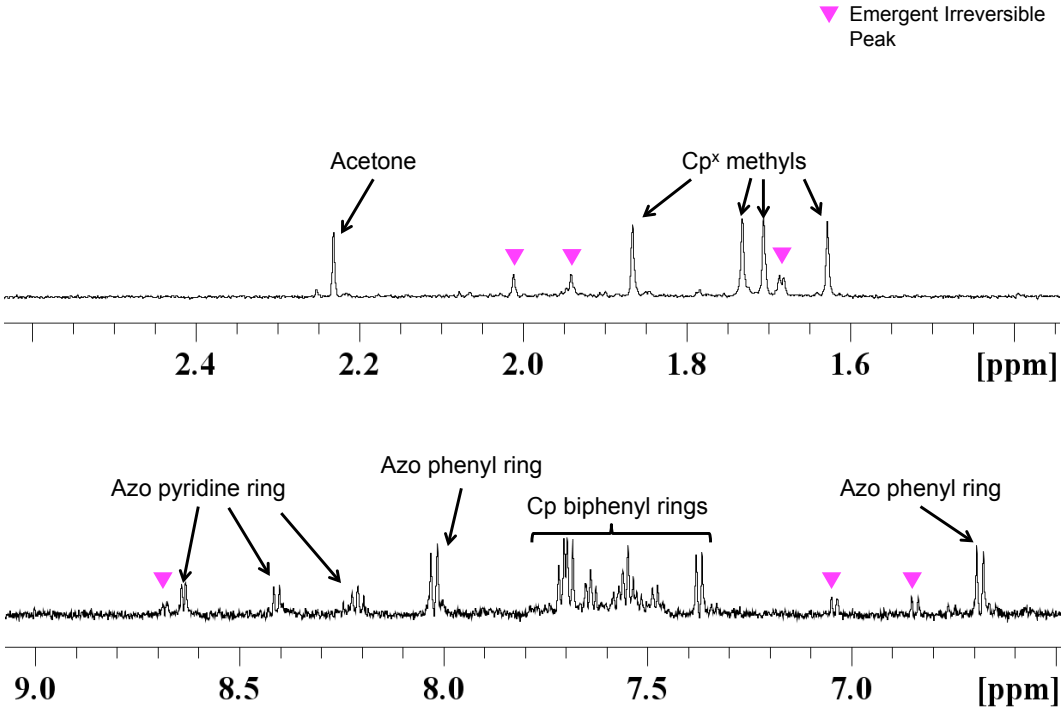

Figure 3.18: Aliphatic (top) and aromatic (bottom) regions of a 600 MHz ^{1}H-NMR spectrum of a 100 μM solution of complex **1** in 10% d_6-DMSO:D_2O, 0.1% 1,4-dioxane (v/v) at 310 K, unbuffered at pD 8. Spectrum taken 10 min after addition of 120 mM [Cl] to a previously chloride-free solution that had been incubated for 24 h. Emergent peaks not corresponding to original complex denoted by pink arrows. Traces of acetone/ether from the NMR tube are visible.

Complex **1** has been shown to be stable in 100% DMSO, spectra in Appendix Figure S21, pg. 292. Therefore the appearance of new peaks in the spectra of chlorido complex **1** over 24 h in addition to concomitant reduction in the

peaks corresponding to the original complex can be attributed to the hydrolysis of complex **1** in the presence of H_2O. The spectrum of Cp* iodido complex **4**, however, does not change over 24 h, indicating that complex **4** does not hydrolyse in the presence of H_2O. The spectrum of chlorido complex **1** under the same conditions with 120 mM NaCl shows no change after 24 h. However, some of the new peaks that appear upon hydrolysis do not disappear upon subsequent addition of 120 mM NaCl. Conversely, the spectrum of Cp* iodido complex **4** with 120 mM NaCl contains new peaks after 24 h. The chemical shifts of these new peaks match exactly that of Cp* chlorido complex **3** under the same conditions, therefore the most likely explanation is that there is some $I \rightarrow Cl$ exchange occurring when complex **4** is in solution with 120 mM NaCl.

A peak at m/z = 709.2 was observed in the ESI-MS spectrum of complex **1** after 24 h in salt-free aqueous solution which matches the theoretical m/z of an analogue of complex **1** in which the metal-bound chloride is replaced by OH.

3.3.7 Effect of Chelating Ligands on Chiral Enantiomer Separation

The results of the previous section highlight a difference in the behaviours of the chlorido complex **1** and the iodido complex **4** in aqueous solution. Enantiomers of organoiridium complexes bearing an azpyNMe$_2$ bidentate ligand have previously been separated successfully, however, isolation of stable enantiomers was not achieved.[103] The increased aqueous stability of the iodido complex, however, may allow for successful isolation. It is widely acknowledged that enantiomers of chemical compounds can exhibit different behaviours. Sometimes the pharmacological effects of enantiomers of the same complex are drastically different and chirally pure molecules can even epimerise *in vivo*.[115] It is therefore important to investigate the chiral separability of any potential clinical drug.

To separate and assess the stability of the enantiomers of complexes **1** − **4**, separations by chiral column were carried out (Figure 3.19) using a CHIRALPAK IC column in normal phase (composition detailed in Figure 3.2) from Chiral Technologies Europe.

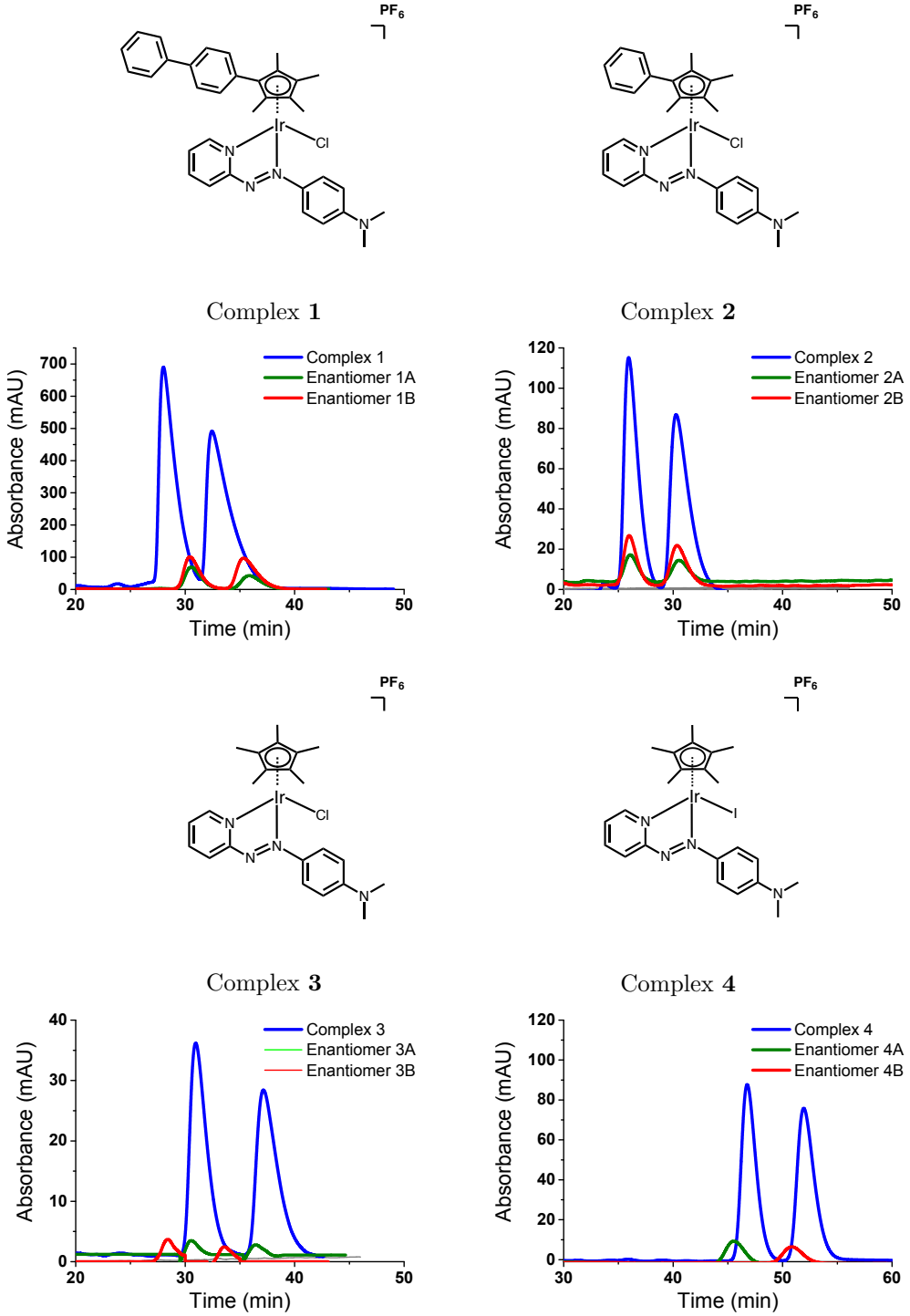

Figure 3.19: Chromatograms of 1 mg/ml solutions of complexes **1** – **4** in EtOH (blue) separated on a CHIRALPAK IC column. Separated enantiomers were stored at 193 K for 20 h then re-injected (red/green).

Two peaks are seen for the injection of complex **1** (blue) which correspond to its two enantiomers, **1A** and **1B**. Separation of enantiomers was possible with impressive resolution, i.e. no peak overlap (Table 3.12), however there are slight unexpected shifts in retention times of some enantiomers relative to the initial complex. These separated peaks were collected, dried under vacuum, stored at 193 K for 20 h then re-injected (red and green). Injection of complex **1A** or **1B** after 20 h resulted in the same two peaks observed. This is also the case for complexes **2** and its enantiomers **2A** and **2B**, as well as complex **3** and its enantiomers **3A** and **3B**.

Injection of complex **4** results in two peaks corresponding to **4A** and **4B**, however re-injection of **4A** after 20 h results on only one peak being observed. The same is true for re-injection of **4B**.

Complexes **1** − **3** bear a monodentate chlorido ligand. They are shown here to exist as racemic mixtures. However, even when dried and stored at 193 K for 20 h their separated enantiomers rapidly epimerise back into a racemic mixture.

Complex **4** bears a monodentate iodido ligand instead of chlorido, but is otherwise structurally identical to complex **3**. This complex also exists as a racemic mixture, however the enantiomers of complex **4** were not only separable, but stable (i.e. did not epimerise), under the same storage conditions as those used for complexes **1** − **3**.

Table 3.12: Retention times, peak integral area percentages, peak widths and separation resolutions for the separation of chiral enantiomers of complexes **1** – **4** and their separated enantiomers **1A** – **4A** and **1B** – **4B** after storage at 193 K for 20 h by CHIRALPAK IC column. Only enantiomers **4A** and **4B** remained enantiomerically pure after storage (highlighted in red). Separation resolution between two peaks calculated as (Ret. Time (peak 1) - Ret. Time (peak 2))/(0.5 x (Peak Width (peak 1) + Peak Width (peak 2)))

Complex	Sample	Ret. Time (min)	Area %	Peak Width (min)	Resolution
	Initial	28.00	51	1.57	2.41
		32.45	49	2.12	
1	Enantiomer 1A	30.56	57	1.58	3.05
		35.86	43	1.89	
	Enantiomer 1B	30.43	46	1.56	2.80
		35.34	54	1.95	
	Initial	25.94	50	1.40	2.72
		30.27	50	1.78	
2	Enantiomer 2A	26.08	51	1.31	3.18
		30.53	49	1.49	
	Enantiomer 2B	25.98	50	1.28	3.32
		30.63	50	1.52	
	Initial	31.10	51	1.60	3.56
		37.36	49	1.92	
3	Enantiomer 3A	30.56	51	1.10	5.00
		36.46	49	1.26	
	Enantiomer 3B	28.41	52	1.05	4.87
		33.57	48	1.07	
	Initial	46.77	50	1.43	3.41
		51.93	50	1.60	
4	Enantiomer 4A	45.54	**100**	1.54	n/a
	Enantiomer 4B	50.84	**100**	1.50	n/a

Separation of the enantiomers of azpyOH complex **7** was also attempted but not achievable under these conditions, most likely due to the difference in bidentate ligand. Due to the highly specific conditions typically required for chiral separation no further separations were attempted for any other complexes.

3.3.8 Antiproliferative Activity against Oesophageal and Nasopharyngeal Cancers

Like CDDP, complexes **1** − **3** are unstable in aqueous solution. That this is suppressible by chloride suggests that hydrolysis is occuring at the Ir-Cl bond. This is supported by the inertness of the iodido complex **4** to hydrolysis and the instability of the chiral enantiomers of complexes **1** − **3**.

Complexes **1** − **3** are shown in Table 3.10 to be highly potent against A2780 ovarian carcinoma, however the MoA is still not well understood. To further assess the effect of the Cp system on antiproliferative activity, and to investigate whether the MoA of complexes **1** − **3** differ in CDDP-sensitive and -insensitive cell lines, they were tested against OE19 and SUNE-1 (Table 3.13). OE19 is a cell line derived from aggressive oesophageal carcinoma, against which CDDP has limited potency. SUNE-1 is a nasopharyngeal carcinoma cell line that is 10× more sensitive to CDDP than OE19. Antiproliferative screenings carried out by Dr. Isolda Romero-Canelón.

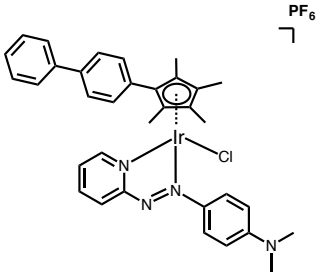

Complex **1**

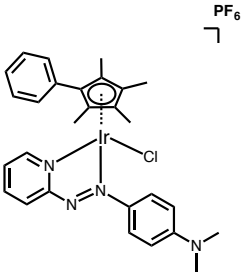

Complex **2**

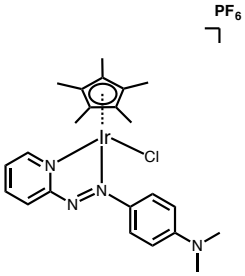

Complex **3**

Table 3.13: Comparison of IC_{50} values (in μM) of complexes **1** − **3** to CDDP against OE19 and SUNE-1.

Complex	OE19	SUNE-1
1	0.195 ± 0.002	0.58 ± 0.04
2	0.3 ± 0.003	1.14 ± 0.01
3	3.6 ± 0.3	10.5 ± 0.6
CDDP	13.43 ± 0.003	1.14 ± 0.01

In both cell lines, the presence of the phenyl ring in the Cp system of complex

2 confers an order of magnitude increase in potency compared to its Cp* analogue, complex **3**. The addition of a second phenyl ring (complex **1**) increases potency by a comparatively small amount.

All 3 complexes are considerably more active than CDDP in OE19, however in SUNE-1, complex **1** is more active, complex **2** has equal activity to CDDP and complex **3** is over an order of magnitude less potent than CDDP. This illustrates the significant impact of the Cp system on the potency of this family of complexes.

3.3.9 MoA Studies in Oesophageal and Nasopharyngeal Cancers by Flow Cytometry

As shown previously in Tables 3.10 and 3.13, extension of the Cp system correlates with an increase in potency against A2780 ovarian carcinoma, OE19 oesophageal carcinoma and SUNE-1 nasopharyngeal carcinoma. To investigate whether this difference in potency is due to changes in MoA, a panel of flow cytometry experiments were conducted on OE19 and SUNE-1 cells exposed to complexes $\mathbf{1}-\mathbf{3}$ to investigate their ability to generate ROS and SO, depolarise the mitochondrial membrane, induce apoptosis, and disrupt the cell cycle.

Flow cytometry is a technique used to analyse the size, shape, and properties of single cells in a mixture by passing them through a capillary narrow enough to allow only a single cell to pass at a time. Each cell passes through a laser beam, causing light to scatter and fluorophores in the cell to fluoresce if the laser light is set to the appropriate wavelength. The flow cytometer detects both scattering and fluorescence from each cell, allowing the cells to be sorted into distinct populations. In this work two fluorescence channels, FL1 (green) and FL2 (orange) are utilised to detect two separate sources of fluorescence from the cells stained with the various fluorescent dyes used throughout the experiments (detailed in subsection 2.3.4). Flow cytometry studies carried out with the help of Dr. Isolda Romero-Canelón and Hannah Bridgewater.

3.3.9.1 ROS and SO Generation

Cancer cells have altered redox states and so are more susceptible to perturbations in their delicate redox balance. Normal cells are less susceptible to this, and so the use of therapeutics which disrupt redox balance by generating ROS and SO may be a way to selectively kill cancer cells.[116] Metal-based complexes of platinum,[46] ruthenium[117] and osmium,[118] have been developed that generate ROS and SO, and/or utilise other redox-based MoAs to exert anticancer activity.[119]

The capacity of complexes **1** – **3** to induce changes in the levels of both general ROS (H_2O_2, peroxynitrate, NO and peroxy/hydroxyl radicals) and SO in OE19, complexes **1** and **2** in SUNE-1, and complex **2** in A2780 were investigated by flow cytometry (Figures 3.20 – 3.22). Pyocyanin, a ROS/SO-generating toxin produced by the bacterium *Pseudomonas aeruginosa*, was used as the positive control.

Gating of the cell populations was determined using the results for the positive and negative controls and kept constant within each experiment, however, in many cases, the gate splits a cell population of complex-treated cells into FL2+ or FL2- when there are clearly not two distinct populations. In these cases the cells classified as FL2- may still be producing SO, however the FL2 gate acts simply as a threshold by which the % of cells above it can be quantified to compare the level of FL2 fluorescence between complexes.

OE19

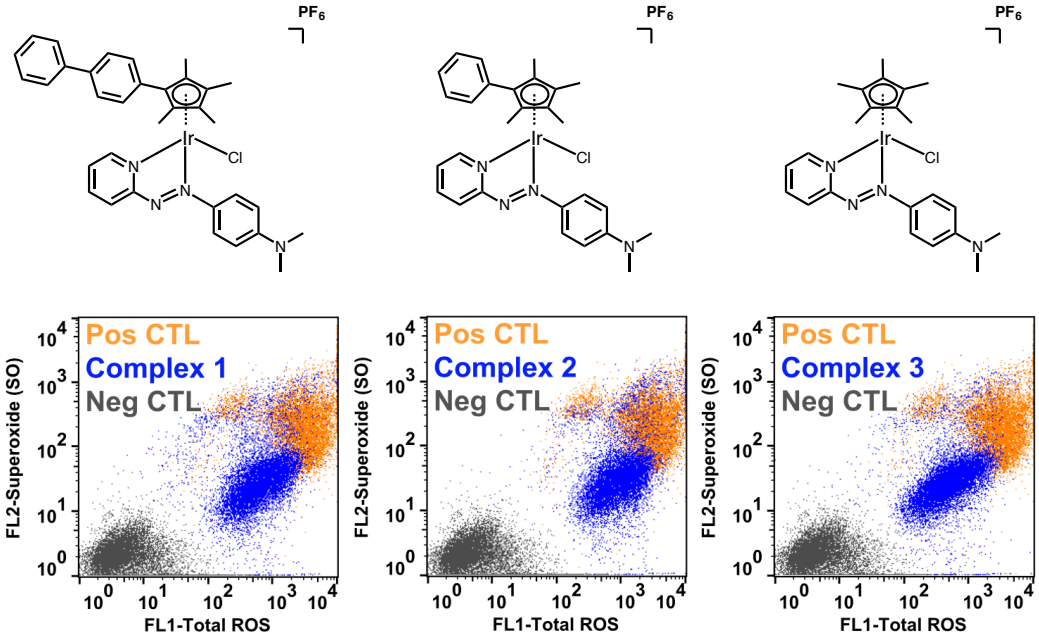

	High Superoxide FL1-FL2+ Q1	High ROS and Superoxide FL1+FL2+ Q2	High ROS FL1+FL2- Q3	Low ROS and Superoxide FL1-FL2- Q4
Neg CTL	0.00 ± 0.01	0.01 ± 0.01	2.1 ± 0.2	97.9 ± 0.2
Complex 1	1.6 ± 0.1 **	15 ± 1 **	82 ± 1 ****	1.05 ± 0.07 ****
Complex 2	0.21 ± 0.09	18.0 ± 0.6 ****	81.5 ± 0.7 **	0.22 ± 0.02 ****
Complex 3	0.60 ± 0.06 **	12.1 ± 0.7 ****	86 ± 1 **	1.0 ± 0.4 ****

Figure 3.20: (Top) Measurement of ROS and SO generation by flow cytometry of OE19 oesophageal carcinoma carcinoma cells exposed to complexes **1** − **3** for 24 h at IC_{50} concentrations at 310 K. Pyocyanin used as positive control (orange). (Bottom) Table of % cell populations obtained from triplicate experiments. Statistical significance between cells exposed to complex vs. negative control was determined by two-sample independent Welch t-tests assuming unequal variance between populations with asterisks corresponding to $p \leq 0.05$ *, $p \leq 0.01$ **, $p \leq 0.001$ ***, $p \leq 0.0001$ ****.

SUNE-1

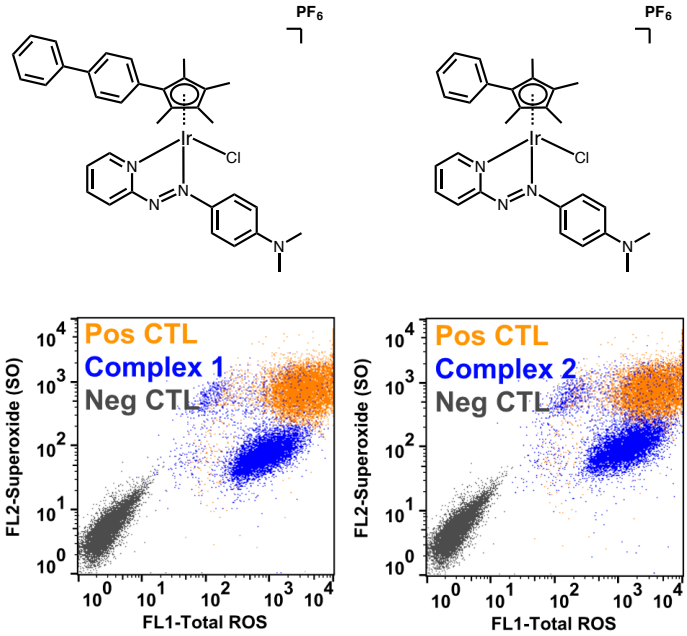

	High Superoxide FL1-FL2+ Q1	High ROS and Superoxide FL1+FL2+ Q2	High ROS FL1+FL2- Q3	Low ROS and Superoxide FL1-FL2- Q4
Neg CTL	0 ± 0	0.01 ± 0.02	0.01 ± 0.02	99.97 ± 0.06
Complex 1	1.1 ± 0.1 ****	6 ± 1 **	91 ± 1 ****	1.5 ± 0.1 ****
Complex 2	0.7 ± 0.2 ****	12 ± 1 **	86 ± 1 ****	1.04 ± 0.06 ****

Figure 3.21: (Top) Measurement of ROS and SO generation by flow cytometry of SUNE-1 nasopharyngeal carcinoma carcinoma cells exposed to complexes **1** and **2** for 24 h at IC_{50} concentrations at 310 K. Pyocyanin used as positive control (orange). (Bottom) Table of % cell populations obtained from triplicate experiments. Statistical significance between cells exposed to complex vs. negative control was determined by two-sample independent Welch t-tests assuming unequal variance between populations with asterisks corresponding to $p \leq 0.05$ *, $p \leq 0.01$ **, $p \leq 0.001$ ***, $p \leq 0.0001$ ****.

A2780

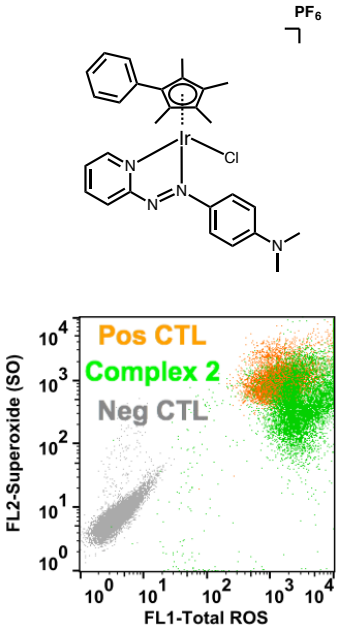

	High Superoxide FL1-FL2+ Q1	High ROS and Superoxide FL1+FL2+ Q2	High ROS FL1+FL2- Q3	Low ROS and Superoxide FL1-FL2- Q4
Neg CTL	0.17 ± 0.07	0	0	99.82 ± 0.07
Complex 2	0.1 ± 0.1	84 ± 1 ****	16 ± 1 ****	0.3 ± 0.5

Figure 3.22: (Top) Measurement of ROS and SO generation by flow cytometry of A2780 ovarian carcinoma cells exposed to complex **2** for 24 h at IC_{50} concentration at 310 K then stained with orange/green fluorescent reagents. Pyocyanin used as positive control (orange). (Bottom) Table of % cell populations obtained from triplicate experiments. Statistical significance between cells exposed to complex vs. negative control was determined by two-sample independent Welch t-tests assuming unequal variance between populations with asterisks corresponding to $p \leq 0.05$ *, $p \leq 0.01$ **, $p \leq 0.001$ ***, $p \leq 0.0001$ ****.

Complexes **1** − **3** generate high levels of ROS and SO in OE19 cells, complexes **1** and **2** in SUNE-1 cells, and complex **2** in A2780 cells. Complex **2** generates more SO in A2780 than in OE19 or SUNE-1, evidenced by the greater level of FL2 fluorescence observed for complex **2**-treated cells in A2780 vs. OE19 or SUNE-1 in addition to a higher % of cell in the FL2+ populations.

3.3.9.2 Mitochondrial Membrane Depolarisation

Complexes **1** − **3** generate significant amounts of ROS and SO in cancer cells. This can have an impact on mitochondrial function. To assess whether the mitochondria of cancer cells were affected, OE19 oesophageal cancer cells exposed to complexes **1** − **3** were assayed for depolarisation of the mitochondrial membrane potential using the cationic dye JC10 (Figure 3.23). JC10 aggregates in the mitochondria and emits detectable fluorescence, however, if the membrane is depolarised, the dye disaggregates and a measurable decrease in fluorescence is observed. 1 μM carbonyl cyanide m-chlorophenyl hydrazone (CCCP), an inhibitor of oxidative phosphorylation, was used as the positive control.

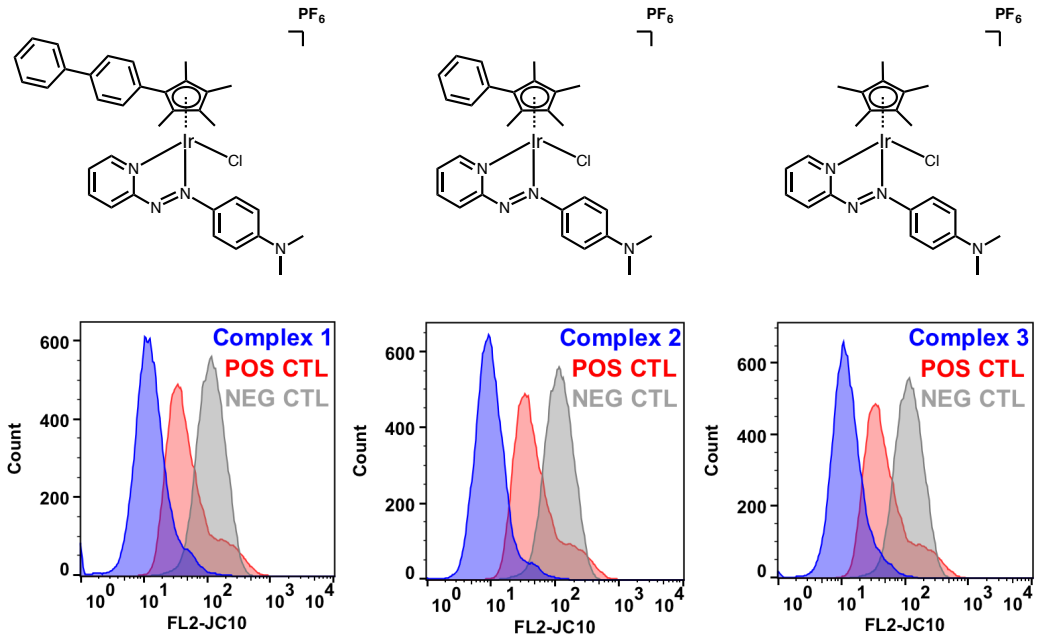

Complex	%Polarised	%Depolarised
Neg CTL	88.1 ± 0.5	11.9 ± 0.5
Pos CTL	28 ± 1	72 ± 1
1	2.17 ± 0.06 ****	98.83 ± 0.06 ****
2	1.07 ± 0.06 ****	98.93 ± 0.06 ****
3	1.3 ± 0.1 ****	98.7 ± 0.1 ****

Figure 3.23: (Top) Depolarisation of mitochondrial membrane potential of OE19 oesophageal carcinoma cells exposed to complexes **1** − **3** for 24 h at IC_{50} concentration at 310 K measured by reduction in JC10 fluorescence. (Bottom) Table of % cell populations with polarised/depolarised mitochondrial membrane potential obtained from triplicate experiments. Statistical significance between cells exposed to complex vs. negative control was determined by two-sample independent Welch t-tests assuming unequal variance between populations with asterisks corresponding to $p \leq 0.05$ *, $p \leq 0.01$ **, $p \leq 0.001$ ***, $p \leq 0.0001$ ****.

Complexes **1** − **3** induce extreme depolarisation of the mitochondrial membrane, greater than that observed in the positive control.

3.3.9.3 Apoptosis Induction

The presence of excessive ROS and mitochondrial damage can induce cell apoptosis. To investigate if complexes **1** – **3** induce apoptosis, and to assess whether extension of the Cp system has any impact, flow cytometry experiments were carried out in OE19, SUNE-1 and A2780 (Figures 3.24 – 3.26) using annexin V and propidium iodide (PI).

Annexin V binds to membrane-bound phosphatidylserine phospholipids, which ordinarily face into the cytoplasm. However, in early apoptosis, these translocate to the outside of the cell membrane and annexin V fluorescence can be detected whilst PI can not. In late apoptosis, the cell membrane becomes permeable and PI can enter, bind DNA, and fluoresce. If only PI fluorescence is observed, the cell has become permeable without apoptosis-induced phosphatidylserine protein translocation taking place. This usually indicates cell necrosis as significant membrane rupturing has to occur to allow PI entry. Therefore, flow cytometry studies using annexin V and PI can reveal if drug exposure induces early apoptosis, late apoptosis, or cell necrosis.

OE19

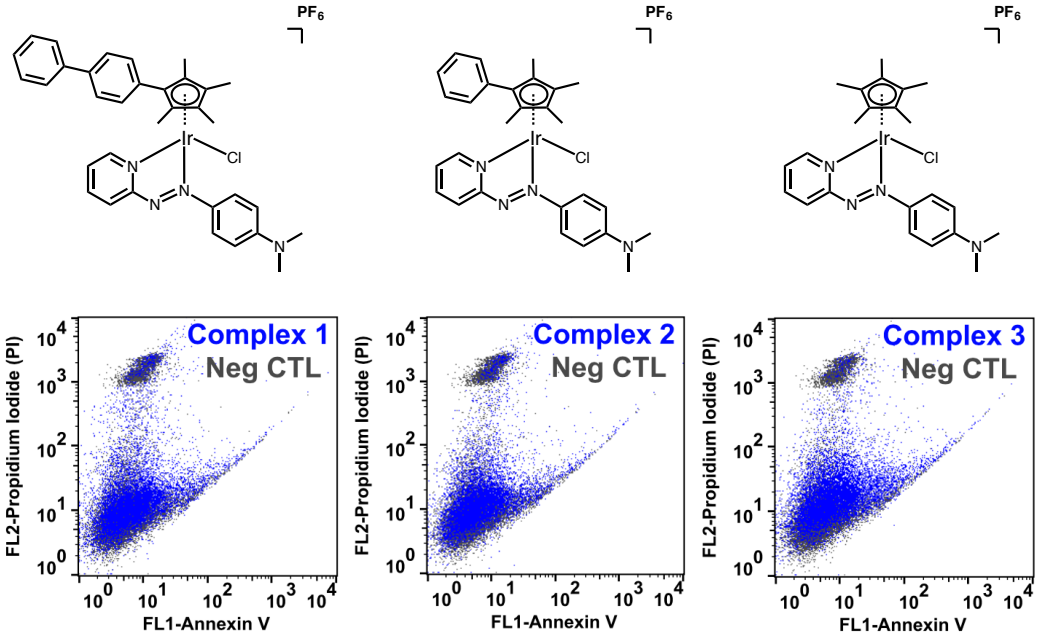

	Non-Viable FL1-FL2+ Q1	Late Apoptotic FL1+FL2+ Q2	Early Apoptotic FL1+FL2- Q3	Viable FL1-FL2- Q4
Neg CTL	14.9 ± 0.5	0.13 ± 0.01	0.67 ± 0.04	84.4 ± 0.4
Complex 1	8.0 ± 0.1 ***	0.27 ± 0.03 **	1.4 ± 0.1 **	90.3 ± 0.3 ****
Complex 2	6.61 ± 0.03 ***	0.31 ± 0.08	1.21 ± 0.04 ****	91.87 ± 0.06 ****
Complex 3	5.74 ± 0.02 ***	0.47 ± 0.08 *	2.0 ± 0.1 ***	91.9 ± 0.2 ****

Figure 3.24: (Top) Measurement of apoptosis induction by flow cytometry of OE19 oesophageal carcinoma cells exposed to complexes **1** − **3** for 24 h at IC_{50} concentrations at 310 K. (Bottom) Table of % cell populations obtained from triplicate experiments. Statistical significance between cells exposed to complex vs. negative control was determined by two-sample independent Welch t-tests assuming unequal variance between populations with asterisks corresponding to $p \leq 0.05$ *, $p \leq 0.01$ **, $p \leq 0.001$ ***, $p \leq 0.0001$ ****.

SUNE-1

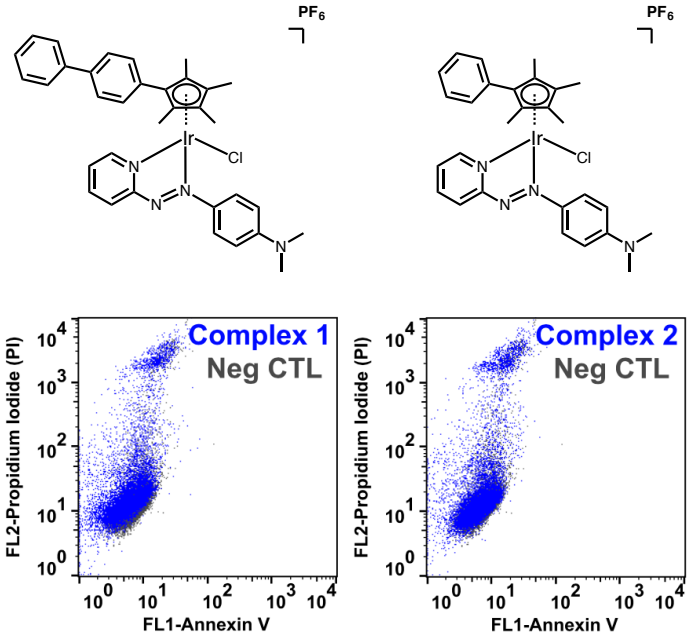

	Non-Viable FL1-FL2+ Q1	Late Apoptotic FL1+FL2+ Q2	Early Apoptotic FL1+FL2- Q3	Viable FL1-FL2- Q4
Neg CTL	3.8 ± 0.1	0 ± 0	0 ± 0	96.2 ± 0.2
Complex 1	11.0 ± 0.7 **	0 ± 0	0 ± 0	89.0 ± 0.7 **
Complex 2	11.5 ± 0.6 **	0 ± 0	0 ± 0	88.5 ± 0.6 **

Figure 3.25: (Top) Measurement of apoptosis induction by flow cytometry of SUNE-1 nasopharyngeal carcinoma cells exposed to complexes **1** and **2** for 24 h at IC_{50} concentrations at 310 K. (Bottom) Table of % cell populations obtained from triplicate experiments. Statistical significance between cells exposed to complex vs. negative control was determined by two-sample independent Welch t-tests assuming unequal variance between populations with asterisks corresponding to $p \leq 0.05$ *, $p \leq 0.01$ **, $p \leq 0.001$ ***, $p \leq 0.0001$ ****.

A2780

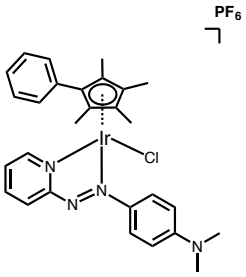

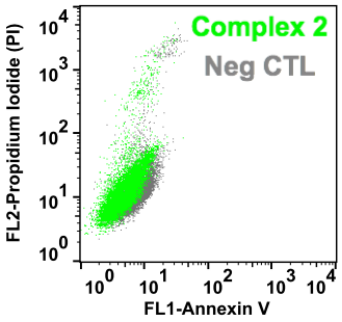

	Non-Viable FL1-FL2+ Q1	Late Apoptotic FL1+FL2+ Q2	Early Apoptotic FL1+FL2- Q3	Viable FL1-FL2- Q4
Neg CTL	1.73 ± 0.09	0	0	98.27 ± 0.09
Complex 2	2.48 ± 0.07 ***	0	0	97.52 ± 0.07 ***

Figure 3.26: (Top) Measurement of apoptosis induction by flow cytometry of A2780 ovarian carcinoma cells exposed to complex **2** for 24 h at IC_{50} concentration at 310 K. (Bottom) Table of % cell populations obtained from triplicate experiments. Statistical significance between cells exposed to complex vs. negative control was determined by two-sample independent Welch t-tests assuming unequal variance between populations with asterisks corresponding to $p \leq 0.05$ *, $p \leq 0.01$ **, $p \leq 0.001$ ***, $p \leq 0.0001$ ****.

At IC_{50} concentration, complexes **1** − **3** induce little to no apoptosis in either OE19 or SUNE-1 cells after 24 h. All complexes slightly increase the population of non-viable cells in all cell lines tested. At 4× IC_{50} concentration, complex **2** has been previously reported to induce early-stage apoptosis after 24 h and late-stage apoptosis after 48 h in A2780 cells.[120]

3.3.9.4 Cell Cycle Analysis

Cells progress through a cycle as they proliferate. This cycle consists primarily of four phases: The G_1-phase, in which the cell begins to increase in size, in preparation for DNA replication, the S-phase in which the cell DNA is replicated, doubling the amount of DNA present, and the G_2/M-phase, in which the cell continues to increase in size. This culminates in mitosis, when the cell divides into two daughter cells, each with one copy of the original cell's DNA. To ensure this process proceeds correctly, there exists cell cycle checkpoints. These are points at which the progression of the cell cycle may be halted in order to repair any damaged DNA or confirm that cell cycle processes are functioning properly.

The first of these is the G_1/S checkpoint, in which the cell will halt cycle progression if there are are not enough resources to successfully undergo replication without putting the cell at risk. The second of these is the G_2/M checkpoint. Here the cell checks that it has enough membrane phospholipids and cytoplasm to produce two daughter cells. It also checks for DNA-damage, as improper DNA replication or pharmacological agents can induce damage that needs to be repaired before the cell cycle can progress safely. This checkpoint ensures that the cell does not undergo division before it has had an opportunity to repair the damaged DNA. The third checkpoint is the metaphase checkpoint, in which the cell checks that the mitotic spindle has formed properly and the chromosomes are properly aligned prior to cytokinesis. Cancer cells regularly bypass these checkpoints and continue to proliferate, regardless of DNA damage, accruing multiple mutations as they do so.

The formation of CDDP adducts on cellular DNA induces an arrest in the S and G_2-phases of the cell cycle, often leading to apoptosis. CDDP-resistant cells tend to have mutations that cause these adducts to either be tolerated or rapidly repaired. In this way cell apoptosis induction is avoided.

To assess whether complex **2** can induce cell cycle arrest, flow cytometry was used to determine the % of the cell population of A2780 cells in each phase, based on the amount of DNA present in the cells visible when stained with PI (Figure 3.27).

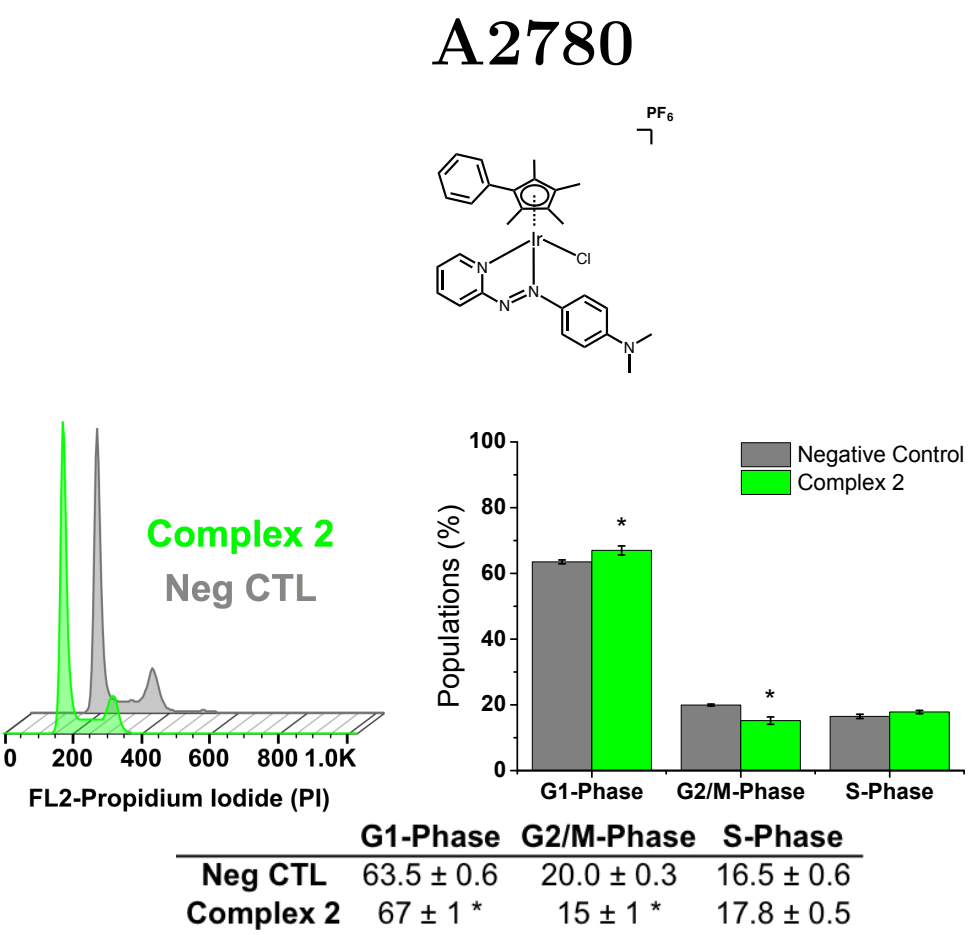

	G1-Phase	G2/M-Phase	S-Phase
Neg CTL	63.5 ± 0.6	20.0 ± 0.3	16.5 ± 0.6
Complex 2	67 ± 1 *	15 ± 1 *	17.8 ± 0.5

Figure 3.27: (Top Left) Cell cycle analysis by flow cytometry of A2780 ovarian carcinoma cells exposed to complex **2** for 24 h at IC_{50} concentration at 310 K. (Top Right) Bar chart of % population of cells in each cell cycle phase. (Bottom) Table of % cell populations obtained from triplicate experiments. Statistical significance between cells exposed to complex vs. negative control was determined by two-sample independent Welch t-tests assuming unequal variance between populations with asterisks corresponding to $p \leq 0.05$ *, $p \leq 0.01$ **, $p \leq 0.001$ ***, $p \leq 0.0001$ ****.

Complex **2** induces a slight increase in the G1 population with a reduction in the number of cells in the G2/M-phase. No significant change in the S-phase population was observed.

3.3.10 GDSC Pharmaco-genomic Screen

Complexes **1** − **3** show considerable potency in multiple cell lines, and the results thus far suggest a unique MoA involving ROS perturbation and mitochondrial damage. Further studies in this area of chemical space are therefore warranted. The MoAs of metallodrugs can often be complex and involve multiple targets, making them difficult to determine. A larger scale systems pharmacology approach may therefore provide a way by which to elucidate these MoAs.

Complex **2** ($Cp^{xph}Ir(azpyNMe_2)Cl]PF_6$) has been previously reported to be highly active against the NCI-60 panel of 60 cancer cell lines from 9 different tissue types displaying superior mean cytotoxicity to CDDP. COMPARE analysis revealed the potential for polypharmacology of complex **2** along with an MoA tunable by modification of the chelating ligand.[102] To further test the anticancer properties of this complex and to search for informative patterns of activity over different tissue types, the Sanger Institute carried out their Genomics of Drug Sensitivity in Cancer large-scale screen using complex **2** on 916 cell lines over 28 tissue types. 809 of these lines were also tested against CDDP for comparison (Figure 3.28).

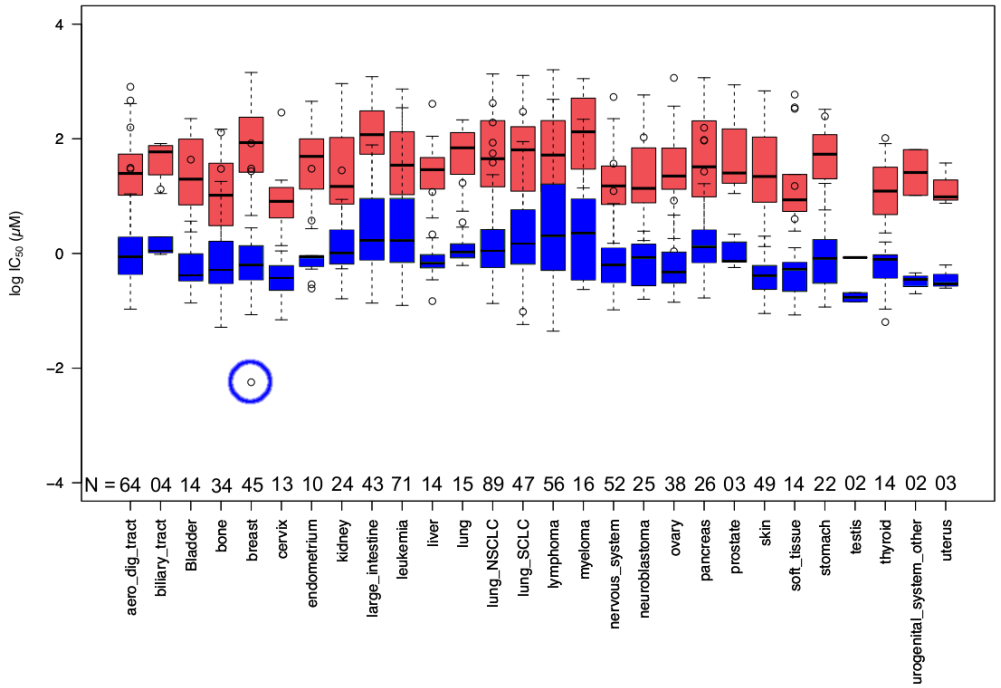

Figure 3.28: Box and whisker plots of complex **2** (blue) and CDDP (red) of IC_{50} values against 809 different cancer cell lines. Cell lines grouped by tissue type where N is the number of cell lines of that tissue type screened. White circles used to mark outliers. The most significant outlier, OCUB-M, is circled in blue.

Complex **2** shows significantly superior mean activity to CDDP in all tissue types, with highest mean activity in cancers of the bladder, cervix, testis, urogenital and uterus. Lowest mean activity was observed in lymphoma and myeloma. One outstanding outlier is observed in the triple-negative breast cancer cell line OCUB-M (denoted by blue ring), in which complex **2** displays vastly superior activity compared to any other cell line.

Valuable information about the MoA of an anticancer complex can be gleaned from not only observing which cell lines are most susceptible to it, but also from those which are least susceptible. Analysis was carried out on the population of outliers amongst cell lines tested against complex **2**. Cell lines were designated as insensitive if their corresponding IC_{50} value was above the upper whisker (Figure 3.29).

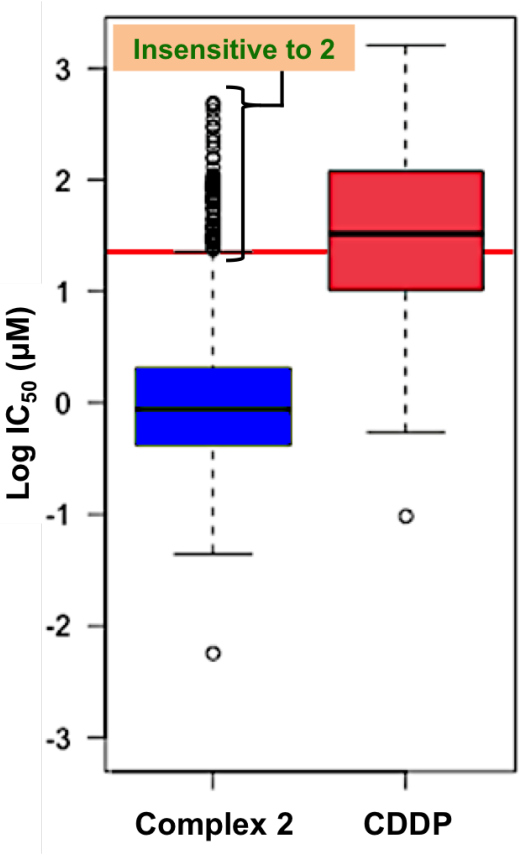

Cell Line	Tissue	log IC_{50} (μM)
WSU-DLCL2	lymphoma	2.69
ESO51	aero_dig_tract	2.67
LU-65	lung_NSCLC	2.62
PF-382	leukemia	2.54
A4-Fuk	lymphoma	2.47
NCI-H2081	lung_SCLC	2.47
NCI-SNU-1	stomach	2.39
U-266	myeloma	2.34
NCI-H2135	lung_NSCLC	2.29
OACM5-1	aero_dig_tract	2.20
PANC-04-03	pancreas	2.19
EW-7	bone	2.11
KM-H2	lymphoma	2.04
NB(TU)1-10	neuroblastoma	2.02
TT2609-C02	thyroid	2.01
OPM-2	myeloma	2.00
PL18	pancreas	1.98
HPAC	pancreas	1.97
THP-1	leukemia	1.97
NCI-H187	lung_SCLC	1.95

Figure 3.29: (Left) Box plots of complex **2** (blue) and CDDP (red) IC_{50} values against all 809 cancer cell lines. Cell lines with an IC_{50} value greater than the upper quartile + 1.5× the interquartile range designated as 'insensitive' (threshold denoted by red line). (Right) The top 25 cell lines least sensitive to complex **2**.

The mean activity of complex **2** is superior to CDDP. Only a small proportion of cell lines tested were insensitive to complex **2** (46 of 916). To examine the origins of these insensitive lines, the % of cell lines of each tissue type deemed to be in the insensitive population was calculated (Figure 3.30).

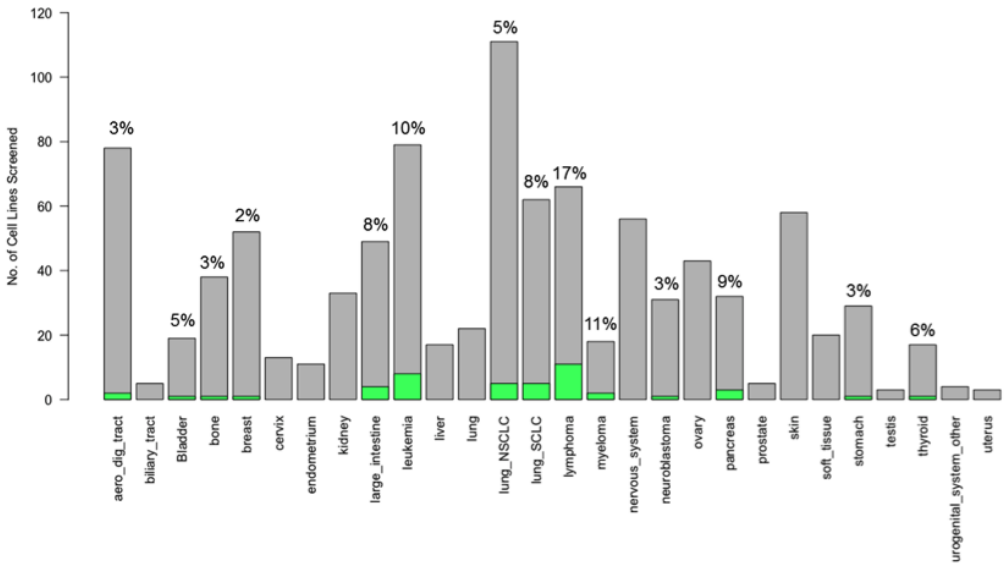

Figure 3.30: Bar plot of the number of cancer cell lines screened against complex **2** separated by tissue type. Cell lines with low sensitivity to complex **2** are highlighted in green. The % of insensitive cell lines for each tissue type is shown above each bar. If no percentage is shown, that tissue type contained no insensitive lines.

The tissues with the largest proportion of cell lines insensitive to complex **2** are the mesodermally-derived blood cancers: Lymphoma, myeloma and leukemia. To further investigate the profiles of cell lines insensitive to complex **2**, the potency of other drugs in the screen against them was examined (Table 3.14).

Table 3.14: The 10 cell lines least sensitive to complex **2** ($IC_{50} > 150$ μM) and their corresponding tissue of origin. The drugs in the screen with the lowest potencies against each cell line and their MoAs are shown.

Subtype	Cell line	Resistance drug	Drug Target
Lung	LU-65	Vorinistat and Piperlongumine	HDAC
	NCI-H2081	Piperlongumine	Increases ROS Levels
	NCI-H2135	Piperlongumine	Increases ROS Levels
Lymphoma	WSU-DLCL2	LAQ824	HDAC
	A4-Fuk	N/A	N/A
Aerodigestive	ESO51	Piperlongumine	Increases ROS Levels
	OACM5-1	TW 37	BCL-2, BCL-XL
Leukemia	PF-382	Piperlongumine	Increases ROS Levels
Myeloma	U-266	NU-7441	DNAPK
Stomach	NCI-SNU-1	BEZ235	PI3K, mTORC1/2

Of the 46 cell lines classified as insensitive to complex **2**, 19 are least sensitive to piperlongumine,[121] a senolytic agent that kills cancer cells by elevating ROS levels and causing DNA damage.[122,123] In subsection 3.3.9.1. it was shown that complexes **1** − **3** generate ROS in multiple cell lines. This further supports the hypothesis that complex **2** and its analogues have ROS-based MoAs.

Information on possible MoAs of a complex can be gained from comparing its cytotoxic profile to others in a large data set. 253 other drugs were screened against the same 809 lines as complex **2**, and the MoA of many of these are known. By comparing the pattern of cytotoxicity between complex **2** and every other drug in the screen across all cell lines, drugs with similar MoAs were identified (Figure 3.31).

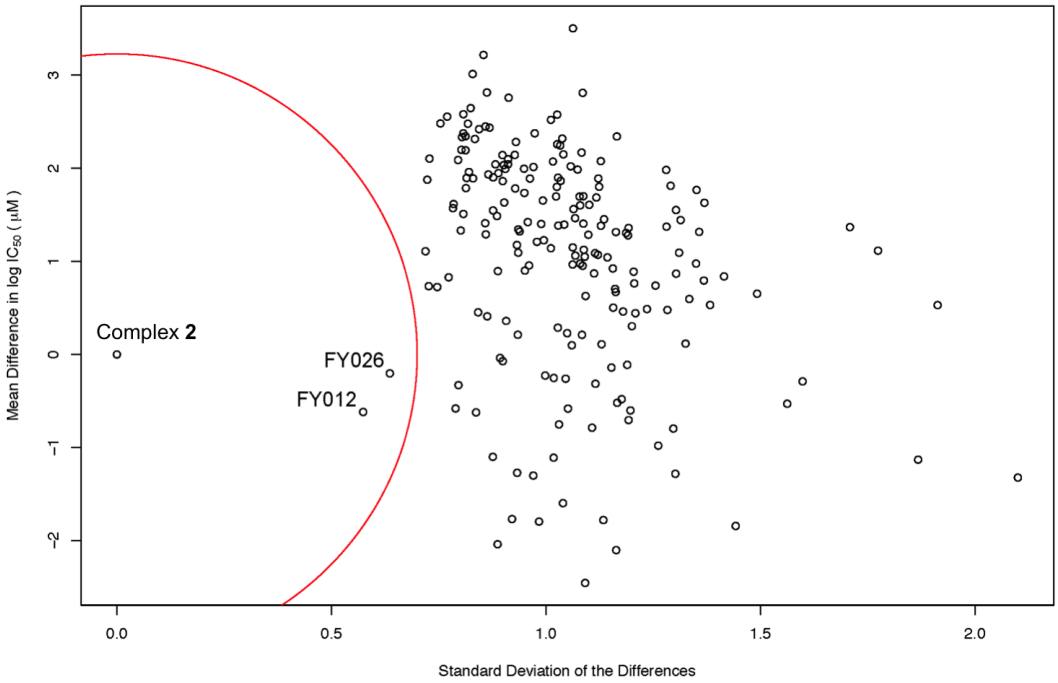

Figure 3.31: Statistical analysis of the pattern of cytotoxicity of complex **2** against 809 cell lines compared to the other 253 drugs in the screen. For each drug the difference in IC_{50} value between itself and complex **2** was taken for each cell line and the standard deviation of these values calculated. Complexes within the red circle show a similar pattern of cytotoxicity to complex **2**.

Complex **2** showed significant similarity in cytotoxic profile with only two other drugs in the screen, the previously reported Os(II) complexes: ([(η^6-bip)Os(azpyNMe$_2$)I]PF$_6$) and ([η^6-p-cymene)Os(azpyNMe$_2$)I]PF$_6$)).[64,124] Interestingly, these two complexes share the same azpyNMe$_2$ bidentate chelating ligand as complex **2** but have a different monodentate ligand and coordinated aromatic system. Other organoiridium and organoosmium complexes with strong structural similarities to complex **2** but different bidentate ligands, were included in this screen. That they did not also show similar cytotoxic profiles to complex **2** is unexpected and of significant interest.

In cell lines in which mutations were present, a multivariate analysis of variance (MANOVA) was used to identify significant correlations between mutation status and sensitivity/insensitivity to complexes. A Benjamin-Hochberg multiple testing correction was used to identify significant results and flag false

positives. This analysis identified a statistically significant correlation between the *KIT* gene and sensitivity to complex **2**.

The *KIT* gene coding mutation is associated with the sensitivity of four non small cell lung carcinoma cell lines to complex **2**. *KIT* encodes the human homolog of the proto-oncogene C-KIT, a type-III transmembrane receptor for the stem cell growth factor. Once bound to the growth factor, this protein activates signal transduction through the cell, affecting cell survival and differentiation.

Complex **2** shows great promise as an anticancer agent and demonstrates a novel MoA. We proceed by generating two similar organoiridium complexes with different Cp systems to complex **2** and investigate how these changes impact both their anticancer potency and their MoAs. In this way, we aim to improve both the anticancer potency of organoiridium complexes and our understanding of how they work.

3.4 Discussion

3.4.1 Aquation and Separation

The complexes in this work bear either a monodentate chlorido or iodido ligand bound to the iridium centre. The solution chemistry of the azpyNMe$_2$ complexes **1** and **4** was investigated, revealing that the chlorido complexes readily hydrolyse in aqueous solution, reaching an equilibrium between chloride-bound and OH/OH$_2$-bound analogues (Figure 3.16, pg. 102). The iodido complex, however, was inert to hydrolysis (Figure 3.17, pg. 103). In biological testings, the complexes were dissolved in cell medium containing 120 mM chloride. This was shown to suppress hydrolysis completely, indicating that complexes $\mathbf{1} - \mathbf{3}$ would remain in their chloride-bound form during cell tests. Once they enter the cells, the chloride concentration decreases and aquation may be possible. The iodido complex **4** showed 40% I $\rightarrow$ Cl exchange over 24 h in solution with 120 mM chloride (Table 3.11, pg. 104), therefore a significant proportion of complex **4** could be converted to complex **3** by the time it reaches cells.

The ^{1}H-NMR spectra show that addition of chloride 24 h after hydrolysis causes the disappearance of some, but not all, of the new peaks that appear during hydrolysis of complex **1** (Figure 3.18, pg. 105). This indicates that, whilst aquation is suppressible and reversible by chloride, certain species form during aquation that are unaffected by addition of chloride post-hydrolysis. High chloride concentration would likely shift the equilibrium between OH/OH$_2$-bound and Cl-bound Ir species, reverting the Ir-OH/OH$_2$ species in the solution back to almost entirely Cl-bound complex. This suggests that species other than OH/OH$_2$-adducts are forming, possibly hydroxido-bridged dimers. This has implications to the form the complex takes in cells, as chloride concentration varies depending on the intracellular location. More extensive investigations into the effect of biologically-relevant chloride concentrations on complex **1** are carried out in Chapter 4.

The reactivities of Ir-Cl and Ir-OH/OH$_2$ species are likely to differ. In the case of CDDP, the OH/OH$_2$-bound Pt species can react with many off-target molecules, reducing the amount of complex that reaches the target site and

therefore also the efficacy of the drug. That complexes **1** − **3** remain their original Ir-Cl species in a solution at the chloride concentration of cell medium in an encouraging result, as it may mean that they are less likely to prematurely hydrolyse and bind off-target molecules in cells.

The halido ligand has a profound effect on not only the hydrolysis, but also the stability of the chiral enantiomers of azpyNMe$_2$ organoiridium complexes. Whilst separation by chiral HPLC with excellent resolution was possible for complexes **1** − **4** (Figure 3.19, pg. 108 and Table 3.12, pg. 110), the separated enantiomers of the chlorido complexes revert readily to a racemic mixture. Separated enantiomers of the iodido complex, however, remained optically pure. There are slight shifts in the retention times of some of the separated peaks, however, this is more likely to be due to slight erroneous variation in the flow speeds between runs rather than any significant chemical changes. This is the first time successful separation and/or isolation of stable enantiomers of an organoiridium iodido complex of this family has been reported. Separation of stable enantiomers has previously been possible for an organoosmium iodido complex bearing the same azpyNMe$_2$ bidentate ligand.[103]

For the chlorido complexes to interconvert, there must be a mechanism facilitating it. Given that the aquation results prove the bound chlorides are labile in aqueous solution, a likely mechanism is simply the approach of a free chloride to the opposite face of the complex to which a chloride is already bound, resulting in the binding of the new chloride and the leaving of the previously-bound chloride (in the manner of an SN2 reaction). The net result of this would be the conversion from one enantiomer to the other. The iodide has been shown to be non-labile, and therefore interconversion does not occur for separated enantiomers of iodido complex **4**. Pharmacological development of therapeutics tends to favour enantiomerically pure substances, meaning that this is a promising result for complex **4**. Future drug development of similar organoiridium complexes with iodido ligands are likely to have stable, isolatable enantiomers which can be tested for differing biological properties. This is discussed further in Chapter 6.

That the Ir-I bond is more resistant to hydrolysis than Ir-Cl is somewhat

unexpected. Cl is more electronegative than I and so it may be expected that the bond with the highly electropositive iridium(III) centre would be stronger with chlorine. Additionally, comparison of the x-ray crystal structures show that the Ir-I bond is longer than Ir-Cl bond in similar complexes (Table 3.9, pg. 90), this is in agreement with literature on similar complexes.[94] The strength of the Ir-I bond may come from the larger van der Waals dispersion forces associated with bonds with large atoms such as iodine. The hydrolysis of the Ru-halide bonds of ruthenium arene complexes has been studied, revealing that in such systems, Ru-I bonds also hydrolyse less readily than Ru-Cl bonds. Calculations of the related reaction energies and reaction barriers to aquation confirmed that the resistance of Ru-I bonds to hydrolysis was due to the higher activation energies inherent in Ru-I hydrolysis relative to Ru-Cl.[114] This may also be the case for Ir-halides.

3.4.2 Structure-Activity Relationships

There is a general correlation of Cp^{xbiph} complexes being more potent than their Cp^{xph} and Cp* analogues. The cyclopentadienyl ligand does not seem to have a large effect on the MoA, and most likely contributes to the level of cellular uptake of the complexes, as is the case in similar organoiridium complexes previously reported in which extension of the Cp system increased uptake, leading to greater cytotoxicity.[86] There is a more complex relation between hydrophobicity and potency than simply more hydrophobic complexes having higher uptake and therefore being more potent, as evidenced in Table 3.10, pg. 93 and Figure 3.13, pg. 94. This is demonstrated by the highly hydrophobic and weakly active complexes **11** and **19**. The reason for the significantly low activity of complex **19** relative to other complexes may be the high molecular mass of its cation (995.26 Da) preventing sufficient uptake into cells. Additionally, the difference in mass between this, and the cation of complex **1** (727.35 Da), the second largest, and most potent complex, is not overly large. The presence of the bromine functional group on the pyridine may also be playing a role in abrogating cytotoxicity, as it is the only feature completely unique to complex **19** compared to the other complexes investigated in this work. An-

other possibility is that the phenyl ortho hydroxyl hydrogens on complexes **11**, **12** and **19** leave when in aqueous solution at physiological pH, allowing the Ir to bind the oxygen atom instead of its chlorido ligand, potentially changing the charge, shape, reactivity and biological properties of the complex. It could, for example, entirely prevent the Ir from binding a key target site. ESI-MS fragments of such O-chelated species have been observed for complex **11** but not for complex **12** or **19**. This may explain the surprising difference in activity between complexes **11** and **12**. Further investigations into the pK_a values of hydroxyl hydrogens of azpyOH complexes are in Chapter 5.

The presence of the monodentate iodido ligand increases the overall hydrophobicity of the complexes, however the iodido complexes **9** and **10** have lower potency than their chlorido analogues **7** and **8**, respectively. The iodido complexes are inert to hydrolysis, a step that is necessary for the MoA of CDDP and many other precious metal-based drugs. It is possible that the cytotoxicity of the chlorido complexes arises from multiple MoAs, some of which could involve hydrolysis at the metal-Cl bond and some not. Abrogation of hydrolysis by replacement with an iodido ligand could result in a complex that cannot exert the same MoA as the chlorido complex, reducing cytotoxicity as observed, however the remaining MoA/MoAs would allow the iodido complexes to remain cytotoxic. That the iodido complexes remain highly cytotoxic proves that hydrolysis is not an essential step in the MoA/MoAs of this family of complexes. Another possibility is that the iodido complexes are activated once in cells, as is the case for some reported organoosmium complexes.[125]

The hydrolysis data does, however, show 40% conversion of iodido complex to chlorido complex at cell media chloride concentration after 24 h. While this could mean that iodido complexes have the same MoA as chlorido complexes, that only 40% conversion occurs after 24 h would mean that the the majority of the complex would still be in the iodido form after 24 h, and even more so in the hours up to that point after exposure. Additionally the concentration of chloride in cell cytoplasm is ca. 5× lower than in cell media. If hydrolysis was a necessary step for anticancer activity, the unconverted iodido complexes would therefore be significantly less active than their chlorido analogues, however this is not the case. Therefore it is highly likely that the iodido complexes are able

to be cytotoxic without prior conversion to chlorido analogues.

Within the Cp^{xbiph} complexes tested, the azpyNMe$_2$ complex **1** was the most potent in A2780 ovarian carcinoma cells (Table 3.10, pg. 93), followed by azpyOH complex **5**, azpy complex **13**, HOazpyNO$_2$ complex **16** and finally azpy(OH)$_2$ complex **11**. There is a noticeable trend that the functional group or groups on the bidentate ligand have a profound effect on the potency of the complexes. Complexes with more electron donating groups on the bidentate ligand. such as NMe$_2$ and OH are more potent than those with neutral or electron withdrawing groups such as H and NO$_2$. The varying levels of electron donation by these functional groups affect the nucleophilicity of the azopyridine ligand. This may alter how much the ligand withdraws electron density from the metal, thereby affecting how readily it hydrolyses and reacts with intracellular targets. It may also affect the mechanism and rate of ROS/SO generation, as well as other MoAs yet fully understood. A similar trend is seen for the Cp^{xph} analogues however this is not observed for the Cp* complexes, indicating a more complex interplay between the effects of the bidentate and Cp ligands on potency.

The azpyNMe$_2$, azpyOH and azpy ligands alone have been shown to be inactive against A2780,[126] as are the iridium dimers.[94] Therefore, coordination to iridium plays a key role in altering the chemical nature of both the complex and the iridium-Cp system such that it can interact with biological targets resulting in cytotoxicity. Complex **1** shows activity in the low nanomolar range (IC_{50} = 95 nM) against A2780 cells. In comparison to organoruthenium complexes bearing the same bidentate and chlorido ligands but different aromatic ligands (biphenyl and para-cymene),[126] these organoiridium complexes are ca. 2 – 4 orders of magnitude more potent, highlighting the importance of the metal centre to potency. In comparison to organoosmium complexes with similar structural differences as described for organorutheniums,[64] these organoiridiums are ca. 1 order of magnitude more potent, with the exception of those bearing the azpy ligand, which are ca. 3 orders of magnitude more potent. Many of the organoiridium complexes tested also exhibit superior potency to CDDP in multiple cell lines. In summary, these organoiridum azopyridine complexes are some of the most potent organometallic anticancer

complexes yet reported.

3.4.3 Catalysis of NADH Oxidation

An organoiridium complex with structure [(Cp^{xbiph})Ir(phenylpyridine)Cl]PF_6 has been previously reported to catalyse the oxidation of NADH with the generation of detectable levels of H_2O_2, as well as generating ROS/SO in cells.[127] A catalytic mechanism for NADH oxidation and H_2O_2 generation was postulated: Hydrolysis of the Ir-Cl complex to Ir-OH_2 followed by abstraction of a hydride from NADH forming NAD^+ and Ir-H then transfer of that hydride to molecular oxygen. Supporting this mechanism is the identification of Ir-H peaks in ^{1}H-NMR spectra.[84,86,101]

Eleven organoiridium complexes were shown to catalyse NADH oxidation, however only [Cp*Ir($HOazpyNO_2$)Cl]PF_6 complex **18** generated detectable levels of H_2O_2, as well as having the highest TON and TOF values. Interestingly, its Cp^{xbiph} and Cp^{xph} analogues, complexes **16** and **17**, respectively, did not generate H_2O_2, and have lower TON and TOF values. Complexes **16** and **18** have almost identical IC_{50} values in A2780 cells and so any difference in behaviour was unexpected. A possible explanation is that the phenyl and biphenyl groups sterically hinder the approach of NADH to the complex, thus reducing the rate of catalysis. Another explanation could simply be that not enough H_2O_2 is being generated by any of the other complexes to be detected by the peroxide test sticks, however complex **19** has the same TON (albeit lower TOF) as complex **18** yet it does not produce detectable levels of H_2O_2. This implies that complexes **18** or **19** catalyse NADH oxidation by a different mechanism to the other complexes tested. If, however, the mechanism of NADH oxidation requires hydrolysis as a prerequisite then the TON and TOF values are not comparable as they would be significantly affected by the rate of hydrolysis.

There is an inverse correlation between the rate of catalysis and potency. This is surprising, but suggests that perhaps a factor that contributes to rapid NADH oxidation, such as the presence of electron withdrawing groups on the

azopyridine ligand, has the opposite effect on potency, and that the MoA likely does not involve NADH oxidation. The most potent complex, **1** exhibits the lowest TON and TOF values whilst the least potent, complex **19**, displays the joint highest TON. Perhaps complexes **16** − **19** hydrolyse readily, contributing to more rapid catalysis, however in cells this may lead to rapid deactivation and reactions with off-target biomolecules, resulting in lower potency.

The iodido ligand has been shown to be inert to hydrolysis, however complex **4** shows some, if very low, catalytic activity. An alternative method of catalysis has been previously proposed in which the azopyridine ligand is reduced.[126] Such a mechanism would not require the hydrolysis of the Ir-halide bond and could explain the catalytic activity of complex **4**.

There is a strong correlation between the electron donating capacity of the functional groups on the azopyridine ligand and the catalytic activity of the complex as a whole. Complexes with the strongly electron-donating NMe_2 group has the lowest catalytic activity, the neither electron-donating or -withdrawing H group correlated with moderate catalytic activity and complexes with the strongly electron-withdrawing group NO_2 showed the highest catalytic activity by ca. 5 – 10×. The electron withdrawing effect of the functional groups may be facilitating catalysis by the previously mentioned azopyridine ligand reduction mechanism by making the azo nitrogen atoms more positive, making the redox reaction more probable. Alternatively, the level of electron donation/withdrawing on the metal centre could be governing the rate of catalysis, if loss of the halido ligand and formation of an Ir-H intermediate is the mechanism by which NADH oxidation is taking place.

Complexes **1** − **3** show little capacity for NADH oxidation, suggesting that NADH is not the primary target for redox perturbation for these complexes. The opposite may be true for complexes **16** − **18** as they exhibit very high TON and TOF values (ca. $>$ 1.3× TON and $>$ 3.7× TOF reported Ir(III) complexes of similar structure under the same conditions.[86,128]

3.4.4 Oxidative Stress

Complex **2** ([Cp^{xph}Ir(azpyNMe$_2$)Cl]PF_6) generates higher levels of FL1 and FL2 fluorescence (10^3 – 10^4 and 10^2 – 10^4, respectively) in A2780 than in OE19 (10^2 – 10^3 and 10^1 – 10^2) or SUNE-1 cells (10^2 – 10^3 and ca. 10^2) and is more cytotoxic to A2780. A possible explanation for this is that A2780 cells have mutations in their OXPHOS machinery, and so they are already under greater levels of oxidative stress.[124] As such, they are vulnerable to further ROS insult. In addition, complex **2** has been shown in previous literature to prevent up-regulation of the genes coding for superoxide dismutase (SOD) and catalase (CAT).[120] These two enzymes are crucial components of the ROS stress response pathway. SOD breaks down SO into oxygen and H_2O_2, which CAT then breaks down into water and oxygen. This may explain the higher level of SO observed in A2780 cells relative to the other cell lines tested. Disruption of SOD and CAT function has downstream effects on other antioxidant enzymes, further exacerbating the damage caused by ROS.[129]

ROS production by complex **2** may be occurring through mitochondria, as well as by other mechanisms. An increase in mitochondrial ROS production has a cyclic effect on mitochondria, causing them to produce even higher levels of ROS.[130] This can lead to mitochondrial DNA damage, damage to mitochondrial proteins, and depolarisation of the mitochondrial membrane.[131] The fact that extreme mitochondrial membrane depolarisation is observed in OE19 cells exposed to complexes **1** – **3** supports the increase of mitochondrial ROS as an MoA for these complexes. Complex **2** shows a similar pattern of activity to the organoosmium complex ([η^6-p-cymene)Os(azpyNMe$_2$)I]PF_6). Disruption of the mitochondrial membrane releases cytochrome c into the cytoplasm which could possibly lead to the induction of intrinsic apoptosis pathways at a later timepoint. This potent complex has been shown to increase ROS in cancer cells, and Os has been shown to localise in the mitochondria of human ovarian cancer cells exposed to it.[132] The mitochondrion is a negatively-charged organelle and consequently localisation of cations here is unsurprising. Additionally the hydrophobic and lipophilic nature of these complexes may also be contributing to mitochondrial localisation.

3.4.5 Apoptosis

No significant induction of apoptosis was observed for complexes **1** − **3** after 24 h exposure, however after 48 h higher concentrations of complex **2** have been shown to induce late apoptosis.[120] After 72 h the cell population recovers. This suggests a wave of apoptotic cell death occurs around the 48 h timepoint. As the Cp system has proven to exert little effect on the MoA, this is likely to also be the case for complexes **1** and **3**. The release of ROS has been shown to modulate apoptosis and may therefore be playing a role in delaying apoptosis.[133] In the cytotoxicity assays the cells are exposed to complex for 24 h then allowed a further 72 h before cell survival percentages are determined. Therefore the low level of cell death observed in the apoptosis assays after only 24 h can be reconciled with the IC_{50} data.

3.4.6 Cell Cycle Arrest

The effect of complex **2** on the cell cycle after 24 h exposure is minimal at IC_{50} concentration, however, higher concentrations of **2** have been shown to induce S-phase arrest in A2780 cells.[120] This type of cell cycle arrest is most commonly associated with DNA damage. Complex **2** could be damaging DNA directly as part of its MoA, or DNA damage could be occurring as a consequence of ROS generation, as DNA, especially its guanine bases,[134] is a common target for ROS. Ovarian cancers lack the proper tools for DNA damage repair.[135] DNA damage may therefore be contributing to the potency of complex **2** against A2780.

It is surprising that the high levels of ROS and SO generated, along with significant mitochondrial membrane depolarisation after 24 h do not correlate with apoptosis or cell cycle disruption at the same timepoint. It would be of interest to carry out future studies on apoptosis and cell cycle disruption at later timepoint to determine when/if a wave of apoptosis and/or cell cycle disruption occurs hours or days after mitochondrial membrane depolarisation. Additionally, investigation into whether other apoptotic events such as caspase activation and PARP cleavage occur at the 24 h timepoint would be valuable

in further understanding the effects that these complexes exert on cells and how cells respond to these effects.

3.4.7 GDSC Pharmaco-genomic Screen

Complex **2** shows great potential as an anticancer agent, exceeding the potency of CDDP over a wide range of cancers of various tissue types. In particular, complex **2** is over 5 orders of magnitude more potent than CDDP against the OCUB-M cell line. OCUB-M is a triple negative breast cancer cell line,[136] meaning that it does not express the gene for the estrogen, progesterone or HER2 hormone receptors.[137] As many breast cancer treatments utilise hormone therapies that target these receptors, triple negative breast cancer is typically more difficult to treat. This is therefore a promising result for complex **2**. Additionally, complex **2** has previously been shown to be active against MDA-MB-468,[102] another triple negative breast cancer cell line.

MDA-MB-468 is likely more susceptible to ROS generation as it exhibits a glucose-6-phosphate dehydrogenase A phenotype. This phenotype means that the glucose-6-phosphate dehydrogenase enzyme does not function properly. A consequence of this is that conversion of glucose-6- phosphate to 6-phosphoglucono-δ-lactone cannot take place. Because of this, NADPH formation from $NADP^+$ cannot occur by this pathway. As NADPH formation is an essential component of gluthathione (GSH) synthesis, MDA-MB-468 cells may therefore display a degree of GSH deficiency. As GSH is a key cellular antioxidant, this may result in susceptibility of MDA-MB-468 cells to ROS-generating agents.[102] Complex **2** is shown here to generate high levels of ROS in A2780, OE19 and SUNE-1 cell lines, and so a ROS-based MoA may be significantly contributing to its potent activity against this, and other cell lines. In a smaller scale screen complex **2** previously exhibited a pattern of antiproliferative activity correlating with drugs that have oxidative stress MoAs.[102]

Postulation of a ROS-based MoA for complex **2** is further supported by its similar resistance profile to piperlongumine, a drug that also relies on a ROS-based MoA to kill cancer cells, involving depletion of cellular GSH, ROS-induced

DNA damage, and induction of apoptosis.[122,123] Piperlongumine, however, does not generate SO, whereas complexes **1** − **3** do. That half of the 10 cell lines most resistant to complex **2** are also least sensitive to piperlongumine over the 251 other drugs in the screen is highly significant. It is feasible that these cells possess a common factor or factors, such as cellular machinery more capable of dealing with ROS insults, for example, higher levels of intracellular antioxidants such as GSH.

The MoAs of complex **2** may be heavily dependent on the bidentate chelating azpyNMe$_2$ ligand. Comparison of the activity level of this complex to other complexes of similar structure with different bidentate ligands revealed that the azpyNMe$_2$ ligand confers a significant increase in potency.[102] The similarity analysis showed that complex **2** has a similar pattern of antiproliferative activity to two organoosmium complexes, both of which bear the azpyNMe$_2$ ligand. It is particularly interesting that these complexes show such striking similarities despite having a different Cp ligand, different monodentate halido ligand, and different metal centre. This highlights the significant impact of the bidentate ligand on the MoA.

Other organoosmium complexes with similar structures but different bidentate ligand included in the screen were not flagged as having a similar cytotoxicity profile to complex **2**, therefore the presence of the azpyNMe$_2$ ligand seems to have the most significant implications to cytotoxic selectivity and MoA, more so than the metal centre, Cp system or halide. The effect of the NMe$_2$ functional group of this ligand on the chemical behaviour and anticancer potency of organoiridium complexes is investigated further in Chapter 4.

The large-scale screen also identified complex **2** as being the only drug out of the 253 screened to which mutations in the *KIT* gene conferred sensitivity. *KIT* mutations have also been associated with an increased sensitivity to imatinib. Functional C-KIT often confers chemoresistance by augmenting the expression of DNA repair genes. The mutated KIT gene may therefore render cells more sensitive to DNA damage. DNA may therefore be a target for complex **2**. This is further supported by correlations of the cytotoxicity pattern of complex **2** with those of a DNA-damaging drug revealed by COMPARE anal-

ysis.[102] Additionally, investigation into the expression levels of DNA damage response proteins of A2780 cells exposed to complex **2** revealed the mobilisation of a BRCA1 DNA damage response, indicating that complex **2** had caused DNA damage.[120] The capability of complex **1**, the Cp^{xbiph} analogue of complex **2**, to damage DNA, is investigated thoroughly in Chapter 4.

3.5 Conclusions

Organoiridium azopyridine complexes represent a largely untapped area of chemical space, however they show promise as anticancer agents. Most of the complexes in this work exhibit superior activity to CDDP in multiple cell lines as well as having lower IC_{50} values than a large proportion of previously published precious metal-based drugs. Additionally, some are highly active in CDDP-resistant cell lines.

Current pharmaco-genomic and experimental evidence supports a redox-based MoA, involving the disruption of the redox balance in cancer cells by generation of ROS and SO. This also holds the potential for ROS-based damage to the mitochondrial membrane, in addition to DNA and proteins, resulting in S-phase cell cycle arrest, a wave of apoptosis, and necrosis. This is a promising MoA for organoiridium azopyridine complexes as cancer cells have higher levels of basal ROS than normal cells and are more sensitive to perturbations in their redox balance, thus cancer cells can be selectively killed whilst minimising risk to normal cells. Additionally, MoAs targeting the ROS stress response pathway hold the potential to circumvent cross-resistance with conventional DNA-targeting drugs such as CDDP, as well as many other clinically-used therapeutics.

Organoiridium azopyridine complexes are easily tunable, allowing for the generation of complexes in high yields with different Cp systems, halides and bidentate ligands by simple synthetic procedures. Studies of the structure-activity relationships of these complexes has revealed how changing these ligands alters their chemical and biological properties in a variety of ways.

The Cp system stabilises the Ir complex as well as affecting hydrophobicity and potency, with extension of the Cp system most likely contributing to increased cellular uptake leading to greater cytotoxicity.

The halide determines whether the complex hydrolyses or not, which may have implications towards binding to intracellular biomolecules as well as whether stable chiral enantiomers of the complex can be isolated.

The bidentate ligand has the greatest effect on the MoA of the complexes, ligands with electron-withdrawing functional groups confer rapid catalytic oxidation of NADH whereas those with electron-donating groups confer potent antiproliferative activity.

The work in this chapter illustrates the potency and versatility of organoiridium complexes as anticancer agents and reveals valuable information about the effects of the various ligands on their behaviour, thereby informing future development of these drugs towards clinical application. Not only do they perform impressively as antiproliferative agents, but one can dramatically change the properties of the complexes with small, synthetically trivial adjustments. This makes an effective basis for future drug discovery with the potential for uncovering new MoAs against cancer and overcoming the growing problems associated with acquired chemotherapeutic resistance and ultimately improving the prognosis of cancer patients.

Chapter 4

Impact of the Azopyridine Ligand on MoA

4.1 Introduction

Genomic instability is a substantial factor in cancer formation and progression. DNA damage, defects in replication or repair, combined with a failure to halt the cell cycle before the damaged DNA is passed on to daughter cells all contribute to carcinogenesis. These genomic defects do, however, provide targets that can be exploited to combat the disease.[138]

One of the foundations of cancer therapy is drug-induced damage to cancer DNA. This is achieved by a variety of chemotherapeutics, such as cisplatin (CDDP) and its derivatives such as carboplatin, which damage DNA by crosslinking guanine bases. Other examples are the drug temozolomide, which alkylates DNA bases, and etoposide, which inhibits the enzyme topoisomerase II, thereby inducing single or double strand breaks in DNA.[139,140]

However, whilst CDDP most effectively kills rapidly proliferating cells such as cancers,[141] it can still cause damage to rapidly proliferating normal cells,[142] leading to unpleasant side effects such as nephrotoxicity, ototoxicity, vomiting and hair loss. Nephrotoxicity is currently the dose limiting factor in CDDP

treatment.[143] This illustrates the need to develop novel, more selective anticancer treatments that attack cancer in new ways with minimal side-effects.

CDDP is of particular relevance as it set a precedent for a great deal of heavy metal-based chemotherapeutic innovation since its anticancer properties were discovered in 1965. CDDP is administered alone or in combination with other therapeutics. Advanced ovarian cancer, for example, is often treated with a combination of CDDP and the tubulin-targeting drug paclitaxel. Many cancers are insensitive to treatment with only one drug and so multiple therapeutics, or indeed one therapeutic with multiple mechanisms of action (MoAs), provide a way to treat such cancers.

Organoiridium complexes that combat cancer utilising one or more MoAs have been reported.[144–146] Examples include induction of autophagy,[147] antiangiogenesis,[146] redox modulation,[84,145,148] perturbation of mitochondrial membrane potential,[127] transfer hydrogenation,[101,149] induction of apoptosis,[150] and DNA interactions.[81,151,152] As such, they show promise as single- and polypharmacological anticancer agents.

A second problem hampering the efficacy of many Pt-based DNA-targeting chemotherapeutics is intrinsic and acquired resistance. Cancer cells can utilise cellular processes such as nucleotide excision repair (NER), mismatch repair (MMR), homologous recombination repair (HRR), and translesion synthesis to remove CDDP-DNA adducts and thereby reduce the antitumour efficacy of CDDP treatment.[153] Other mechanisms such as decreased drug uptake, increased drug efflux, and higher intracellular levels of drug-inactivating molecules, such as glutathione (GSH), further contribute to CDDP resistance.[154]

These factors illustrate the need to overcome these obstacles without compromising anticancer activity. New metal-based therapeutics offer promising ways to do so.

Organometallic anticancer complexes that interact with DNA have been reported.[155–157] Ir(III) complexes can do so through a variety of mechanisms[158,159] such as intercalation,[160] coordination to nucleotides,[92,102,161,162]

binding to quadruplex DNA,[163] strand cleavage,[164] and groove binding.[165] In doing so, they exert cytotoxic and cytostatic effects on cancer cells.

In order to overcome the increasing problem of cancer drug resistance, it is of paramount importance that new chemotherapeutics are produced that either target cancer DNA in different ways to current chemotherapeutics or augment/replace DNA targeting with other effective MoAs. The Pt drug CDDP and its derivatives, in particular, have been well-researched. The anticancer properties of Ir-based chemotherapeutics are comparatively less well explored.

An organoiridium half-sandwich complex incorporating a pentamethyl cyclopentadienyl ligand and an N,N-chelating ligand has previously been reported to be active against cancer cell lines displaying both intrinsic and acquired CDDP resistance.[158]

Synthetic extension of the Cp system by the addition of phenyl rings has been shown to increase the hydrophobicity, cellular uptake and consequently the anticancer potency of many organoiridium half-sandwich complexes.[86,92,101]

Additionally, it has been shown that the coordination of a strong π-acceptor phenylazopyridine ligand to a metal centre significantly affects the chemical and biological behaviour, depending on the nature of the substituents on the phenyl ring, in organometallic complexes of Ru,[126] Os[66] and Ir.[102]

The previously reported Ir(III) complex $[Cp^{xph}Ir(azpyNMe_2)Cl]PF_6$ (Complex **2**) has shown potent anticancer activity against the A2780 ovarian carcinoma cell line *in vitro*, in addition to cell lines of the NCI-60 panel and large-scale GDSC pharmaco-genomic screen (see Chapter 3), displaying greater average potency than CDDP.[102] The presence of the $azpyNMe_2$ bidentate ligand confers high potency to this complex when compared to others of similar structure with different bidentate azopyridine ligands. The NMe_2 family of complexes in particular showed great promise as anticancer agents. The significance of this functional group, with regards to anticancer potency and MoA, warrants investigation.

In this chapter, two novel Ir(III) complexes, each bearing a Cp^{xbiph} system, a bidentate phenylazopyridine ligand, and a monodentate chlorido ligand, are

studied (Figure 4.1). The sole structural difference between them is the functional group in the para-position of the phenylazopyridine phenyl ring. Complex **1** bears the NMe_2 group, whilst complex **13** bears hydrogen (i.e. an unsubstitued para position). Their stability, anticancer potency, selectivity, and efficacy against dsDNA virus-infected and CDDP-resistant cell lines have been assessed and a panel of experiments carried out to investigate differences in their MoAs.

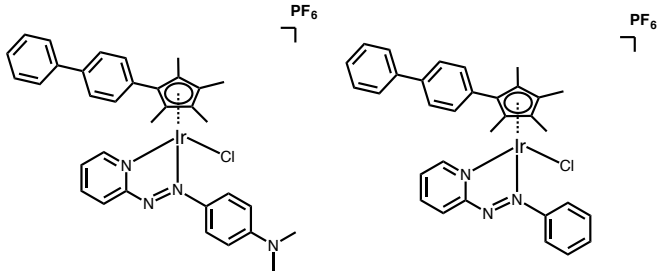

Complex **1** Complex **13**

Figure 4.1: Complexes **1** and **13** studied in this chapter.

Based on previously reported work on similar complexes, in addition to the results described in Chapter 3, DNA interaction and induction of oxidative stress are hypothesised as possible MoAs for these complexes. Thorough investigations are made into the way these complexes interact with DNA, as well as their capacity to generate reactive oxygen species (ROS) and interact with antioxidants.

4.2 Experimental Methods

4.2.1 DNA Interaction Studies

Oligonucleotide binding studies, UV studies, dichroism studies, ethidium bromide (EtBr) flourescence experiments and gel electrophoresis experiments on complexes **1** and **13** were carried out by the Brabec Group, Institute of Biophysics, Academy of Sciences of the Czech Republic.

4.2.1.1 Nucleotide Interactions

Solutions of 1:1 complex:nucleotide at 300 μM (5-AMP, 5-GMP, 5-CMP or 5-TMP) were prepared in 5% CD_3CN:D_2O. ^{1}H-NMR spectra were taken on a 600 MHz NMR machine at 310 K 10 min after mixing and after 24 h incubation at 310 K. All stocks and solids were pre-incubated at 310 K.

4.2.1.2 Buffer Preparation

Experiments were carried out in either 0.01 M Tris-HCl buffer or phosphate buffer, as detailed in the appropriate section.

Phosphate buffer (100 mL, 0.1 M, pH = 7.4) was prepared by mixing 40.5 mL 0.2 M sodium phosphate, dibasic dihydrate ($Na_2HPO_4 \bullet 2H_2O$) with 9.5 mL 0.2 M sodium phosphate, monobasic monohydrate ($NaH_2PO_4 \bullet H_2O$) and 50 mL H_2O. This was further diluted as required in 18.2 Milli-Q H_2O.

4.2.1.3 Preparation of ctDNA

Deoxyribonucleic acid sodium salt from calf thymus, Type I, fibres (ctDNA) was purchased from Sigma Aldrich (UK) and a 2 mg/ml solution in 10 mM buffer was prepared by gentle stirring then incubation at 277 K for 24 h followed by gentle mixing by inspiration/aspiration by micropipette. This was diluted as appropriate in buffer. The solution was either used immediately

or frozen at 193 K until the day of the experiment then thawed at ambient temperature and used immediately.

To confirm the DNA was protein-free the solution was standardized spectrophotometrically before freezing and after thawing (Figure 4.2).

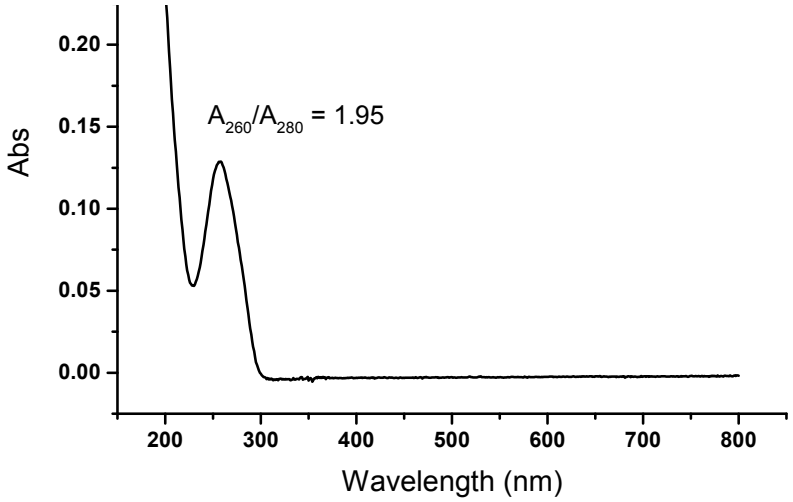

Figure 4.2: UV-Vis spectrum of ctDNA in phosphate buffer diluted further in phosphate buffer so A $\leq$ 1. $A_{260}/A_{280} \geq 1.8$ so the DNA is sufficiently pure and protein-free.[166] The base pair concentration of the DNA was calculated from the spectrum using its known molar absorption coefficient at 260 nm (6600 $M^{-1}cm^{-1}$).[167]

4.2.1.4 Dichroism Studies

Linear and circular dichroism studies carried out on ctDNA in 0.01 M Tris.HCl (pH 7.4, 310 K) incubated with increasing concentrations of complex **1** or **13**.

4.2.1.5 Gel Electrophoresis

Native gel electrophoresis was carried out on supercoiled plasmid DNA (pBR322) incubated with complex for 24 h at 310 K.

4.3 Results

4.3.1 Intracellular Aquation

The MoA of a drug is often linked to the behaviour of the complex when in aqueous solution. CDDP's MoA is reliant on the lability of the chlorides bound to the Pt centre. In Chapter 3, the extent of hydrolysis of complex **1** was investigated. More in-depth kinetic investigations are now carried out to better describe the hydrolysis process for complex **1**.

A hydrolysis equilibrium between chloride-bound Ir and water-bound Ir governed by chloride concentration is hypothesised (Figure 4.3).

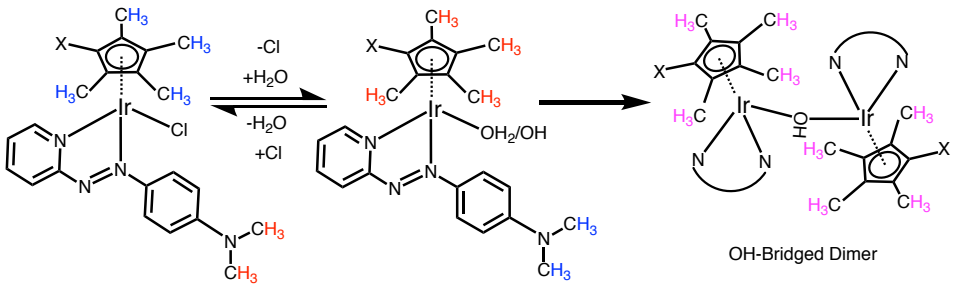

Figure 4.3: Proposed hydrolysis equilibrium for the complexes studied in this work. Aquation monitored by following the chemical shift of ^{1}H-NMR peaks corresponding to NMe_2 hydrogens for complex **1** or Cp^x ring methyl hydrogens for complex **13** coloured above.

^{1}H-NMR experiments were carried out in which a spectrum of a 100 μM solution of complex **1** in 10% d_6-DMSO:D_2O, 0.1% 1,4-dioxane (v/v) at 310 K, unbuffered at pD 8 with no chloride was taken every hour to monitor the kinetics of hydrolysis (Figure 4.4). In addition, experiments were carried out in parallel in 120 mM NaCl solution to simulate the chloride concentration present in the cell growth medium used for *in vitro* cancer cell experiments.

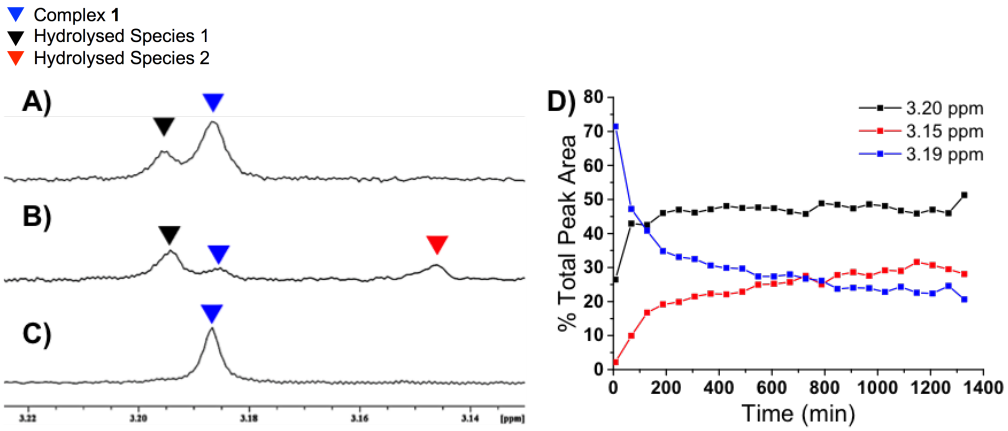

Figure 4.4: Monitoring of the hydrolysis of complex **1** by 600 MHz ^{1}H-NMR spectra of a 100 μM solution of complex **1** in 10% d_6-DMSO:D_2O, 0.1% 1,4-dioxane (v/v) at 310 K, unbuffered at pD 8 by tracking peaks corresponding to NMe_2 hydrogens. (A) 10 min after sample preparation, (B) 24 h after sample preparation, (C) 24 h after sample preparation in 120 mM NaCl solution, (D) Relative % integrals of peaks corresponding to NMe_2 hydrogens of complex **1** tracked over 24 h.

Further experiments were carried out in the presence of 4 mM, 23 mM and 104 mM NaCl to simulate the chloride concentration in the cell nucleus, cytosol and blood plasma, respectively[168] (Figure 4.5 – 4.8) Thus the nature of the complexes both in aqueous solution and in an intracellular environment can be predicted.

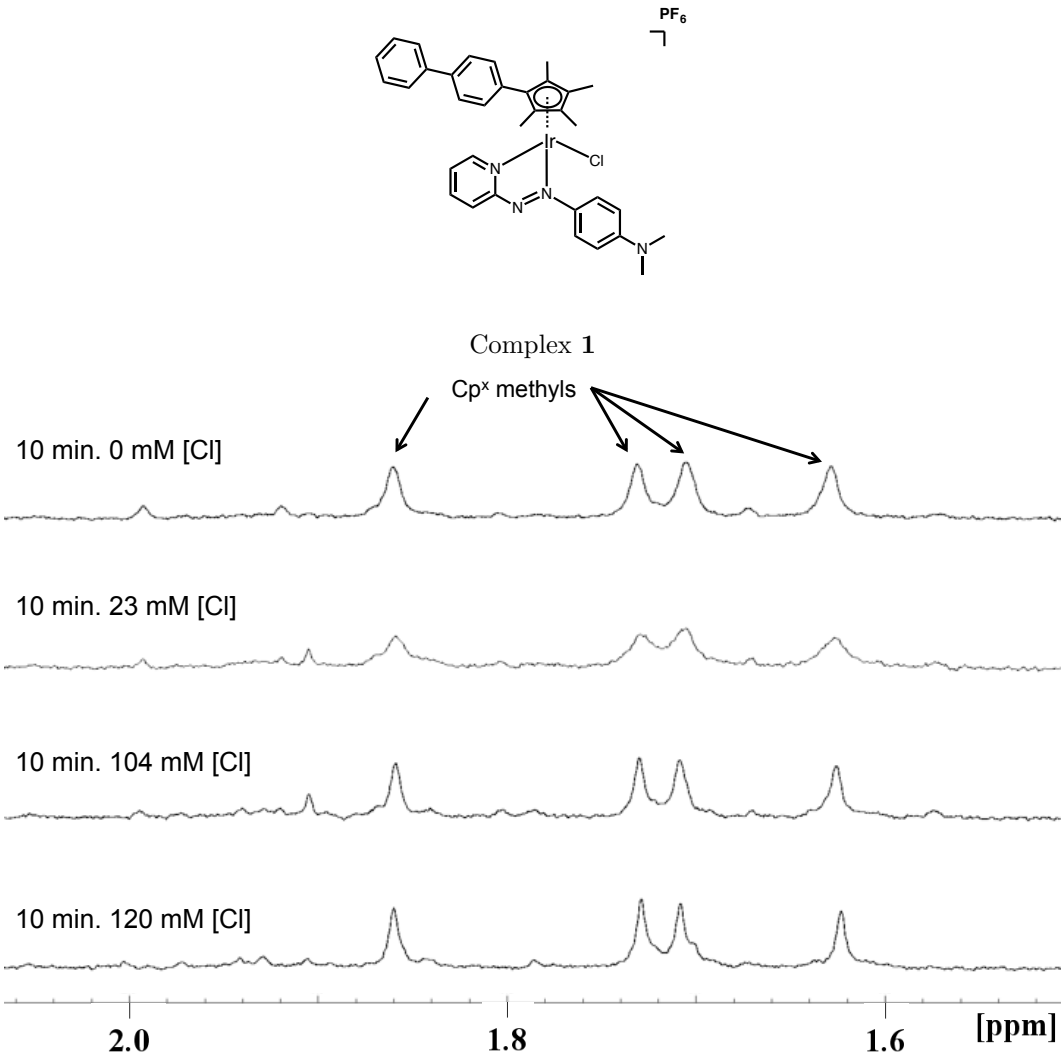

Figure 4.5: Aliphatic region of 600 MHz ^{1}H-NMR spectra of 100 μM solutions of complex **1** in 10% d_6-DMSO:D_2O, 0.1% 1,4-dioxane (v/v) at 310 K, unbuffered at pD 8 incubated with chloride at 4 mM, 23 mM, 104 mM and 120 mM for 10 min.

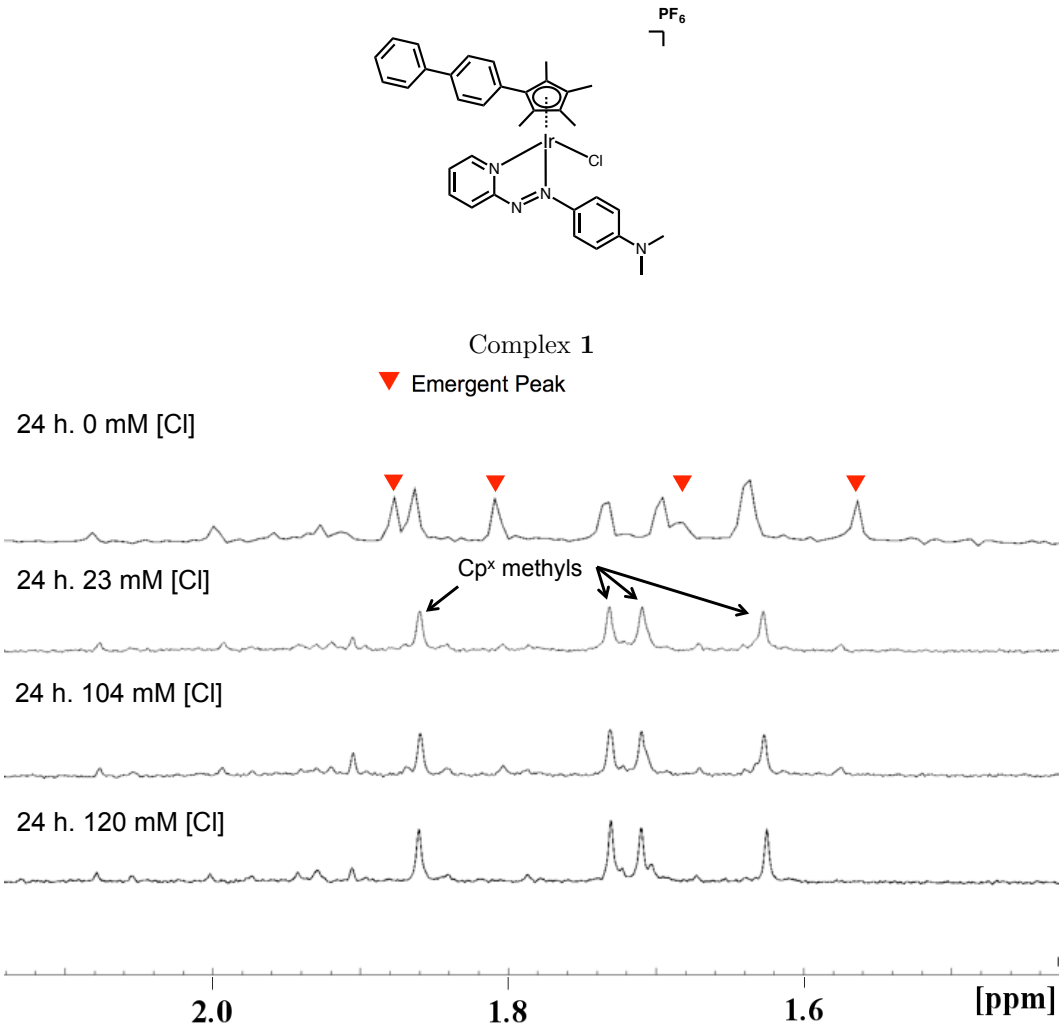

Figure 4.6: Aliphatic region of 600 MHz ^{1}H-NMR spectra of 100 µM solutions of complex **1** in 10% d_6-DMSO:D_2O, 0.1% 1,4-dioxane (v/v) at 310 K, unbuffered at pD 8 incubated with chloride at 4 mM, 23 mM, 104 mM and 120 mM for 24 h.

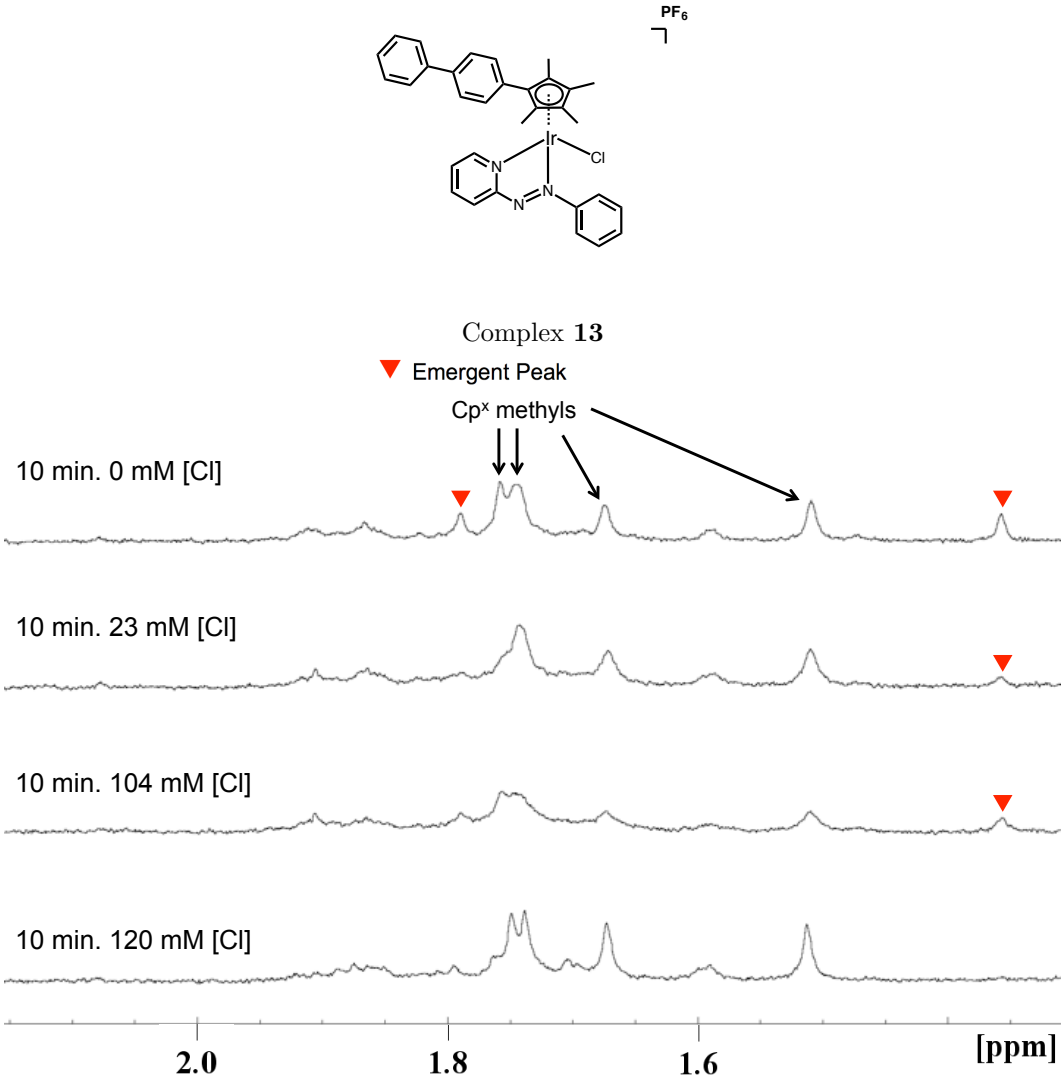

Figure 4.7: Aliphatic region of 600 MHz ^{1}H-NMR spectra of 100 µM solutions of complex **13** in 10% d_6-DMSO:D_2O, 0.1% 1,4-dioxane (v/v) at 310 K, unbuffered at pD 8 incubated with chloride at 4 mM, 23 mM, 104 mM and 120 mM for 10 min.

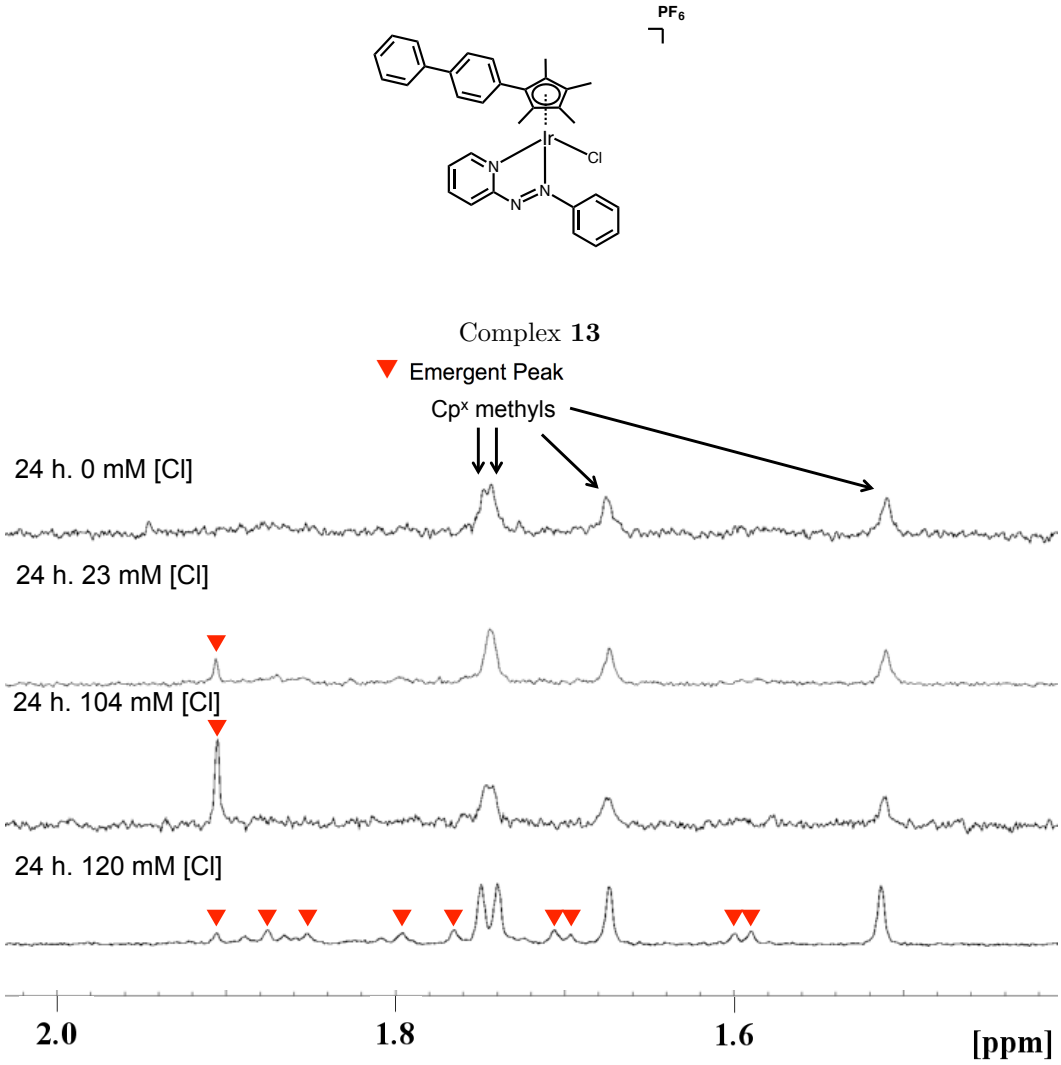

Figure 4.8: Aliphatic region of 600 MHz ^{1}H-NMR spectra of 100 μM solutions of complex **13** in 10% d_6-DMSO:D_2O, 0.1% 1,4-dioxane (v/v) at 310 K, unbuffered at pD 8 incubated with chloride at 4 mM, 23 mM, 104 mM and 120 mM for 24 h. Emergent peaks denoted with red arrows.

The presence of chloride at 4 mM, 23 mM and 104 mM partially suppresses the hydrolysis of complex **1**, but not **13**. For complex **13** ([η^5-Cp^{xbiph}Ir(azpy)Cl]PF_6), new peaks are seen after 24 h, even in the presence of 120 mM NaCl and, as is the case for complex **1**, two new species are observed. ESI-MS peaks were observed for the cations of complexes **1** and **13** coordinated to OH instead of Cl, with m/z = 709.2 and 666.2, most likely corresponding to **1-OH** (calculated m/z = 709.25) and **13-OH** (calculated m/z = 666.21),

respectively.

In Chapter 3, it was determined that the products of hydrolysis of complex **1** do not disappear upon the addition of chloride. To determine whether this is the case for complex **13**, the experiment was repeated without chloride, then 120 mM chloride was subsequently added after 24 h incubation as solid NaCl, and another spectrum was taken (Figure 4.9).

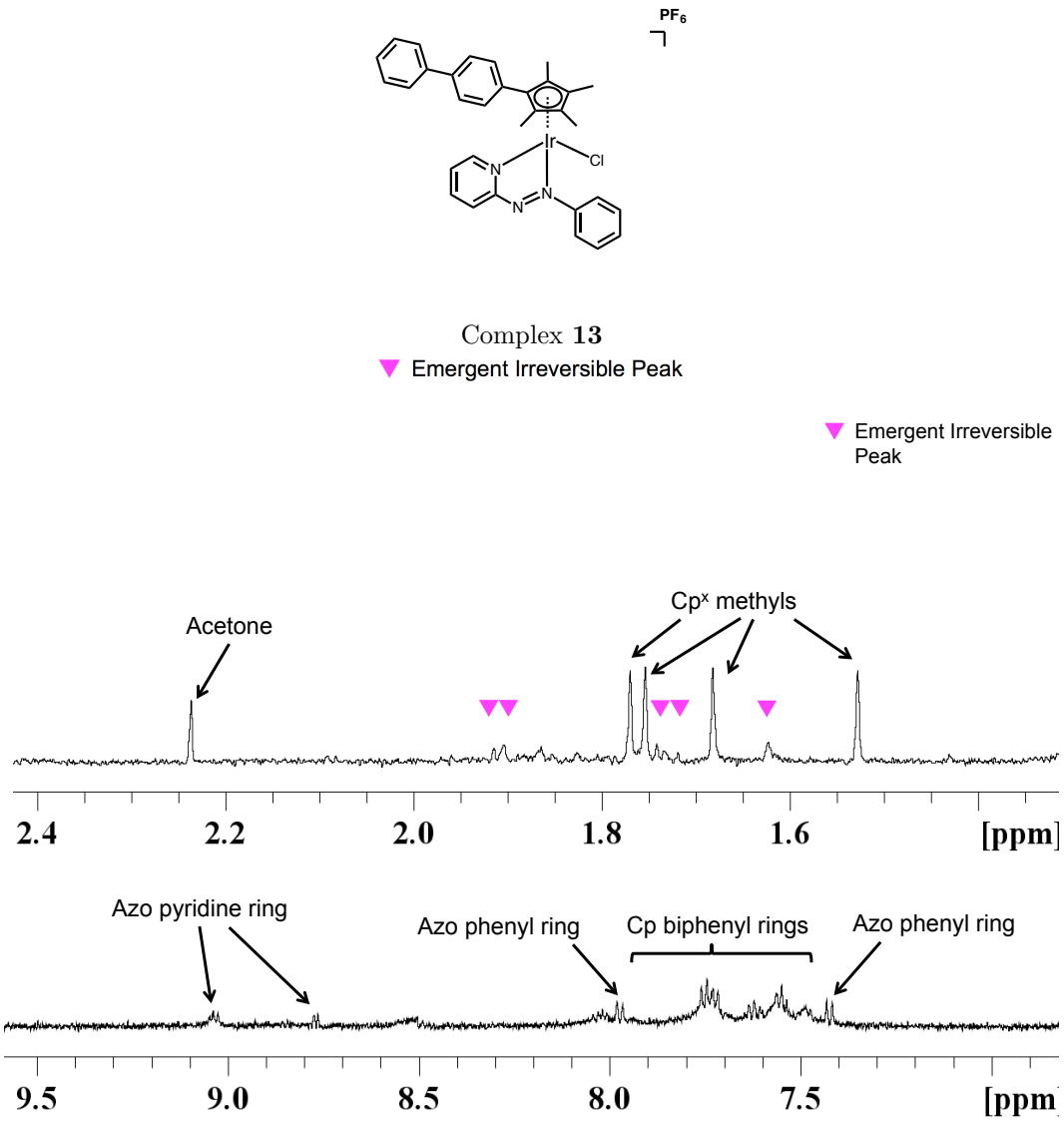

Figure 4.9: Aliphatic (top) and aromatic (bottom) regions of a 600 MHz ^{1}H-NMR spectrum of a 100 μM solution of complex **13** in 10% d_6-DMSO:D_2O, 0.1% 1,4-dioxane (v/v) at 310 K, unbuffered at pD 8. Spectrum taken 10 min after addition of 120 mM [Cl] to a previously chloride-free solution that had been incubated for 24 h. Emergent peaks not corresponding to original complex denoted by pink arrows. Traces of acetone/ether from the NMR tube are visible.

Complex **1** undergoes 79% hydrolysis in 24 h and two new species are observed, one appearing earlier and more rapidly than the other. This hydrolysis is partially suppressed by $\geq$ 4 mM NaCl. Complex **13** undergoes hydrolysis

even in the presence of 120 mM NaCl. Due to multiple overlapping peaks and the complexity of the spectra, exact quantification of the extent of hydrolysis was not possible for complex **13**.

4.3.2 Aqua Adduct pK_a Determination

As complexes **1** and **13** do not have any bound hydrogens with pK_a values within a biologically-relevant or easily measurable pH range, experiments were carried out to determine the pK_a values for hydrogens on the bound H_2O ligands of their aqua adducts **1-OH$_2$** and **13-OH$_2$**.

To investigate this, pH titrations were carried out and the samples analysed by UV-vis spectroscopy. Data were plotted as absorbance at a maximum vs. pH, and a Boltzmann sigmoidal curve was fitted to determine the midpoint and therefore the pK_a (Figure 4.10).

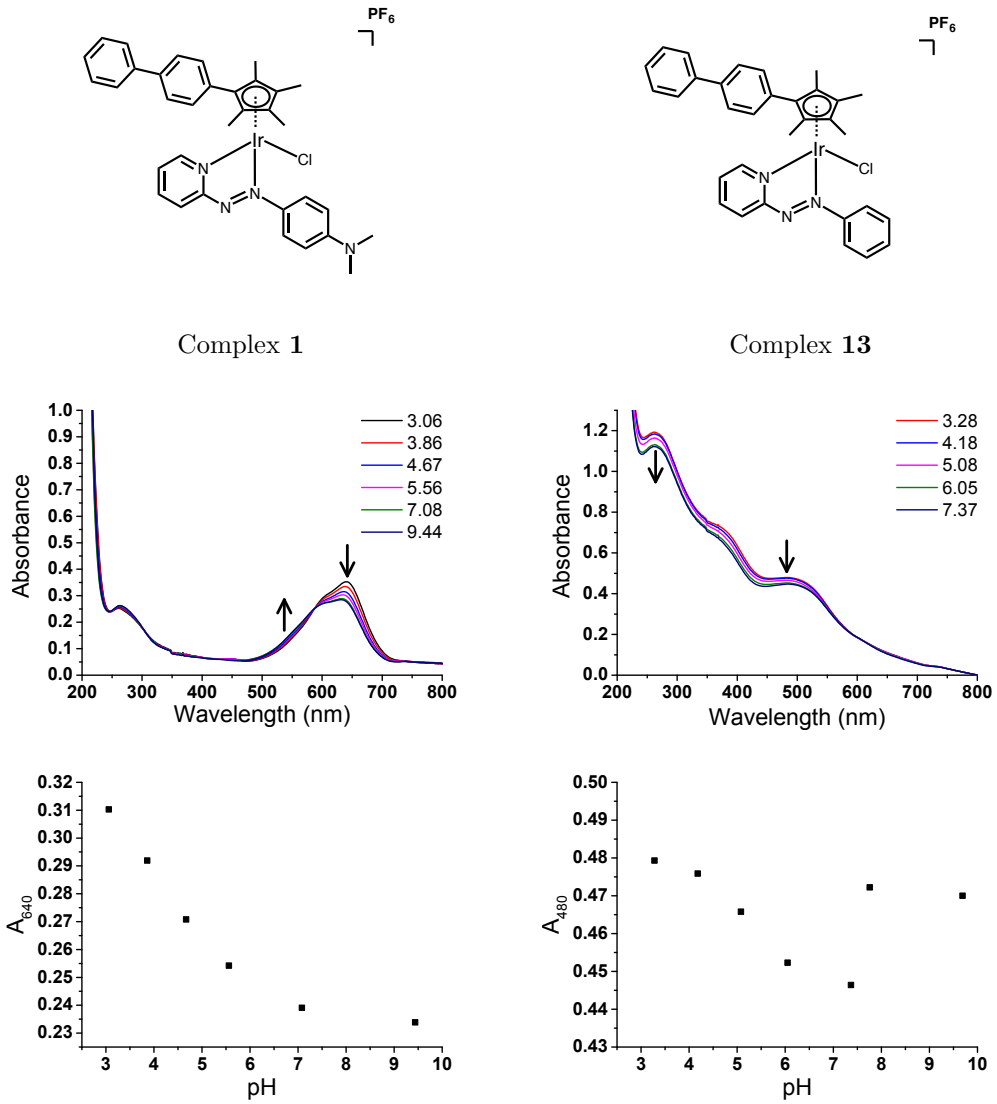

Figure 4.10: UV spectra of pH titrations of complex **1** (Left) and complex **13** (Right) after 24 h incubation in H_2O to form aqua adducts. Arrows indicate the effect of base addition. Plots of absorbances at maxima vs. pH shown beneath UV spectra.

The changes in the absorbance maximum at 640 nm upon base addition did not follow the expected Boltzmann sigmoidal curve for **1-OH**$_2$ and so determination of its pK_a value was not possible. No significant changes in the spectrum of complex **13** were observed over pH range ca. 3 – 8, nor was an isosbestic point observed. Therefore no pK_a value could be obtained for **13-OH**$_2$.

4.3.3 Nucleotide Binding Studies

Direct coordination of anticancer complexes to DNA base pairs is a well-known mechanism of anticancer action. Preliminary investigations into potential nucleotide binding properties of the complexes were carried out by LC-MS (Appendix Figures S22 – S30, pg. 295 – 303) ^{1}H-NMR studies on 1:1 solutions of nucleotide:complex. The nucleotides used were 5'-AMP, 5'-GMP, 5'-CMP, and 5'-TMP (Figures 4.11 – 4.13).

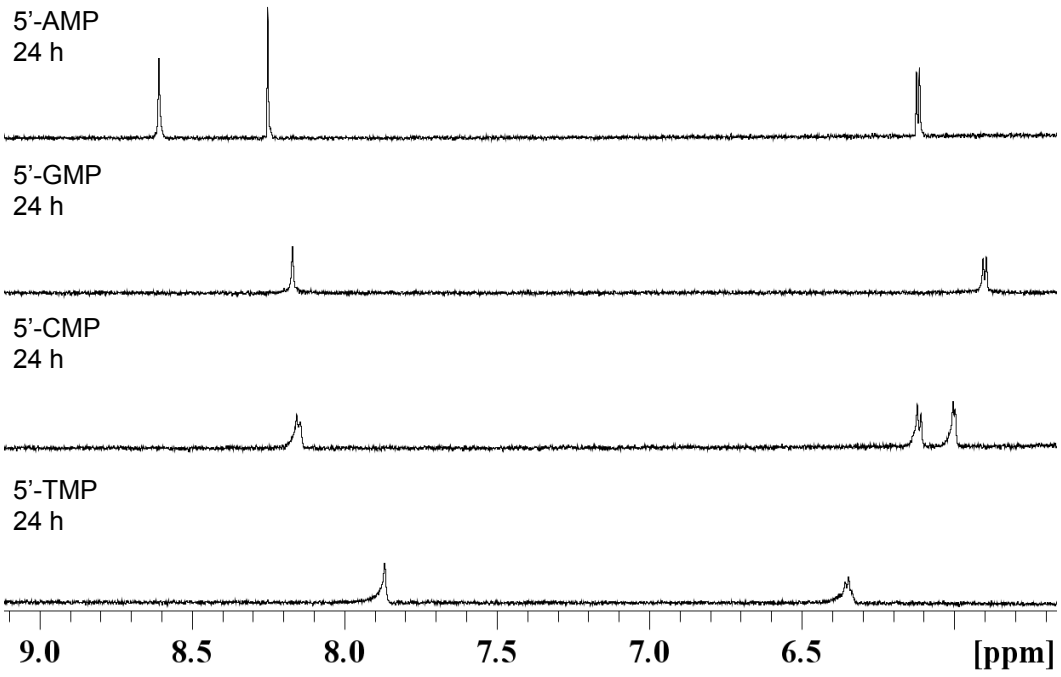

Figure 4.11: Aromatic region of 400 MHz ^{1}H-NMR spectra of 300 μM of nucleotides 5'-AMP, 5'-GMP, 5'-CMP or 5'-TMP incubated in 50% MeOD:D_2O for 24 h at 310 K.

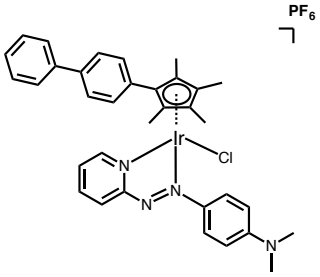

Complex **1**

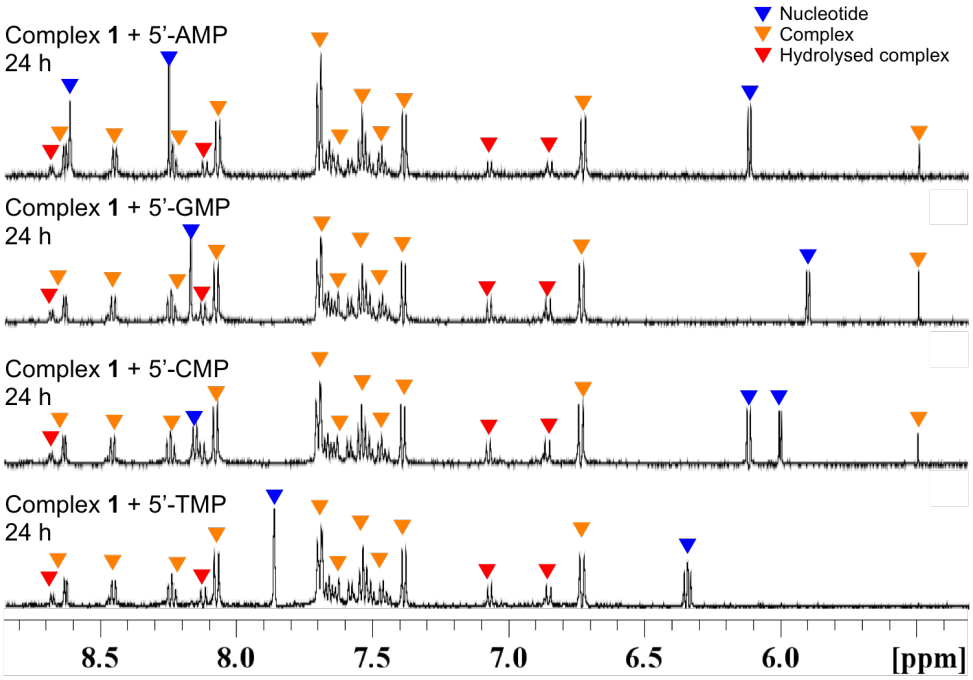

Figure 4.12: Aromatic region of 400 MHz ^{1}H-NMR spectra of 300 μM of nucleotides 5'-AMP, 5'-GMP, 5'-CMP or 5'-TMP incubated with 300 μM complex **1** in 50% MeOD:D_2O for 24 h at 310 K. Peaks corresponding to nucleotides denoted with blue triangles. Peaks corresponding to complex **1** or its products of hydrolysis denoted with orange or red triangles, respectively.

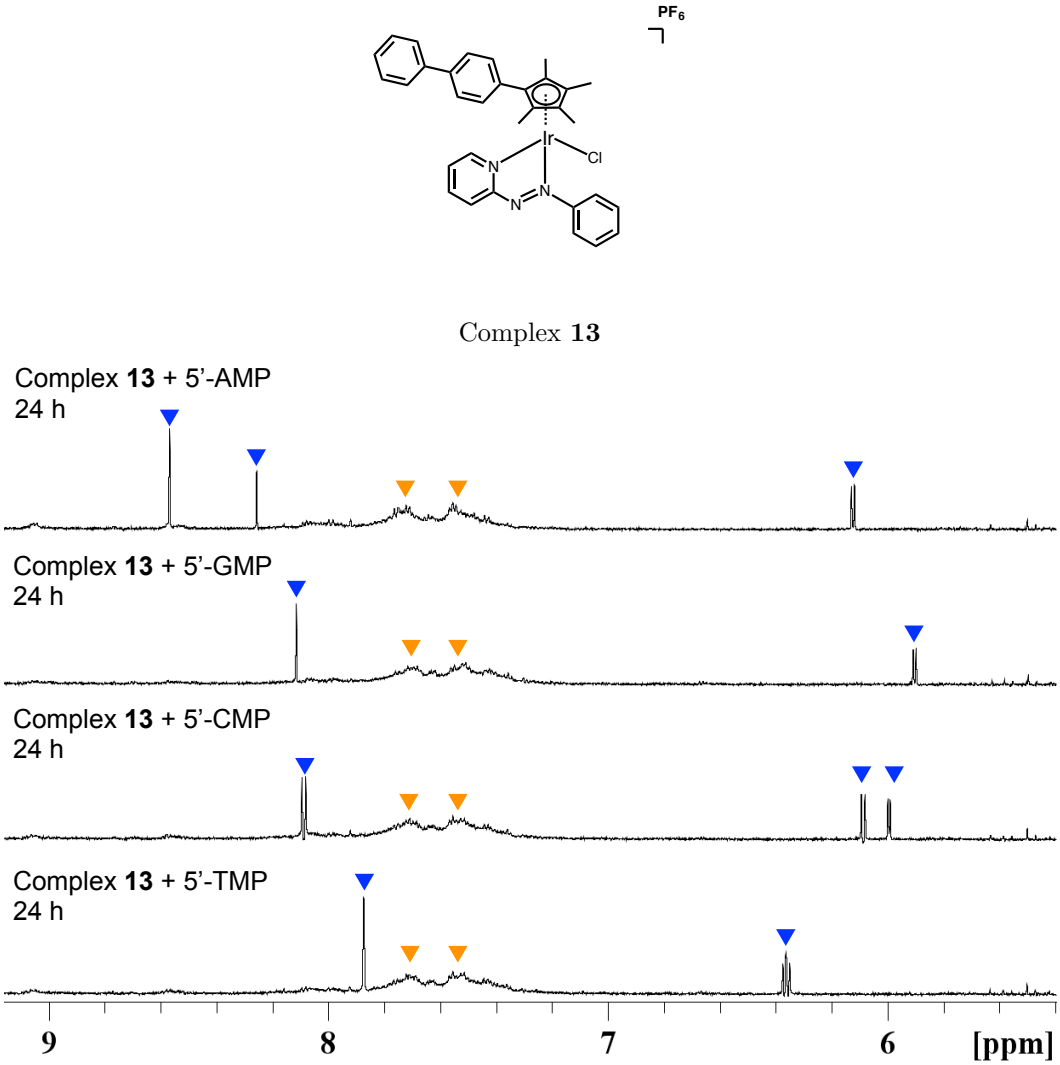

Figure 4.13: Aromatic region of 400 MHz ^{1}H-NMR spectra of 300 μM of nucleotides 5'-AMP, 5'-GMP, 5'-CMP or 5'-TMP incubated with 300 μM complex **13** in 50% MeOD:D_2O for 24 h at 310 K. Peaks corresponding to nucleotides denoted with blue triangles. Peaks corresponding to complex **1** or its products of hydrolysis denoted with orange triangles.

No significant new peaks that could correspond to complex-nucleotide adducts appeared in any spectra after 24 h incubation at 310 K.

To further test for different DNA binding modes in a system more representative of cellular DNA, further investigations were carried out using oligonucleotides containing a mixture of nucleobases, with one of the strands bear-

ing only a single guanine for the purposes of detecting direct modification to guanine, such as that achieved by CDDP. To test for direct modification to nucleotides in a DNA strand, complexes were incubated for 24 h with a single stranded (ss) or double stranded (ds) oligonucleotide radiolabelled with ^{32}P at its 5'-end then subjected to denaturation by 8 M urea, which disrupts the hydrogen bonding in DNA needed to maintain its structure (Figure 4.14). These experiments were carried out by the Brabec Group, Institute of Biophysics, Academy of Sciences of the Czech Republic.

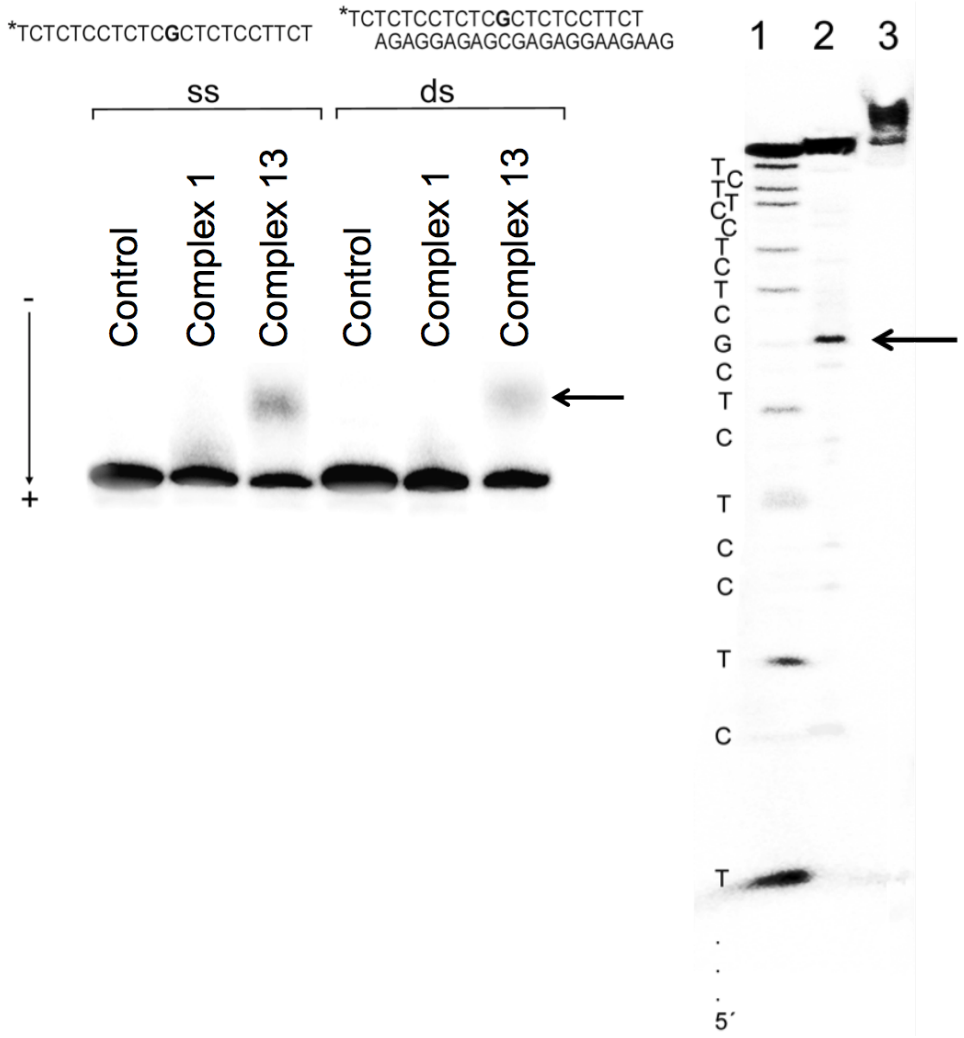

Figure 4.14: (Left) Autoradiogram of denaturing 24% PAA/8 M Urea gel. 22-mer single (ss)- or double-stranded (ds) oligonucleotide ^{32}P-labeled at its 5'- end incubated with complexes at a ratio of 10 mol. of complex per one mol. of oligonucleotide strand for 24 h at 310 K. (Right) Autoradiogram of the products of the reaction between DMS and the 5'- end, ^{32}P-labelled 22-mer oligonucleotide. Lanes: 1, a Maxam-Gilbert-specific reaction (T-residues) for the untreated oligonucleotide; 2, reaction of untreated oligonucleotide with DMS; 3, DMS reaction with the product isolated from the gel after treatment with complex **13**.

There were no significant differences between complex **1** and the control, however complex **13** induced the appearance of a new band corresponding to an adduct of the complex with the oligonucleotide. This adduct was cut from

the gel, the products eluted and purified by precipitation and subjected to reaction with dimethyl sulphate (DMS) followed by hot piperidine. If the N7 site of guanine is unmetallated, DMS will specifically methylate this site and hot piperidine will be able to cleave DNA at guanine, and a band will be seen corresponding to the cleaved strand. However, no bands for cleaved DNA were seen for the **13-DNA** adduct. Therefore, DMS was unreactive to it. Therefore, it is highly likely that complex **13** metallates guanine at N7.

4.3.4 Ultraviolet-Visible (UV-Vis) Spectroscopy of ctDNA

Preliminary examination of a complex's affinity for DNA was carried out using UV-Vis spectroscopy. Increasing amounts of ctDNA were added to 20 μM of complex in 0.01 M Tris.HCl buffer (pH 7.4, 295 K) and the consequential decrease in relative absorbance at the complex's maxima measured (Figure 4.15). These experiments were carried out by the Brabec Group, Institute of Biophysics, Academy of Sciences of the Czech Republic.

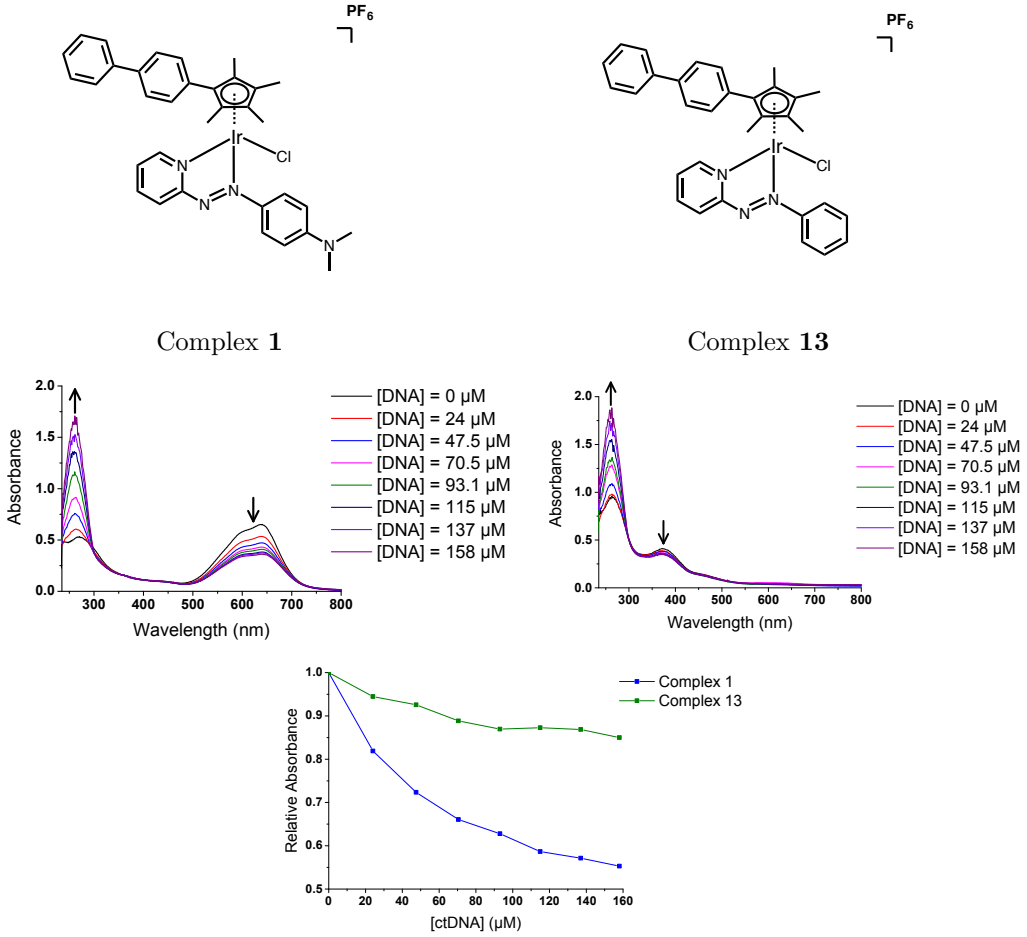

Figure 4.15: Absorption spectra of 20 μM of complex **1** (Top Left) and complex **13** (Top Right) in 0.01 M Tris.HCl buffer (pH 7.4, 295 K) after 10 min incubation with increasing amounts of ctDNA. The arrow indicates the absorption changes upon increasing concentration of ctDNA. (Bottom) A comparison of the relative absorbances of the complexes at their corresponding maxima (those above 300 nm where DNA does not absorb) upon increasing ctDNA concentration.

After 10 min incubation the absorption change is far more pronounced for complex **1**, however, the size of the absorbance change may vary between complexes, therefore further experiments are required to better understand their DNA-interacting properties.

4.3.5 Linear Dichroism (LD) of ctDNA

Due to the linear nature of its superstructure, ctDNA molecules generate a LD spectra when aligned in a couette. The effect of complexes on the alignment of DNA can be measured by LD. As such, solutions of unaligned small molecules alone, such as the complexes studied in this work, do not produce LD peaks. However, if the complexes interact with DNA in a specific, regular orientation they will align and therefore induce an LD peak in the region in which they absorb. LD titrations were performed on ctDNA incubated with complexes **1** or **13** for 24 h (Figure 4.16). These experiments were carried out by the Brabec Group, Institute of Biophysics, Academy of Sciences of the Czech Republic.

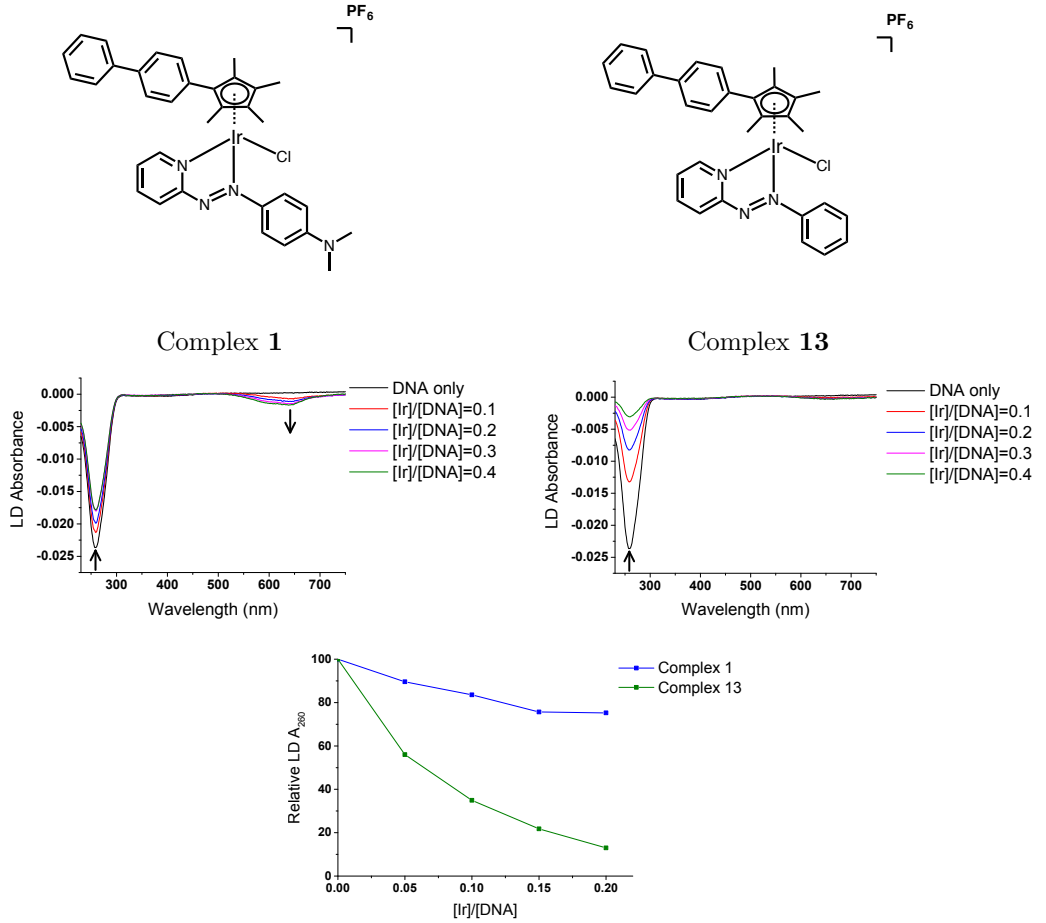

Figure 4.16: LD spectra of ctDNA after 24 h incubation with increasing concentration of complex **1** (Top Left) and **13** (Top Right) in 0.01 M Tris.HCl (pH 7.4, 310 K). (Bottom) Comparison of the LD signal of ctDNA at 260 nm upon addition of complexes **1** or **13**.

Complex **1** induces a negative LD signal in the visible light region of the LD spectrum, at around 600 – 700 nm, mirroring that of its UV-Vis absorbance spectrum. This shows that it interacts with ctDNA, as ctDNA alone does not produce an LD signal above 300 nm. The magnitude of this signal is proportional to the ratio of complex to DNA bases. In contrast, no induced LD signal is visible upon addition of complex **13** to ctDNA. Additionally, the LD signal of ctDNA at 260 nm is reduced upon addition of either complex, indicating delinearisation of the DNA. The magnitude of this reduction is significantly greater for complex **13** than for complex **1**.

4.3.6 Circular Dichroism (CD) of ctDNA

CD measures the difference in absorbances between left and right-handed circularly polarised light. Due to its helical nature, ctDNA produces a distinctive CD spectrum. If a complex interacts with DNA in a specific orientation it can generate a CD peak due to the induced chirality generated by its presence. To assess the effects of complexes **1** and **13** on the CD spectrum of ctDNA, CD titrations were performed on ctDNA incubated with complexes **1** and **13** for 10 min and 24 h (Figure 4.17). These experiments were carried out by the Brabec Group, Institute of Biophysics, Academy of Sciences of the Czech Republic.

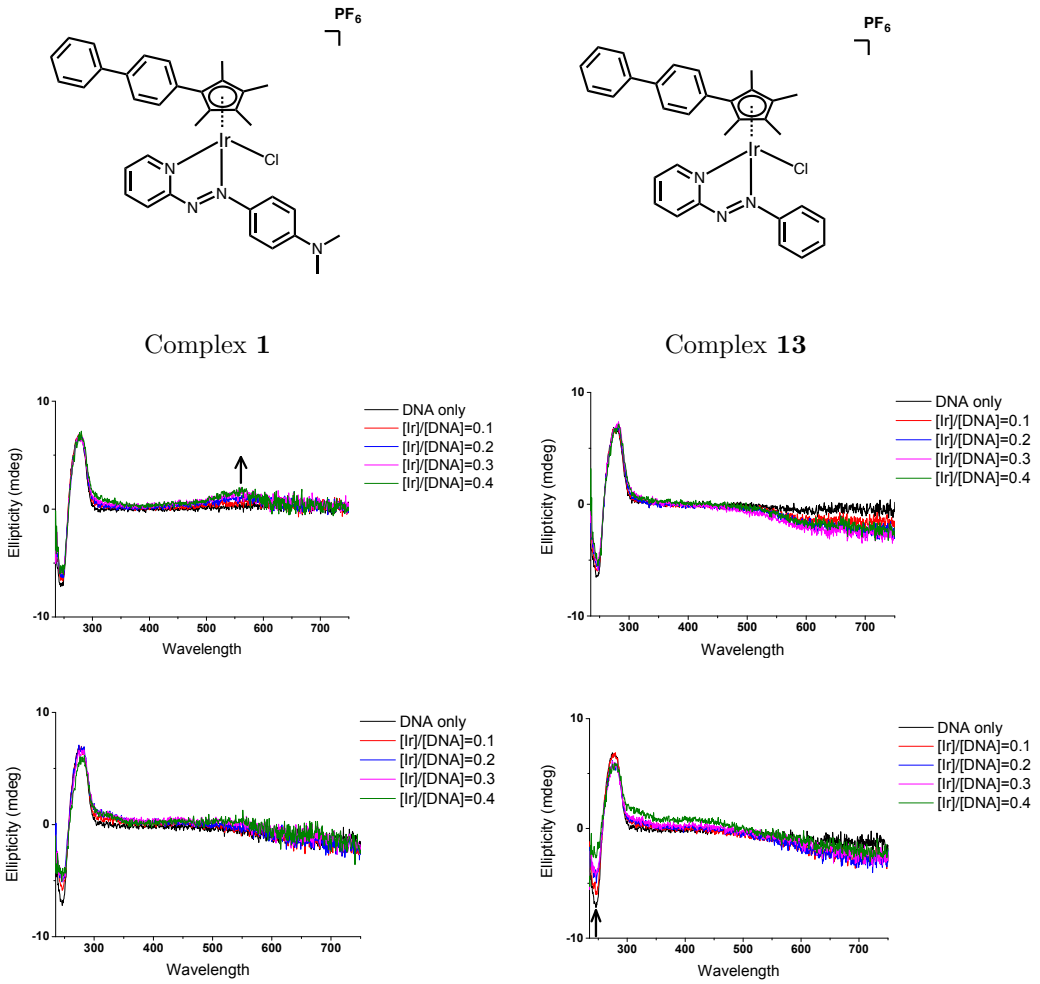

Figure 4.17: CD spectra of ctDNA after 10 min incubation with increasing concentration of complex **1** (Top left) or **13** (Top right) or 24 h incubation with complex **1** (Bottom left) or **13** (Bottom right) in 0.01 M Tris.HCl (pH 7.4, 310 K).

An induced positive band is observed in the CD spectrum in the 500 – 600 nm region 10 min after addition of the azpyNMe$_2$ complex **1**. However, this is no longer visible after 24 h. The azpy complex **13** induces no CD signal in the visible light region after 10 min or 24 h of incubation with complex **13**. The magnitude of the CD signals produced by ctDNA at 244 nm (due to helicity) and 274 nm (due to base stacking) are significantly reduced by complex **1** and even more so by complex **13** after 24 h. Chiral molecules absorb left

and right-handed circularly polarised light differently, generating CD spectra. Conversely, racemic mixtures do not induce any CD signals. That complex **1** has been shown to exist as a racemic mixture in Chapter 3 further confirms that the induced positive band is due to DNA modification.

4.3.7 Ethidium Bromide (EtBr) DNA-Binding Studies

EtBr is a fluorescent molecule with a central heterocyclic phenanthroline moiety that intercalates into the major groove of DNA. Intercalating agents force apart the base pairs of DNA, partially unwinding the double helix and causing the overall length of the strand to increase. Since viscosity is proportional to the cube of the length of the DNA in the solution, intercalation can translate into comparatively large changes in viscosity.[169] Measurement of DNA viscosity upon incubation with complexes **1** and **13** for 10 min or 24 h showed no significant changes in viscosity (Figure 4.18). These experiments were carried out by the Brabec Group, Institute of Biophysics, Academy of Sciences of the Czech Republic.

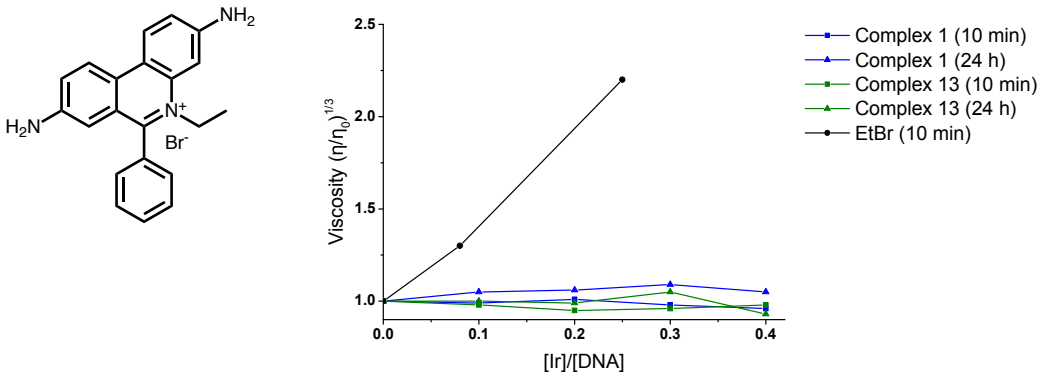

Figure 4.18: (Left) EtBr. (Right) The relative specific viscosity of ctDNA solution after 10 min or 24 h incubation with complex **1** or complex **13** in a 0.01 M Tris.HCl buffer at 310 K. η is the viscosity of the solution in the presence of complexes and η^{θ} is the viscosity of the control (DNA without complex). DNA solution viscosity after 10 min incubation with EtBr also shown.

When EtBr binds DNA its fluorescence increases ca. 20-fold. This is due to its outer phenyl ring projecting out into the hydrophobic environment between the base pairs. Here the rate of transfer of excited state photons to water molecules is reduced, as is the fluorescence quenching effect of water on EtBr, and fluorescence increases.[170] If EtBr is displaced from DNA, or its binding is inhibited, there is a measurable decrease in fluorescence. The DNA-interacting capability of complexes can be deduced from the effects on EtBr fluorescence,

and so EtBr binding studies were carried out with complexes **1** and **13** (Figure 4.19). Addition of complex **1** to DNA treated with EtBr causes a significant decrease in EtBr fluorescence after 10 min, whereas only a small decrease is observed upon complex **13** addition. Conversely, EtBr binding was inhibited for DNA incubated with the complexes over 24 h. Complex **1** inhibits EtBr binding slightly more than complex **13**, and the level of inhibition is dependent on complex concentration.

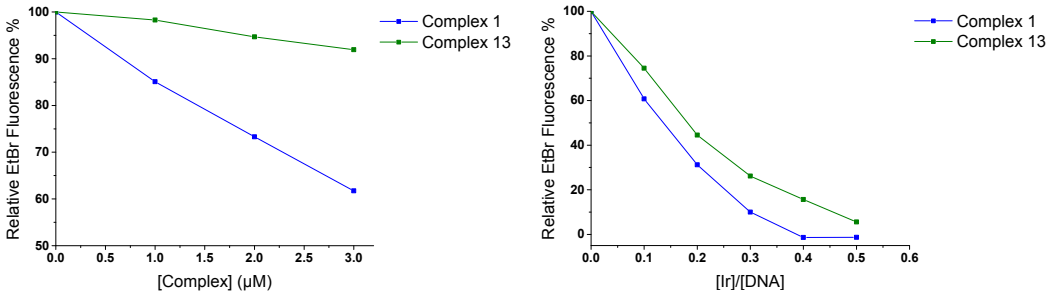

Figure 4.19: (Left) EtBr displacement by complexes **1** and **13**. ctDNA (3.9 μM) pretreated with EtBr (1.3 μM) was titrated and incubated for 10 min with increasing concentrations of complexes in 0.01 M Tris.HCl buffer (pH 7.4, 310 K). (Right) Inhibition of EtBr intercalation by complexes **1** and **13**. ctDNA was incubated with complexes for 24 h then EtBr was added and its fluorescence measured.

4.3.8 DNA Unwinding and Scission

Cellular DNA is often supercoiled. Unwinding or damaging cancer DNA can have implications for cell survival. To unwind supercoiled DNA, a nick must be made in the DNA deoxyribose-phosphate backbone between two bases to allow it to unwind into its relaxed form. To investigate the effects of the complexes on circular supercoiled dsDNA, electrophoresis studies were carried out using the dsDNA plasmid pBR322 (Figure 4.20). These experiments were carried out by the Brabec Group, Institute of Biophysics, Academy of Sciences of the Czech Republic.

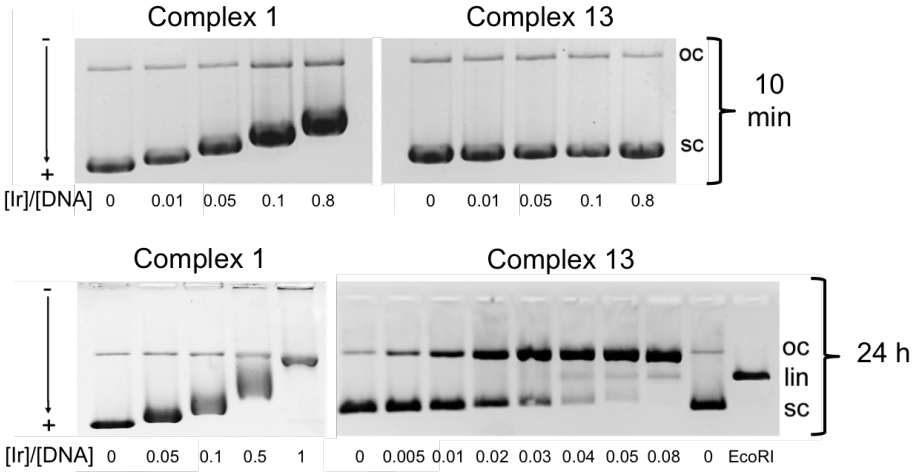

Figure 4.20: Native gel electrophoresis studies of unwinding of supercoiled (sc) plasmid DNA (pBR322) into open-circular (oc) form incubated with complexes in 0.01 M Tris-HCl buffer (pH 7.4) for 10 min or 24 h at 310 K. [Ir]/[DNA] ratio shown beneath lanes. The endonuclease EcoRI was used as the positive control for DNA linearisation.

After 10 min incubation with complex **1**, some unwinding of the plasmid was observed, whereas complex **13** induced no changes. Conversely, the magnitude of unwinding by complex **1** does not change significantly after 24 h incubation, whereas plasmid incubated with complex **13** for 24 h is significanty unwound even at concentrations as low as 1:200 complex:base pair. Additionally, complex **13** generates bands in the gel corresponding to linearised (lin) DNA, confirmed by the positive control of plasmid incubated with the endonuclease EcoRI, which is known to cleave both DNA strands into linear fragments.

4.3.9 Potency, Cross-resistance and Selectivity

The results obtained in Chapter 3 against A2780 ovarian carcinoma were compared to A2780cis ovarian carcinoma with acquired CDDP resistance, A549 lung carcinoma and MRC-5 normal human lung fibroblasts. (Table 4.1). Antiproliferative screenings against A2780 and MRC-5 carried out by Dr. Isolda Romero-Canelón, Ji-Inn Song and Bindy Heer.

Table 4.1: Comparison of IC_{50} values (in μM) of complexes **1**, **13** and CDDP across a panel of cell lines with standard deviations obtained from duplicates of triplicate experiments. Cells were exposed to complex for 24 h, followed by a 72 h recovery period in complex-free medium. Cell lines tested were A2780 ovarian carcinoma, A2780cis ovarian carcinoma with acquired CDDP resistance, A549 lung carcinoma, CNE1 and CNE2 nasopharyngeal carcinomas, and MRC-5 normal human lung fibroblasts. CDDP IC_{50} values obtained experimentally or from previously published work.[145] (*n.d.* = not determined).

Complex	A2780	A2780cis	A549	CNE1	CNE2	MRC-5
1	0.095 ± 0.006	0.68 ± 0.03	2.7 ± 0.3	7.1 ± 0.8	0.98 ± 0.04	3.4 ± 0.5
13	0.126 ± 0.002	9.4 ± 0.7	10.9 ± 0.2	11.10 ± 0.009	4.7 ± 0.5	*n.d.*
CDDP	1.2 ± 0.2	11.5 ± 0.3	3.3 ± 0.1	7.7 ± 0.2	7.7 ± 0.3	16.2 ± 0.6

The cytotoxicity of complex **1** was superior to CDDP in all cell lines tested, with an especially low nanomolar IC_{50} value against A2780. This is significantly more potent than many reported precious metal-based chemotherapeutics.

The selectivity of complex **1** was measured by comparing its cytotoxicity in A2780 cells to MRC-5 normal (non-cancerous) lung fibroblasts (Table 4.2) to allow for comparison with the selectivity of other reported complexes determined in the same way.[84,171] These fibroblasts, like cancers, are fast-replicating, so low toxicity towards these are likely to translate to even lower toxicity to other healthy, slower replicating cells in patients. When comparing cytotoxicity in A549 lung carcinoma to MRC-5 lung fibroblasts, complex **1** is 1.3× selective, whereas CDDP is 4.9× selective.

Acquired resistance to one drug can confer resistance to other drugs with similar MoAs, resulting in cancers that are ultimately more difficult to treat. The level of cross-resistance of complex **1** and **13** with CDDP was measured

by comparing IC_{50} values in A2780 ovarian carcinoma and A2780cis ovarian carcinoma with acquired CDDP resistance (Table 4.2).

Table 4.2: Comparison of cross-resistance and selectivity factors for complexes and CDDP. Cross-resistance factor defined as IC_{50} in A2780cis/A2780. Selectivity factor defined as IC_{50} in MRC-5/A2780 (*n.d.* = not determined).

Complex	Cross-resistance	Selectivity
1	7x	36x
13	75x	*n.d.*
CDDP	10x	14x

Complex **1** was ca. 36× more cytotoxic to A2780 than to MRC-5. In comparison, CDDP is ca. 14× more cytotoxic to A2780 than to MRC-5. Both complexes show a degree of cross resistance with CDDP, however complex **13** shows an order of magnitude higher cross-resistance than **1**.

4.3.10 MoA Studies in Ovarian Carcinoma by Flow Cytometry

As complexes **1** and **13** are highly active against A2780 ovarian carcinoma, further experiments were carried out on this cell line by flow cytometry to assess for possible differences in MoA by investigating the complexes' ability to produce ROS and superoxide (SO), induce apoptosis and disrupt the cell cycle (Figures 4.21 – 4.23), the significance of which is detailed in Chapter 3. As the complexes differ by only one functional group, any differences in MoA can be attributed directly to the presence of that group. Flow cytometry studies carried out with the help of Dr. Isolda Romero-Canelón and Hannah Bridgewater.

4.3.10.1 ROS and Superoxide (SO) Generation

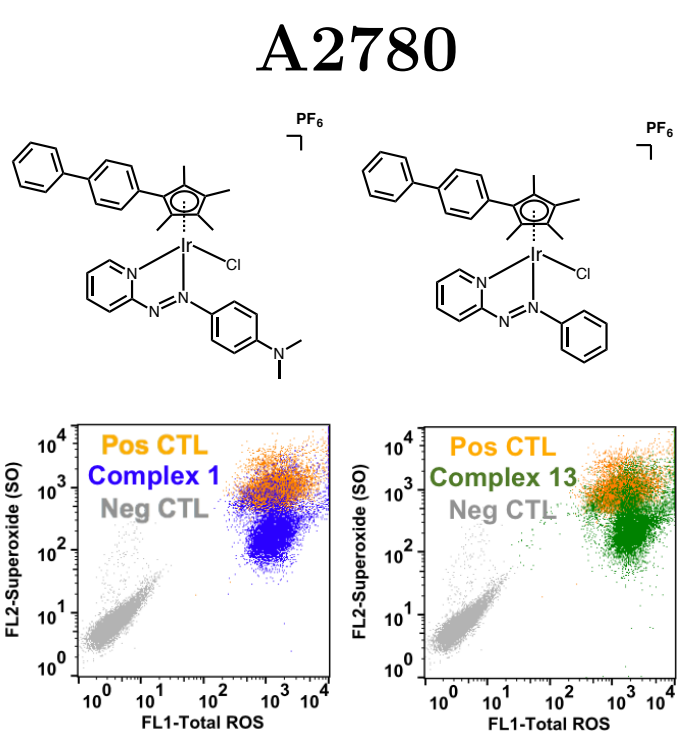

	High Superoxide	High ROS and Superoxide	High ROS	Low ROS and Superoxide
	FL1-FL2+	FL1+FL2+	FL1+FL2-	FL1-FL2-
Neg CTL	0.17 ± 0.07	0	0	99.82 ± 0.07
Complex 1	0.01 ± 0.01 ****	44 ± 1 ****	56 ± 1 ****	0.1 ± 0.3 ****
Complex 13	0.10 ± 0.09	65 ± 2 ****	34 ± 1 ****	0.3 ± 0.4 ****

Figure 4.21: Measurement of ROS and SO generation by flow cytometry of A2780 ovarian carcinoma cells exposed to complexes **1** (Left) and **13** (Right) for 24 h at IC_{50} concentrations at 310 K. Cells stained with orange/green fluorescent reagents. Pyocyanin used as positive control (orange). (Bottom) Table of % cell populations obtained from triplicate experiments. Statistical significance between cells exposed to complex vs. negative control was determined by two-sample independent Welch t-tests assuming unequal variance between populations with asterisks corresponding to $p \leq 0.05$ *, $p \leq 0.01$ **, $p \leq 0.001$ ***, $p \leq 0.0001$ ****.

Both complexes generated very high levels of ROS and SO, with complex **13** generating slightly higher levels of both overall.

4.3.10.2 Cell Cycle Analysis

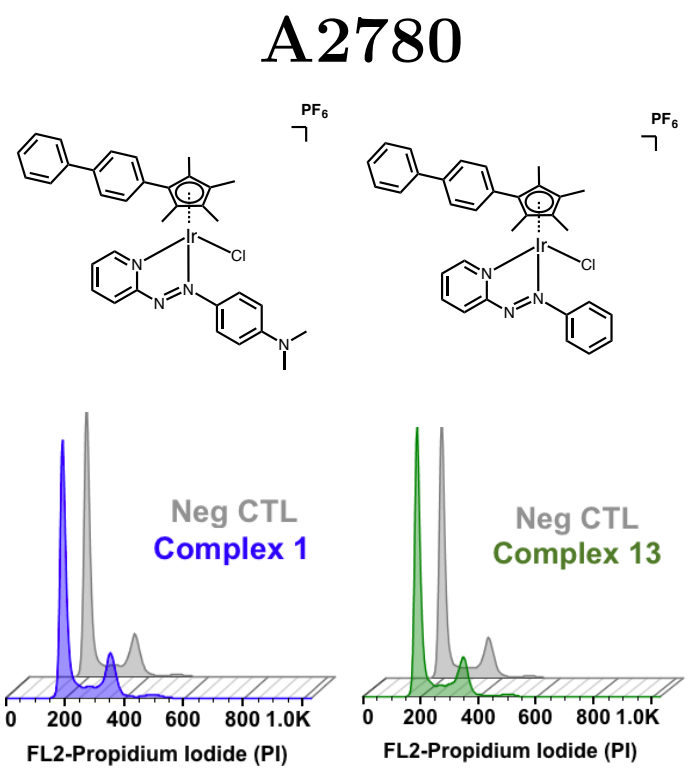

	G1-Phase	S-Phase	G2/M-Phase
Neg CTL	63.5 ± 0.6	16.5 ± 0.6	20.0 ± 0.3
Complex 1	61.4 ± 0.7 *	17 ± 1	21.8 ± 0.8
Complex 13	64.6 ± 0.3	17.0 ± 0.4	18.4 ± 0.1 **

Figure 4.22: Cell cycle analysis by flow cytometry of A2780 ovarian carcinoma cells exposed to complexes **1** (Left) and **13** (Right) for 24 h at IC_{50} concentrations at 310 K. Cells stained with Propidium iodide (PI). (Bottom) Table of % cell populations obtained from triplicate experiments. Statistical significance between cells exposed to complex vs. negative control was determined by two-sample independent Welch t-tests assuming unequal variance between populations with asterisks corresponding to $p \leq 0.05$ *, $p \leq 0.01$ **, $p \leq 0.001$ ***, $p \leq 0.0001$ ****.

Complex **1** induces a small but statistically significant reduction in the G_1-phase population, whereas complex **13** induces a more significant reduction in the G_2-phase population. No significant accumulation of cells in any phase was observed.

4.3.10.3 Apoptosis Induction

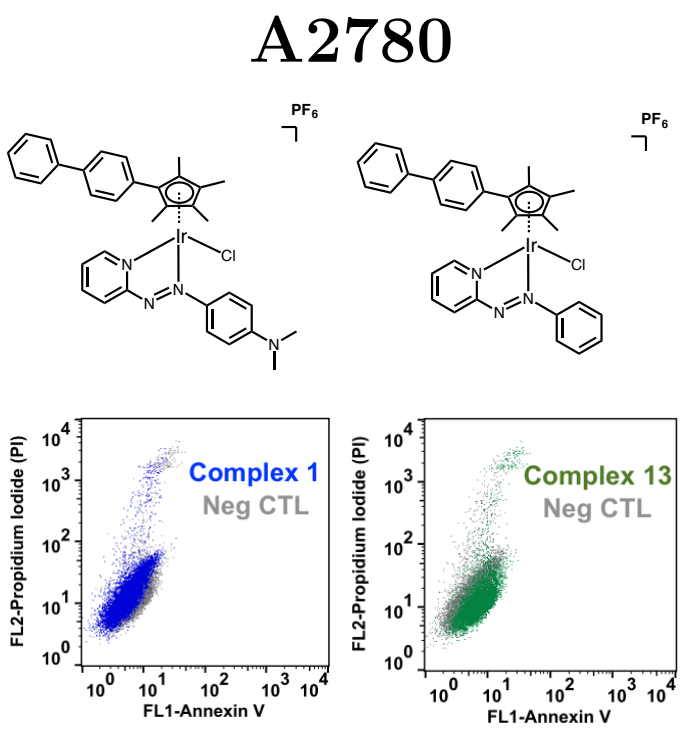

	Viable	Non-Viable	Early Apoptotic	Late Apoptotic
	FL1-FL2-	FL1-FL2+	FL1+FL2-	FL1+FL2+
Neg CTL	98.27 ± 0.09	1.73 ± 0.09	0	0
Complex 1	97.39 ± 0.04 ****	2.61 ± 0.04 ****	0	0
Complex 13	97.5 ± 0.2 *	2.5 ± 0.2 **	0	0

Figure 4.23: Measurement of apoptosis induction by flow cytometry of A2780 ovarian carcinoma cells exposed to complexes **1** (Left) and **13** (Right) for 24 h at IC_{50} concentrations at 310 K. Cells stained with Propidium iodide (PI). (Bottom) Table of % cell populations obtained from triplicate experiments. Statistical significance between cells exposed to complex vs. negative control was determined by two-sample independent Welch t-tests assuming unequal variance between populations with asterisks corresponding to $p \leq 0.05$ *, $p \leq 0.01$ **, $p \leq 0.001$ ***, $p \leq 0.0001$ ****.

Exposure to complex **1** for 24 h causes a significant increase in the population of non-viable cells without any visible induction of early or late-stage apoptosis. The same increase is seen for cells exposed to complex **13** but to a less statistically significant degree.

4.3.11 Interaction with Glutathione

Given that both complexes generate high levels of both ROS and SO in cells, it is likely that their MoA is linked to the level of oxidative stress. Many cancer cells counteract ROS level elevation by upregulation of cellular antioxidants such as glutathione (GSH). GSH is a redox-active tripeptide molecule composed of the amino acids glycine, cysteine and glutamate (Figure 4.24).[172]

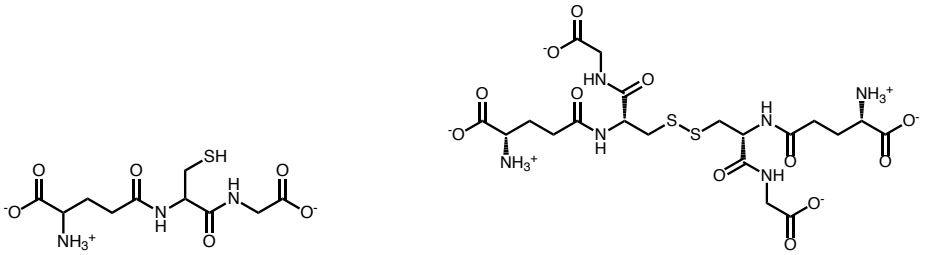

Figure 4.24: (Left) Glutathione in its reduced form (GSH). (Right) Glutathione in its its oxidised dimerised form (GSSG).

GSH is present in millimolar concentrations inside the cell and is involved in a multitude of metabolic pathways. Inactivation of anticancer therapeutics by GSH is common,[173] and increased levels of intracellular GSH is one of the mechanisms by which some cancers display resistance to CDDP.[154] To investigate whether GSH or its oxidised form glutathione disulphide (GSSG) interacts with complex **1** and **13**, 1:1 solutions of GSH/GSSG:complex were studied by ^{1}H-NMR (Figures 4.25 – 4.32) and LC-MS (Appendix Figures S31 – S39, pg. 304 – 312).

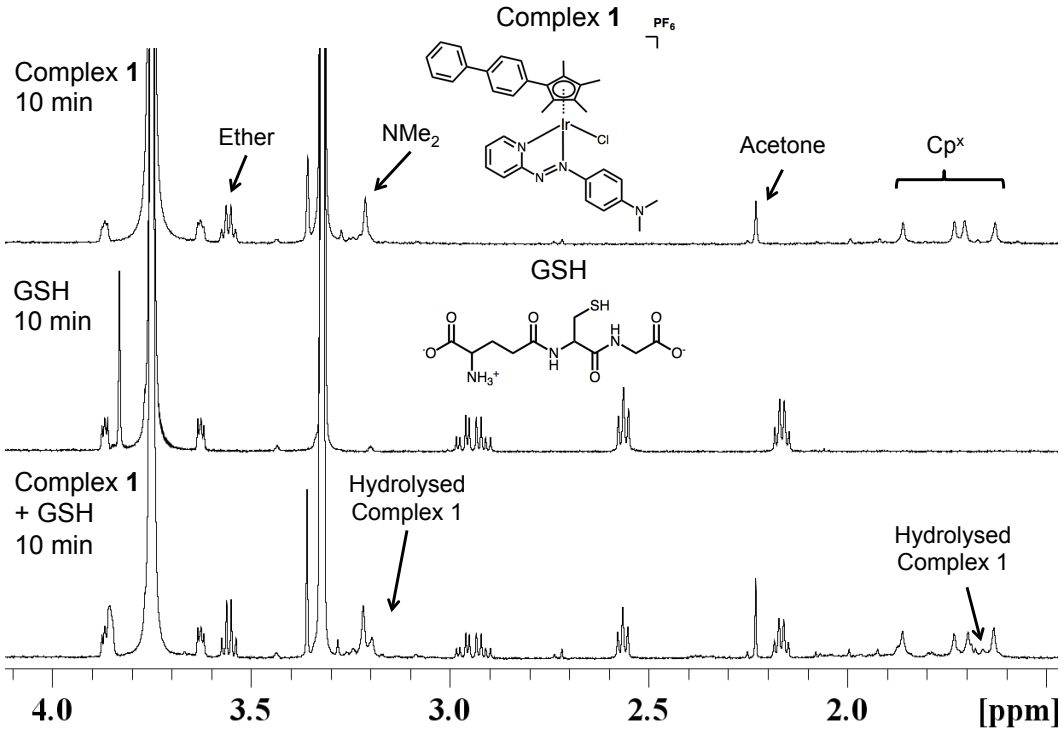

Figure 4.25: Aliphatic region of 600 MHz ^{1}H-NMR spectra of a 300 μM solution of complex **1** in 25% MeOD:D_2O, 0.1% 1,4-dioxane (v/v) at 310 K, unbuffered at pH 7 incubated with 300 μM GSH for 10 min. Traces of acetone/ether from the NMR tube are visible.

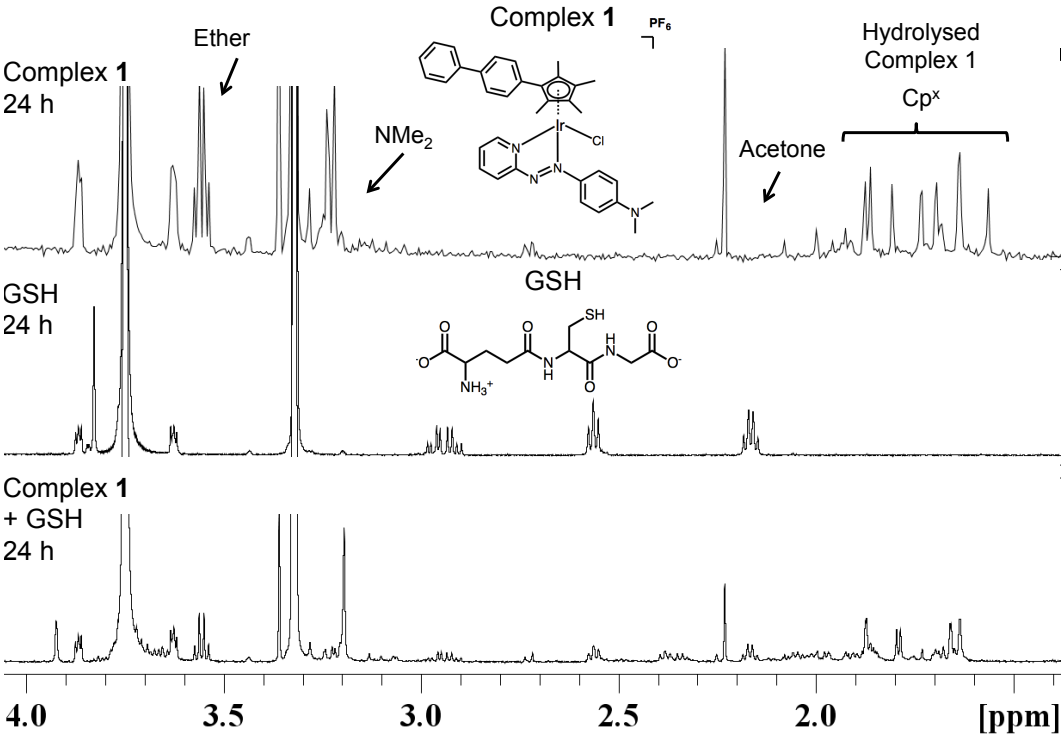

Figure 4.26: Aliphatic region of 600 MHz ^{1}H-NMR spectra of a 300 μM solution of complex **1** in 25% MeOD:D_2O, 0.1% 1,4-dioxane (v/v) at 310 K, unbuffered at pH 7 incubated with 300 μM GSH for 24 h. Traces of acetone/ether from the NMR tube are visible.

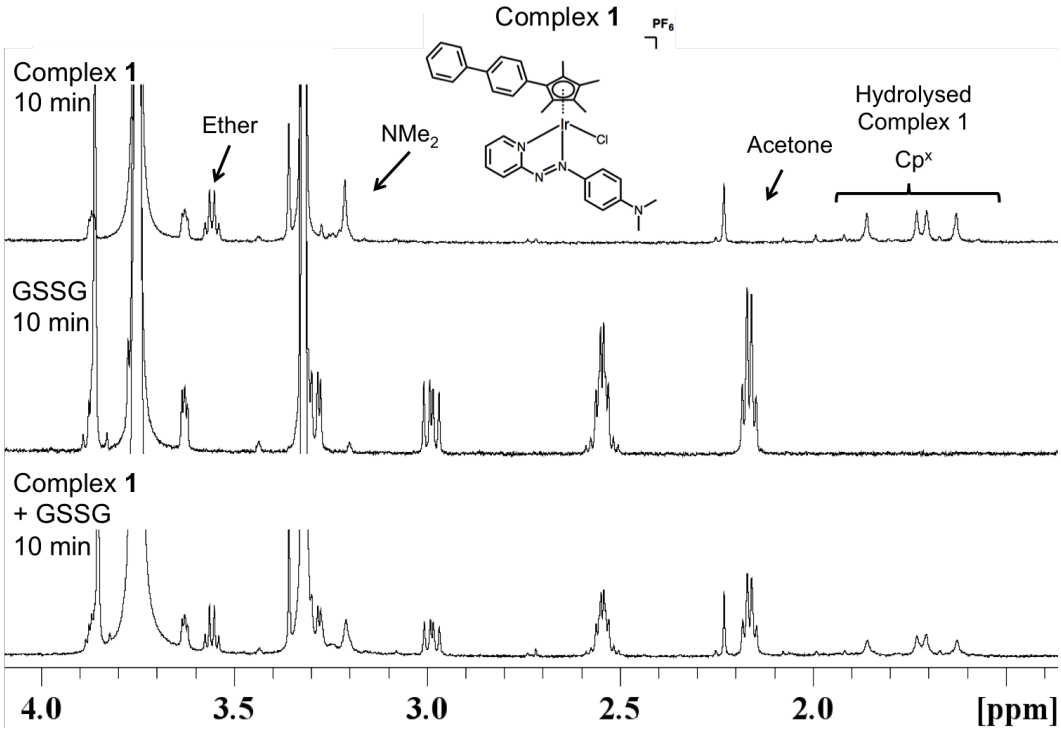

Figure 4.27: Aliphatic region of 600 MHz ^{1}H-NMR spectra of a 300 μM solution of complex **1** in 25% MeOD:D_2O, 0.1% 1,4-dioxane (v/v) at 310 K, unbuffered at pH 7 incubated with 300 μM GSSG for 10 min. Traces of acetone/ether from the NMR tube are visible.

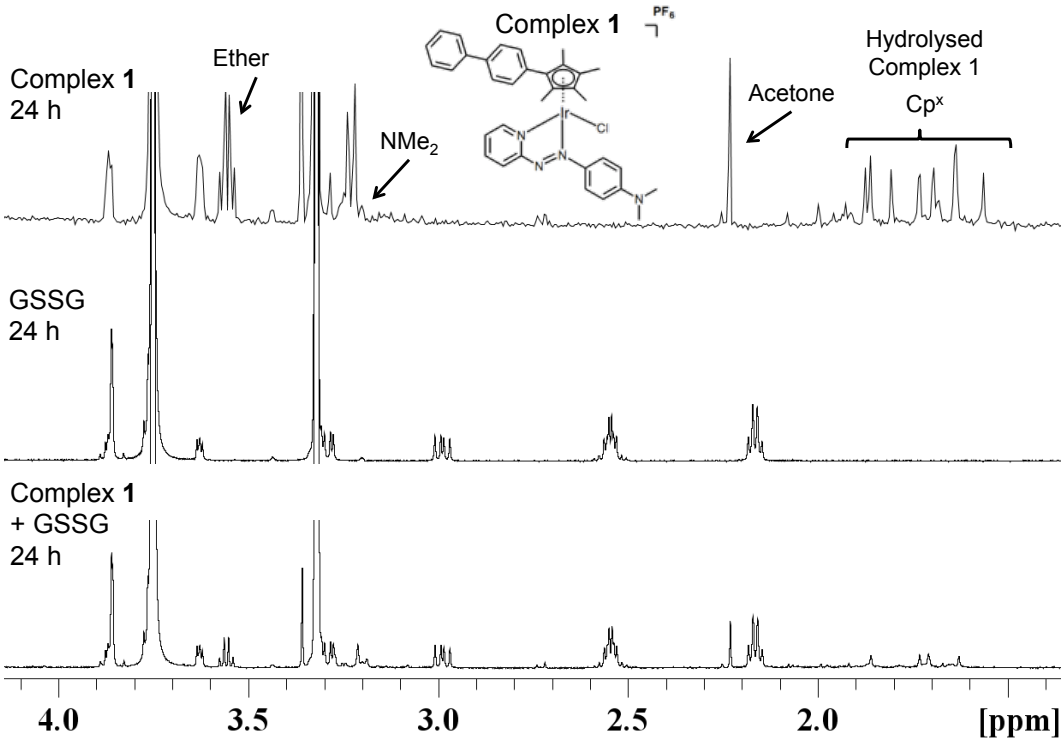

Figure 4.28: Aliphatic region of 600 MHz ^{1}H-NMR spectra of a 300 μM solution of complex **1** in 25% MeOD:D_2O, 0.1% 1,4-dioxane (v/v) at 310 K, unbuffered at pD 7 incubated with 300 μM GSSG for 24 h. Traces of acetone/ether from the NMR tube are visible.

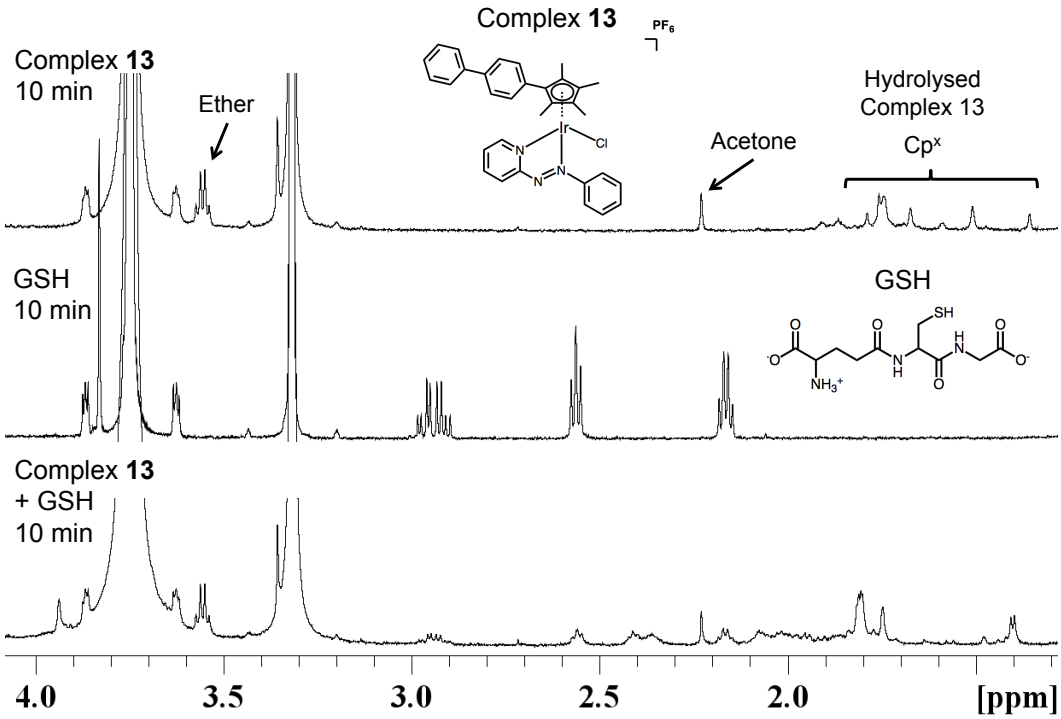

Figure 4.29: Aliphatic region of 600 MHz ^{1}H-NMR spectra of a 300 μM solution of complex **13** in 25% MeOD:D_2O, 0.1% 1,4-dioxane (v/v) at 310 K, unbuffered at pH 7 incubated with 300 μM GSH for 10 min. Traces of acetone/ether from the NMR tube are visible.

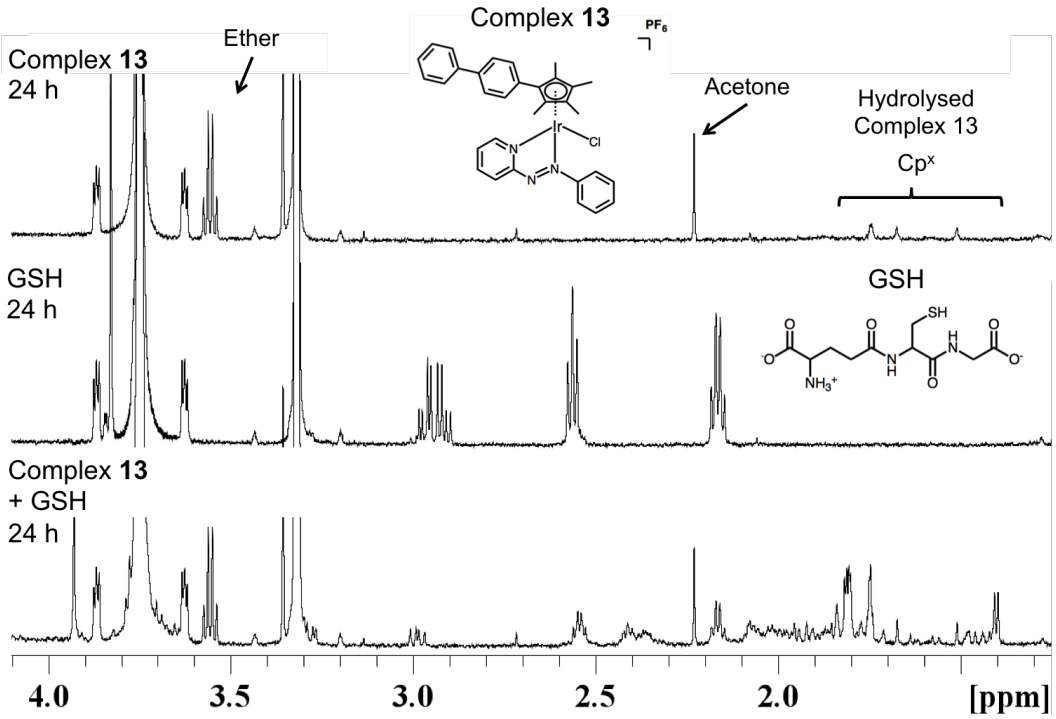

Figure 4.30: Aliphatic region of 600 MHz ^{1}H-NMR spectra of a 300 μM solution of complex **13** in 25% MeOD:D_2O, 0.1% 1,4-dioxane (v/v) at 310 K, unbuffered at pH 7 incubated with 300 μM GSH for 24 h. Traces of acetone/ether from the NMR tube are visible.

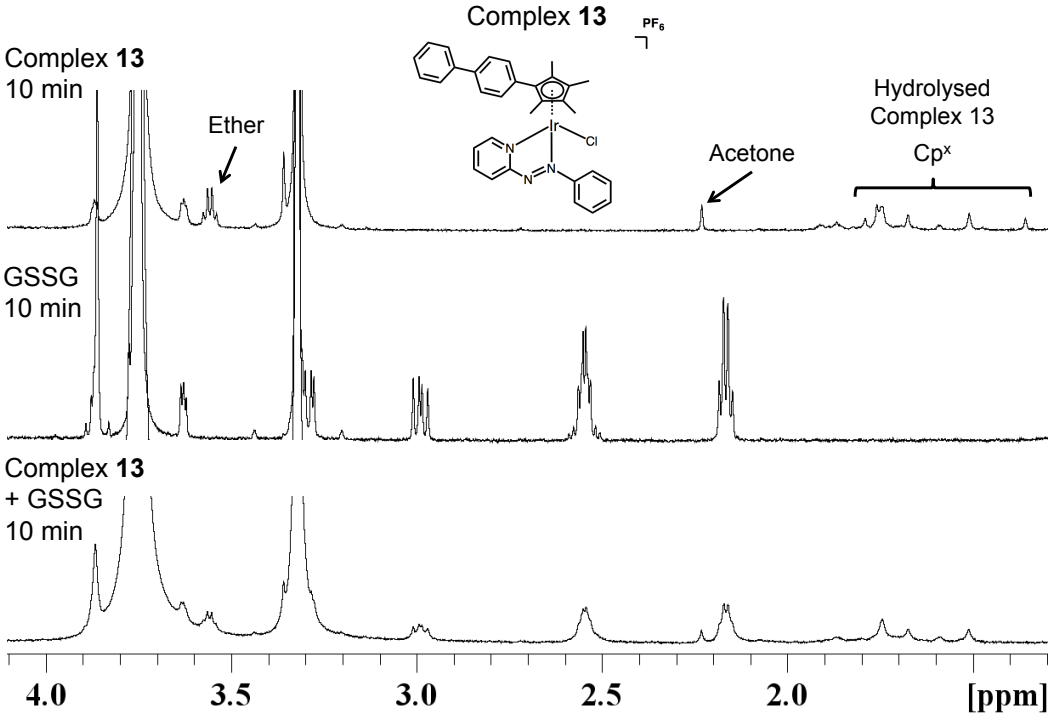

Figure 4.31: Aliphatic region of 600 MHz ^{1}H-NMR spectra of a 300 μM solution of complex **13** in 25% MeOD:D_2O, 0.1% 1,4-dioxane (v/v) at 310 K, unbuffered at pH 7 incubated with 300 μM GSSG for 10 min. Traces of acetone/ether from the NMR tube are visible.

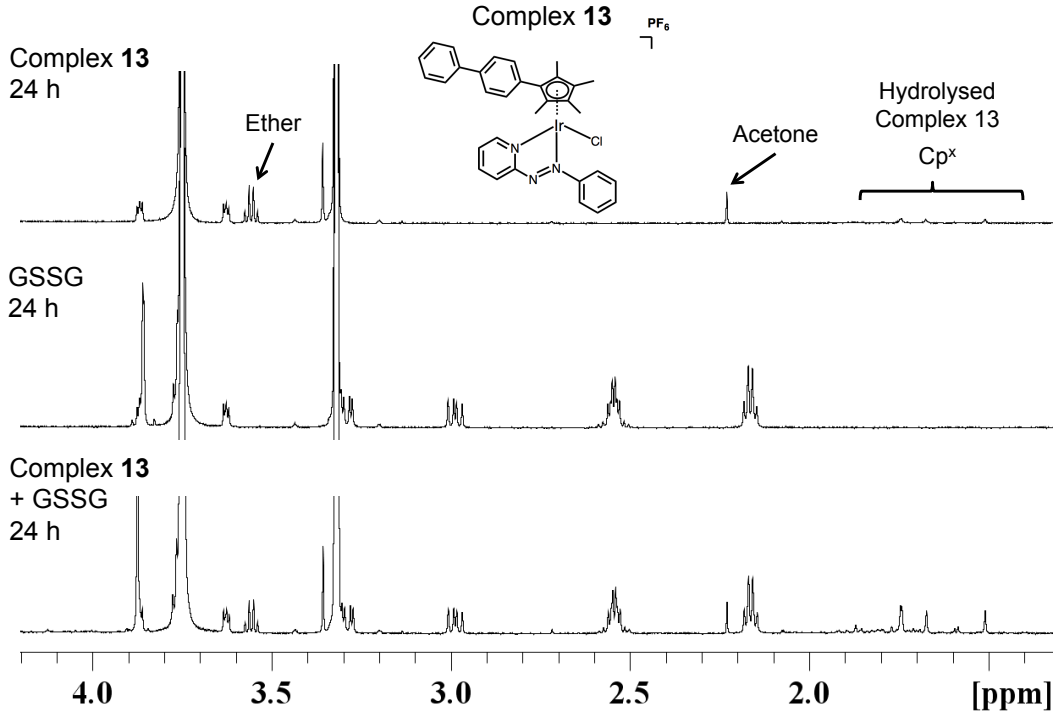

Figure 4.32: Aliphatic region of 600 MHz ^{1}H-NMR spectra of a 300 μM solution of complex **13** in 25% MeOD:D_2O, 0.1% 1,4-dioxane (v/v) at 310 K, unbuffered at pH 7 incubated with 300 μM GSSG for 24 h. Traces of acetone/ether from the NMR tube are visible.

In the LC trace for complex **1** a small peak (1.9% of total peak area integrals) corresponding to a GS adduct (**1-GS**) was observed, however the remaining peak corresponded to the adduct-free cation of complex **1** only. No adducts were seen of complex **13**. Some very small changes were seen in the ^{1}H-NMR spectra of both complexes when incubated with GSH for 24 h. No interaction of either complex with GSSG was observed by ^{1}H-NMR or LC-MS.

4.3.12 Effect of Redox Modulation on Anticancer Activity

The rate-limiting step of GSH synthesis in cells is the linkage of the cysteine and glutamic acid residue. This is catalysed by the enzyme γ-glutamylcysteine synthetase. The activity of this enzyme can be inhibited by L-buthionine-S,R-sulfoximine (L-BSO), leading to lower cellular GSH levels. N-Acetylcysteine (NAC) is a synthetic precursor to GSH, and so treatment with NAC will increase cellular GSH levels. Co-administration of organometallic complexes with L-BSO or NAC has previously been reported to alter cytotoxicity.[84,102,104,125,171] To investigate how modulation of the level of GSH affects the anticancer potency of complexes **1** and **13**, they were co-administered with 5 μM of either L-BSO or NAC and their cytotoxicities determined in EBV-positive OE19 oesophageal carcinoma and compared to the results for administration of complex only (Figure 4.33). This cell line was selected in order to compare IC_{50} values between EBV-negative and EBV-positive OE19 however the data for EBV-positive OE19 could not be fitted to Boltzmann sigmoidal curves at the concentrations tested and so was instead presented as complex concentration vs. % cell survival. Complex concentrations tested were ca. 0.01 μM – 10 μM and 0.01 μM – 100 μM for CDDP and determined exactly by ICP-OES and % cell survival normalised to negative controls as described in Chapter 2.

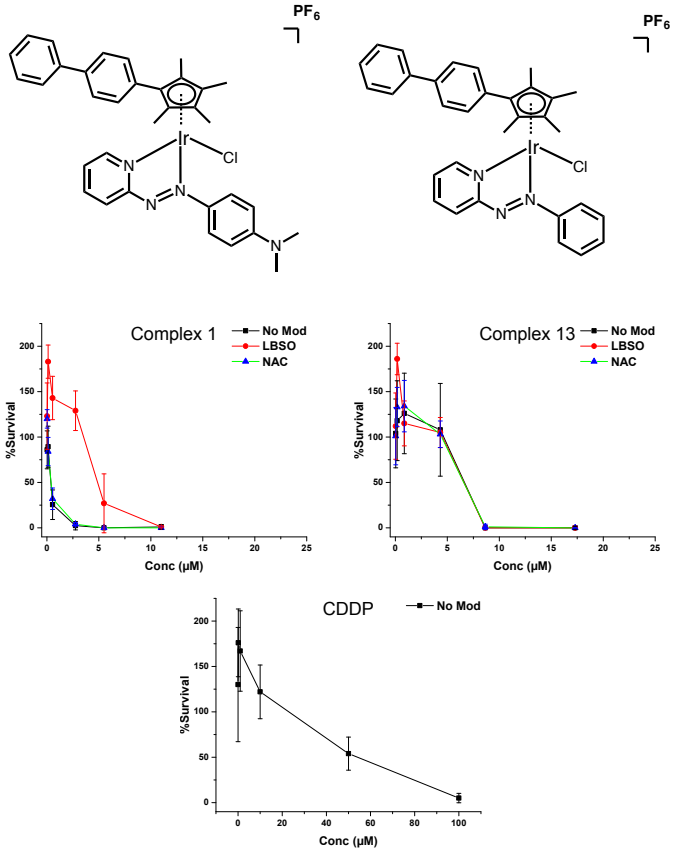

Figure 4.33: Cytotoxicities of complexes **1** and **13** and CDDP against EBV-positive oesophageal carcinoma cells, co-administered with 5 μM of L-BSO, NAC or neither. Drug treatment was for 24 h, followed by 72 h recovery period. Data and standard deviations were obtained from duplicates of triplicate experiments for cells co-administered with 5 μM of L-BSO, NAC. Data and standard deviations were obtained from quadruplicates of triplicate experiments for cells treated with no modulator (drug only).

Complex **1** displays superior cytotoxicity to both complex **13** and CDDP. Complex **13** shows higher cytotoxicity than CDDP.

Co-administration of complexes **1** or **13** with NAC has no effect on toxicity towards this cell line within the standard deviations of the replicates. Co-administration of complex **1** with L-BSO significantly reduces cytotoxicity whereas it has is no significant effect on the cytotoxicity of complex **13**.

4.4 Discussion

Discovery of the MoA and biological targets of a drug are important factors contributing to whether a new drug passes clinical trials. This work in this chapter has taken significant steps in revealing some of these mechanisms for the novel complexes **1** ([η^5-Cp^{xbiph}Ir(azpyNMe$_2$)Cl]PF$_6$) and **13** ([η^5-Cp^{xbiph}Ir(azpy)Cl]PF$_6$). Previous research on organoiridium complexes of similar structure to these has shown that they can have multiple target sites,[145] and possess a variety of possible MoAs including, amongst others, DNA intercalation,[158] disruption of cellular redox balance,[84] and NADH oxidation.[86] Based on the results presented here, and in Chapter 3, it is probable that complexes **1** and **13** utilise one or more of these to kill cancer cells. Considering the enormous heterogeneity of cancer as a disease, the development of drugs with polypharmacological MoAs may be a more effective way to combat the broad and complex range of cancers that exist, as opposed to single target therapeutics.

4.4.1 Intracellular Aquation

It is apparent that both complexes hydrolyse in aqueous solution (Figure 4.4, pg. 153) but are stable in organic solvents. This shows that upon addition of H_2O, the rate of the forward reaction, Ir-Cl to Ir-OH_2, is far greater than the backward reaction, Ir-OH_2 to Ir-Cl. That the complexes do not appear to hydrolyse to completion suggests that after 24 h an equilibrium point is reached in which some of the complex remains in its Ir-Cl form. Surprisingly, a third species is visible after 24 h in aqueous solution. While not confirmed, this may be an hydroxido-bridged dimer of the complex, which would explain why some peaks disappear after post-hydrolysis addition of NaCl (shift in equilibrium causing OH_2/OH species to convert back to Cl species) and some new peaks remain despite the increase in chloride concentration (OH-bridged iridium dimer). Hydroxido-bridged Cp* Ir dimers have been reported,[94] therefore formation of hydroxido-bridged dimers is a feasible hypothesis, although no ESI-MS peaks corresponding to such a dimer were observed. (Appendix

Figure S40, pg. 313) A larger molecule such as an iridium dimer could easily fragment, increasing the difficulty of observing its whole molecular ion in ESI-MS experiments. A softer ionisation technique such as Matrix-assisted laser desorption ionisation (MALDI) may be able to circumvent this problem. Formation of DMSO adducts is unlikely as no peaks corresponding to DMSO adducts were observed in ESI-MS spectra of DMSO:H_2O solutions of either complex.

Since the azpyNMe$_2$, azpy and Cp ligands have been shown to be non-cytotoxic to cancer cells,[126] and both complexes continue to display potent cytotoxicity, it is unlikely that breakdown of these complexes by loss of these ligands is occurring, and the emergent NMR peaks are likely due to loss of chloride and replacement by water. The observation of ESI-MS peaks corresponding to **1-OH** and **13-OH**, support this.

The pK_a value for the aqua adducts of complexes **1** and **13** could not be determined by UV pH titrations (Figure 4.10, pg. 162). However, alteration of the pH did induce some small changes in their UV spectra. This may be down to a complicated interplay between the equilibrium between Ir-Cl and Ir-OH_2/OH and that which exists between Ir-OH_2 and Ir-OH dependent on pH. Another possible explanation is that base addition, increasing the concentration of OH^-, further complicates the hydrolytic behaviour of the complexes. The formation of hydroxido dimers, if this is indeed occurring, could even further complicate the solution chemistry. It may also be possible to overcome these obstacles by carrying out NMR experiments at varying pH values. Nothing ws observed that could indicate deprotonation of ring methyls was observed in NMR spectra of either complex.

Hydrolysis of complex **1** is completely suppressed by 120 mM chloride and almost entirely suppressed by 4 – 104 mM chloride (Figures 4.4 and 4.5, pg. 153 and 154), suggesting that it will remain in the chloride-bound iridium form in cell medium (DMEM/RPMI), as medium contains 120 mM chloride. Upon reaching areas of the cell in which the chloride concentration is markedly lower, such as the nucleus, some hydrolysis may take place, however the majority of the complex would likely remain in the Ir-Cl form. This may result in non-

coordinative interaction with DNA, rather than direct coordination of the metal centre, such as that which is observed between CDDP and DNA.

That complex **13** hydrolysis is not suppressible by physiologically-relevant levels of chloride (Figures 4.6 and 4.7, pg. 155 and 156) indicates that it would likely hydrolyse in the cell nucleus. This could allow it to directly coordinate to DNA. It could, however, also hydrolyse in the cell cytosol. This may cause it to bind off-target molecules and could contribute to its lower potency relative to complex **1**.

Azopyridine ligands are strong π-acceptors and will withdraw electron density from the metal to some extent. The only difference between complexes **1** and **13** is the NMe_2 functional group on the azopyridine ligand. This, therefore, must be the reason behind the difference in hydrolytic behaviour between the two complexes. The electron donating effect of complex **1**'s NMe_2 group pushes electron density onto the Ir, which should weaken the Ir-Cl bond thereby promoting hydrolysis, however complex **1** hydrolyses less readily than complex **13**. Additionally, the previously reported complex **2** ($[\eta^5$-$Cp^{xph}Ir(azpyNMe_2)Cl]PF_6$) (structure in section 3.2.1) bearing the same $azpyNMe_2$ and chlorido ligands as **1** has been shown to be resistant to hydrolysis.[102] Density functional theory (DFT) calculations could be used to accurately determine the effect of the NMe_2 group on the Ir centre.

Conversely, in the case of complex **13**, the lack of the electron donating effect of the NMe_2 group may be altering the electronic state of the iridium to enough of a degree, such that binding of water is greatly favoured over chloride, and the presence of high levels of chloride does not shift the equilibrium enough to entirely prevent hydrolysis.

These results indicate that, in cells, complex **1** would exist predominantly in its chloride-bound form whereas most of complex **13** would be in its OH_2/OH-bound form. Therefore, complex **1** can still display nanomolar potency in multiple cell lines without activation by hydrolysis being necessary, unlike CDDP. This is especially interesting as it exhibits much lower cross-resistance than complex **13**. Previously reported precious metal-based complexes of similar structure have been shown to display cytotoxicity without hydrolysis.[126,145]

4.4.2 DNA Binding and Cleavage

Exploration of the DNA-interacting properties of the complexes has revealed some surprising differences between complexes **1** and **13**, despite their strong structural similarities. The effect of the difference in just one functional group between complexes **1** and **13** (NMe_2 vs. H) on their effects on DNA is large. Given that another highly similar complex, bearing both the extended cyclopentadienyl system, an N,N-chelated bidentate ligand and a monodentate chlorido ligand,[158] showed DNA intercalation, it was surprising that neither complex **1** nor **13** intercalates into DNA. While both can displace and inhibit EtBr binding to DNA (Figure 4.19, pg. 177), this is not proof of intercalation, as EtBr binding can be disturbed by other non-intercalative effects on the DNA, such as minor groove-binding. Furthermore, were intercalation occurring, the viscosity of DNA would increase upon complex addition, which it does not (Figure 4.18, pg. 176). Additionally, the UV-Vis spectra would likely have shown a red or blue shift for the peaks of the complex if they were intercalating into DNA, instead they remain at the same wavelengths (Figure 4.15, pg. 170). Furthermore, the LD signal would become more negative as intercalation would lengthen the DNA and increase its rigidity, instead, the opposite is observed (Figure 4.16, pg. 172). Thus intercalation with DNA is unlikely for either complex.

Complex **13** has been shown to coordinate directly to guanine at N7, forming a stable enough adduct as to persist after treatment with 8 M urea, which disrupts the hydrogen bonding between bases and would remove any complex not strongly bound to the oligonucleotide (Figure 4.14, pg. 167). CDDP is also coordinates to guanine and this similarity may be a contributing factor to the high cross-resistance of complex **13** with CDDP (Table 4.2, pg. 180), if this was the case, then they may have similar MoAs. However, this has only been observable in oligonucleotides and not in single nucleotides (Figure 4.13, pg. 165), although an oligonucleotide is a more representative model of cellular DNA than single nucleotides are. An even more representative system is ctDNA, in which CD and LD studies show a clear interaction with both complexes (Figures 4.16 and 4.17, pg. 172 and 174). The induction of a CD band by complex **1** proves its interaction with the DNA, and the LD signal

induced by complex **1** further supports this. Considering that intercalation and direct nucleotide coordination have been ruled out for complex **1** yet it can still interact with DNA and inhibit/displace EtBr (although DNA cleavage may also be playing a part in displacing EtBr), the most likely binding site for it is the DNA minor groove.

The differences in mechanism of DNA modification and cleavage must be due to the effect of the NMe_2 group. The electron donating effect of this group would make the iridium centre of complex **1** less positive than that of complex **13**, reducing its electrophilicity and possibly explaining its inability to strongly coordinate to the N7 of guanine. Complex **13** would therefore have a more electropositive centre allowing it to coordinate to N7 within 24 h. The mechanism of cleavage may be hydrolytic, by nucleophilic attack on the DNA phosphate backbone, with the metal acting as a Lewis acid activating water, hydroxide, or the phosphate group. The more electropositive centre of complex **13** may allow it to behave as a more effective Lewis acid resulting in its greater DNA cleaving ability.

Another possible explanation for the guanine adduct observed for complex **13**, but not complex **1**, may be due to the hydrolytic behaviour of the complexes. Complex **1** appears to be more resistant to hydrolysis than complex **13**, therefore complex **1** may remain in its chloride-bound form, rendering it unable to modify guanine. This, in fact, may also explain the difference in timescale over which the two complexes exert effects on DNA: Complex **1** interacts non-coordinatively with DNA inducing measurable changes and generating SSBs after only 10 min (Figure 4.20, pg. 178). Conversely, complex **13** shows little to no measurable effect on DNA after 10 min however, after 24 h, the magnitude of its DNA distorting effects, nuclease activity and binding strength are significantly superior to complex **1**. All DNA experiments were, however, carried out in chloride-free aqueous solution. Therefore complex **1** would be even less likely to hydrolyse in cells where chloride is present. If rapid hydrolysis of complex **13** is occurring, but not of complex **1**, then upon reaching the DNA/oligonucleotides, complex **1** would still be in its chloride-bound form, whereas complex **13** would be predominantly an aqua adduct.

Complex **1** exists as a cation in solution, therefore rapid noncoordinative interaction with negatively charged DNA molecules is unsurprising. Complex **13**-OH_2/OH may interact less readily with DNA in this way, exhibiting only minor noncovalent preassociation. Instead, over 24 h, **13**-OH_2/OH coordinates directly to guanine, likely by a mechanism involving loss of H_2O, similar to CDDP. Another reason why complex **1** preferentially binds to the minor groove may be its 3D structure, as shown in Chapter 3. The crystal structure shows a flatter, more planar bidentate ligand than that of complex **13**. This may fit in the DNA minor groove more readily.

Complex **13** can induce SSBs and DSBs in DNA even at very low concentrations, an ability not present in CDDP and only weakly in complex **1**, which produces SSBs when at high concentrations and does not generate DSBs. Unlike the drug etoposide, these complexes generate strand breaks in cell-free systems and thus do not rely on cell topoisomerases to do so. This nuclease activity may explain the concentration-dependent reduction of the CD, and LD DNA bands as cleavage of the DNA would significantly alter the DNA superstructure manifesting as a visible reduction in CD and LD bands as both the aligment and helicity of the DNA are disrupted by cleavage. This is in contrast to dichroism studies of CDDP with DNA, in which the intensity of the positive CD band of B-DNA at 275 nm is increased as a consequence of DNA modification by CDDP that reflects distortions in DNA of a nondenaturational nature.[174] Again, the explanation of the difference between the DNA-cleaving abilities of complex **1** and **13** may be their hydrolytic behaviour. If DNA cleavage requires, or is more easily facilitated by, direct coordination of the complex, then complex **13**'s ready and rapid hydrolysis would favour direct DNA coordination and cleavage by either a hydrolytic or oxidative mechanism.[175] Additionally, both complexes generate ROS/SO in cells which could be partially responsible for DNA cleavage, although in Chapter 3 it has been shown that neither produce H_2O_2 in cell-free systems.

4.4.3 Antiproliferative Activity

That both complexes exhibit such potent anticancer activity over a range of cancer cells of different tissue types is encouraging. The more potent a complex is, the lower the dose that can be given to patients to treat the cancer. Additionally, the high selectivity of complex **1** ([η^5-Cp^{xbiph}Ir(azpyNMe$_2$)Cl]PF$_6$) for A2780 vs. MRC-5 normal fibroblasts indicates its potential for lower side-effects and dose-limiting organ toxicity in patients. Current Pt-based drugs are facing a number of clinical difficulties, including dose-limiting organ toxicity[143] and other side effects caused by CDDP-induced damage to normal proliferating cells.[142] In addition, many cancers exhibit both acquired and intrinsic CDDP-resistance. Complex **1** provides a promising example of how an organoiridium complex can exceed the potency, selectivity, and resistance profile of CDDP. Complex **1** is significantly more potent (A2780 IC$_{50}$ = 95 nM) and selective (36×) than many other reported precious metal-based complexes in the same cell lines under the same conditions. These include: CDDP (A2780 IC$_{50}$ = 1,200 nM, 14× selective), the highly potent and selective organoiridium complex ZL105 ([η^5-Cp^{xbiph})Ir(2-phenylpyridine)pyridine]PF$_6$, A2780 IC$_{50}$ = 120 nM, 13× selective)[84] and the highly potent and selective organoosmium complex FY26 ([η^6-p-cymene)Os(azpyNMe$_2$)I]PF$_6$) (A2780 IC$_{50}$ = 160 nM, 28× selective).[171] This is extremely promising for complex **1**.

4.4.4 Glutathione and Redox Modulation

After activation, CDDP is susceptible to deactivation by glutathione (GSH), as the platinum centre binds strongly and irreversibly to the thiolate sulphur of GSH and so can no longer modify DNA.[176] Additionally, higher levels of glutathione are often present in CDDP-resistant cancer cells.[177,178] That complex **1** is more resistant to hydrolysis may contribute to its low level of interaction with glutathione. However, complex **13** does not appear to interact with glutathione to any extent, even in a chloride-free system, hence these complexes both seem to be resistant to inactivation by glutathione. The relative unreactivity of both complexes with equimolar amounts of GSH is encouraging, as

they are more likely to be able to overcome GSH-based resistance mechanisms in cancer cells, especially since many previously reported organoiridium complexes with monodentate chlorido ligands are susceptible to rapid GSH binding and possibly subsequent deactivation.[101] Resistance to deactivation by GSH may partially explain the high potency of complex **1** against A2780cis. It is somewhat surprising that complex **13** does not interact with GSH, as it displays high cross-resistance with CDDP. This indicates that one or more of the other mechanisms of CDDP resistance are responsible for the lower potency of complex **13** in A2780cis.

Neither increasing, nor decreasing, the levels of cellular GSH by L-BSO or NAC appears to significantly affect the potency of **13**, however co-administration with L-BSO surprisingly reduces the cytotoxicity of complex **1**. While this is in contrast to many previously reported precious metal-based complexes, redox modulation has not previously been carried out on organoiridium azopyridine complexes. A possible explanation for the reduction of complex **1**'s potency by L-BSO is that its MoA is somehow reliant on the presence of GSH. That the activity of complex **1** is unaffected by NAC correlates with the fact that it shows significant potency in A2780cis, a cell line resistant to CDDP, as one of the known mechanisms by which it resists CDDP's cytotoxic effect is by increasing GSH levels. These results are also further supported by both complexes' observed low/unreactivity to GSH in ^{1}H-NMR spectra (Figures 4.25 – 4.32. pg. 186 – 193) and LC-MS experiments (Appendix Figures S31 – S39, pg. 304 – 312). L-BSO modulation has been shown to be a way of increasing potency and selectivity,[171] however, complex **1** is already highly potent and selective. Resistance to inactivation by GSH, as well as the retention of potent antiproliferative activity in cells when co-administered with NAC, increasing the cellular GSH levels, are highly desirable traits and promising results for both complexes.

4.4.5 MoA Investigations

Mechanistic insights into an organoiridum complex of similar structure showed a correlation with agents with oxidative stress-based MoAs.[179] Both complexes

induce a significant ROS and SO response in A2780 after 24 h (Figure 4.21, pg. 182). Cell mitochondria are a major source of both ROS and SO.[112] Therefore, it is possible that both complexes affect cell mitochondria. The mitochondria are primarily negatively-charged organelles, and so considering that both complexes exist as cations, the targeting of a proportion of these complexes to mitochondria is plausible. Os complexes bearing structural similarities to complexes **1** and **13** have recently been shown to do so.[132] Additionally, A2780 cells harbour mutations in their mitochondrial DNA which translate into defects in NADH dehydrogenase, an important enzyme in the mitochondrial respiratory chain.[124] This may be contributing to the extremely high cytotoxicity of complex **1** to A2780. These results are further supported by those in Chapter 3, showing ROS/SO generation by complex **1** in OE19 and SUNE-1 cells, in addition to depolarisation of the mitochondrial membrane potential by complex **1** in OE19. This impaired capacity of cancer cells to respond to ROS insults relative to healthy cells highlights a way to selectively target and kill cancer cells with these organoiridium complexes.

CDDP has been shown to reduce the % population of cells in the G1-phase in A2780 cells after 24 h exposure by inducing S-phase arrest.[145] Complex **1** induces no significant increase in any cell population (Figure 4.22, pg. 183), indicating that there is no significant cell cycle arrests caused after 24 h exposure, thus exhibiting a different effect on the cell cycle to CDDP and other precious metal-based complexes bearing structural similarities.[145] Complex **13** induces a more significant reduction in the G2/M population, however, there is no significant accumulation of cells in any other phase. CDDP is known to induce significant S-phase arrest, therefore these results support a different MoA to CDDP for these complexes.

Complex exposure appears to induce low levels of cell necrosis in the first 24 h (Figure 4.23, pg. 184), with no visible induction of apoptosis, mirroring the results for complex **1** in OE19 and SUNE-1 described in Chapter 3. Similar results are observed in previous work on highly similar complexes, however a wave of necrosis after 24 h is followed by apoptosis induction after 48 h.[120] Therefore, it is likely that the majority of cell death occurs 48-72 h after drug exposure. This correlates with the high level of cytotoxicity determined by

the antiproliferative assays in which the cells are given 72 h to recover before cell survival percentages are determined. It is possible that these complexes do not exert their primary MoA until > 24 h after exposure. Since there is no significant accumulation of cells in the sub-G1 phase of the cell cycle, which would be indicative of apoptotic cell death, it is unsurprising that no induction of apoptosis is seen here, at least in the 24 h timeframe measured. Therefore, either the complexes take > 24 h to induce apoptosis or cell cycle arrest, or they do not at any point. In either case, both display a very different cytotoxic profile to CDDP. This is encouraging, as cancers resistant to CDDP are best treated by drugs which attack them in different ways.

4.5 Conclusions

In conclusion, these organoiridium anticancer complexes show very high potency against a variety of cancer cell lines, with complex **1** ([η^5-Cp^{xbiph}Ir(azpyNMe$_2$)Cl]PF$_6$) showing selectivity exceeding that of CDDP, as well as other highly potent and selective precious metal-based drugs, in addition to considerably lower cross-resistance with CDDP than complex **13** ([η^5-Cp^{xbiph}Ir(azpy)Cl]PF$_6$).

A single small change in the bidentate ligand of these complexes has a profound effect on not only their level of potency, but also the mechanism by which they interact with DNA and kill cells. Polypharmacology is probable for both complexes including cancer cell death induced by DNA modification and cleavage, and disruption of cellular redox balance by ROS and SO production.

The NMe$_2$ group appears to be of vital importance to the potency and MoA of the complex. The electon-donating effect of the group results in a complex that is more inert to hydrolysis, rapidly binds the DNA minor groove, is more potent against various cancers, selective, and less cross-resistant. The guanine-binding azpy complex **13**, is a more effective DNA cleaver, induces higher ROS and SO, and is unreactive to GSH.

The results in this chapter further elucidate the MoAs and anticancer proper-

ties of organoiridium azopyridine complexes, in addition to revealing how the para-group on bidentate ligand can determine the MoA. These results show that complex **1**, in particular, holds great promise as an anticancer therapeutic, warranting *in vivo* experiments to determine anticancer potency and selectivity in a model more representative of human cancer.

Chapter 5

Complexes Bearing azpyOH Bidentate Ligands

5.1 Introduction

The azpyOH ligand has previously been utilised as a bidentate ligand in organoosmium and organoruthenium systems, generating potent anticancer complexes.[104,126] The potential of this ligand in organoiridiums, however, has not been previously explored.

The results in Chapter 3 show that azpyOH complexes **5** − **10** are highly potent and more hydrophilic in comparison with the other organoiridiums studied. These are both highly desirable properties for anticancer therapeutics. Dissolution of the complex in purely aqueous solution remains another obstacle hampering the elevation of organoiridium complexes into clinical drugs, as the majority of complexes studied in Chapters 3 and 4 have low water solubility. Many such complexes require the presence of DMSO to ensure the complex is fully dissolved in preparation for biological experiments. The azpyOH complexes, however, may be the key to overcoming this obstacle.

In this chapter, the properties of novel azpyOH anticancer complexes described in Chapter 3 are investigated to further understand the impact of the various

ligands on the properties, potency, and MoAs of organoiridium complexes. The effect of the halide and counterion on water solubility is explored, as well as the relationship between the complex structure and the pK_a of the azpyOH hydroxyl group. The antiproliferative activity of the complexes are investigated in a larger panel of cell lines including CDDP-resistant ovarian carcinoma, and MoA investigations are made into the complexes' ability to interact with DNA, generate ROS and SO, depolarise mitochondria, and induce apoptosis. The toxicity of two azpyOH complexes are compared in a zebrafish model, to demonstrate the effect of the halido ligand on *in vivo* toxicity.

5.2 Experimental Methods

5.2.1 pK_a Determination by UV-Vis Spectrophotometry

The pK_a values of hydroxyl groups in complexes were determined by addition of μL amounts of either dilute perchloric acid in acetic acid or a weak solution of KOH to a solution of complex in 5% DMSO:H_2O or H_2O and the changes monitored by UV-Vis spectroscopy. Changes in absorbance maxima over different pH values were plotted and a sigmoid curve fitted using a Maxwell-Boltzmann curve fitting algorithm and the midpoint calculated to determine the pK_a.

5.2.2 Linear Dichroism

Stocks of complexes were prepared in HPLC-grade acetonitrile and added to the DNA in 10 mM phosphate buffer solution so that the final solution comprised of 5% acetonitrile. This was kept constant for all samples in the titration series. The concentration of the DNA was kept at 90 μM and the complex concentration increased from 0 – 90 μM in 10 μM increments. Complexes were incubated with DNA at 310 K for 24 h.

LD spectra were measured over 190 – 350 nm range at a couette spin speed of 3,000 rpm, using a bandwidth of 2 nm, and a data pitch of 0.2 nm. Scanning speed used was 100 nm/min, with a response time of 2 s. Baseline spectra of an appropriate buffer were recorded for LD. Baseline spectra for each of the LD samples were recorded with spinning turned off. All measurements were carried out at 310 K before LD measurements were taken.

5.2.3 Circular Dichroism

Stocks of complexes were prepared in HPLC-grade acetonitrile and added to the DNA in 10 mM phosphate buffer solution so that the final solution com-

prised of 5% acetonitrile. This was kept constant for all samples throughout the experiment. The concentration of DNA was kept at 90 μM throughout and the complex:DNA ratio varied from 1:1 to 1:3. Complexes were incubated with DNA at 310 K for 24 h before CD measurements were taken. CD measurements were taken from 180 nm – 800 nm. A scanning speed of 100 nm/min was used, with a response time of 1 s, a bandwidth of 2 nm, a data pitch of 0.2 nm at 310 K with 9 accumulations taken for each data point. Baseline spectra of an appropriate buffer were recorded for CD.

5.2.4 Toxicity in Zebrafish

Zebrafish experiments were carried out at the University of Warwick School of Life Sciences using Singapore wild-type zebrafish embryos. Maintenance of animals was carried out in accordance with ASPA1986 and approved by the University Ethical Review Committee. Zebrafish were housed in 3.5 L tanks and checked daily or as required. Zebrafish were fed 2 – 4 times a day and daily checks were carried out to ensure water quality was maintained. Fish were mated once a week starting at two pairs per 1 L breeding tank. Embryos were collected and transferred to petri dishes. New, healthy zebrafish embryos were harvested and seeded in 24-well plates at one embryo/well. A serial dilution of six concentrations of the complex to be tested was added to 20 of these wells with the remaining 4 used as negative controls. DMSO at an identical % to that present in the complex solutions was used as the solvent control and 3,4-dichloroaniline used as the positive control. Embryos incubated at 301.5 K for 96 h after which zebrafish % survival was assessed by embryo coagulation, visible heartbeat, tail detachment and somite formation. Experiments were carried out in duplicates of triplicates. Complex concentrations were corrected by ICP-OES, used to determine the concentration of Ir in the drug stocks and % survival was plotted against complex concentration. Boltzmann sigmoidal curves were fitted to determine the LC_{50} values and standard deviations. Zebrafish maintenance carried out by Ian Bagley and *In vivo* toxicity experiments were carried out by Hannah Bridgewater and Dr. James P. Coverdale under the guidance of Dr. Karuna Sampath at the University of

Warwick School of Life Sciences.

5.2.5 Water Solubility Determination

A saturated solution of the complex was prepared by the addition of complex to DDW, followed by sonication for 1 h at ambient temperature. This was repeated until visible solid remained in the solution after sonication. The mixture was then filtered through glass microfibre filter paper and celite. The resulting filtrate was analysed by UV-Vis spectrometry.

5.3 Results

5.3.1 pK_a Determination

The protonation/deprotonation of the para-OH group on the phenyl ring of azpyOH complexes has a large effect on the level of electron density in the bidentate ligand, such that a dramatic colour change occurs between yellow and purple when the solution pH exceeds/deceeds the pK_a of the hydroxyl hydrogen. Not only does the loss of a proton affect the electronic state of the complex, but also the overall charge. Since the complexes were synthesised as cations paired with a negatively charged counterion, the loss of a proton leaves them as neutral complexes. Global charge can have a significant impact on the behaviour and potency of a complex, therefore, the pK_a values of relevant hydrogens in the complexes were determined by UV-Vis spectroscopy (Figures 5.1 and 5.2).

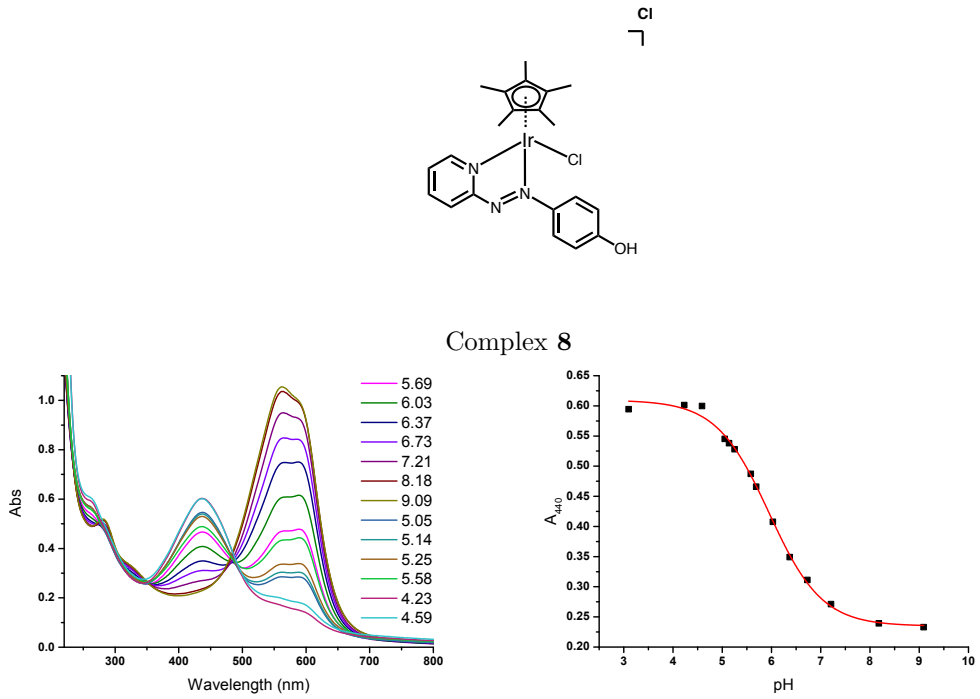

Figure 5.1: (Left) UV spectra of a pH titration of complex **8** in H_2O. Each line represents the spectrum at a particular pH value. (Right) A Boltzmann sigmoidal curve fitted to a plot of pH vs. absorbance at a maximum to determine pK_a.

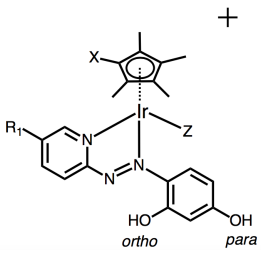

Complex	Structure	pK_{a1} (para OH)	pK_{a2} (ortho OH)
5	$[(Cp^{xbiph})Ir(azpyOH)Cl]PF_6$	5.52 ± 0.08	*n/a*
6	$[(Cp^{xph})Ir(azpyOH)Cl]PF_6$	5.88 ± 0.01	*n/a*
7	$[(Cp^*)Ir(azpyOH)Cl]PF_6$	5.88 ± 0.02	*n/a*
8	$[(Cp^*)Ir(azpyOH)Cl]Cl$	5.99 ± 0.02	*n/a*
9	$[(Cp^*)Ir(azpyOH)I]PF_6$	6.50 ± 0.02	*n/a*
10	$[(Cp^*)Ir(azpyOH)I]I$	*n.d.*	*n/a*
11	$[(Cp^{xbiph})Ir(azpy(OH)_2)Cl]PF_6$	*n.d.*	*n.d.*
12	$[(Cp^*)Ir(azpy(OH)_2)Cl]PF_6$	4.79 ± 0.05	9.80 ± 0.04
19	$[(Cp^{xbiph})Ir(Brazpy(OH)NEt_2)Cl]PF_6$	*n/a*	6.78 ± 0.06

Figure 5.2: The pK_a values of OH groups in complexes determined by pH titration and analysed by UV-Vis spectroscopy. Boltzmann sigmoidal curve fitted to determine pK_a. Error obtained from curve-fitting algorithm rather than experimental replicates. (*n/a* = not applicable. *n.d.* = not determined.)

Interestingly, the pK_a values for the hydroxyl hydrogens of Cp^{xph} complex **6** and its Cp* analogue, complex **7**, are identical, whereas their Cp^{xbiph} analogue, complex **5**, has a lower pK_a. These are also comparable with similar Os and Ru complexes bearing the same azpyOH ligand.[104] Complexes **7** and **8** have differing pK_a values despite only differing in counterion. The iodido complex **9** has a significantly higher pK_a value than its chlorido analogue, complex **7**. The para hydroxl hydrogen of azpy$(OH)_2$ complex **12** has a much lower pK_a than any of the azpyOH complexes investigated, however, the pK_a of its ortho hydroxyl hydrogen is far higher. The pK_a value of the ortho hydroxyl hydrogen of Brazpy(OH)NEt_2 complex **19** is lower than that of the ortho hydroxyl hydrogen of azpy$(OH)_2$ complex **12**.

5.3.2 Water Solubility

Whilst many advances have been made in drug formulation and delivery systems, high water solubility remains a very desirable factor for drug candidates. Many of the complexes in this work have very low water solubility, requiring the presence of DMSO for biological experiments. Further synthesis experiments were therefore carried out to improve the water solubility without sacrificing complex anticancer potency. To achieve this, complexes were synthesised with alternative counterions and the amount of solid complex required to saturate a solution of 18.2 MilliQ water at 298 K after 10 min sonication recorded.

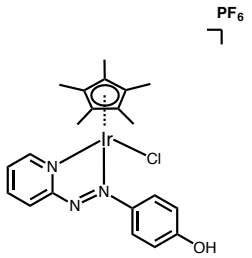

Complex **7**

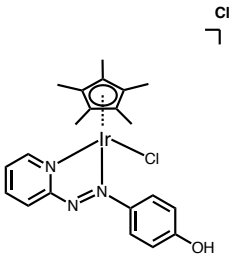

Complex **8**

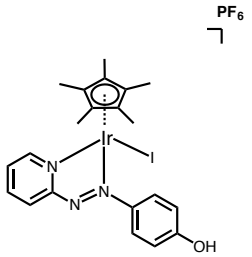

Complex **9**

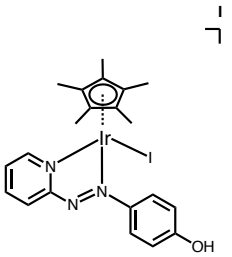

Complex **10**

Solutions of complexes **7** and **9** bearing the PF_6 counterions became saturated at < 2 mg complexes, even after sonication. Solutions of complexes **8** and **10**, chloride and iodide counterion analogues of complexes **7** and **9**, remained unsaturated even after 30 mg of complex was dissolved. Quantitative ICP-OES studies into the effect of the counterion on complex solubility are warranted.

5.3.3 Aquation Studies

As previously mentioned in Chapters 3 and 4, organoiridium complexes bearing azopyridine bidentate ligands and monodentate chlorido ligands can undergo hydrolysis at the Ir-Cl bond (Figure 5.3). This has been shown to have implications for potency and MoA. Hydrolysis is also dependent on the chloride concentration, which is known to vary in different cellular compartments. To replicate the chloride concentration in cell medium, experiments were repeated in 120 mM [Cl] solution.

Due to the limited water solubility of many of the complexes in this work, 10% DMSO was used to augment complex solubility in the *in vitro* experiments. DMSO has been known to detrimentally affect the anticancer activity of chemotherapeutics such as CDDP.[180] To examine whether this is true for these complexes, their stability in DMSO was examined by ^{1}H-NMR (Appendix Figure S21, pg. 292 – 294). Spectra of all complexes were identical both 15 min, and 19 days after sample preparation, and no DMSO adducts were detected by ESI-MS experiments.

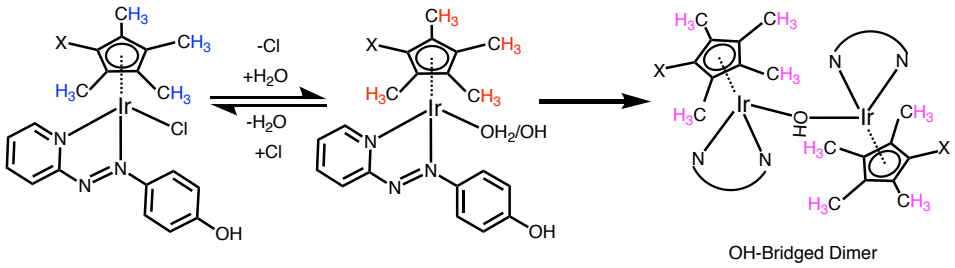

Figure 5.3: Proposed hydrolysis equilibrium for the complexes studied in this work. Aquation monitored by following the chemical shift of ^{1}H-NMR peaks corresponding to Cp^{x} ring methyl hydrogens for complexes **5** – **10** coloured above.

To investigate whether changing the Cp system or halide bound to the iridium centre of azpyOH complexes affects hydrolysis, solutions of complexes **5** – **10** were monitored over 24 h by ^{1}H-NMR in 10% d_6-DMSO:D_2O, 0.1% 1,4-dioxane at 310 K (Figures 5.4 – 5.9) and the extent of hydrolysis calculated by the peak integrals (Table 5.1).

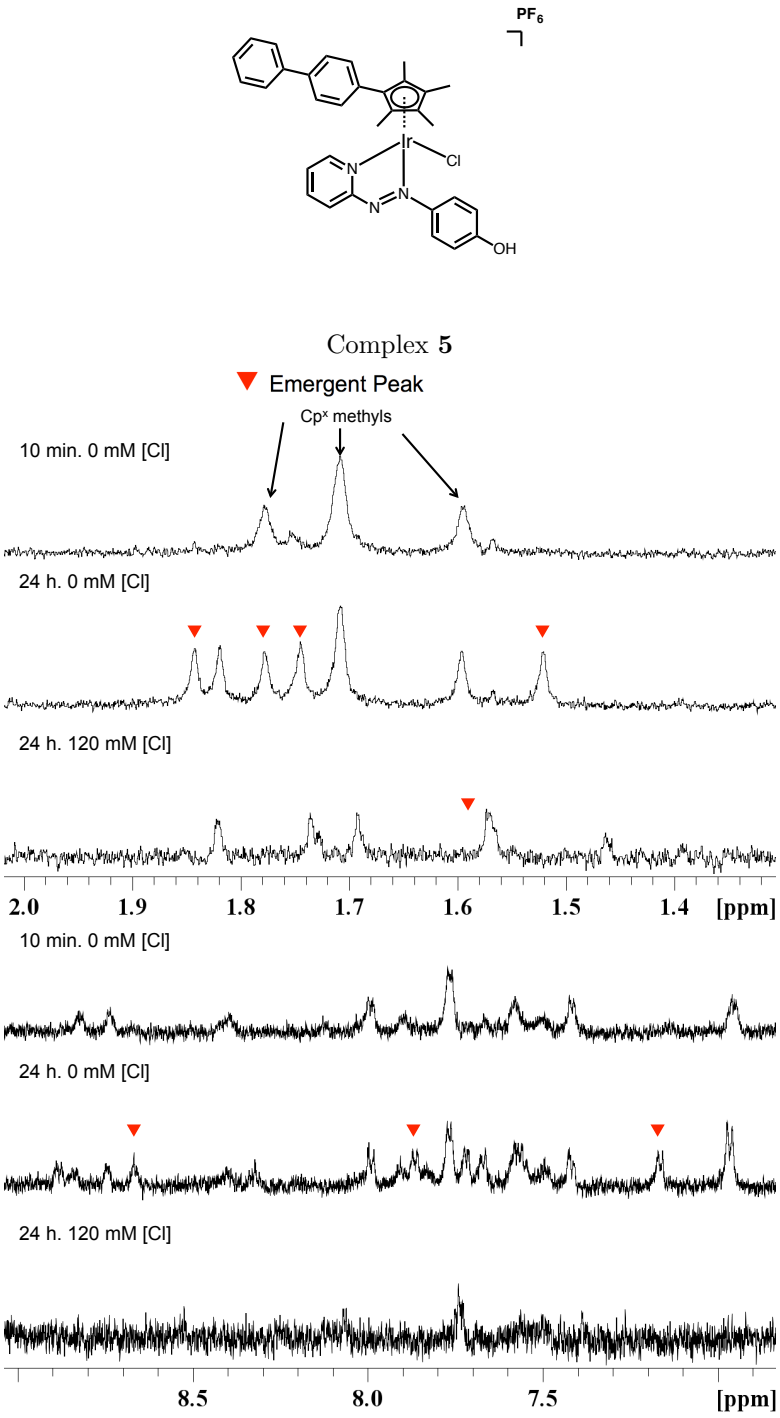

Figure 5.4: Hydrolysis of complex **5** studied by 600 MHz ^{1}H-NMR spectra of a 100 μM solution of complex **5** in 10% d_6-DMSO:D_2O, 0.1% 1,4-dioxane (v/v) at 310 K, unbuffered at pD 8. Spectra shown 10 min after sample preparation, 24 h after sample preparation, and 24 h after sample preparation in 120 mM NaCl solution. Emergent peaks not corresponding to original complex denoted by red arrows.

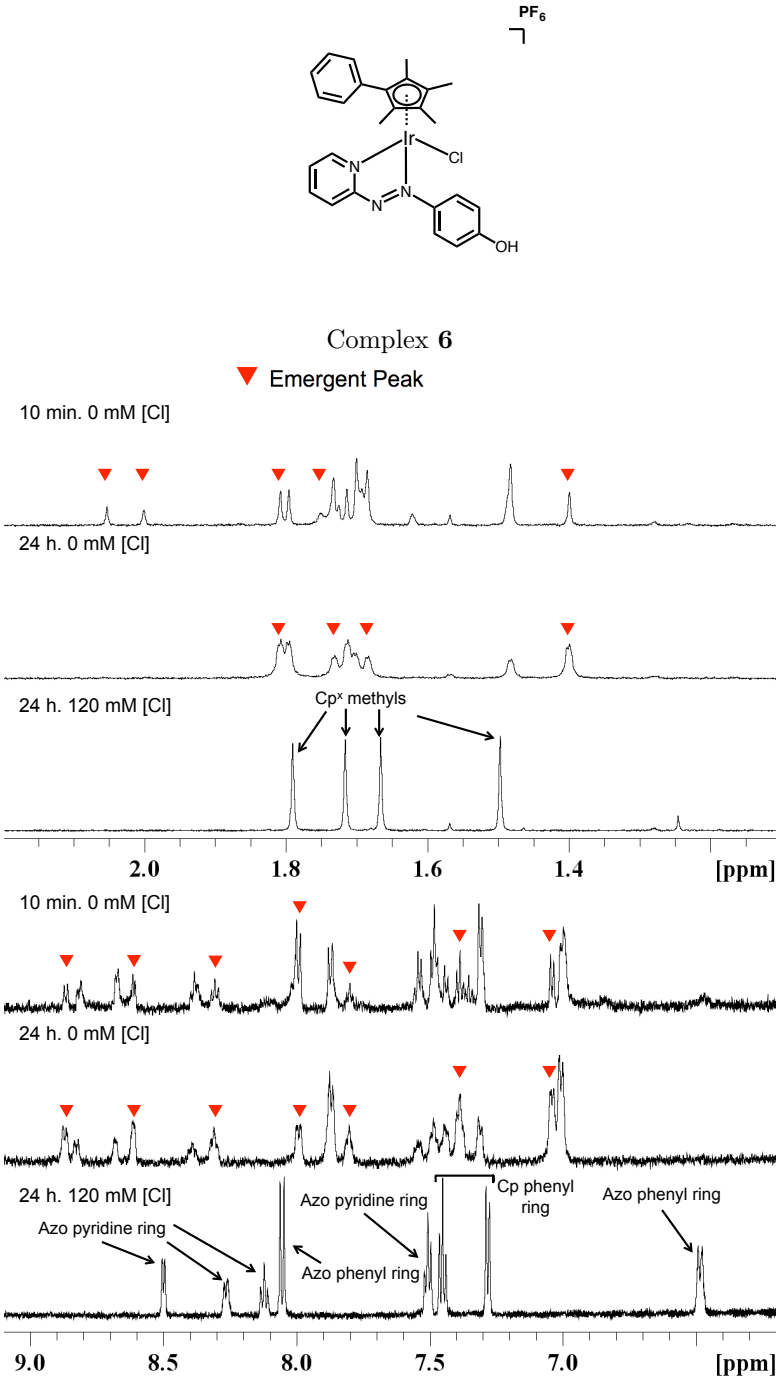

Figure 5.5: Hydrolysis of complex **6** studied by 600 MHz ^{1}H-NMR spectra of a 100 μM solution of complex **6** in 10% d_6-DMSO:D_2O, 0.1% 1,4-dioxane (v/v) at 310 K, unbuffered at pD 8. Spectra shown 10 min after sample preparation, 24 h after sample preparation, and 24 h after sample preparation in 120 mM NaCl solution. Emergent peaks not corresponding to original complex denoted by red arrows.

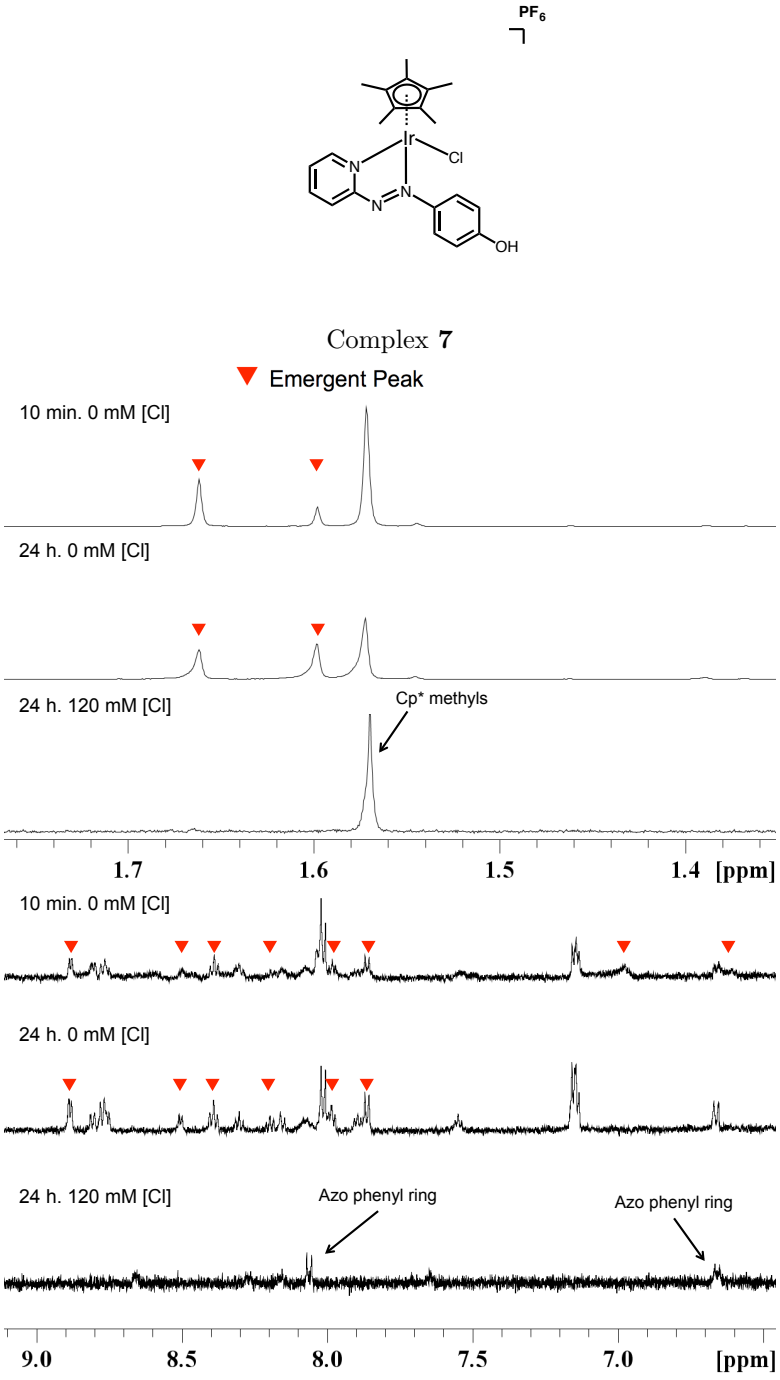

Figure 5.6: Hydrolysis of complex **7** studied by 600 MHz ^{1}H-NMR spectra of a 100 μM solution of complex **7** in 10% d_6-DMSO:D_2O, 0.1% 1,4-dioxane (v/v) at 310 K, unbuffered at pD 8. Spectra shown 10 min after sample preparation, 24 h after sample preparation, and 24 h after sample preparation in 120 mM NaCl solution. Emergent peaks not corresponding to original complex denoted by red arrows.

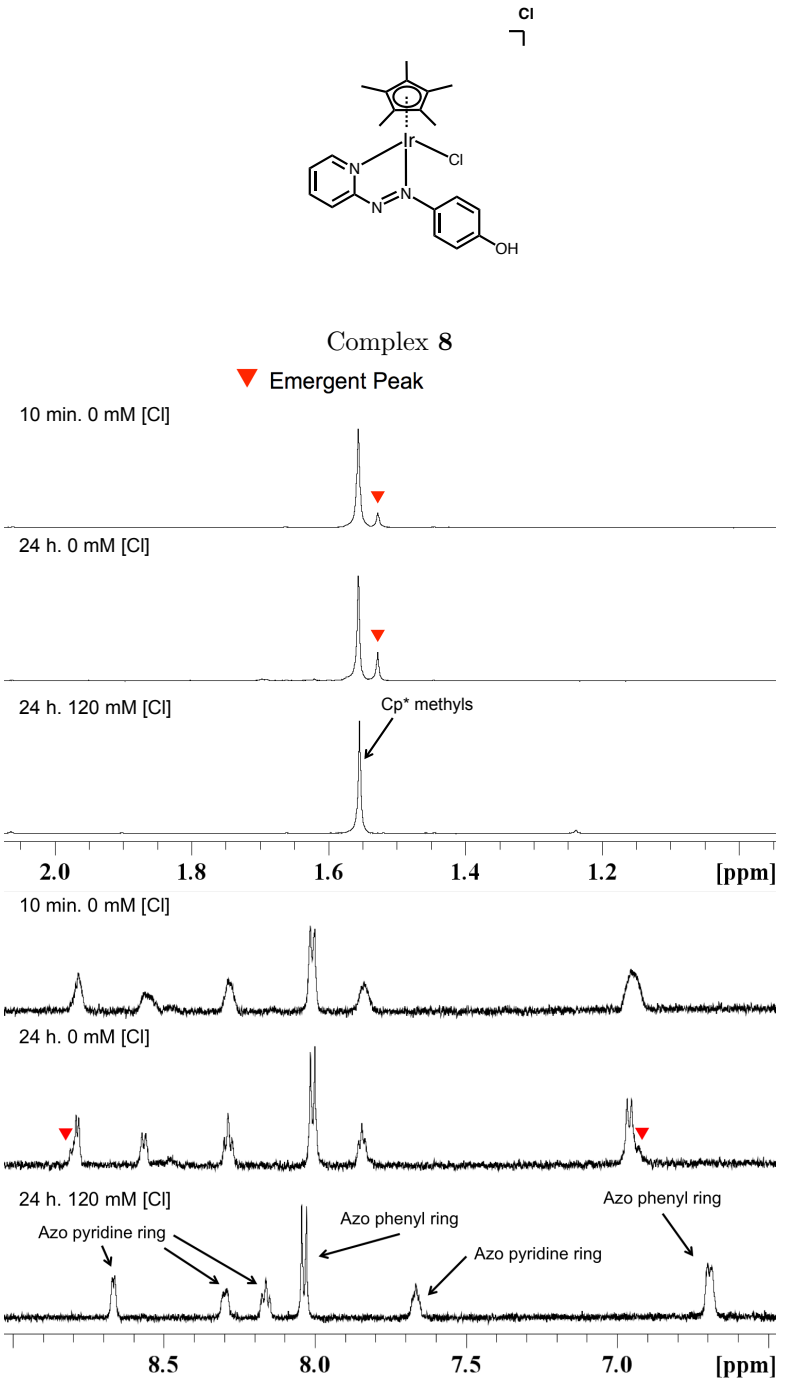

Figure 5.7: Hydrolysis of complex **8** studied by 600 MHz ^{1}H-NMR spectra of a 100 μM solution of complex **8** in 10% d_6-DMSO:D_2O, 0.1% 1,4-dioxane (v/v) at 310 K, unbuffered at pD 8. Spectra shown 10 min after sample preparation, 24 h after sample preparation, and 24 h after sample preparation in 120 mM NaCl solution. Emergent peaks not corresponding to original complex denoted by red arrows.

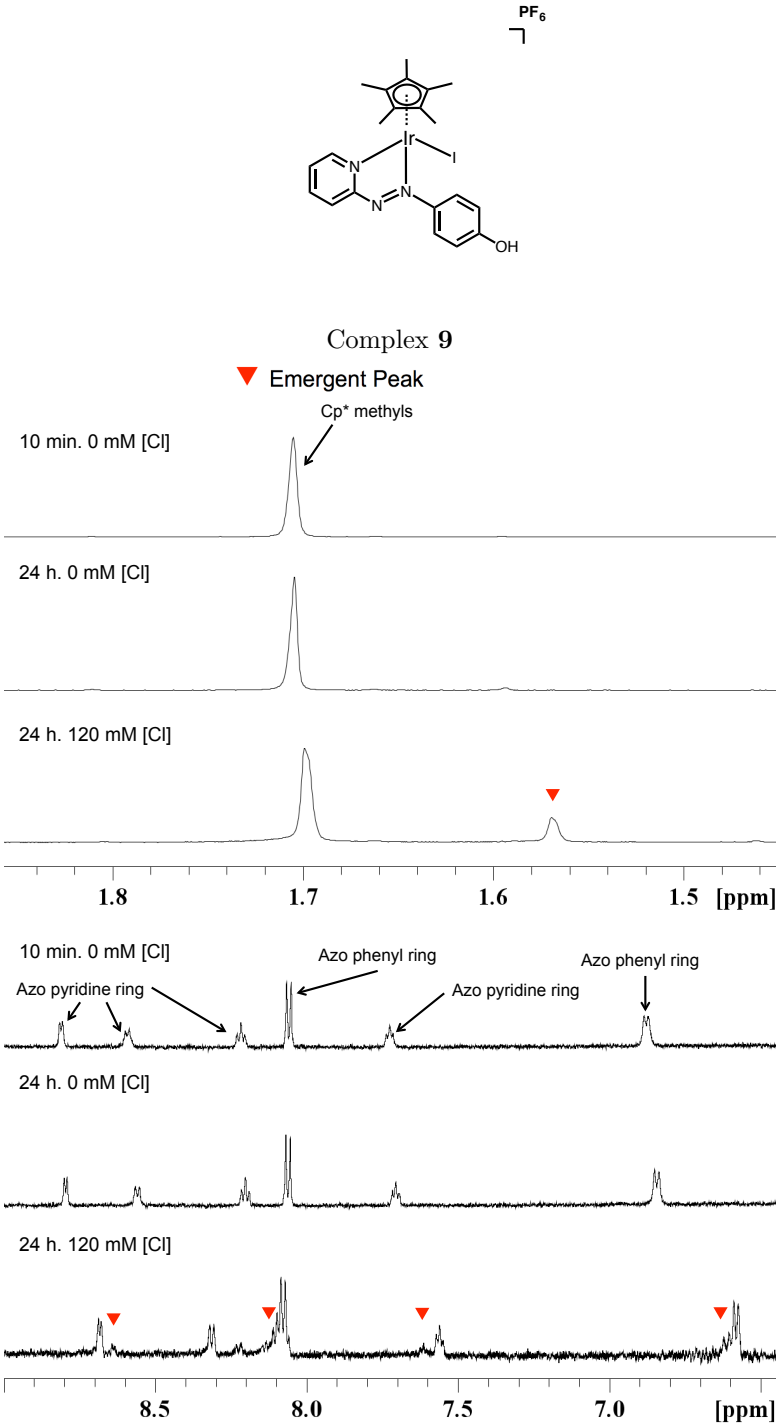

Figure 5.8: Hydrolysis of complex **9** studied by 600 MHz ^{1}H-NMR spectra of a 100 μM solution of complex **9** in 10% d_6-DMSO:D_2O, 0.1% 1,4-dioxane (v/v) at 310 K, unbuffered at pD 8. Spectra shown 10 min after sample preparation, 24 h after sample preparation, and 24 h after sample preparation in 120 mM NaCl solution. Emergent peaks not corresponding to original complex denoted by red arrows.

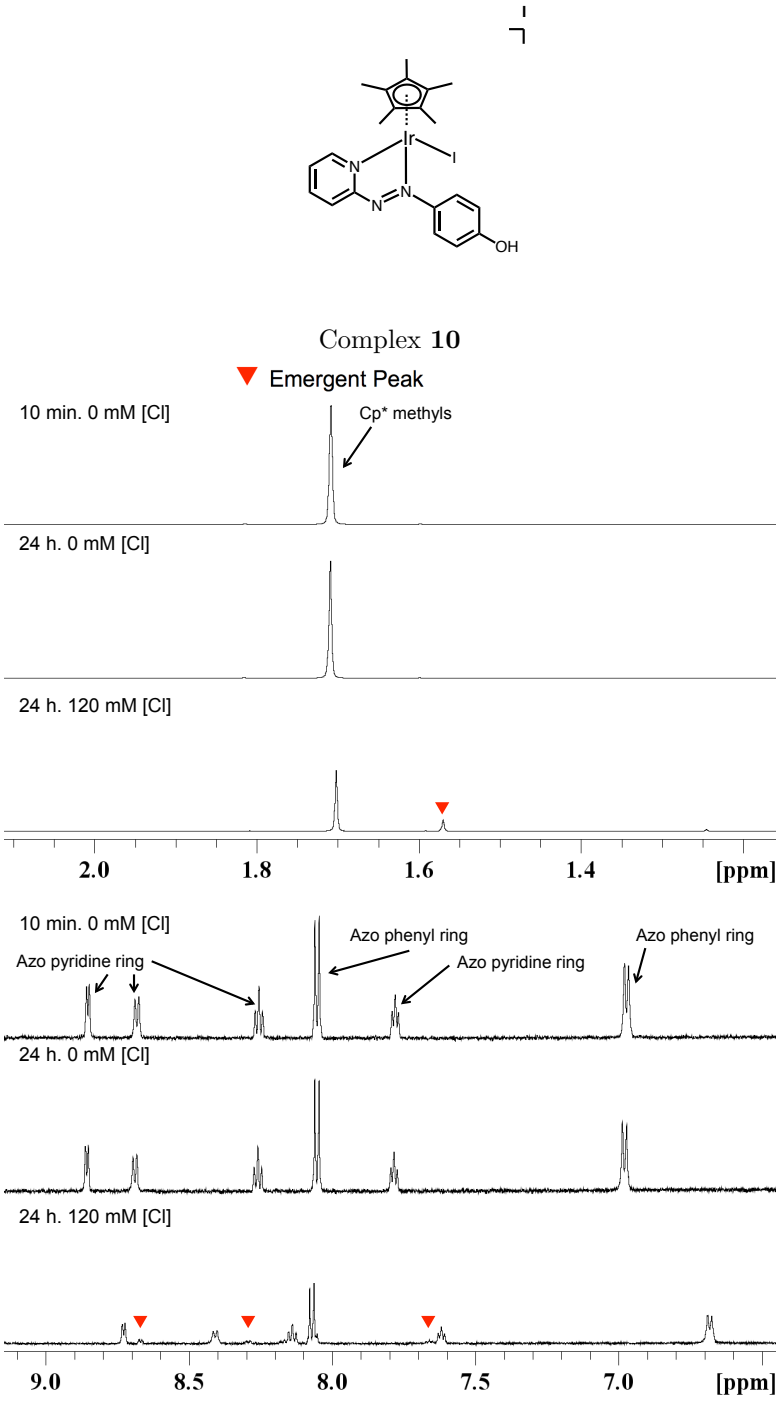

Figure 5.9: Hydrolysis of complex **10** studied by 600 MHz ^{1}H-NMR spectra of a 100 μM solution of complex **10** in 10% d_6-DMSO:D_2O, 0.1% 1,4-dioxane (v/v) at 310 K, unbuffered at pD 8. Spectra shown 10 min after sample preparation, 24 h after sample preparation, and 24 h after sample preparation in 120 mM NaCl solution. Emergent peaks not corresponding to original complex denoted by red arrows.

Complex	Structure	% Extent of Hydrolysis (0 mM [Cl])	% Extent of Hydrolysis (120 mM [Cl])
5	$[Cp^{xbiph}Ir(azpyOH)Cl]PF_6$	50%	0%
6	$[Cp^{xph}Ir(azpyOH)Cl]PF_6$	66%	0%
7	$[Cp^*Ir(azpyOH)Cl]PF_6$	53%	0%
8	$[Cp^*Ir(azpyOH)Cl]Cl$	66%	0%
9	$[Cp^*Ir(azpyOH)I]PF_6$	0%	19%*
10	$[Cp^*Ir(azpyOH)I]I$	0%	15%*

*Complexes **9** and **10** did not hydrolyse in the presence on 120 mM [Cl], instead exchanging a % of their iodido ligands for chlorido ones.

Table 5.1: Hydrolysis data for complexes **5** − **10** monitored over 24 h by ^{1}H-NMR in 10% d_6-DMSO:D_2O, 0.1% 1,4-dioxane at 310 K. Experiments were repeated with the addition of 120 mM NaCl to assess suppression of hydrolysis by chloride.

To better assess the relationship between the structure of azpyOH organoiridium complexes and their rates of hydrolysis, timescale ^{1}H-NMR experiments were carried out on 100 μM solutions of each complex in 10% d_6-DMSO:D_2O, 0.1% 1,4-dioxane (v/v) at 310 K, unbuffered at pD 8 over 24 h taking spectra every hour (Figure 5.10).

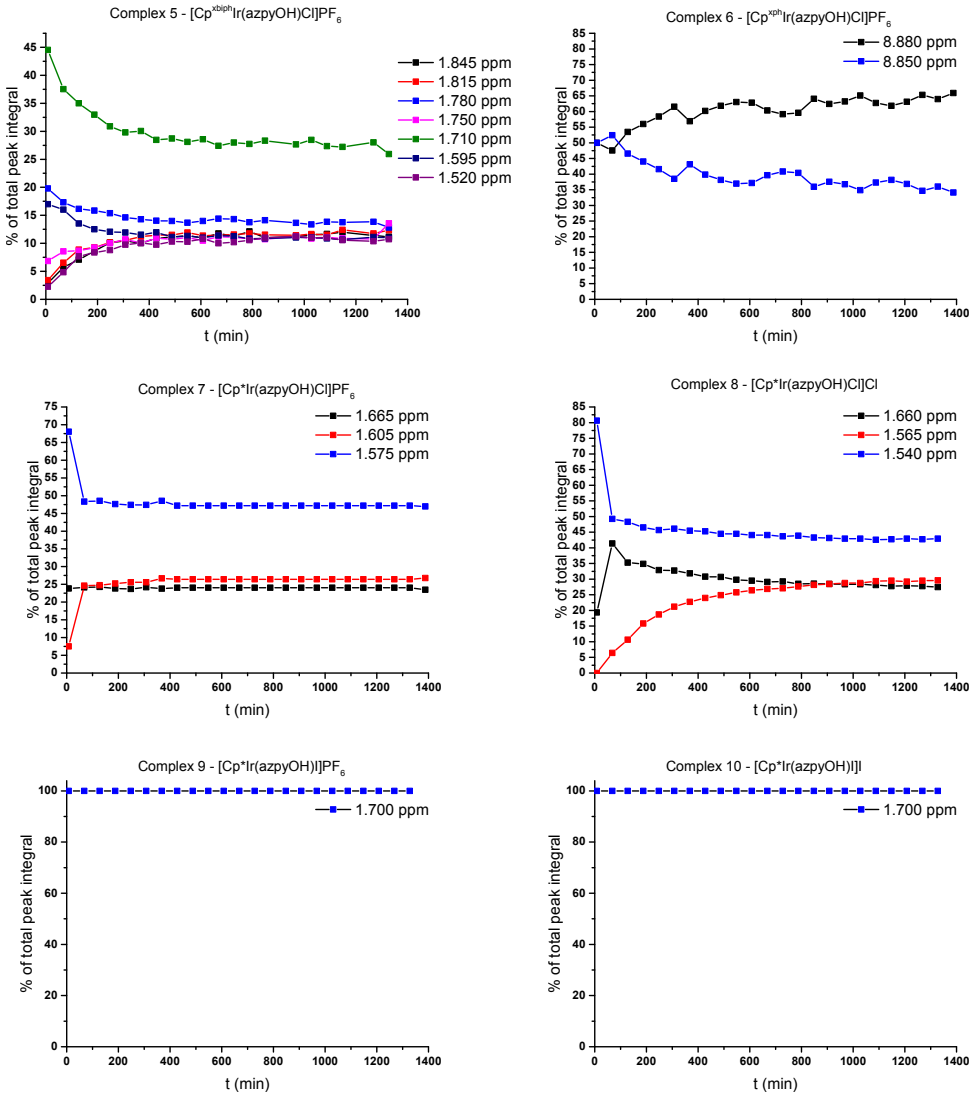

Figure 5.10: Monitoring of the hydrolysis of complexes **5** – **10** studied by 600 MHz ^{1}H-NMR spectra of a 100 μM solution of complex **1** in 10% d_6-DMSO:D_2O, 0.1% 1,4-dioxane (v/v) at 310 K, unbuffered at pD 8 by tracking relative % integrals of peaks corresponding to Cp^x ring methyl hydrogens for complexes **5**, and **7** – **10**. Complex **6** hydrolysis was monitored by tracking % integral of aromatic doublet due to overlaps in the Cp methyl hydrogen peaks making accurate quantification impossible in this region.

Complexes **5** – **8** bearing the monodentate chlorido ligand hydrolyse in water, whereas complexes **9** and **10** that bear the monodentate iodido ligand are completely inert to hydrolysis. The half-lives of complexes **7** and **8** are <10

min whereas the half-life for complex **5** is ca. 128 min, and for **6**, ca. 248 min. Complexes **7** [Cp*Ir(azpyOH)Cl]PF_6 and **8** [Cp*Ir(azpyOH)Cl]Cl differ only in their counterion, however this appears to have implications towards hydrolysis. For complex **8**, which bears a Cl counterion, the appearance of new peaks occurs more slowly than for its analogue, complex **7**, which bears a PF_6 counterion.

The Cp ligand appears to have little impact on the extent of hydrolysis, however the Cp^{xbiph} complex **5** and Cp^{xph} complex **6** appear to hydrolyse more slowly than their Cp* analogue, complex **7**, as evidenced by the slower rate of the disappearance of the peaks corresponding to the complex in its Ir-Cl form.

As is the case for azpyNMe_2 complexes **1** − **3**, investigated in Chapter 4, a third species appears when the chlorido complexes undergo hydrolysis (indicated in red for complexes **7** and **8**). This peak appears only after hydrolysis begins, and, in the case of complex **8**, it appears alongside a concomitant reduction in the other emergent peak, hypothesised to correspond to an Ir-OH_2 species (indicated in black). The appearance of a third species is not observed in the aromatic region of the spectra of complex **6** however this is likely still occurring, causing the complexity seen in the aliphatic region of the ^{1}H-NMR spectra.

5.3.4 Antiproliferative Activity

In Chapter 3, azpyOH complexes **5** – **10** were shown to have potency exceeding that of CDDP against A2780 ovarian carcinoma cells *in vitro*. Of the library of complexes investigated in Chapter 3, the azpyOH family of complexes were the least hydrophobic. High hydrophobicity usually correlates with high potency,[86] however, the azpyOH complexes displayed higher potency than nearly all other complexes in this work. Additionally, their pattern of activity was unusual. Usually a potency trend of $Cp^{xbiph} > Cp^{xph} > Cp^*$ is observed, however for azpyOH complexes the potencies of the Cp^{xbiph}, Cp^{xph} and Cp^* analogues, complexes **5** – **7** did not follow this expected trend. To further investigate the antiproliferative properties of complexes **5** – **10**, experiments were carried out on a panel of cancer cells of various tissue types (Table 5.2). Antiproliferative screenings against A2780, OE19 and SUNE-1 carried out by Dr. Isolda Romero-Canelón, Ji-Inn Song and Bindy Heer.

Table 5.2: Comparison of IC_{50} values (in μM) of azpyOH complexes **5** – **10** against a panel of cell lines. CDDP values obtained experimentally or from previously published work.[145] (*n.d.* = not determined)

Complex	A2780	A2780cis	A549	CNE1	CNE2	OE19	SUNE-1
5	0.14 ± 0.09	0.25 ± 0.06	5.2 ± 0.3	5 ± 1	10.62 ± 0.04	0.40 ± 0.03	0.72 ± 0.04
6	0.108 ± 0.009	0.22 ± 0.02	0.89 ± 0.03	5.03 ± 0.06	1.6 ± 0.2	0.30 ± 0.01	1.7 ± 0.2
7	0.12 ± 0.04	0.114 ± 0.003	1.5 ± 0.3	5.7 ± 0.2	2.3 ± 0.3	1.15 ± 0.02	1.5 ± 0.2
8	0.17 ± 0.07	0.062 ± 0.004	5.12 ± 0.09	1.2 - 6.2	1.12 ± 0.09	*n.d.*	*n.d.*
9	0.25 ± 0.02	*n.d.*	1.01 ± 0.08	*n.d.*	1.26 ± 0.04	*n.d.*	*n.d.*
10	0.34 ± 0.02	0.049 ± 0.001	1.5 ± 0.4	1.2 - 6.2	2.2 ± 0.2	*n.d.*	*n.d.*
CDDP	1.2 ± 0.2	11.5 ± 0.3	3.3 ± 0.1	7.7 ± 0.2	7.7 ± 0.3	13.43 ± 0.003	1.14 ± 0.01

All complexes tested are ca. 1 – 2 orders of magnitude more potent than CDDP in A2780cis (ovarian carcinoma with acquired CDDP resistance). Complexes **5** and **6** are less potent in A2780cis than in A2780, i.e. they exhibit some cross-resistance with CDDP, whilst complex **7** shows no significant difference in toxicity towards A2780 vs. A2780cis. Conversely, [(Cp*)Ir(azpyOH)Cl]Cl complex **8** and [(Cp*)Ir(azpyOH)I]I complex **10**, both exhibit low nanomolar IC_{50} values of 62 nm and 49 nm against A2780cis and are ca. 185× and 235× more potent than CDDP, respectively.

In A549 and CNE2, the Cp^{xbiph} complex **5** is, surprisingly, significantly less

potent that its Cp^{xph} and Cp* analogues, complexes **6** and **7**, although all three have similar activity in CNE1.

The Cp* iodido complex **9** is slightly less potent in A2780 than its Cp* chlorido analogue. Complex **7**, however, is significantly more potent in A549 and CNE2.

Chlorido complexes **7** and **8** display similar potencies in most cell lines, which is expected as they only differ in their counterion, however there are some surprising exceptions in A2780 and A549. This is also the case for their iodido analogues complexes **9** and **10**.

The Cp^{xbiph}, Cp^{xph} and Cp* analogues, complexes **5** − **7** are considerably more active than CDDP in OE19, however in SUNE-1 only complex **5** is more active. The expected potency trend of of $Cp^{xbiph} > Cp^{xph} > Cp^*$ was, again, not observed for these complexes. In OE19, the Cp^{xph} analogue, complex **6**, was the most potent, whereas in SUNE-1 it was the least potent. In some cases, the IC_{50} differences amongst these complexes are small and may therefore not be biologically significant, however the Cp system clearly has an impact on potency in these azpyOH complexes, however, their effect is likely more complicated than in other families of organoiridium complexes.

5.3.5 MoA Studies in Oesophageal and Nasopharyngeal Cancers by Flow Cytometry

The effect of the Cp system does not follow the expected potency trend in azpyOH complexes **5** − **7**. To investigate whether this is due to changes in MoAs, a panel of flow cytometry experiments were conducted on OE19 and SUNE-1 cells exposed to complexes **5** − **7**. Flow cytometry studies carried out with the help of Dr. Isolda Romero-Canelón and Hannah Bridgewater.

5.3.5.1 ROS and SO Generation

The capacity of complexes **5** – **7** to generate ROS/SO in OE19 and complex **5** in SUNE-1 were investigated (Figures 5.11 and 5.12).

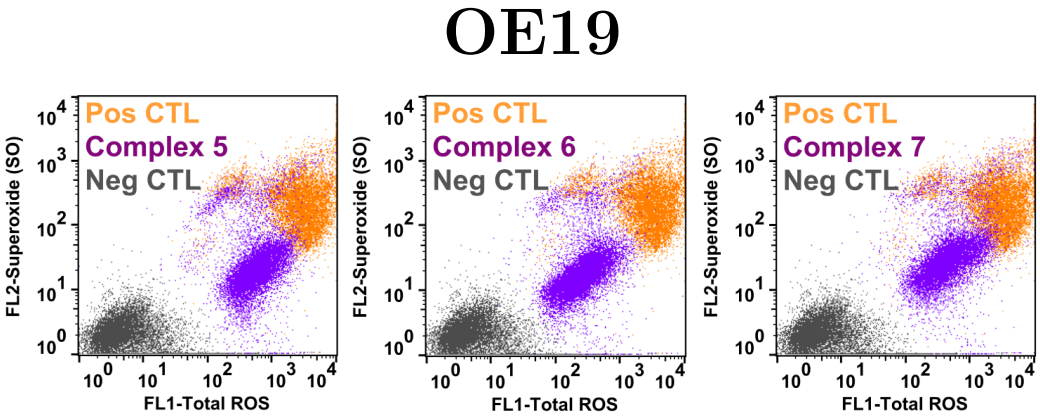

	High Superoxide FL1-FL2+ Q1	High ROS and Superoxide FL1+FL2+ Q2	High ROS FL1+FL2- Q3	Low ROS and Superoxide FL1-FL2- Q4
Neg CTL	0.00 ± 0.01	0.01 ± 0.01	2.1 ± 0.2	97.9 ± 0.2
Complex 5	0.85 ± 0.05 **	11.7 ± 0.2 ****	86.7 ± 0.2 **	0.7 ± 0.1 ****
Complex 6	1.1 ± 0.1 **	7.1 ± 0.2 ****	87 ± 2 **	5 ± 2 ***
Complex 7	0.47 ± 0.08 ***	13.6 ± 0.5 **	85.0 ± 0.9 **	0.8 ± 0.3 ****

Figure 5.11: (Top) Measurement of ROS and SO generation by flow cytometry of OE19 oesophageal carcinoma carcinoma cells exposed to complexes **5** – **7** for 24 h at IC_{50} concentrations at 310 K then stained with orange/green fluorescent reagents. Pyocyanin used as positive control (orange). (Bottom) Table of % cell populations obtained from triplicate experiments. Statistical significance between cells exposed to complex vs. negative control was determined by two-sample independent Welch t-tests assuming unequal variance between populations with asterisks corresponding to $p \leq 0.05$ *, $p \leq 0.01$ **, $p \leq 0.001$ ***, $p \leq 0.0001$ ****.

SUNE-1

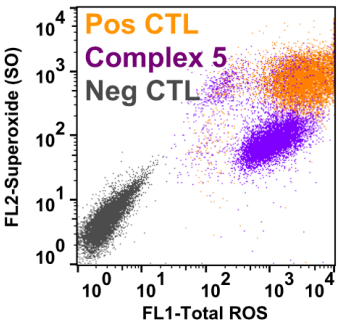

	High Superoxide FL1-FL2+ Q1	High ROS and Superoxide FL1+FL2+ Q2	High ROS FL1+FL2- Q3	Low ROS and Superoxide FL1-FL2- Q4
Neg CTL	0 ± 0	0.01 ± 0.02	0.01 ± 0.02	99.97 ± 0.06
Complex 5	0.4 ± 0.2 ****	9 ± 1 **	90 ± 1 ****	0.81 ± 0.07 ****

Figure 5.12: (Top) Measurement of ROS and SO generation by flow cytometry of SUNE-1 nasopharyngeal carcinoma carcinoma cells exposed to complex **5** for 24 h at IC_{50} concentrations at 310 K then stained with orange/green fluorescent reagents. Pyocyanin used as positive control (orange). (Bottom) Table of % cell populations obtained from triplicate experiments. Statistical significance between cells exposed to complex vs. negative control was determined by two-sample independent Welch t-tests assuming unequal variance between populations with asterisks corresponding to $p \leq 0.05$ *, $p \leq 0.01$ **, $p \leq 0.001$ ***, $p \leq 0.0001$ ****.

Complexes **5** − **7** generate similarly high levels of ROS and SO in OE19, as does complex **5** in SUNE-1.

5.3.5.2 Apoptosis Induction

Flow cytometry experiments were carried out on complexes **5** – **7** in OE19 and complex **5** in SUNE-1 to investigate their ability to induce apoptosis (Figures 5.13 and 5.14).

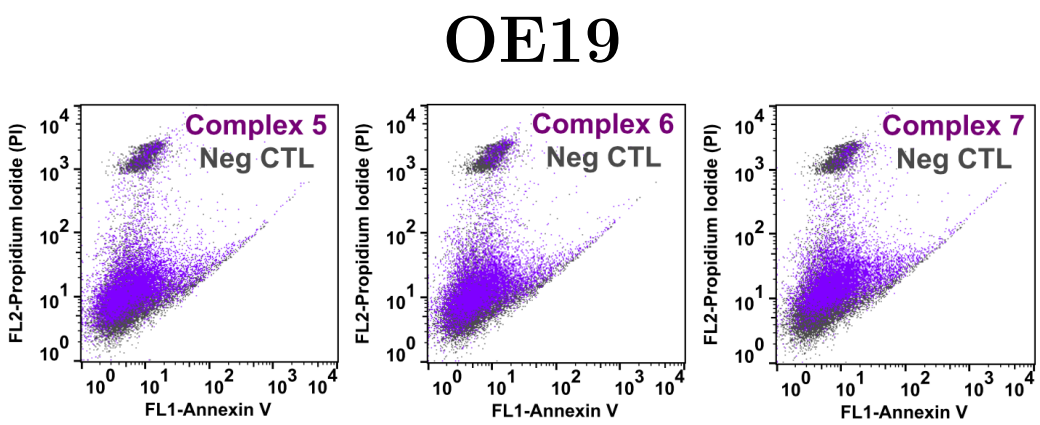

	Non-Viable FL1-FL2+ Q1	Late Apoptotic FL1+FL2+ Q2	Early Apoptotic FL1+FL2- Q3	Viable FL1-FL2- Q4
Neg CTL	14.9 ± 0.5	0.13 ± 0.01	0.67 ± 0.04	84.4 ± 0.4
Complex 5	7.9 ± 0.3 ****	0.35 ± 0.04 **	1.35 ± 0.04 ****	90.4 ± 0.3 ****
Complex 6	6.6 ± 0.2 ***	0.29 ± 0.04 *	1.06 ± 0.08 **	92.0 ± 0.3 ****
Complex 7	6.69 ± 0.05 ***	0.44 ± 0.01 ****	1.8 ± 0.1 **	91.1 ± 0.2 ****

Figure 5.13: (Top) Measurement of apoptosis induction by flow cytometry of OE19 oesophageal carcinoma cells exposed to complexes **5** – **7** for 24 h at IC_{50} concentrations at 310 K. (Bottom) Table of % cell populations obtained from triplicate experiments. Statistical significance between cells exposed to complex vs. negative control was determined by two-sample independent Welch t-tests assuming unequal variance between populations with asterisks corresponding to $p \leq 0.05$ *, $p \leq 0.01$ **, $p \leq 0.001$ ***, $p \leq 0.0001$ ****.

SUNE-1

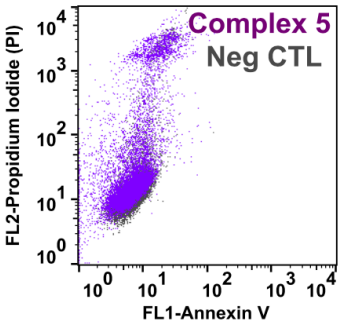

	Non-Viable FL1-FL2+ Q1	Late Apoptotic FL1+FL2+ Q2	Early Apoptotic FL1+FL2- Q3	Viable FL1-FL2- Q4
Neg CTL	3.8 ± 0.1	0 ± 0	0 ± 0	96.2 ± 0.2
Complex 5	14.9 ± 0.4 ****	0.01 ± 0.02	0 ± 0	85.1 ± 0.4 ****

Figure 5.14: (Top) Measurement of apoptosis induction by flow cytometry of SUNE-1 nasopharyngeal carcinoma cells exposed to complex **5** for 24 h at IC_{50} concentrations at 310 K. (Bottom) Table of % cell populations obtained from triplicate experiments. Statistical significance between cells exposed to complex vs. negative control was determined by two-sample independent Welch t-tests assuming unequal variance between populations with asterisks corresponding to $p \leq 0.05$ *, $p \leq 0.01$ **, $p \leq 0.001$ ***, $p \leq 0.0001$ ****.

Complexes **5** − **7** induce little to no apoptosis in OE19 after 24 h. The same is true for complex **5** in SUNE-1.

5.3.5.3 Mitochondrial Membrane Depolarisation

To determine if complexes **5** – **7** could induce mitochondrial membrane depolarisation and to investigate if the Cp system had any impact, investigations were carried out by flow cytometry in OE19 (Figure 5.15).

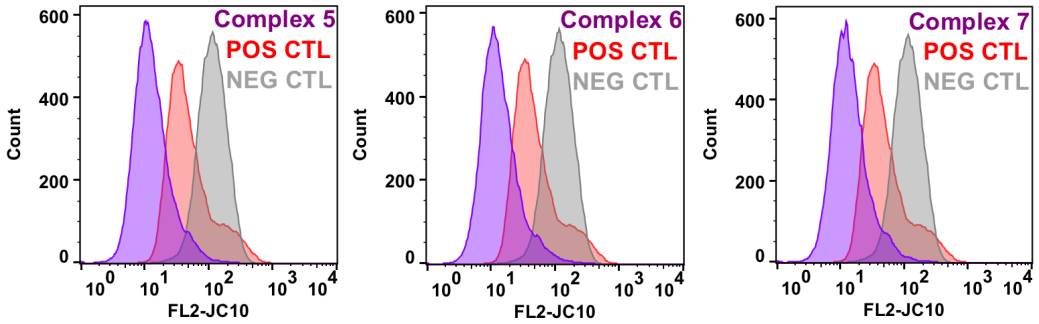

Complex	%Polarised	%Depolarised
Neg CTL	88.1 ± 0.5	11.9 ± 0.5
Pos CTL	28 ± 1	72 ± 1
5	3.4 ± 0.3 ****	96.6 ± 0.3 ****
6	2.93 ± 0.06 ****	97.07 ± 0.06 ****
7	2.47 ± 0.06 ****	97.53 ± 0.06 ****

Figure 5.15: (Top) Depolarisation of mitochondrial membrane potential of OE19 oesophageal carcinoma cells exposed to complexes **5** – **7** for 24 h at IC_{50} concentration at 310 K measured by reduction in JC10 fluorescence. (Bottom) Table of % cell populations with polarised/depolarised mitochondrial membrane potential obtained from triplicate experiments. Statistical significance between cells exposed to complex vs. negative control was determined by two-sample independent Welch t-tests assuming unequal variance between populations with asterisks corresponding to $p \leq 0.05$ *, $p \leq 0.01$ **, $p \leq 0.001$ ***, $p \leq 0.0001$ ****.

Complexes **5** – **7** induce extreme depolarisation of the mitochondrial membrane, greater than that observed for the positive control.

5.3.6 Effect of Redox Modulation on Anticancer Activity

In Chapter 4, two organoiridium complexes were shown to generate ROS and SO in cells. It was then shown that co-administration of L-BSO or NAC with organoiridium complexes can have an effect on their cytotoxicity. Complexes **5** − **7** have been shown to generate ROS and SO and so investigations into the effects of redox modulators on their cytotoxicity is warranted.

To investigate how modulation of the level of GSH affects the anticancer potency of complexes **5** − **7**, they were co-administered with 5 μM of either L-BSO or NAC and their cytotoxicities determined in EBV-positive OE19 oesophageal carcinoma and compared to the results for administration of complex only, and CDDP (Figure 5.16).

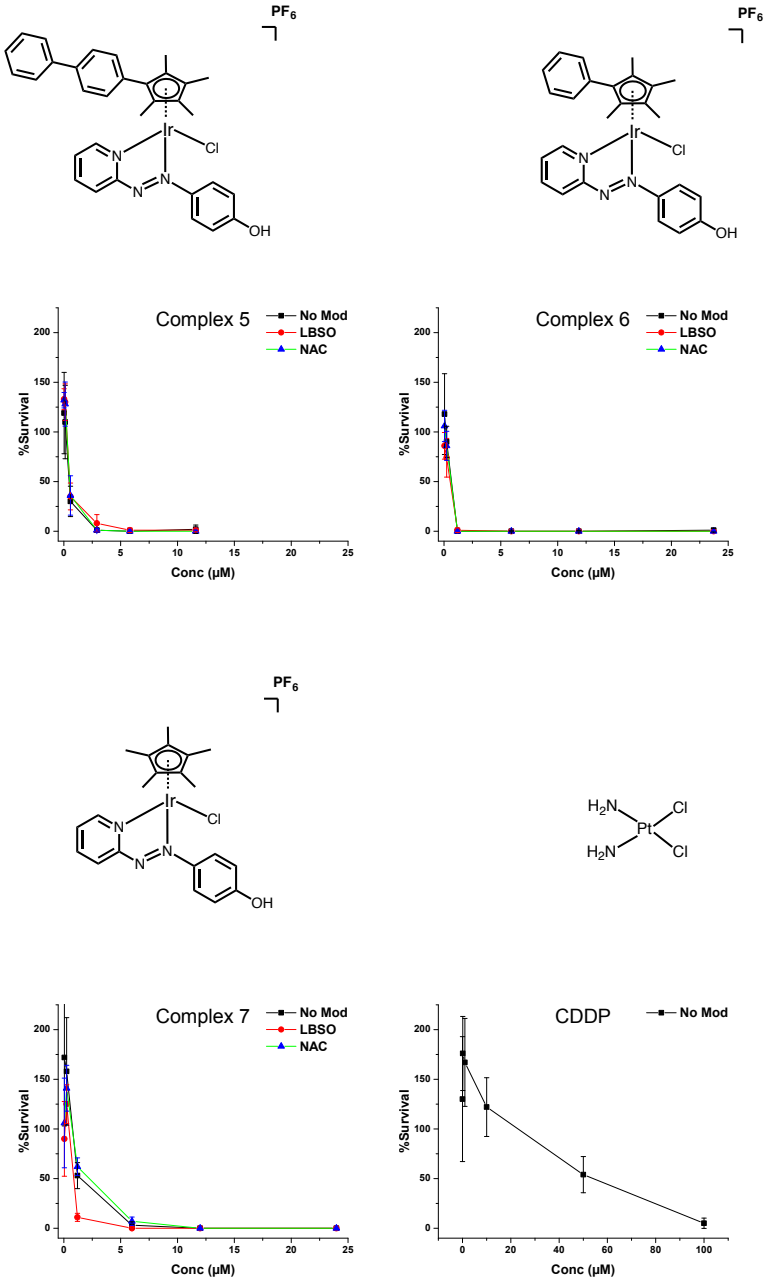

Figure 5.16: Cytotoxicities of complexes **5** – **7** and CDDP against EBV-positive oesophageal carcinoma cells, co-administered with 5 μM of L-BSO, NAC or neither. Drug treatment was for 24 h, followed by 72 h recovery period. Data and standard deviations were obtained from duplicates of triplicate experiments for cells co-administered with 5 μM of L-BSO, NAC. Data and standard deviations were obtained from quadruplicates of triplicate experiments for cells treated with no modulator (drug only).

Complexes **5** − **7** are highly cytotoxic to EBV-positive OE19, more so than CDDP, with Cp^{xph} complex **6** exhibiting the highest cytotoxicity of the three, as it does in A2780, A549, CNE2 and OE19. Co-administration of NAC has no observable effect on the cytotoxicity of any of the three complexes. Co-administration of L-BSO has no observable effect on the cytotoxicity of complexes **5** or **6** three complexes, however an increase in cytotoxicity is observed for complex **7**.

5.3.7 Circular Dichroism (CD)

The effect of two organoiridium complexes, **1** and **13**, on ctDNA was investigated by CD in Chapter 4. Complexes can induce peaks in the CD spectra of DNA by associating with the helix in a specific orientation. To investigate whether azpyOH complexes **5** and **7** can interact with helical DNA, preliminary CD experiments were carried out with 1:3, 2:3 and 1:1 ratios of [Ir]:[DNA] (Figure 5.17).

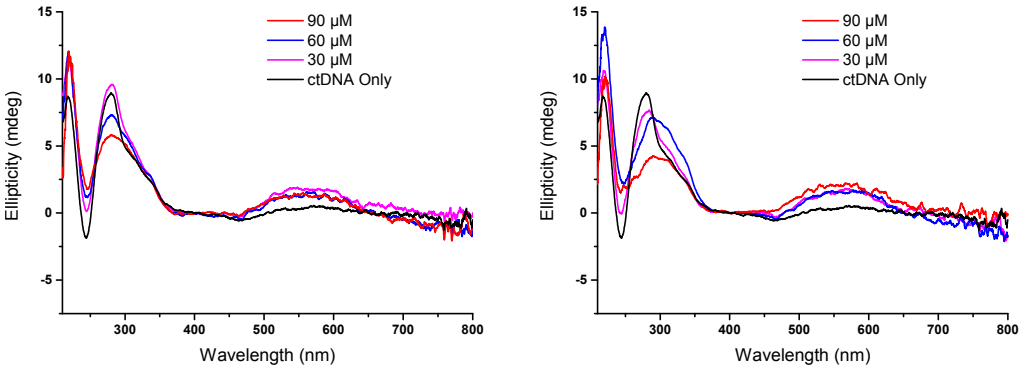

Figure 5.17: CD spectra of 90 µM ctDNA incubated for 24 h with increasing concentrations of complex **5** (Left) or complex **7** (Right)

Both the Cp^{xbiph} azpyOH complex **5** and its Cp* analogue, complex **7**, induce a CD peak in the 500 – 600 nm region, matching their corresponding UV-Vis spectra. Additionally, both complexes reduce the magnitude of the CD signal of ctDNA at 260 nm, and this effect increases with increasing complex concentration.

5.3.8 Linear Dichroism (LD)

The effect of two organoiridium complexes, **1** and **13**, on ctDNA was investigated by LD in Chapter 4. Both complexes cleaved and distorted the DNA superstructure, reducing the magnitude of the LD signal at 260 nm. To investigate whether azpyOH complexes **5** and **7** can affect the DNA superstructure, preliminary LD experiments were carried out with a 1:1 ratio of [Ir]:[DNA] (Figure 5.18).

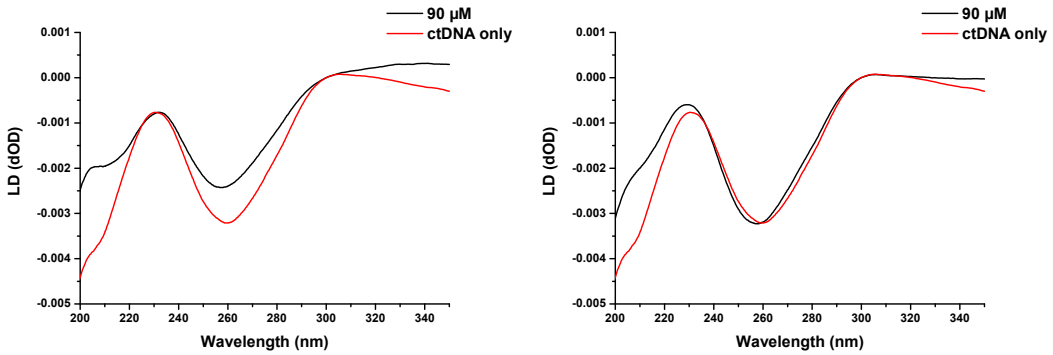

Figure 5.18: Linear dichroism spectra of 90 µM ctDNA incubated for 24 h with 90 µM of complex **5** (Left) or complex **7** (Right).

The Cp^{xbiph} azpyOH complex **5** induces a slight decrease in the magnitude of the ctDNA LD signal at 260 nm, whereas its Cp* analogue, complex **7**, induces almost no change in the spectrum.

In comparison with the significant effects azpyNMe_2 complex **1** and azpy complex **13** exert on DNA at ratios as low as 1:100 [Ir]:[DNA], azpyOH complexes **5** and **7** exert little to no effects observable by CD or LD. Therefore no further DNA interaction investigations were carried out.

5.3.9 Toxicity in Zebrafish

The properties of organoosmium and organoruthenium azopyridine anticancer complexes bearing monodentate chlorido or iodido ligands has been investigated.[145] The iodido complexes were more potent than their chlorido analogues, did not exhibit cross-resistance with CDDP, and were more selective. The azpyOH chlorido complex **7** and its iodido analogue, complex **9**, have already been shown to be highly potent. Additionally, the chlorido complex readily hydrolyses, whereas the iodido does not, potentially having implications in uptake and MoA. To assess whether changing the halide of organoiridium azopyridine complexes has an impact on *in vivo* toxicity, experiments were carried out in an animal model.

The zebrafish (*Danio rerio*) is a well-established model organism in developmental biology. Strikingly, 70% of protein-coding human genes are related to genes found in the zebrafish and 84% of genes known to be associated with human disease have a counterpart in zebrafish.[181] Zebrafish represent a whole-organism vertebrate with many of the high-throughput advantages of cell-screening assays as they can live in a 96-well plate and readily absorb chemicals from the water. Additonally, they develop most of their major organs within a week, allowing for rapid assays. These properties make zebrafish ideal for early *in vivo* drug-toxicity screening.[182–184] To investigate the difference in toxicity between the Cp* chlorido complex **7** and its iodido analogue, complex **9**, their toxicities to zebrafish were compared (Figure 5.19).

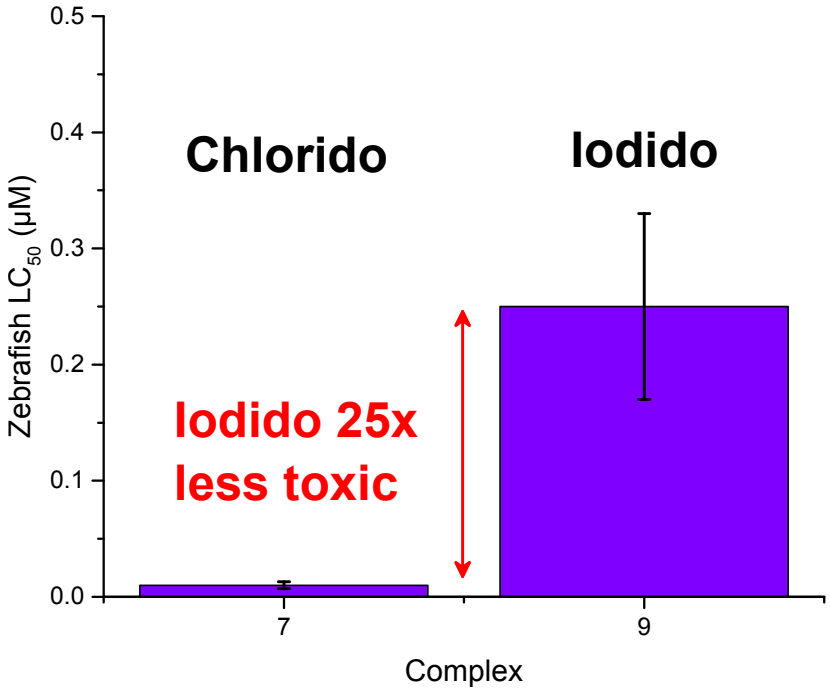

Figure 5.19: LC_{50} values (in μM) of complexes **7** and **9** in zebrafish (*Danio rerio*). Higher LC_{50} values indicate lower toxicity.

Strikingly, the iodido complex **9** is ca. 25× less toxic to zebrafish than its otherwise identical chlorido analogue, complex **7**. However, the toxicities of both complexes are higher than that of the clinically-utilised drugs CDDP and carboplatin, which have zebrafish LC_{50} values of 0.6 μM and 5.7 μM, respectively.

5.4 Discussion

The azpyOH family of organoiridium complexes are novel and previously unexplored. In chapter 3, it was shown how azpyOH complexes **5** − **7** exhibited an unusual pattern of activity in A2780 ovarian carcinoma, as well as being highly potent and more hydrophilic than the majority of the other complexes studied in this work. The work carried out in this chapter has shed considerable light on the properties of azpyOH complexes, as well as elucidating their potential as anticancer agents and their possible MoAs.

5.4.1 Water Solubility

Solubility in water is a highly desirable feature in drugs. The vast majority of organoiridium complexes, and indeed many precious metal-based drugs, are not completely soluble in water and require additional solvents such as DMSO or more complex delivery systems, such as vesicles or nanoparticles. Changing the counterions of azpyOH complexes from PF_6 to chloride or iodide is demonstrated to dramatically increase solubility without compromising potency (Table 5.2, pg. 226). This may also hold true for other organoiridium complexes and could result in more favourable formulation if a drug of this family were to reach clinical trials as high solubility in water obviates the need for complex and expensive delivery mechanisms. Water soluble drugs, such as picoplatin, are also highly favourable for patients as they can be administered orally as opposed to the less pleasant intravenous administration required for CDDP.

5.4.2 Aquation

The azpyOH complexes **5** − **8** bearing the chlorido monodentate ligand hydrolyse readily in water, whereas the iodido complexes **9** and **10** do not. This is also the case for their azpyNMe_2 analogues, complexes **3** and **4**, studied in Chapter 3. Therefore, the monodentate halido ligand is the primary structural feature governing hydrolysis of organoiridium azopyridine complexes. This is

unsurprising as ruthenium complexes bearing the same bidentate ligand and monodentate halido ligand also hydrolyse,[96] as do many reported Ir(III) complexes or similar structure bearing chlorine as a monodentate ligand.[86,94]

There is a small difference in rate and extent of hydrolysis between Cp^{xbiph} and Cp^{xph} azpyOH complexes **5** and **6** and their Cp* analogue, complex **7** (Table 5.1, pg. 223 and Figure 5.10, pg. 224). The slower hydrolysis of complexes **5** and **6** relative to complex **7** could be due to the extended rings on the Cp systems of complexes **5** and **6** sterically hindering the approach of water molecules and/or the release of the chlorido ligand. Another possible explanation of this could be the slight difference in the pK_a values of their azopyridine phenyl hydroxyl groups. The hydroxyl group of complex **5** has a lower pK_a value than that of complexes **6** and **7** (Figure 5.2, pg. 214), therefore, at pH 7, slightly more of the complex will be in its deprotonated form, resulting in a complex with a global charge of 0, instead of $^+$. Perhaps the deprotonated neutral complex accepts water as a ligand (and concomitant loss of chloride) less readily than the protonated complex does. Another possible explanation for the difference in rate between these complexes, observable by the significantly steeper curve of Cp* complex **7** compared to Cp^{xbiph} complex **5**, is that the biphenyl group may play a part in sterically hindering the approach of water molecules to the iridium centre of complex **5**, slightly reducing its ability to hydrolyse.

There is a difference in the rates and extents of hydrolysis between Cp* complex **7** and its analogue, complex **8**, which bears a chloride counterion instead of PF_6. This is likely due to the presence of additional chloride suppressing hydrolysis, as increasing chloride concentration has been shown to slow and suppress hydrolysis in Chapters 3 and 4.

As is the case for the azpyNMe_2 complexes $\mathbf{1}-\mathbf{3}$, the ^{1}H-NMR studies indicate three species present when hydrolysing in aqueous solution. The same is true for their otherwise identical azpyOH analogues, complexes $\mathbf{5}-\mathbf{7}$. Due to the structural similarities between the complexes, the hypothesis that OH-bridged dimers were forming between azpyNMe_2 complexes is a sensible conclusion for azpyOH complexes also.

As is the case for its azpyNMe$_2$ analogue, complex **4**, azpyOH iodido complexes **9** and **10** undergo conversion from iodido to chlorido when in 120 mM chloride solution. As this is the concentration of chloride in cell medium, there is a possibility that a proportion of molecules of complex **9** and **10** are converted to chlorido analogues before they reach cells. This is unlikely to be an issue, however, as after 24 h incubation at 310 K, only 19% of complex **9** and 15% of complex **10** are converted. During antiproliferative assays, the solution of complex in 120 mM chloride medium is applied to cells within one hour of preparation from solid. Therefore the time for iodido to chlorido conversion in cell medium before the complexes reach cells is minimised.

5.4.3 MoA Investigations

Flow cytometry studies indicate that azpyOH complexes are likely to have similar MoAs to azpyNMe$_2$ complexes. Both azpyNMe$_2$ and azpy OH complexes generate significant ROS and SO in OE19 oesophageal carcinoma cells, with the azpyNMe$_2$ complexes generating slightly more than their azpyOH analogues. This may be due to the slightly higher electron donating property of the NMe$_2$ group relative to the OH group.

None of the azpyNMe$_2$ complexes **1** − **3** or the azpyOH complexes **5 - 7** induced apoptosis after 24 h, and all slightly increased the proportion of non-viable cells. This indicates that, for all of the complexes tested, either apoptosis is not an MoA, or it occurs after $>$ 24 h.

All complexes tested induced extreme depolarisation of the mitochondrial membrane, the azpyOH complexes doing so to a slightly lesser degree than the azpyNMe$_2$ ones. Whilst this indicates that this could be an MoA for azpyOH complexes, they are less likely to localise to the negatively charged mitochondria than the cationic azpyNMe$_2$ complexes due to their neutral global charge at physiological pH, although this does not rule out mitochondrial damage as a possible MoA.

Unlike its azpyNMe$_2$ and azpy analogues, complexes **1** and **13**, the otherwise identical Cp^{xbiph} azpyOH complex **5** has very little effect on the LD spectrum

of DNA and its Cp* analogue, complex **7** has no effect, even at a 1:1 [Ir]:[DNA] ratio after 24 h incubation. Conversely, complexes **1** and **13** can cleave DNA at concentrations as low as a 1:100 [Ir]:[DNA] ratio and distort the LD spectra at a 1:10 [Ir]:[DNA] ratio under the same conditions. The reason behind this is most likely the neutral global charge of azpyOH complexes at physiological pH, as DNA is a negatively charged molecule and the azpyNMe$_2$ and azpy analogues are cationic. The slight association of the Cp^{xbiph} azpyOH complex to ctDNA, relative to its non-interacting Cp* analogue, may be due to base stacking of the biphenyl rings with DNA bases, inducing a slight change in the spectrum. Whilst this indicates little to no DNA interaction for azpyOH complexes, there does, however, appear to be slight induction of a CD signal at the wavelengths corresponding to the azpyOH complexes, as well as reducing the magnitude of the ctDNA CD signal at 260 nm, indicating that there may be some association of the complexes with DNA. This does only occur at relatively high concentrations and, were it cleaving DNA like complexes **1** and **13**, would also induce changes in the LD spectrum. As neither azpyOH complex do so, the most likely explanation of the changes in the CD spectra is that the complexes induce very low levels of DNA unwinding at high concentrations after 24 h. These results indicate that DNA interaction is unlikely to be an MoA for azpyOH complexes.

5.4.4 Hydroxyl pK$_a$ and Antiproliferative Activity

Whilst healthy cells tend to maintain an intracellular pH of 7.1 – 7.2, tumours often have a more acidic microenvironment. This is due to increased reliance on glycolysis, poor vascular perfusion, and hypoxia, especially in the central region of tumours. This can lead to an extracellular pH of as low as 6.5.[185] The intracellular pH, however, remains around 7.2 – 7.4 even in acute acidosis.[186] Cancer cells have the cellular apparatus to sense extracellular pH, and adapt, driving disease progression.[187]

Unlike the azpyNMe$_2$ complexes, the azpyOH complexes bear hydrogens with pK$_a$ values within physiological pH range (Figure 5.2, pg. 214). These pK$_a$ values lie in the range of 5.5 – 6.5. This means that, in cell medium, and in

most biological compartments, the complexes will exist primarily in a form in which the hydroxyl group will be deprotonated. This changes the global charge from $^{+}$ to 0. Global charge can have a significant impact on drug uptake mechanisms and reactions with cellular targets, setting them apart from the other complexes studied in this work. Many conventional drug targets, such as the mitochondria or DNA, are negatively charged, therefore, whilst cationic complexes may be more likely to target these sites, neutral complexes may instead target elsewhere.

The presence of the iodido ligand causes a significant shift in the pK_a value (from 5.88 to 6.50) relative to its chlorido analogue. This is likely due to the additional electron density contributed by the iodido ligand. This is a significant shift in pK_a, and as pH is measured on a log scale, means that significantly more of iodido complex **9** would be in its protonated form when in a significantly acidic tumour microenvironment relative to its chlorido analogue complex **7**. As healthy, non-cancerous cells do not tend to generate an acidic microenvironment, this may be a way by which to tune azpyOH complexes to utilise different uptake mechanisms to selectively kill cancer cells over healthy ones. The mechanism of cellular uptake of organoruthenium complexes has been shown to be different for those bearing the monodentate iodido ligand vs. those with the chlorido ligand.[188] This may also be the case for organoiridium complexes.

The presence of one phenyl ring on the Cp system has no effect of the pK_a, whereas the presence of a biphenyl ring on the Cp system reduces pK_a slightly (from 5.88 to 5.52). The biphenyl may be slightly withdrawing electron density from the metal, lowering the pK_a. This may be the cause of the unusual trend in potency observed in azpyOH complexes, where a general trend of Cp^{xph} >Cp* >Cp^{xbiph} is observed, instead of the more common trend of Cp^{xbiph} >Cp^{xph} >Cp*. Another possible reason for the lower potency of Cp^{xbiph} complex **5** may be that the large, bulky biphenyl ring hinders uptake for neutral azpyOH complexes. This is unlikely to be the case for non-azpyOH organoiridium complexes due to the highly potent activities displayed by non-azpyOH Cp^{xbiph} complexes, however it is possible that neutral organoiridium complexes follow different uptake pathways to cationic ones.

All azpyOH complexes tested were highly potent in multiple cell lines. A trend of particular interest is that the Cp* azpyOH complexes are significantly more potent than their azpyNMe_2, azpy, azpy$(OH)_2$ ad HOazpyNO_2 analogues. This is particularly promising as the Cp phenyl ring could be hydroxylated in the liver during detoxification, for example, by cytochrome P-450.[189] The more water-soluble and hydrophilic Cp* azpyOH complexes may be more easily excreted by the body than complexes with other Cp systems or bidentate ligands, whilst still retaining potent anticancer activities. For this reason, they show further promise as potential clinical therapeutics.

The azpyOH complexes show a much lower degree of cross resistance with CDDP than any other family of organoiridium complexes in this work. This may again be due to their main structural difference, a neutral global charge at physiological pH, possibly necessitating a different mechanism of cell uptake. One of the mechanisms of CDDP resistance is reduced uptake/increased efflux, so perhaps the neutral azpyOH complexes are taken up more readily and/or pumped out less readily than other, positively-charged organoiridium complexes. Alternatively, one of the other common mechanisms of CDDP resistance, intracellular deactivation by thiol-containing molecules such as GSH or increased DNA damage repair, may be contributing to the lower activity of non-azpyOH Cp* complexes relative to azpyOH complexes. In Chapter 4 an azpyNMe_2 complex and an azpy complex are shown to be mostly or completely unreactive with GSH, and both complexes display moderate to signficant cross-resistance with CDDP as well as interacting with DNA, indicating a DNA damage-based MoA. The azpyOH complexes **5** and **7** show little to no interaction with ctDNA, therefore increased DNA damage repair may be the major contributor to CDDP cross-resistance for non-azpyOH complexes. The azpyOH family, therefore, remains a candidate for overcoming all three of these mechanisms of cross-resistance, highlighted by the extremely potent IC_{50} values of 62 nm and 49 nm in A2780cis for Cp* azpyOH complexes **8** and **10**, respectively, although A2780 is an unusually sensitive cell line and therefore lower IC_{50} values are to be be expected.

5.4.5 Effect of Halido Ligand on Zebrafish Toxicity

The iodido complex **8** is ca. 25× less toxic to zebrafish than is otherwise identical chlorido analogue, complex **7** (Figure 5.19, pg. 240). This striking difference in toxicity between otherwise identical chlorido and iodido azpyOH complexes is highly encouraging, indicating a way to reduce toxicity *in vivo*. In cancer cells, the iodido complex **9** also retains potency, in some cases it is more potent than its chlorido analogue, complex **7**. The use of organoiridium iodido complexes, therefore, presents a way by which to effectively kill cancer cells, whilst reducing *in vivo* toxicity, and warrants future research in other organoiridium azopyridine systems. Possible reasons for the reduced toxicity of the iodido complex could be its inertness to hydrolysis, preventing it from subsequently binding to off-target molecules, which could contribute to toxicity, or lower uptake by normal cells relative to cancerous ones. As previously mentioned, the difference in pK_a values, and therefore global charge at different pH environments, may also affect drug uptake into various intracellular compartments, contributing to differences in toxicity. Previous research into organoosmium and organoruthenium complexes has shown that their iodido complexes were more potent than their chlorido analogues, as well as being more selective for cancer cells over normal cells.[145]

5.5 Conclusions

The azpyOH complexes **5** − **10** represent a novel set of organoiridiums that have not been previously investigated. They have been shown to be the most hydrophilic of the complexes studied in this work (Chapter 3, Figure 3.12, pg. 92), as well as becoming highly water soluble when the counterion is changed. In addition to this, they exhibit significant anticancer potency down to the low nanomolar range. The complexes show little to no cross-resistance with CDDP, and the alteration of the halido ligand from chloride to iodide has been shown to reduce *in vivo* toxicity in zebrafish by ca. 25×, as well as increasing potency in multiple cancer cell lines. Unlike the azpyNMe_2 and azpy family of complexes, the azpyOH complexes have a global charge of 0 at physiological pH and display little to no interaction with DNA, however they do appear to share ROS and SO generation as an MoA. The azpyOH family of complexes remain highly potent even with Cp* as the stabilising ligand, which reduces potency in most non-azpyOH complexes tested. In conclusion, azpyOH complexes represent an avenue of research into organoiridium complexes with the potential to generate complexes with higher solubility, greater potency, and lower *in vivo* toxicity than previously reported organoiridiums, with the potential to become clinically-utilised therapeutics in the future.

Chapter 6

Conclusions and Future Work

6.1 Summary

This work has explored a previously untapped area of chemical space, generating, characterising, and purifying 17 novel organoiridium(III) azopyridine complexes. The anticancer activity of these, and other complexes in this work, has been thoroughly investigated in multiple cancer cell lines. The potency of many of these complexes is greater than that of cisplatin (CDDP), and that of many other clinically-utilised pharmaceuticals, in addition to being more potent that many prominent metal-based complexes reported in literature. Many of these complexes are also cytotoxic to CDDP-resistant cancer cells.

The complexes in this work are tunable by synthetically trivial adjustments. The charge, solubility, hydrophobicity, hydrolytic behaviour, and mechanism of action (MoA) can all be modified, in some cases dramatically, by changes in a single functional group. This demonstrates the versatility of organoiridium(III) azopyridine complexes as a platform for effective drug design.

The MoA of some of these complexes has been investigated by small- and large-scale screens, revealing a MoA based on reactive oxygen species (ROS) and superoxide (SO) generation in addition to mitochondrial membrane depolarisation, with DNA a possible additional target. Cancer cells have higher levels of basal ROS, therefore a ROS-based MoA holds the potential to selec-

tively kill cancer cells over normal ones. Complex **1** is demonstrated to be more selectively cytotoxic for A2780 ovarian carcinoma vs. MRC-5 normal lung fibroblasts than CDDP, as well as many reported metal-based complexes.

Whilst these complexes are not yet ready for clinical trials, great steps have been made towards developing effective organoiridium(III) azopyridine drugs and understanding their MoA. Further research could progress one or more of these complexes into the first stage of clinical trials and beyond. Suggestions of the most pertinent experiments to be carried out follow.

6.2 Future Work

6.2.1 Improved Drug Design

Many of the complexes in this work exhibit superior cytotoxicity to CDDP, as well as many other clinically utilised therapeutics in multiple cell lines. Complex **2**, in particular, displayed impressive cytotoxicity in the GDSC large-scale pharmaco-genomic screen against ca. 900 cell lines.

The Cp system, bidentate azopyridine ligand, monodentate halido ligand, and counterion, each have significant implications for anticancer activity, selectivity, and solubility of organoiridium complexes. This work has revealed structure-activity relationships and trends within this family of complexes that can be applied to future drug design to improve upon their anticancer activity, selectivity, and solubility.

In regards to generating novel organoiridium azopyridine complexes, further exploration of chemical space is warranted. Additionally, the combination of multiple separate structural features that have been shown to confer desirable traits into novel complexes may result in drugs that exceed the already considerable potency of previous organoiridium complexes. A selection of potential complexes to be synthesised that, based on this work, are likely to possess higher potency, selectivity and solubility than existing organoiridium drugs are shown (Figure 6.1).

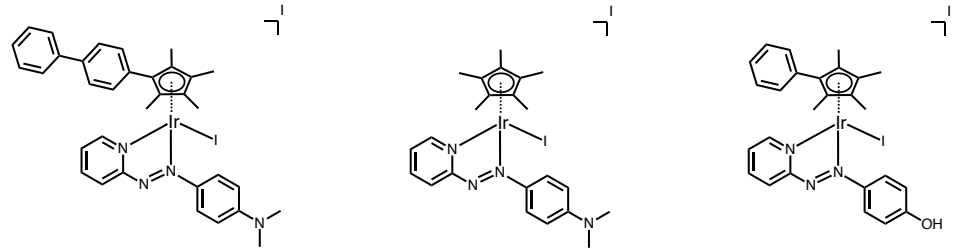

Suggested Complex **A** Suggested Complex **B** Suggested Complex **C**

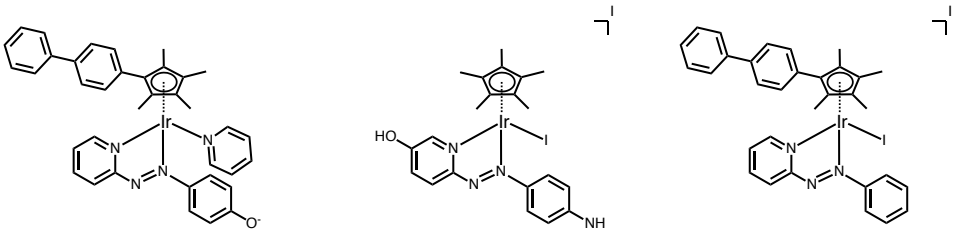

Suggested Complex **D** Suggested Complex **E** Suggested Complex **F**

Figure 6.1: Structures of suggested complexes **A** − **F** likely to prove promising in future research.

Complex **A** is an iodido analogue of the extremely potent novel complex **1** ([Cp^{xbiph}Ir(azpyNMe$_2$)Cl]PF_6) described in Chapters 3 and 4. Complex **1** exhibited higher potency than a vast majority of existing precious metal-based drugs in A2780 ovarian carcinoma with a low nanomolar IC_{50} value (95 nm). In Chapter 5, the presence of the iodido ligand conferred a net increase in potency, as well as a ca. 25× decrease in *in vivo* toxicity in a zebrafish model. Additionally, in Chapter 3, separation and isolation of stable chiral enantiomers of azpyNMe$_2$ iodido complex **4** ([Cp*Ir(azpyNMe$_2$)I]PF_6) was achieved. Thus separation, isolation, and purification of suggested complex **A** ought to be possible by the same method, as the Cp system did not have any effect on the separability of the chlorido analogues of the same complexes, and therefore a Cp^{xbiph} azpyNMe$_2$ iodido complex is highly likely to be separable under the same conditions. Prior to this, the previously separated stable enantiomers of complex **4** should be desalted, purified, and their antiproliferative activity assessed and compared to a racemic mixture. If the antiproliferative activities of the enantiomers differ this would be highly informative and could have

significant implications on MoA.

Suggested complexes **A** − **C**, **E** and **F** have an iodide counterion. In Chapter 5 it was shown how switching from a PF_6 counterion to either a chlorido or iodide counterion dramatically increased the water solubility of complexes without compromising anticancer potency. For ease of synthesis and purification, an iodide counterion is suggested for complexes bearing a monodentate iodido ligand. By generating complexes with more clinically desirable counterions, high water solubility and easier drug formulation can be more easily achieved.

In Chapter 3 it was shown that the novel azpyOH complex **6** bearing an Cp^{xph} system displayed high potency in multiple cancer cell lines. This complex was further investigated in Chapter 5. The iodido analogue of the Cp*azpyOH complex **7** exhibited higher net potency and lower toxicity in zebrafish, suggesting that generating an iodido analogue of Cp^{xph} complex **6** may result in an even more potent and selective complex.

Coordination of a pyridine monodentate ligand to an organoiridium complex has been previously reported for a complex bearing a C'N-chelated bidentate ligand, resulting in a highly potent and selective complex.[84] Attempts to coordinate a pyridine monodentate ligand to N'N-chelated azopyridine complexes **1** − **3** were unsuccessful. This was likely due to the fact that coordinating a pyridine ligand in place of a chlorido one would increase the global charge by +1. Such a complex would then have a net global charge of 2+, which may not be energetically feasible or stable. In Chapter 5, the pK_a values of azpyOH complexes were investigated. Their pK_a values ranged from 5.52 – 6.50. This means that the complexes will exist in a mostly deprotonated form at physiological pH, resulting in neutral complexes with a global charge of 0. This may then make it possible to coordinate a pyridine monodentate ligand to the Ir centre, resulting in complex **D** with a global charge of 1+, which is more likely to be stable. Additionally, were complex **D** synthesised in a basic environment, it may be able to release its monodentate ligand when placed into an acidic environment, such as in a cancer cell, depending on the pK_a of its hydroxyl group. Cancer cells have an acidic microenvironment, so such a complex could be both a cytotoxic agent and a pH-dependent delivery system

for a variety of ligands.

The novel HOazpyNO_2 complexes **16** − **18** showed high potency in A2780 carcinoma. They were also shown to be capable of oxidising coenzyme NADH. This could be a possible MoA. Such complexes may be reduceable under the right conditions, forming complexes with an NH_2 group instead of NO_2. This group could be used to form a peptide bond with a carboxylic acid group, possibly with a polymer, opening up a variety of new possible drug delivery mechanisms, such as linking multiple organoiridium complexes onto a polymer or nanoparticle.

Complex **13** ([Cp^{xbiph}Ir(azpy)Cl]PF_6) showed significant DNA cleavage capabilities. The exact mechanism of this is currently unknown. Synthesis of complex **F**, an iodido analogue of complex **13**, would likely be inert to hydrolysis, as are all the iodido complexes studied in this work. If the DNA cleavage activity of complex **13** depends on the presence of the chlorido ligand, or its release and concomitant hydrolysis, the complex **F** would be unable to cleave DNA. Therefore, complex **F** could be used to elucidate the DNA-cleavage mechanism of complex **13**. Additionally, if complex **F** does not cleave DNA, and is shown to be significantly less cytotoxic than complex **13**, then DNA cleavage would be implicated as a probable MoA for complex **13**.

6.2.2 Further MoA Investigations

Elucidation of the MoA of a drug is one of the most important and challenging steps in progressing a novel complex from the lab to clinical trials and beyond. In this work, steps have been taken towards discovering and understanding the anticancer MoAs of a variety of organoiridium azopyridine complexes, as well as the impact that the chelating ligands have on the MoA. Further investigations into the MoAs of these complexes could provide valuable avenues for future research.

6.2.3 GDSC Pharmaco-genomic Screening

Of all the MoA investigations carried out as part of this work, the GDSC pharmaco-genomic screen represents the greatest in scale. As well as assessing the potencies of potential drugs against hundreds of cancer cell lines of various tissue types, such screens also have the potential to yield a significant amount of valuable information about MoAs due to the genomic information documented for each cell line. Additionally, the pattern of activity can be compared to other clinically-utilised therapeutics, revealing similarities and further elucidating the MoA of novel anticancer complexes. Four complexes of particular interest in this work, complexes **1**, **7**, **9** and **13**, may yield particularly interesting results if submitted for such a screen.

6.2.4 Uptake and Subcellular Distribution

Part of elucidating the MoA of a drug involves discovering its cellular targets. The uptake and subcellular distribution of Ir complexes can be determined by cell testings followed by microwave digestion and ICP-MS.[86] Further subcellular localisation information can be obtained by synchrotron X-ray fluorescence experiments.[132] These can both direct future MoA investigations as well as support previous ones. In particular, complexes **1** and **13**, which have been shown to interact with DNA as a possible MoA, would benefit greatly from quantification of their level of nuclear accumulation.

6.2.5 DNA Binding

Complexes **1** and **13** were both shown to interact with DNA in different ways. The results suggested that complex **1** noncoordinatively binds DNA in the minor groove. Experiments investigating whether complex **1** can displace or inhibit the binding of the known minor groove binding agent Hoescht 33258 would be valuable in definitively proving this as a method of binding. Isolation of a crystal of either complex **1** or **13** bound to DNA would be extremely valuable if an X-ray structure could be determined. Alternatively, DFT exper-

iments could be carried out to determine the electrostatic potential surfaces of complexes **1** and **13**, potentially allowing their mechanism of binding to DNA to be calculated theoretically. DFT calculations may also aid in elucidating the exact mechanism of DNA cleavage for both complexes, as well as possibly explaining why complex **13** possesses significantly higher cleavage activity than complex **1**.

6.2.6 Tumour Xenograft Experiments

The potent organoosmium complex FY26 ([η^6-p-cymene)Os(azpyNMe$_2$)I]PF$_6$), bearing the same azpyNMe$_2$ bidentate ligand as complexes **1** − **4**, was tested in a nude mouse tumour HCT-116 xenograft model, showing no significant toxicity at a dose 6 times higher than the maximum tolerated dose of CDDP in the same tumour model.[64] Additionally, this complex induced a statistically significant delay in tumour growth in the HCT-116 model.[68] Complex **1** has shown higher potency in A2780 cells, in addition to lower relative toxicity in MRC-5 normal fibroblasts than FY26, indicating the potential for even greater anti-tumour activity and lower toxicity than FY26 in a tumour xenograft model.

6.3 Conclusions

Organoiridium(III) azopyridine complexes hold potential as a new family of anticancer drugs. They bear an MoA that has the potential to kill cancer cells more effectively and selectively than many clinically-utilised therapeutics by perturbation of their delicate ROS balance. Further research is required to fully understand the MoA of these complexes and to determine their *in vivo* toxicity before they can be evaluated for entry into clinical trials.

References

[1] A. S. Ahmad, N. Ormiston-Smith and P. D. Sasieni, *Br. J. Cancer*, 2015, **112**, 943–7.

[2] H. Jayasekara, R. J. MacInnis, R. Room and D. R. English, *Alcohol Alcohol*, 2016, **51**, 315–30.

[3] World Health Organisation, *Cancer Fact sheet N297*, 2017.

[4] D. H. Lynch, *Am. J. Reprod. Immunol. Microbiol.*, 1987, **15**, 24–28.

[5] M. Otto, *Expert Rev. Anti. Infect. Ther.*, 2011, **9**, 389–392.

[6] L. Bernstein, C. L. Pearce, I. Cheng and K. D. Henderson, in *Holl. Frei cancer Med. 8*, B.C. Decker., Hamilton, Ontario:, 2010, ch. 13, pp. 237–247.

[7] R. Doll and R. Peto, *J. Natl. Cancer Inst.*, 1981, **66**, 1192–1308.

[8] P. Anand, A. B. Kunnumakara, C. Sundaram, K. B. Harikumar, S. T. Tharakan, O. S. Lai, B. Sung and B. B. Aggarwal, *Pharm. Res.*, 2008, **25**, 2097–2116.

[9] S. McGuire, *Adv. Nutr. An Int. Rev. J.*, 2016, **7**, 418–419.

[10] A. D. Joshi, R. Corral, C. Catsburg, J. P. Lewinger, J. Koo, E. M. John, S. A. Ingles and M. C. Stern, *Carcinogenesis*, 2012, **33**, 2108–2118.

[11] W. Zheng and S. A. Lee, *Nutr. Cancer*, 2009, **61**, 437–446.

[12] L. R. Ferguson, *Meat Sci.*, 2010, **84**, 308–313.

[13] NTP (National Toxicology Program) and Department of Health and Human Services, *Report on Carcinogens, Fourteenth Edition. Nickel Compounds and Metallic Nickel*, 2016, http://ntp.niehs.nih.gov/go/roc.

[14] A. Wicki and J. Hagmann, *Swiss Med. Wkly.*, 2011, **141**, w13250.

[15] M. Seget, D. Karolczak, M. Wilk, A. Blaszczyk, L. Szylberg, E. Florek and A. Marszalek, *Przegl. Lek.*, 2012, **69**, 904–907.

[16] C. C. M. Garcia, J. P. F. Angeli, F. P. Freitas, O. F. Gomes, T. F. de Oliveira, A. P. M. Loureiro, P. Di Mascio and M. H. G. Medeiros, *J. Am. Chem. Soc.*, 2011, **133**, 9140–3.

[17] R. Fabiani, P. Rosignoli, A. De Bartolomeo, R. Fuccelli and G. Morozzi, *Mutat. Res.*, 2007, **629**, 7–13.

[18] X. Y. Liu, M. X. Zhu and J. P. Xie, *Toxicol. Mech. Methods*, 2010, **20**, 36–44.

[19] I. Koturbash, A. Scherhag, J. Sorrentino, K. Sexton, W. Bodnar, J. A. Swenberg, F. A. Beland, F. P. M. DeVillena, I. Rusyn and I. P. Pogribny, *Toxicol. Sci.*, 2011, **122**, 448–456.

[20] D. M. Parkin, *Int. J. Cancer*, 2006, **118**, 3030–44.

[21] C. Wong and K. Goh, *Biomed. Imaging Interv. J.*, 2006, **2**, e7.

[22] H. Takeda, A. Takai, T. Inuzuka and H. Marusawa, *J. Gastroenterol.*, 2017, **52**, 26–38.

[23] S. B. Pattle and P. J. Farrell, *Expert Opin. Biol. Ther.*, 2006, **6**, 1193–1205.

[24] C. Wood and W. Harrington, *Cell Res.*, 2009, **15**, 947–52.

[25] Cancer Research UK Cancer Survival Group, *Cancer Research UK, England and Wales Survival (2010-2011)*, 2014.

[26] P. C. A. Bruijnincx and P. J. Sadler, *Curr. Opin. Chem. Biol.*, 2008, **12**, 197–206.

[27] K. L. Haas and K. J. Franz, *Chem. Rev.*, 2009, **109**, 4921–4960.

[28] M. Frezza, S. Hindo, D. Chen, A. Davenport, S. Schmitt, D. Tomco and Q. P. Dou, *Curr. Pharm. Des.*, 2010, **16**, 1813–25.

[29] Y. K. Yan, M. Melchart, A. Habtemariam and P. J. Sadler, *Chem. Commun.*, 2005, 4764.

[30] B. Rosenberg, L. Van Camp and T. Krigas, *Nature*, 1965, **205**, 698–699.

[31] B. Rosenberg, L. VanCamp, J. E. Trosko and V. H. Mansour, *Nature*, 1969, **222**, 385–6.

[32] M. G. Apps, E. H. Y. Choi and N. J. Wheate, *Endocr. Relat. Cancer*, 2015, **22**, R219–33.

[33] S. Dilruba and G. V. Kalayda, *Cancer Chemother. Pharmacol.*, 2016, **77**, 1103–1124.

[34] L. Kelland, *Nat. Rev. Cancer*, 2007, **7**, 573–584.

[35] S. A. Abramkin, U. Jungwirth, S. M. Valiahdi, C. Dworak, L. Habala, K. Meelich, W. Berger, M. A. Jakupec, C. G. Hartinger, A. A. Nazarov, M. Galanski and B. K. Keppler, *J. Med. Chem.*, 2010, **53**, 7356–7364.

[36] U. Jungwirth, D. N. Xanthos, J. Gojo, A. K. Bytzek, W. Korner, P. Heffeter, S. A. Abramkin, M. A. Jakupec, C. G. Hartinger, U. Windberger, M. Galanski, B. K. Keppler and W. Berger, *Mol. Pharmacol.*, 2012, **81**, 719–728.

[37] E. S. Antonarakis and A. Emadi, *Cancer Chemother. Pharmacol.*, 2010, **66**, 1–9.

[38] A. Bergamo, R. Gagliardi, V. Scarcia, A. Furlani, E. Alessio, G. Mestroni and G. Sava, *J. Pharmacol. Exp. Ther.*, 1999, **289**, 559–64.

[39] A. Vacca, M. Bruno, A. Boccarelli, M. Coluccia, D. Ribatti, A. Bergamo, S. Garbisa, L. Sartor and G. Sava, *Br. J. Cancer*, 2002, **86**, 993–8.

[40] G. Sava, R. Gagliardi, A. Bergamo, E. Alessio and G. Mestroni, *Anticancer Res.*, 1999, **19**, 969–972.

[41] G. Sava, S. Zorzet, C. Turrin, F. Vita, M. R. Soranzo, G. Zabucchi, M. Cocchietto, A. Bergamo, S. DiGiovine, G. Pezzoni, L. Sartor and S. Garbisa, *Clin. Cancer Res.*, 2003, **9**, 1898–1905.

[42] S. Leijen, S. A. Burgers, P. Baas, D. Pluim, M. Tibben, E. van Werkhoven, E. Alessio, G. Sava, J. H. Beijnen and J. H. M. Schellens, *Invest. New Drugs*, 2015, **33**, 201–14.

[43] S. Kapitza, M. A. Jakupec, M. Uhl, B. K. Keppler and B. Marian, *Cancer Lett.*, 2005, **226**, 115–121.

[44] M. Galanski, V. B. Arion, M. A. Jakupec and B. K. Keppler, *Curr. Pharm. Des.*, 2003, **9**, 2078–89.

[45] C. G. Hartinger, S. Zorbas-Seifried, M. A. Jakupec, B. Kynast, H. Zorbas and B. K. Keppler, *J. Inorg. Biochem.*, 2006, **100**, 891–904.

[46] C. Hartinger, M. Jakupec, S. Zorbas-Seifried, M. Groessl, A. Egger, W. Berger, H. Zorbas, P. Dyson and B. Keppler, *Chem. Biodivers.*, 2008, **5**, 2140–2155.

[47] W. H. Ang, A. Casini, G. Sava and P. J. Dyson, *J. Organomet. Chem.*, 2011, **696**, 989–998.

[48] B. Wu, M. S. Ong, M. Groessl, Z. Adhireksan, C. G. Hartinger, P. J. Dyson and C. A. Davey, *Chemistry*, 2011, **17**, 3562–6.

[49] P. Nowak-Sliwinska, J. R. Van Beijnum, A. Casini, A. A. Nazarov, G. Wagnières, H. Van Den Bergh, P. J. Dyson and A. W. Griffioen, *J. Med. Chem.*, 2011, **54**, 3895–3902.

[50] C. Scolaro, A. Bergamo, L. Brescacin, R. Delfino, M. Cocchietto, G. Laurenczy, T. J. Geldbach, G. Sava and P. J. Dyson, *J. Med. Chem.*, 2005, **48**, 4161–4171.

[51] R. F. S. Lee, S. Escrig, M. Croisier, S. Clerc-Rosset, G. W. Knott, A. Meibom, C. A. Davey, K. Johnsson and P. J. Dyson, *Chem. Commun.*, 2015, **51**, 16486–9.

[52] A. Weiss, X. Ding, J. R. van Beijnum, I. Wong, T. J. Wong, R. H. Berndsen, O. Dormond, M. Dallinga, L. Shen, R. O. Schlingemann, R. Pili, C. M. Ho, P. J. Dyson, H. van den Bergh, A. W. Griffioen and P. Nowak-Sliwinska, *Angiogenesis*, 2015, **18**, 233–244.

[53] H. Chen, J. A. Parkinson, R. E. Morris and P. J. Sadler, *J. Am. Chem. Soc.*, 2003, **125**, 173–186.

[54] H. Chen, J. A. Parkinson, S. Parsons, R. A. Coxall, R. O. Gould and P. J. Sadler, *J. Am. Chem. Soc.*, 2002, **124**, 3064–3082.

[55] R. E. Morris, R. E. Aird, P. Del Socorro Murdoch, H. Chen, J. Cummings, N. D. Hughes, S. Parsons, A. Parkin, G. Boyd, D. I. Jodrell and P. J. Sadler, *J. Med. Chem.*, 2001, **44**, 3616–3621.

[56] R. E. Aird, J. Cummings, A. A. Ritchie, M. Muir, D. I. Jodrell, R. E. Morris, H. Chen and P. J. Sadler, *Br. J. Cancer*, 2002, **86**, 1652–1657.

[57] J. P. C. Coverdale, I. Romero-canelón, C. Sanchez-cano, G. J. Clarkson, A. Habtemariam, M. Wills and P. J. Sadler, *Nat. Chem.*, DOI: 10.1038/nchem.2918.

[58] B. Cebrián-Losantos, A. A. Krokhin, I. N. Stepanenko, R. Eichinger, M. A. Jakupec, V. B. Arion and B. K. Keppler, *Inorg. Chem.*, 2007, **46**, 5023–33.

[59] A. Egger, B. Cebrián-Losantos, I. N. Stepanenko, A. A. Krokhin, R. Eichinger, M. A. Jakupec, V. B. Arion and B. K. Keppler, *Chem. Biodivers.*, 2008, **5**, 1588–1593.

[60] P. S. Kuhn, G. E. Büchel, K. K. Jovanović, L. Filipović, S. Radulović, P. Rapta and V. B. Arion, *Inorg. Chem.*, 2014, **53**, 11130–11139.

[61] G. E. Buchel, I. N. Stepanenko, M. Hejl, M. A. Jakupec, B. K. Keppler and V. B. Arion, *Inorg. Chem.*, 2011, **50**, 7690–7697.

[62] A. Dorcier, W. H. Ang, S. Bolano, L. Gonsalvi, L. Juillerat-Jeannerat, G. Laurenczy, M. Peruzzini, A. D. Phillips, F. Zanobini and P. J. Dyson, *Organometallics*, 2006, **25**, 4090–4096.

[63] A. Dorcier, C. G. Hartinger, R. Scopelliti, R. H. Fish, B. K. Keppler and P. J. Dyson, *J. Inorg. Biochem.*, 2008, **102**, 1066–1076.

[64] Y. Fu, A. Habtemariam, A. M. Pizarro, S. H. Van Rijt, D. J. Healey, P. A. Cooper, S. D. Shnyder, G. J. Clarkson and P. J. Sadler, *J. Med. Chem.*, 2010, **53**, 8192–8196.

[65] S. H. van Rijt, I. Romero-Canelón, Y. Fu, S. D. Shnyder and P. J. Sadler, *Metallomics*, 2014, **6**, 1014.

[66] N. R. Champness, *Dalt. Trans.*, 2011, **40**, 10311.

[67] A. Bergamo, A. Masi, A. F. A. Peacock, A. Habtemariam, P. J. Sadler and G. Sava, *J. Inorg. Biochem.*, 2010, **104**, 79–86.

[68] S. D. Shnyder, Y. Fu, A. Habtemariam, S. H. van Rijt, P. A. Cooper, P. M. Loadman and P. J. Sadler, *Medchemcomm*, 2011, **2**, 666.

[69] S. M. Meier, M. Hanif, Z. Adhireksan, V. Pichler, M. Novak, E. Jirkovsky, M. A. Jakupec, V. B. Arion, C. A. Davey, B. K. Keppler and C. G. Hartinger, *Chem. Sci.*, 2013, **4**, 1837.

[70] S. H. Van Rijt, A. F. Peacock, R. D. Johnstone, S. Parsons and P. J. Sadler, *Inorg. Chem.*, 2009, **48**, 1753–1762.

[71] A. F. A. Peacock, M. Melchart, R. J. Deeth, A. Habtemariam, S. Parsons and P. J. Sadler, *Chemistry*, 2007, **13**, 2601–13.

[72] A. F. A. Peacock, S. Parsons and P. J. Sadler, *J. Am. Chem. Soc.*, 2007, **129**, 3348–57.

[73] L. Messori, G. Marcon, P. Orioli, M. Fontani, P. Zanello, A. Bergamo, G. Sava and P. Mura, *J. Inorg. Biochem.*, 2003, **95**, 37–46.

[74] G. Marcon, A. Casini, P. Mura, L. Messori, A. Bergamo and P. Orioli, *Met. Based. Drugs*, 2000, **7**, 195–200.

[75] A. Casini, F. Edafe, M. Erlandsson, L. Gonsalvi, A. Ciancetta, N. Re,

A. Ienco, L. Messori, M. Peruzzini and P. J. Dyson, *Dalt. Trans.*, 2010, **39**, 5556–63.

[76] T. Giraldi, G. Sava, G. Mestroni, G. Zassinovich and D. Stolfa, *Chem. Biol. Interact.*, 1978, **22**, 231–238.

[77] G. Sava, P. Piccini, G. Mestroni, G. Zassinovich and A. Bontempi, *In Vivo*, 1987, **1**, 27–30.

[78] S. Scha and W. S. Sheldrick, *J. Organomet. Chem.*, 2007, **692**, 1300–1309.

[79] S. J. Lucas, R. M. Lord, R. L. Wilson, R. M. Phillips, V. Sridharan and P. C. McGowan, *Dalt. Trans.*, 2012, **41**, 13800.

[80] R. P. Paitandi, S. Mukhopadhyay, R. S. Singh, V. Sharma, S. M. Mobin and D. S. Pandey, *Inorg. Chem.*, 2017, **56**, 12232–12247.

[81] J. Ruiz, V. Rodríguez, N. Cutillas, K. G. Samper, M. Capdevila, Ò. Palacios and A. Espinosa, *Dalt. Trans.*, 2012, **41**, 12847.

[82] M. Ali Nazif, J. A. Bangert, I. Ott, R. Gust, R. Stoll and W. S. Sheldrick, *J. Inorg. Biochem.*, 2009, **103**, 1405–1414.

[83] P. Štarha, A. Habtemariam, I. Romero-Canelón, G. J. Clarkson and P. J. Sadler, *Inorg. Chem.*, 2016, **55**, 2324–2331.

[84] Z. Liu, I. Romero-Canelõn, B. Qamar, J. M. Hearn, A. Habtemariam, N. P. Barry, A. M. Pizarro, G. J. Clarkson and P. J. Sadler, *Angew. Chemie - Int. Ed.*, 2014, **53**, 3941–3946.

[85] Z. Liu, R. J. Deeth, J. S. Butler, A. Habtemariam, M. E. Newton and P. J. Sadler, *Angew. Chemie - Int. Ed.*, 2013, **52**, 4194–4197.

[86] A. J. Millett, A. Habtemariam, I. Romero-Canelón, G. J. Clarkson and P. J. Sadler, *Organometallics*, 2015, **34**, 2683–2694.

[87] R. Marrington, T. R. Dafforn, D. J. Halsall, J. I. MacDonald, M. Hicks and A. Rodger, *Analyst*, 2005, **130**, 1608.

[88] R. Marrington, T. R. Dafforn, D. J. Halsall and A. Rodger, *Biophys. J.*, 2004, **87**, 2002–2012.

[89] O. V. Dolomanov, L. J. Bourhis, R. J. Gildea, J. A. K. Howard and H. Puschmann, *J. Appl. Crystallogr.*, 2009, **42**, 339–341.

[90] G. M. Sheldrick, *Acta Crystallogr. Sect. A, Found. Adv.*, 2015, **71**, 3–8.

[91] G. M. Sheldrick, *Acta Crystallogr. Sect. C, Struct. Chem.*, 2015, **71**, 3–8.

[92] Z. Liu, A. Habtemariam, A. M. Pizarro, S. A. Fletcher, A. Kisova, O. Vrana, L. Salassa, P. C. Bruijnincx, G. J. Clarkson, V. Brabec and P. J. Sadler, *J. Med. Chem.*, 2011, **54**, 3011–3026.

[93] M. Björgvinsson, S. Halldorsson, I. Arnason, J. Magull and D. Fenske, *J. Organomet. Chem.*, 1997, **544**, 207–215.

[94] Z. Liu, *PhD Thesis*, University of Warwick, 2011.

[95] J. Tönnemann, J. Risse, Z. Grote, R. Scopelliti and K. Severin, *Eur. J. Inorg. Chem.*, 2013, **2013**, 4558–4562.

[96] S. J. Dougan, M. Melchart, A. Habtemariam, S. Parsons and P. J. Sadler, *Inorg. Chem.*, 2006, **45**, 10882–10894.

[97] *R Core Team, R Foundation for Statistical Computing*, 2014.

[98] *OriginLab Northampton MA*, 2010.

[99] V. Vichai and K. Kirtikara, *Nat. Protoc.*, 2006, **1**, 1112–6.

[100] P. Skehan, R. Storeng, D. Scudiero, A. Monks, J. McMahon, D. Vistica, J. T. Warren, H. Bokesch, S. Kenney and M. R. Boyd, *J. Natl. Cancer Inst.*, 1990, **82**, 1107–12.

[101] Z. Liu and P. J. Sadler, *Acc. Chem. Res.*, 2014, **47**, 1174–1185.

[102] J. M. Hearn, I. Romero-Canelón, B. Qamar, Z. Liu, I. Hands-Portman and P. J. Sadler, *ACS Chem. Biol.*, 2013, **8**, 1335–1343.

[103] R. J. McQuitty, *PhD Thesis*, University of Warwick, 2013.

[104] Y. Fu, *PhD Thesis*, University of Warwick, 2011.

[105] A. M. Urbanska, E. D. Karagiannis, G. Guajardo, R. S. Langer and D. G. Anderson, *Biomaterials*, 2012, **33**, 4752–61.

[106] C. A. Lipinski, F. Lombardo, B. W. Dominy and P. J. Feeney, *Adv. Drug Deliv. Rev.*, 2012, **64**, 4–17.

[107] M. S. Surapaneni, S. K. Das and N. G. Das, *ISRN Pharmacol.*, 2012, **2012**, 623139.

[108] S. A. Abraham, D. N. Waterhouse, L. D. Mayer, P. R. Cullis, T. D. Madden and M. B. Bally, *Methods Enzymol.*, 2005, **391**, 71–97.

[109] P. R. Rich, *Biochem. Soc. Trans.*, 2003, **31**, 1095–105.

[110] P. Belenky, K. L. Bogan and C. Brenner, *Trends Biochem. Sci.*, 2007, **32**, 12–19.

[111] M. Murphy, *Biochem. J.*, 2009, **417**, 1–13.

[112] S. Dröse and U. Brandt, *Adv. Exp. Med. Biol.*, 2012, **748**, 145–169.

[113] J. Wang and J. Yi, *Cancer Biol. Ther.*, 2008, **7**, 1875–1884.

[114] F. Wang, A. Habtemariam, E. P. L. van der Geer, R. Fernández, M. Melchart, R. J. Deeth, R. Aird, S. Guichard, F. P. A. Fabbiani, P. Lozano-Casal, I. D. H. Oswald, D. I. Jodrell, S. Parsons and P. J. Sadler, *Proc. Natl. Acad. Sci. U. S. A.*, 2005, **102**, 18269–74.

[115] S. W. Smith, *Toxicol. Sci.*, 2009, **110**, 4–30.

[116] D. Trachootham, J. Alexandre and P. Huang, *Nat. Rev. Drug Discov.*, 2009, **8**, 579–591.

[117] T. Bugarcic, A. Habtemariam, R. J. Deeth, F. P. A. Fabbiani, S. Parsons and P. J. Sadler, *Inorg. Chem.*, 2009, **48**, 9444–53.

[118] I. Romero-Canelón and P. J. Sadler, *Inorg. Chem.*, 2013, **52**, 12276–12291.

[119] U. Jungwirth, C. R. Kowol, B. K. Keppler and G. Christian, *Antioxid. Redox Signal.*, 2012, **15**, 1085–1127.

[120] J. M. Hearn, G. M. Hughes, I. Romero-Canelón, A. F. Munro, B. Rubio-Ruiz, Z. Liu, N. O. Carragher and P. J. Sadler, *Metallomics*, DOI: 10.1039/C7MT00242D.

[121] Y. Wang, J. Chang, X. Liu, X. Zhang, S. Zhang, X. Zhang, D. Zhou and G. Zheng, *Aging (Albany. NY).*, 2016, **8**, 2915–2926.

[122] L. Raj, T. Ide, A. U. Gurkar, M. Foley, M. Schenone, X. Li, N. J. Tolliday, T. R. Golub, S. A. Carr, A. F. Shamji, A. M. Stern, A. Mandinova, S. L. Schreiber and S. W. Lee, *Nature*, 2011, **475**, 231–4.

[123] H. Dhillon, S. Chikara and K. M. Reindl, *Toxicol. Reports*, 2014, **1**, 309–318.

[124] J. M. Hearn, I. Romero-Canelón, A. F. Munro, Y. Fu, A. M. Pizarro, M. J. Garnett, U. McDermott, N. O. Carragher and P. J. Sadler, *Proc. Natl. Acad. Sci. U. S. A.*, 2015, **112**, E3800–5.

[125] R. J. Needham, C. Sanchez-Cano, X. Zhang, I. Romero-Canelón, A. Habtemariam, M. S. Cooper, L. Meszaros, G. J. Clarkson, P. J. Blower and P. J. Sadler, *Angew. Chem. Int. Ed. Engl.*, 2017, **56**, 1017–1020.

[126] S. J. Dougan, A. Habtemariam, S. E. McHale, S. Parsons and P. J.

Sadler, *Proc Natl Acad Sci U S A*, 2008, **105**, 11628–11633.

[127] Z. Liu, I. Romero-Canelón, A. Habtemariam, G. J. Clarkson and P. J. Sadler, *Organometallics*, 2014, **33**, 5324–5333.

[128] Z. Liu and P. J. Sadler, *Acc. Chem. Res.*, 2014, **47**, 1174–1185.

[129] S. Turkseven, A. Kruger, C. J. Mingone, P. Kaminski, M. Inaba, L. F. Rodella, S. Ikehara, M. S. Wolin and N. G. Abraham, *Am. J. Physiol. Heart Circ. Physiol.*, 2005, **289**, H701–H707.

[130] F. S. Hosnijeh, Q. Lan, N. Rothman, C. San Liu, W.-l. Cheng, A. Nieters, P. Guldberg, A. Tjønneland, D. Campa, A. Martino, H. Boeing, A. Trichopoulou, P. Lagiou, D. Trichopoulos, V. Krogh, R. Tumino, S. Panico, G. Masala, E. Weiderpass, J. M. Huerta Castaño, E. Ardanaz, N. Sala, M. Dorronsoro, J. R. Quirós, M.-J. Sánchez, B. Melin, A. S. Johansson, J. Malm, S. Borgquist, P. H. Peeters, H. B. Bueno-de Mesquita, N. Wareham, K.-T. Khaw, R. C. Travis, P. Brennan, A. Siddiq, E. Riboli, P. Vineis and R. Vermeulen, *Blood*, 2014, **124**, 530–5.

[131] C. Henchcliffe and M. F. Beal, *Nat. Clin. Pract. Neurol.*, 2008, **4**, 600–9.

[132] C. Sanchez-Cano, I. Romero-Canelón, Y. Yang, I. J. Hands-Portman, S. Bohic, P. Cloetens and P. J. Sadler, *Chemistry*, 2017, **23**, 2512–2516.

[133] H. U. Simon, A. Haj-Yehia and F. Levi-Schaffer, *Apoptosis*, 2000, **5**, 415–418.

[134] N. R. Jena, *J. Biosci.*, 2012, **37**, 503–507.

[135] J. Assis, D. Pereira and R. Medeiros, *World J. Clin. Oncol.*, 2013, **4**, 14–24.

[136] T. Sawada, Y. S. Chung, B. Nakata, T. Kubo, Y. Kondo, T. Sogabe, N. Onoda, Y. Ogawa, N. Yamada and M. Sowa, *Hum Cell*, 1994, **7**, 138–144.

[137] W. D. Foulkes, I. E. Smith and J. S. Reis-Filho, *N. Engl. J. Med.*, 2010, **363**, 1938–1948.

[138] C. J. Lord and A. Ashworth, *Nature*, 2012, **481**, 287–294.

[139] A. Ciccia and S. J. Elledge, *Mol. Cell*, 2010, **40**, 179–204.

[140] Y. Pommier, E. Leo, H. Zhang and C. Marchand, *Chem. Biol.*, 2010, **17**, 421–433.

[141] B. A. Woynarowska and J. M. Woynarowski, *Biochim. Biophys. Acta* -

Mol. Basis Dis., 2002, **1587**, 309–317.

[142] K. Cheung-Ong, G. Giaever and C. Nislow, *Chem. Biol.*, 2013, **20**, 648–659.

[143] P. J. Loehrer and L. H. Einhorn, *Ann. Intern. Med.*, 1984, **100**, 704–13.

[144] V. Novohradsky, L. Zerzankova, J. Stepankova, A. Kisova, H. Kostrhunova, Z. Liu, P. J. Sadler, J. Kasparkova and V. Brabec, *Metallomics*, 2014, **6**, 1491–1501.

[145] I. Romero-Canelón, L. Salassa and P. J. Sadler, *J. Med. Chem.*, 2013, **56**, 1291–1300.

[146] A. Kastl, A. Wilbuer, A. L. Merkel, L. Feng, P. Di Fazio, M. Ocker and E. Meggers, *Chem. Commun.*, 2012, **48**, 1863–1865.

[147] L. He, S. Y. Liao, C. P. Tan, Y. Y. Lu, C. X. Xu, L. N. Ji and Z. W. Mao, *Chem Commun*, 2014, **50**, 5611–5614.

[148] P. K. Sasmal, C. N. Streu and E. Meggers, *Chem. Commun.*, 2013, **49**, 1581–1587.

[149] A. L. Noffke, A. Habtemariam, A. M. Pizarro and P. J. Sadler, *Chem. Commun.*, 2012, **48**, 5219.

[150] Y. Geldmacher, K. Splith, I. Kitanovic, H. Alborzinia, S. Can, R. Rubbiani, M. A. Nazif, P. Wefelmeier, A. Prokop, I. Ott, S. Wölfl, I. Neundorf and W. S. Sheldrick, *J. Biol. Inorg. Chem.*, 2012, **17**, 631–646.

[151] I. Iavicoli, V. Cufino, M. Corbi, M. Goracci, E. Caredda, A. Cittadini, A. Bergamaschi and A. Sgambato, *Toxicol. Vitr.*, 2012, **26**, 963–969.

[152] Y. Fan, C. Li, H. Cao, F. Li and D. Chen, *Biomaterials*, 2012, **33**, 4220–4228.

[153] V. Brabec and J. Kasparkova, *Drug Resist. Updat.*, 2005, **8**, 131–146.

[154] P. A. Andrews, *Cancer Treat. Res.*, 1994, **73**, 217–48.

[155] H. Kostrhunova, J. Florian, O. Novakova, A. F. Peacock, P. J. Sadler and V. Brabec, *J. Med. Chem.*, 2008, **51**, 3635–3643.

[156] A. M. Pizarro and P. J. Sadler, *Biochimie*, 2009, **91**, 1198–1211.

[157] J. Pracharova, L. Zerzankova, J. Stepankova, O. Novakova, N. J. Farrer, P. J. Sadler, V. Brabec and J. Kasparkova, *Chem. Res. Toxicol.*, 2012, **25**, 1099–1111.

[158] V. Novohradsky, Z. Liu, M. Vojtiskova, P. J. Sadler, V. Brabec and

J. Kasparkova, *Metallomics*, 2014, **6**, 682–690.

[159] X. Song, Y. Qian, R. Ben, X. Lu, H. L. Zhu, H. Chao and J. Zhao, *J. Med. Chem.*, 2013, **56**, 6531–6535.

[160] H.-K. Liu and P. J. Sadler, *Acc. Chem. Res.*, 2011, **44**, 349–359.

[161] Z. Liu, L. Salassa, A. Habtemariam, A. M. Pizarro, G. J. Clarkson and P. J. Sadler, *Inorg. Chem.*, 2011, **50**, 5777–5783.

[162] P. Annen, S. Schildberg and W. S. Sheldrick, *Inorganica Chim. Acta*, 2000, **307**, 115–124.

[163] S. Lin, L. Lu, T. S. Kang, J. L. Mergny, C. H. Leung and D. L. Ma, *Anal. Chem.*, 2016, **88**, 10290–10295.

[164] P. A. Vekariya, P. S. Karia, J. V. Vaghasiya, S. Soni, E. Suresh and M. N. Patel, *Polyhedron*, 2016, **110**, 73–84.

[165] H. Ahmad, A. Wragg, W. Cullen, C. Wombwell, A. J. H. M. Meijer and J. A. Thomas, *Chemistry*, 2014, **20**, 3089–96.

[166] J. Sambrook and D. W. Russell, *Molecular Cloning: A Laboratory Manual*, Cold Spring Harbor Laboratory Press, 3rd edn., 2001.

[167] M. E. Reichmann, S. A. Rice, C. A. Thomas and P. Doty, *J. Am. Chem. Soc.*, 1954, **76**, 3047–3053.

[168] M. Jennerwein and P. A. Andrews, *Drug Metab. Dispos.*, 1995, **23**, 178–184.

[169] J. A. Bordelon, K. J. Feierabend, S. A. Siddiqui, L. L. Wright and J. T. Petty, *J. Phys. Chem. B*, 2002, **106**, 4838–4843.

[170] J. Olmsted and D. R. Kearns, *Biochemistry*, 1977, **16**, 3647–54.

[171] I. Romero-Canelón, M. Mos and P. J. Sadler, *J. Med. Chem.*, 2015, **58**, 7874–7880.

[172] M. Deponte, *Biochim. Biophys. Acta*, 2013, **1830**, 3217–66.

[173] G. K. Balendiran, R. Dabur and D. Fraser, *Cell Biochem. Funct.*, 2004, **22**, 343–352.

[174] V. Brabec, V. Kleinwächter, J. L. Butour and N. P. Johnson, *Biophys. Chem.*, 1990, **35**, 129–41.

[175] S. G. K.R., B. B. Mathew, C. Sudhamani and H. B. Naik, *Biomed. Biotechnol.*, 2014, **2**, 1–9.

[176] L. Galluzzi, L. Senovilla, I. Vitale, J. Michels, I. Martins, O. Kepp,

M. Castedo and G. Kroemer, *Oncogene*, 2012, **31**, 1869–1883.

[177] B. Jamali, M. Nakhjavani, L. Hosseinzadeh, S. Amidi, N. Nikounezhad and F. H Shirazi, *Iran. J. Pharm. Res. IJPR*, 2015, **14**, 513–9.

[178] A. K. Godwin, A. Meister, P. J. O'Dwyer, C. S. Huang, T. C. Hamilton and M. E. Anderson, *Proc. Natl. Acad. Sci. U. S. A.*, 1992, **89**, 3070–3074.

[179] J. M. Hearn, I. Romero-Canelon, B. Qamar, Z. Liu, I. Hands-Portman and P. J. Sadler, *ACS Chem. Biol.*, 2013, **8**, 1335–1343.

[180] M. D. Hall, K. A. Telma, K.-E. Chang, T. D. Lee, J. P. Madigan, J. R. Lloyd, I. S. Goldlust, J. D. Hoeschele and M. M. Gottesman, *Cancer Res.*, 2014, **74**, 3913–3922.

[181] K. Howe, M. D. Clark, C. F. Torroja, J. Torrance, C. Berthelot, M. Muffato, J. E. Collins, S. Humphray, K. McLaren, L. Matthews, S. McLaren, I. Sealy, M. Caccamo, C. Churcher, C. Scott, J. C. Barrett, R. Koch, G.-J. Rauch, S. White, W. Chow, B. Kilian, L. T. Quintais, J. A. Guerra-Assunção, Y. Zhou, Y. Gu, J. Yen, J.-H. Vogel, T. Eyre, S. Redmond, R. Banerjee, J. Chi, B. Fu, E. Langley, S. F. Maguire, G. K. Laird, D. Lloyd, E. Kenyon, S. Donaldson, H. Sehra, J. Almeida-King, J. Loveland, S. Trevanion, M. Jones, M. Quail, D. Willey, A. Hunt, J. Burton, S. Sims, K. McLay, B. Plumb, J. Davis, C. Clee, K. Oliver, R. Clark, C. Riddle, D. Elliot, D. Eliott, G. Threadgold, G. Harden, D. Ware, S. Begum, B. Mortimore, B. Mortimer, G. Kerry, P. Heath, B. Phillimore, A. Tracey, N. Corby, M. Dunn, C. Johnson, J. Wood, S. Clark, S. Pelan, G. Griffiths, M. Smith, R. Glithero, P. Howden, N. Barker, C. Lloyd, C. Stevens, J. Harley, K. Holt, G. Panagiotidis, J. Lovell, H. Beasley, C. Henderson, D. Gordon, K. Auger, D. Wright, J. Collins, C. Raisen, L. Dyer, K. Leung, L. Robertson, K. Ambridge, D. Leongamornlert, S. McGuire, R. Gilderthorp, C. Griffiths, D. Manthravadi, S. Nichol, G. Barker, S. Whitehead, M. Kay, J. Brown, C. Murnane, E. Gray, M. Humphries, N. Sycamore, D. Barker, D. Saunders, J. Wallis, A. Babbage, S. Hammond, M. Mashreghi-Mohammadi, L. Barr, S. Martin, P. Wray, A. Ellington, N. Matthews, M. Ellwood, R. Woodmansey, G. Clark, J. D. Cooper, J. Cooper, A. Tromans, D. Grafham, C. Skuce, R. Pandian, R. Andrews, E. Harrison, A. Kim-

berley, J. Garnett, N. Fosker, R. Hall, P. Garner, D. Kelly, C. Bird, S. Palmer, I. Gehring, A. Berger, C. M. Dooley, Z. Ersan-Ürün, C. Eser, H. Geiger, M. Geisler, L. Karotki, A. Kirn, J. Konantz, M. Konantz, M. Oberländer, S. Rudolph-Geiger, M. Teucke, C. Lanz, G. Raddatz, K. Osoegawa, B. Zhu, A. Rapp, S. Widaa, C. Langford, F. Yang, S. C. Schuster, N. P. Carter, J. Harrow, Z. Ning, J. Herrero, S. M. J. Searle, A. Enright, R. Geisler, R. H. A. Plasterk, C. Lee, M. Westerfield, P. J. de Jong, L. I. Zon, J. H. Postlethwait, C. Nüsslein-Volhard, T. J. P. Hubbard, H. Roest Crollius, J. Rogers and D. L. Stemple, *Nature*, 2013, **496**, 498–503.

[182] T. P. Barros, W. K. Alderton, H. M. Reynolds, A. G. Roach and S. Berghmans, *Br. J. Pharmacol.*, 2008, **154**, 1400–1413.

[183] P. Goldsmith, *Curr. Opin. Pharmacol.*, 2004, **4**, 504–512.

[184] A. L. Rubinstein, *Expert Opin. Drug Metab. Toxicol.*, 2006, **2**, 231–240.

[185] A. I. Hashim, X. Zhang, J. W. Wojtkowiak, G. V. Martinez and R. J. Gillies, *NMR Biomed.*, 2011, **24**, 582–591.

[186] M. Damaghi, J. W. Wojtkowiak and R. J. Gillies, *Front. Physiol.*, 2013, **4**, 370.

[187] P. Swietach, R. D. Vaughan-Jones, A. L. Harris and A. Hulikova, *Philos. Trans. R. Soc. B Biol. Sci.*, 2014, **369**, 20130099–20130099.

[188] I. Romero-Canelón, A. M. Pizarro, A. Habtemariam and P. J. Sadler, *Metallomics*, 2012, **4**, 1271.

[189] P. D. Lotlikar and T.-F. Wang, *Toxicol. Lett.*, 1982, **11**, 173–179.

Appendix

IC_{50} Data

Table S1: Compilation of IC_{50} values (in μM) for complexes **1** − **19** in all cell lines in all chapters of this work. Data obtained from triplicate experiments. Cell lines tested were A2780 ovarian carcinoma, A2780cis ovarian carcinoma with acquired CDDP resistance, A549 lung carcinoma, and CNE1 nasopharyngeal carcinoma. CDDP values obtained experimentally or from previously published work,[145] continued on next page (*n.d.* = not determined).

Complex	A2780	A2780cis	A549	CNE1
1	0.095 ± 0.006	0.68 ± 0.03	2.7 ± 0.3	7.1 ± 0.8
2	0.101 ± 0.001	*n.d.*	*n.d.*	*n.d.*
3	1.59 ± 0.03	*n.d.*	*n.d.*	*n.d.*
4	*n.d.*	*n.d.*	*n.d.*	*n.d.*
5	0.14 ± 0.09	0.25 ± 0.06	5.2 ± 0.3	5 ± 1
6	0.108 ± 0.009	0.22 ± 0.02	0.89 ± 0.03	5.03 ± 0.06
7	0.12 ± 0.04	0.114 ± 0.003	1.5 ± 0.3	5.7 ± 0.2
8	0.17 ± 0.07	0.062 ± 0.004	5.12 ± 0.09	1.2 - 6.2
9	0.25 ± 0.02	*n.d.*	1.01 ± 0.08	*n.d.*
10	0.34 ± 0.02	0.049 ± 0.001	1.5 ± 0.4	1.2 - 6.2
11	5.0 ± 0.5	*n.d.*	*n.d.*	*n.d.*
12	0.776 ± 0.002	*n.d.*	*n.d.*	*n.d.*
13	0.126 ± 0.002	9.4 ± 0.7	10.9 ± 0.2	> 10
14	0.22 ± 0.02	*n.d.*	*n.d.*	*n.d.*
15	1.5 ± 0.2	*n.d.*	*n.d.*	*n.d.*
16	0.4 ± 0.1	*n.d.*	*n.d.*	*n.d.*
17	0.184 ± 0.002	*n.d.*	*n.d.*	*n.d.*
18	0.43 ± 0.04	*n.d.*	*n.d.*	*n.d.*
19	16 ± 6	*n.d.*	*n.d.*	*n.d.*
CDDP	1.2 ± 0.2	11.5 ± 0.3	3.3 ± 0.1	7.7 ± 0.2

Table S2: Compilation of IC_{50} values (in μM) for complexes **1** − **19** in all cell lines in all chapters of this work. Data obtained from triplicate experiments. Cell lines tested were CNE2 nasopharyngeal carcinoma, MRC-5 normal human lung fibroblasts, OE19 oesophageal carcinoma, and SUNE-1 nasopharyngeal carcinoma. CDDP values obtained experimentally or from previously published work,[145] continued from next page (*n.d.* = not determined).

Complex	CNE2	MRC-5	OE19	SUNE-1
1	0.98 ± 0.04	3.4 ± 0.5	0.195 ± 0.002	0.58 ± 0.04
2	*n.d.*	*n.d.*	0.3 ± 0.003	1.14 ± 0.01
3	*n.d.*	*n.d.*	3.6 ± 0.3	10.5 ± 0.6
4	*n.d.*	*n.d.*	*n.d.*	*n.d.*
5	10.62 ± 0.04	*n.d.*	0.40 ± 0.03	0.72 ± 0.04
6	1.6 ± 0.2	*n.d.*	0.30 ± 0.01	1.7 ± 0.2
7	2.3 ± 0.3	*n.d.*	1.15 ± 0.02	1.5 ± 0.2
8	1.12 ± 0.09	*n.d.*	*n.d.*	*n.d.*
9	1.26 ± 0.04	*n.d.*	*n.d.*	*n.d.*
10	2.2 ± 0.2	*n.d.*	*n.d.*	*n.d.*
11	*n.d.*	*n.d.*	*n.d.*	*n.d.*
12	*n.d.*	*n.d.*	*n.d.*	*n.d.*
13	4.7 ± 0.5	*n.d.*	*n.d.*	*n.d.*
14	*n.d.*	*n.d.*	*n.d.*	*n.d.*
15	*n.d.*	*n.d.*	*n.d.*	*n.d.*
16	*n.d.*	*n.d.*	*n.d.*	*n.d.*
17	*n.d.*	*n.d.*	*n.d.*	*n.d.*
18	*n.d.*	*n.d.*	*n.d.*	*n.d.*
19	*n.d.*	*n.d.*	*n.d.*	*n.d.*
CDDP	7.7 ± 0.3	16.2 ± 0.6	13.43 ± 0.003	1.14 ± 0.01

Structures of Complexes Synthesised in this Thesis

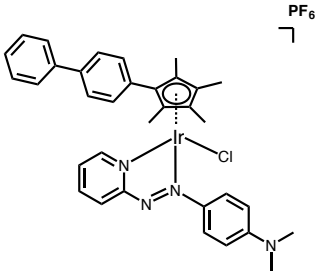

Complex **1***

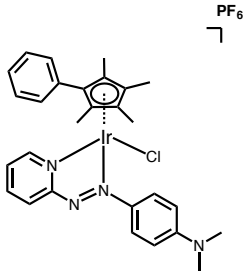

Complex **2**

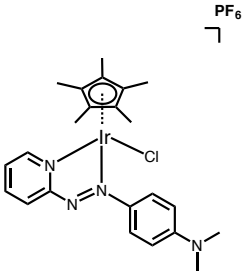

Complex **3**

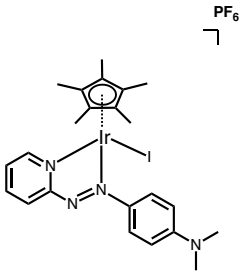

Complex **4**

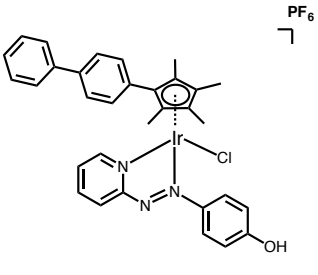

Complex **5***

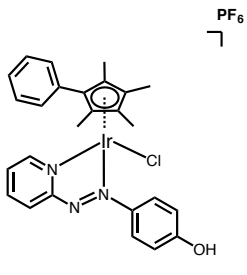

Complex **6***

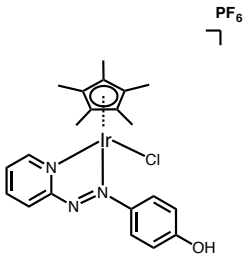

Complex **7**

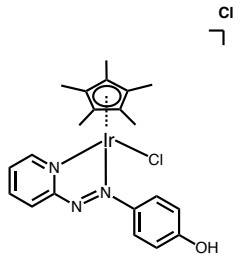

Complex **8***

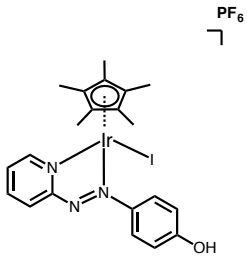

Complex **9**

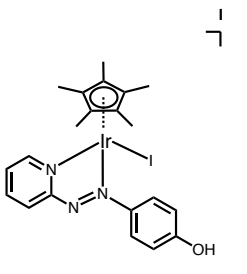

Complex **10***

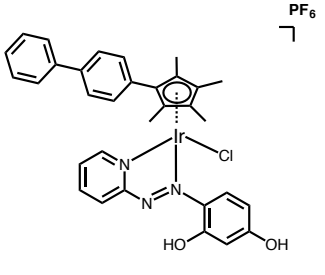

Complex **11**

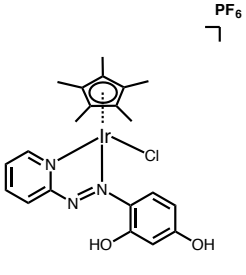

Complex **12**

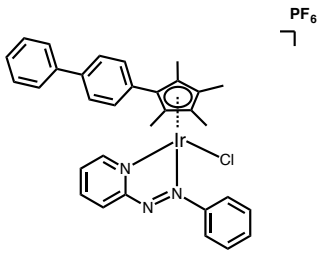

Complex **13***

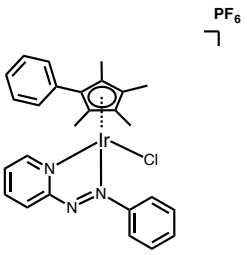

Complex **14***

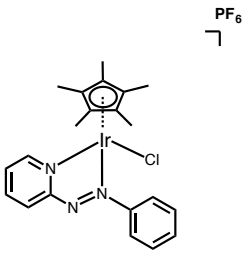

Complex **15**

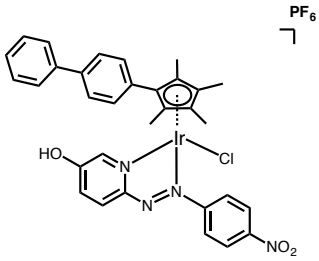

Complex **16**

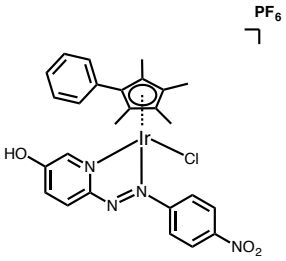

Complex **17**

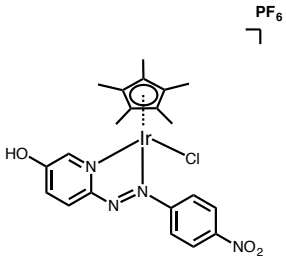

Complex **18**

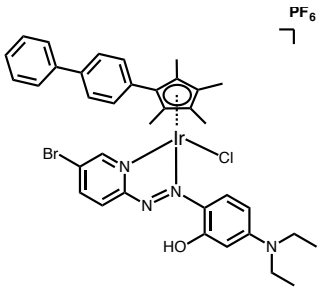

Complex **19**

Figure S1: Structures of complexes **1** − **19** studied in this work. A crystal structure was obtained for complexes marked with an asterisk (*) Families of complexes grouped by bidentate azopyridine ligand. The azpyNMe_2 family consists of complexes **1** − **4**, the azpyOH family of complexes **5** − **10**, the azpy$(OH)_2$ family of complexes **11** and **12**, the azpy family of complexes **13** − **15**, the HOazpyNO_2 family of complexes **16** − **18**, and the single Brazpy(OH)NEt_2 complex **19**.

LC-MS Characterisation Data

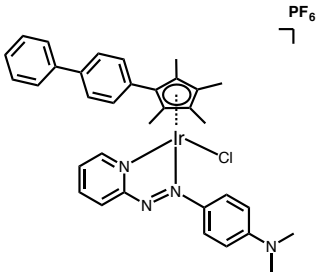

Complex **1**

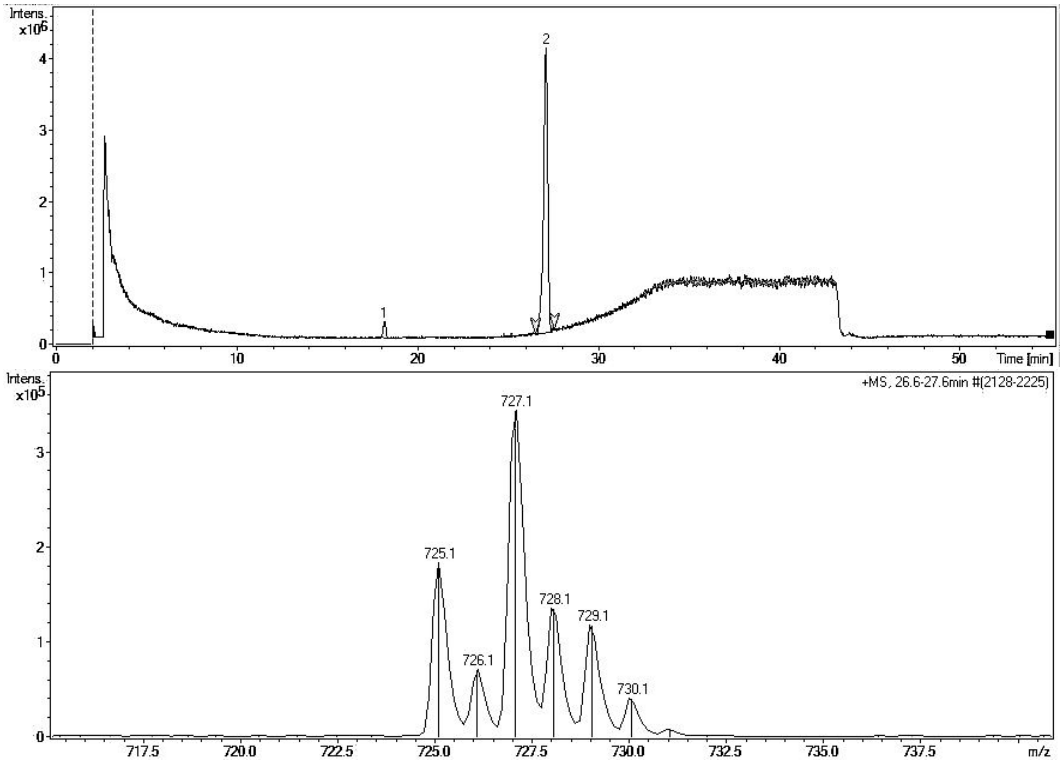

Figure S2: (Top) LC trace of complex **1**. (Bottom) Primary MS fragment of highlighted LC peak.

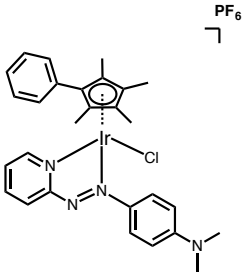

Complex **2**

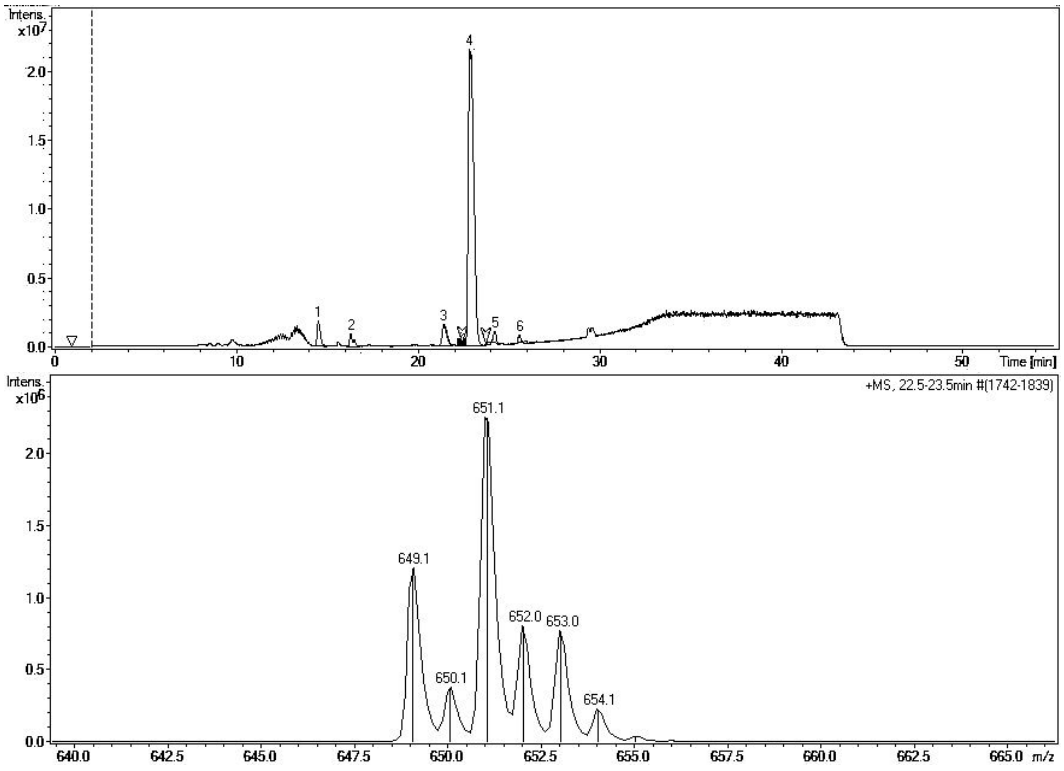

Figure S3: (Top) LC trace of complex **2**. (Bottom) Primary MS fragment of highlighted LC peak.

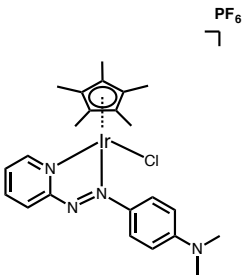

Complex **3**

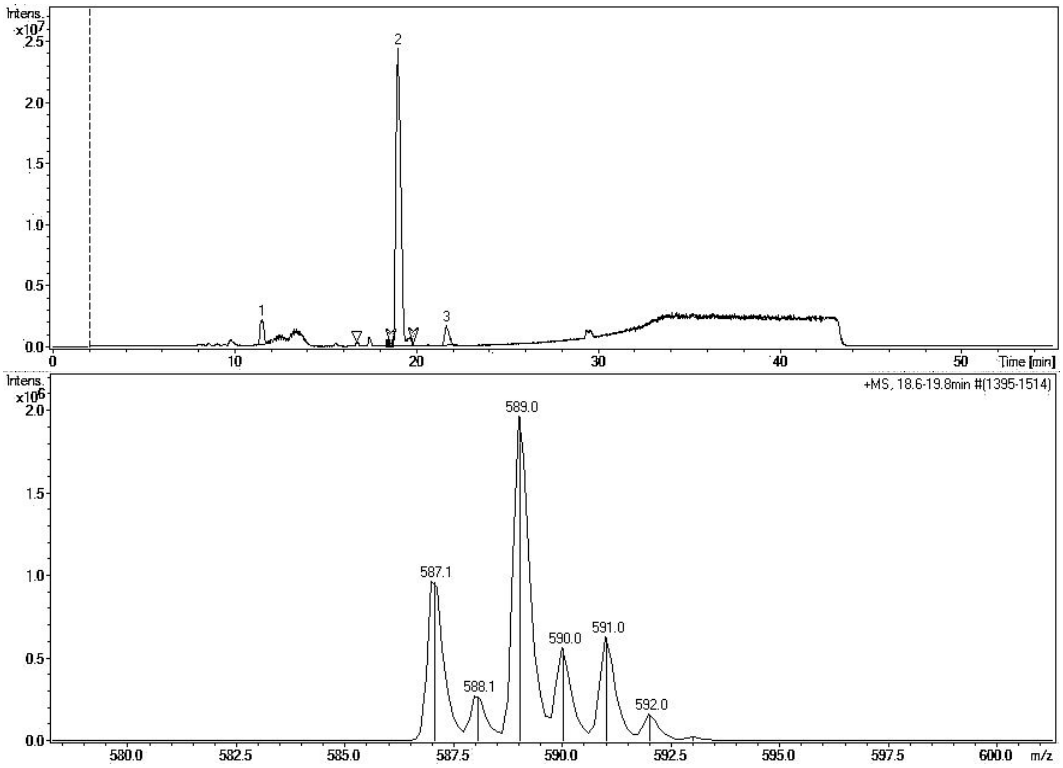

Figure S4: (Top) LC trace of complex **3**. (Bottom) Primary MS fragment of highlighted LC peak.

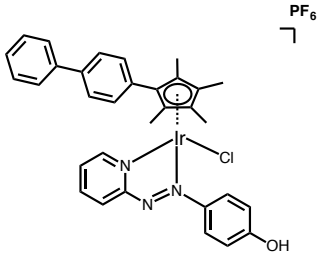

Complex **5**

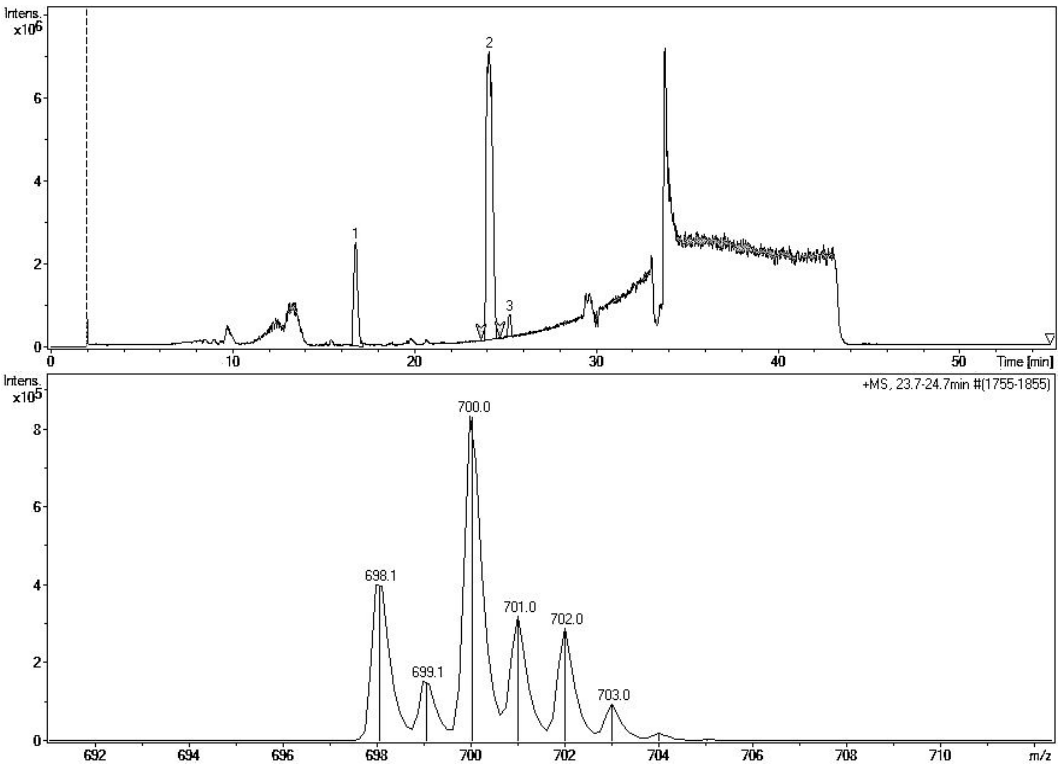

Figure S5: (Top) LC trace of complex **5**. (Bottom) Primary MS fragment of highlighted LC peak.

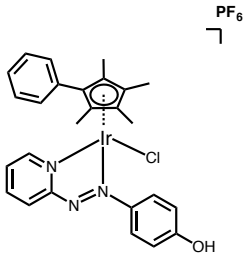

Complex **6**

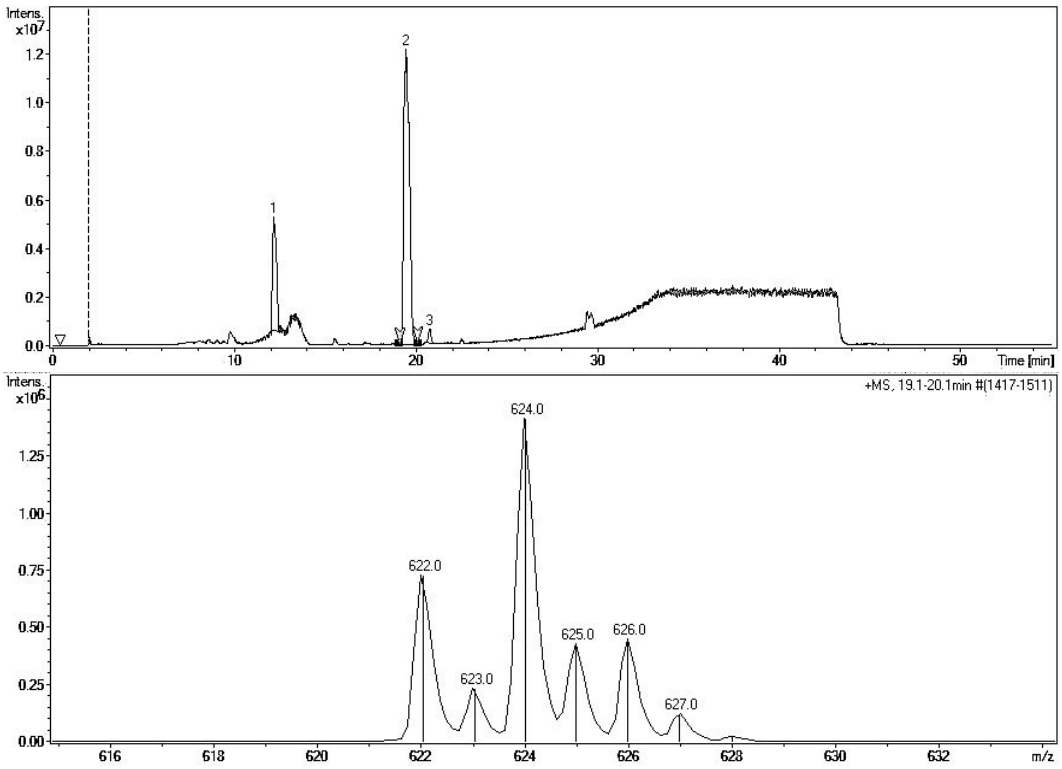

Figure S6: (Top) LC trace of complex **6**. (Bottom) Primary MS fragment of highlighted LC peak.

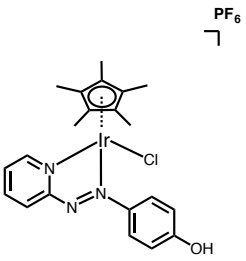

Complex **7**

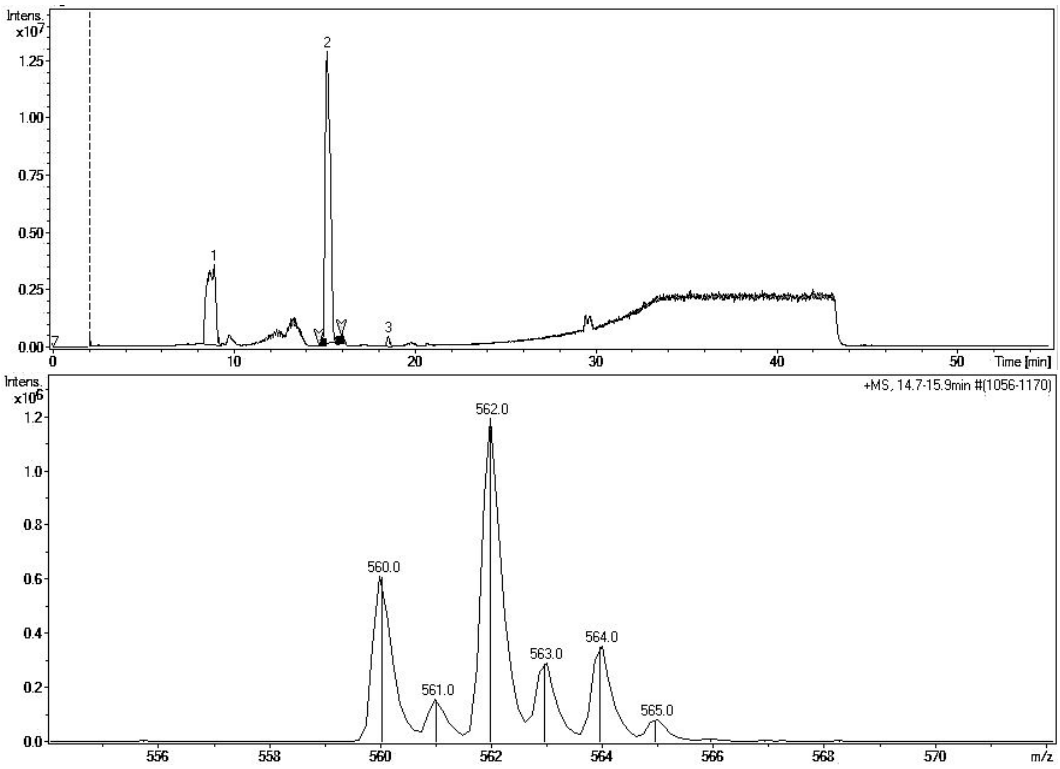

Figure S7: (Top) LC trace of complex **7**. (Bottom) Primary MS fragment of highlighted LC peak.

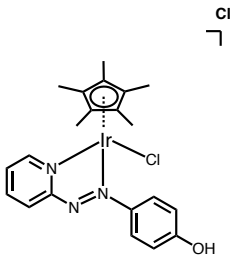

Complex **8**

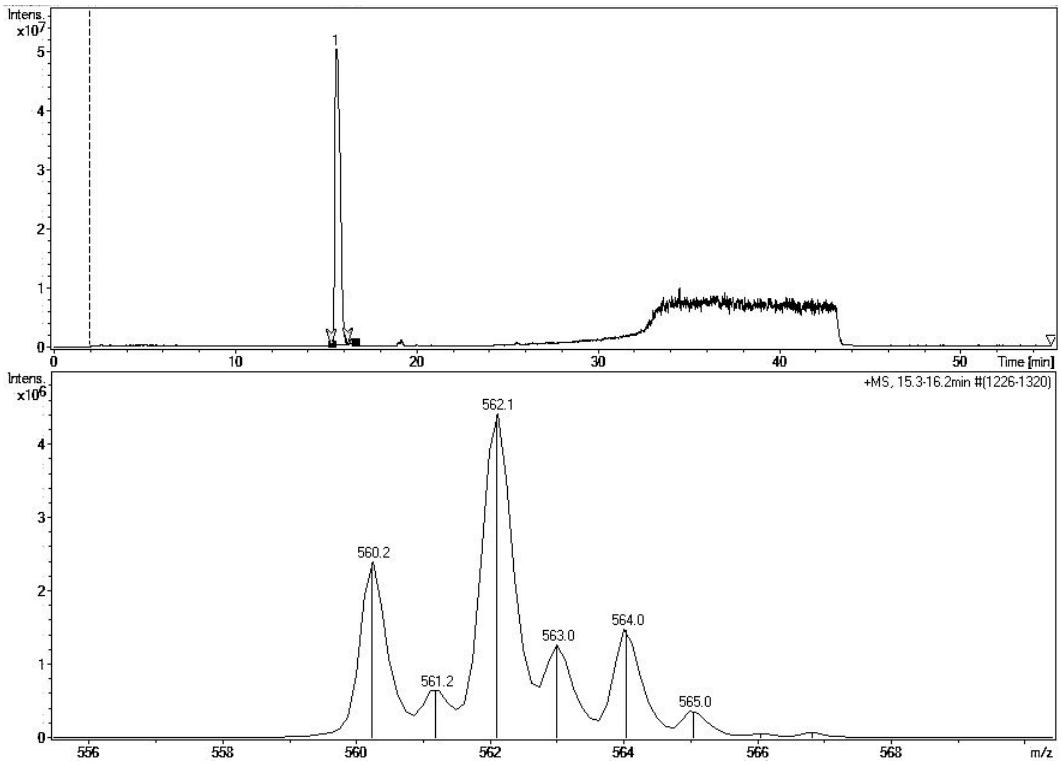

Figure S8: (Top) LC trace of complex **8**. (Bottom) Primary MS fragment of highlighted LC peak.

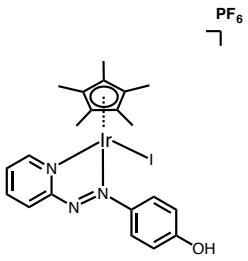

Complex **9**

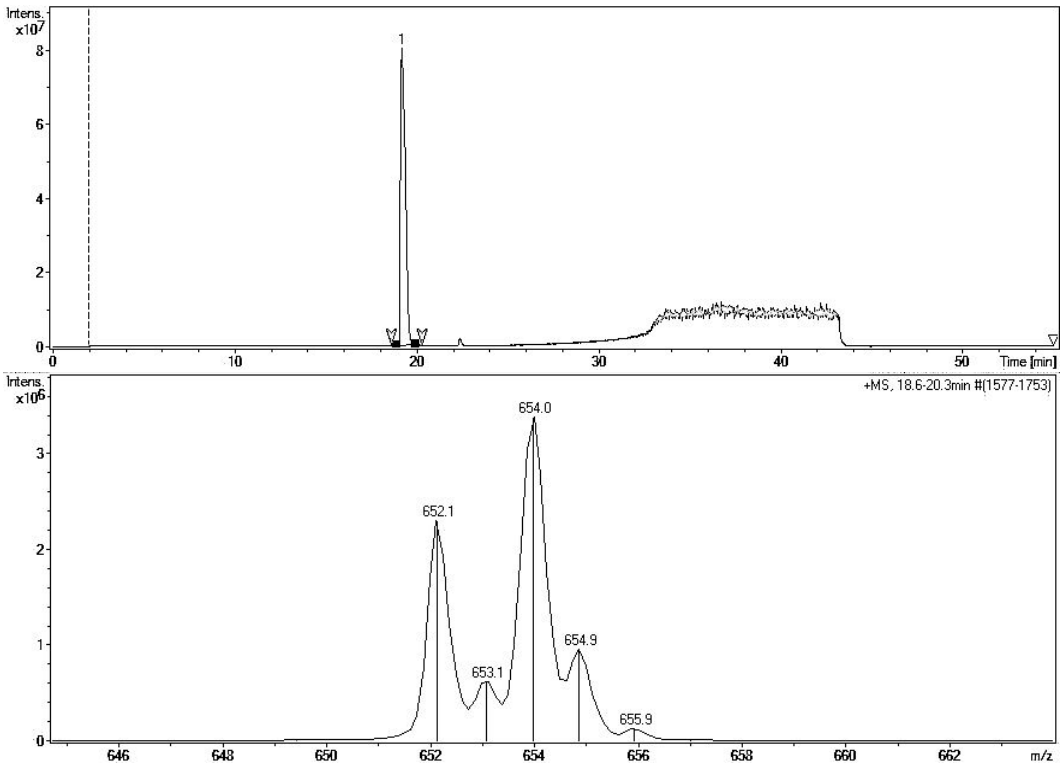

Figure S9: (Top) LC trace of complex **9**. (Bottom) Primary MS fragment of highlighted LC peak.

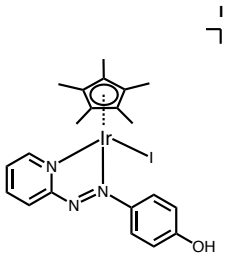

Complex **10**

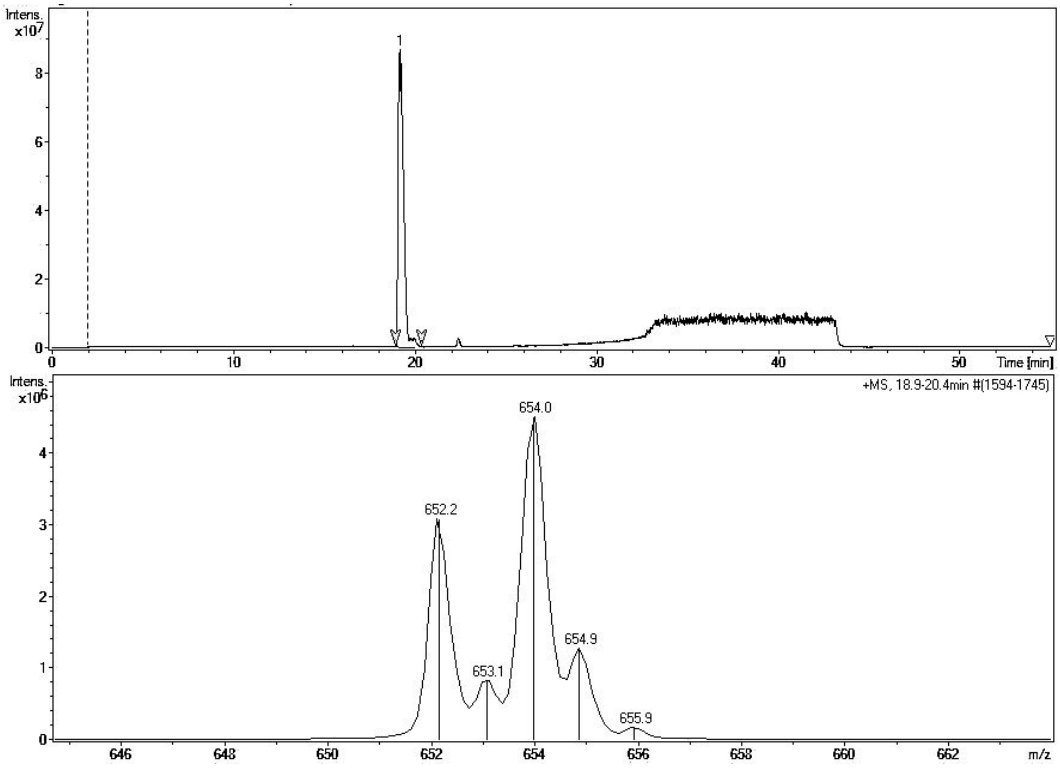

Figure S10: (Top) LC trace of complex **10**. (Bottom) Primary MS fragment of highlighted LC peak.

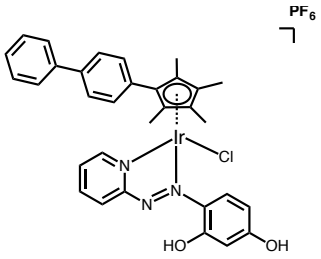

Complex **11**

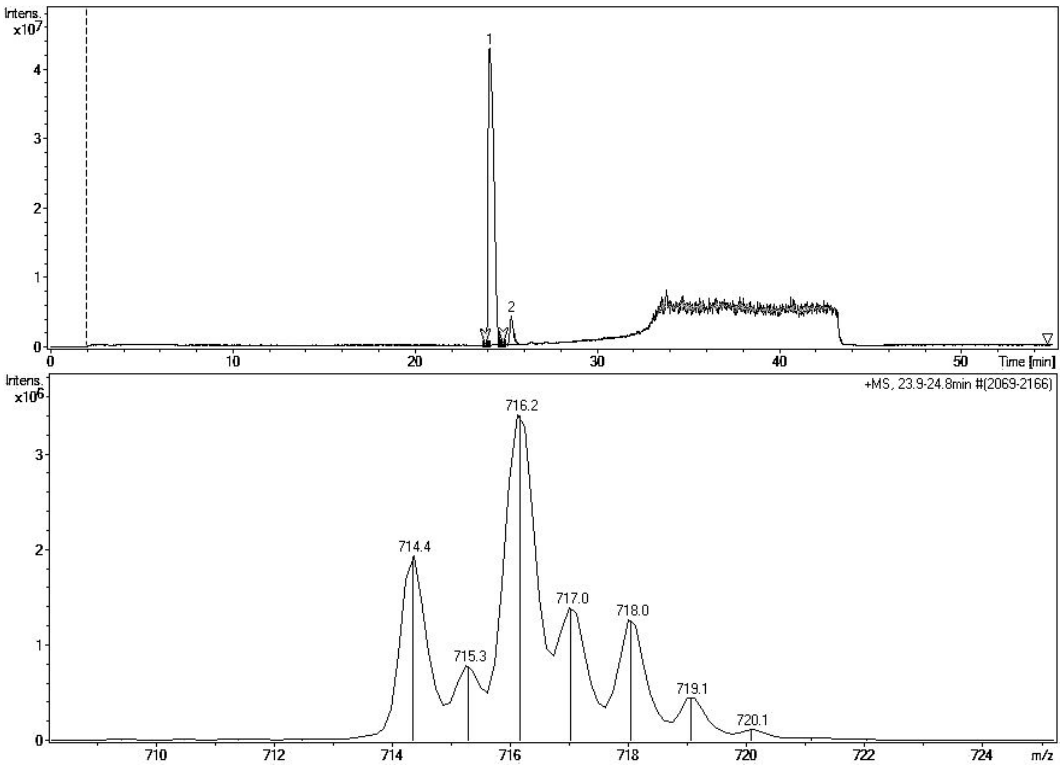

Figure S11: (Top) LC trace of complex **11**. (Bottom) Primary MS fragment of highlighted LC peak.

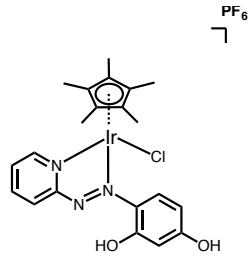

Complex **12**

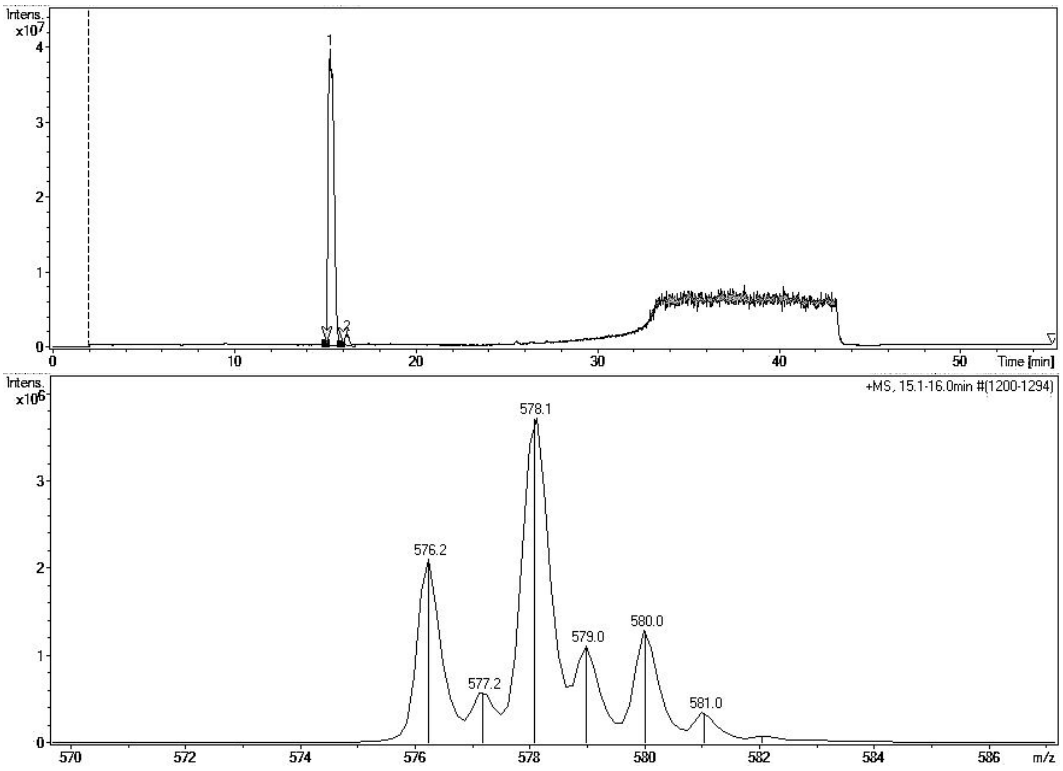

Figure S12: (Top) LC trace of complex **12**. (Bottom) Primary MS fragment of highlighted LC peak.

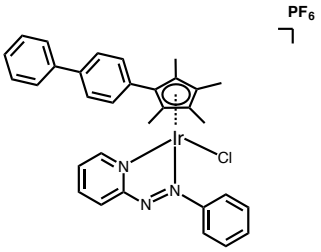

Complex **13**

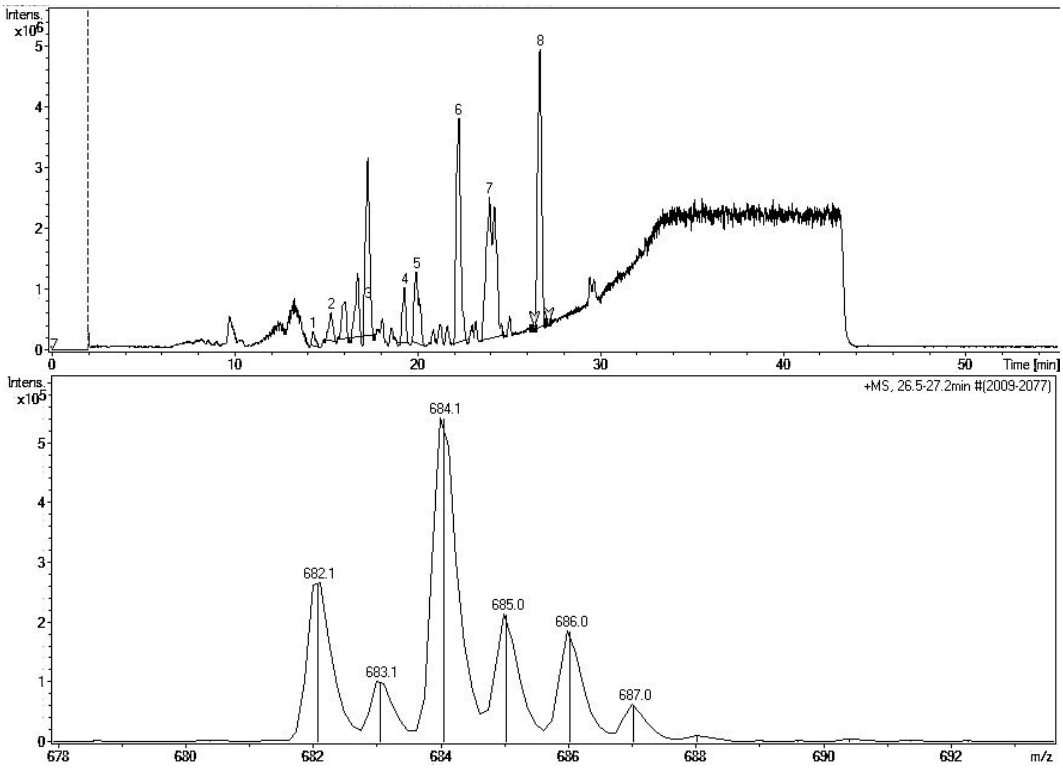

Figure S13: (Top) LC trace of complex **13**. (Bottom) Primary MS fragment of highlighted LC peak.

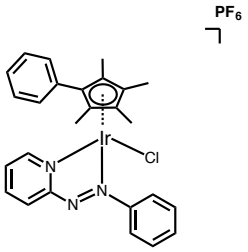

Complex **14**

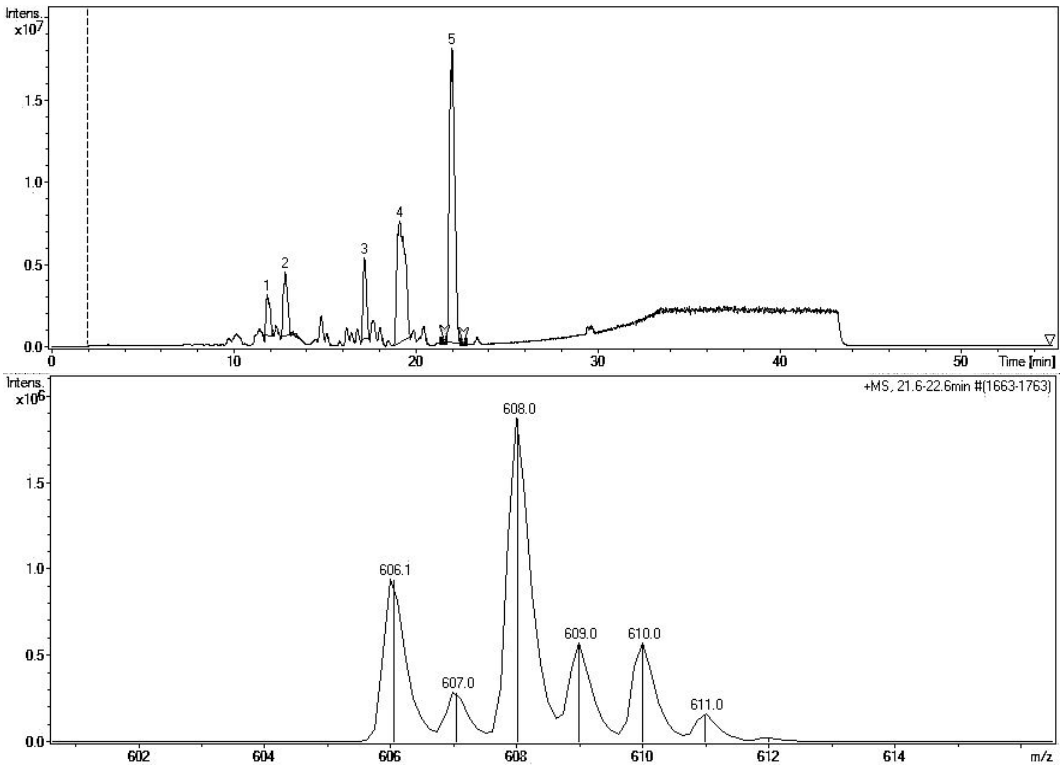

Figure S14: (Top) LC trace of complex **14**. (Bottom) Primary MS fragment of highlighted LC peak.

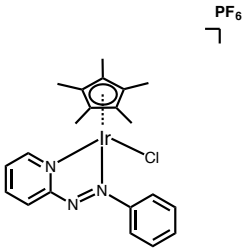

Complex **15**

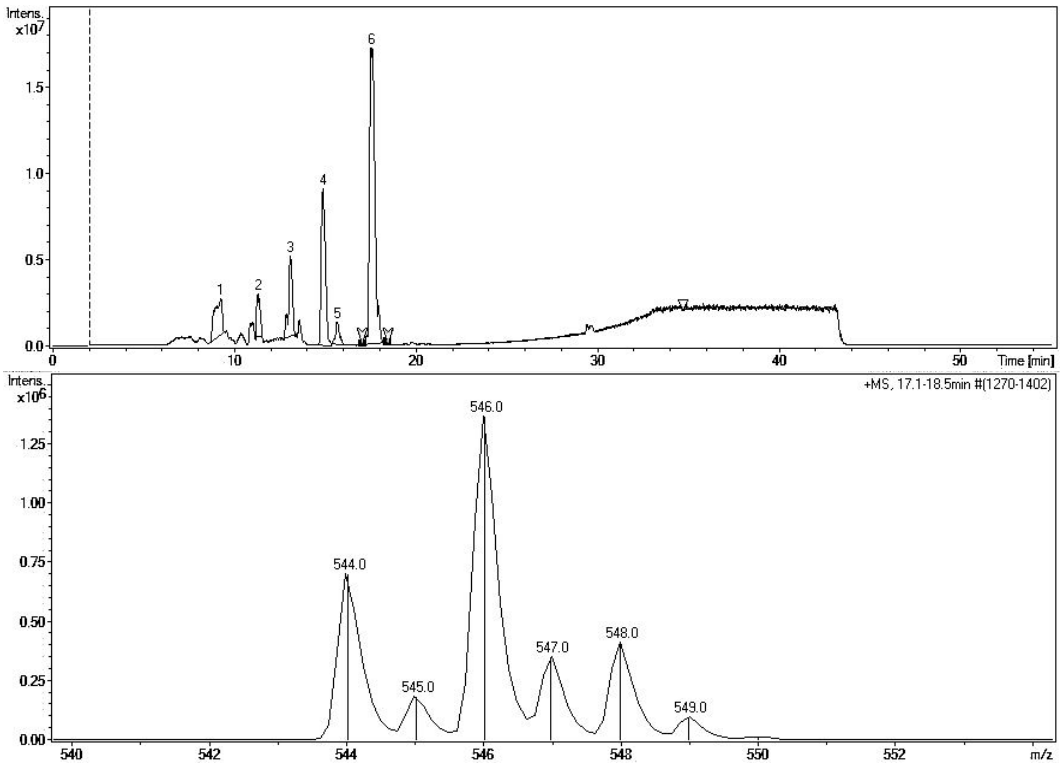

Figure S15: (Top) LC trace of complex **15**. (Bottom) Primary MS fragment of highlighted LC peak.

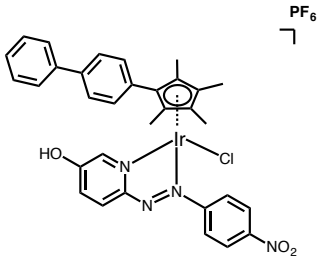

Complex **16**

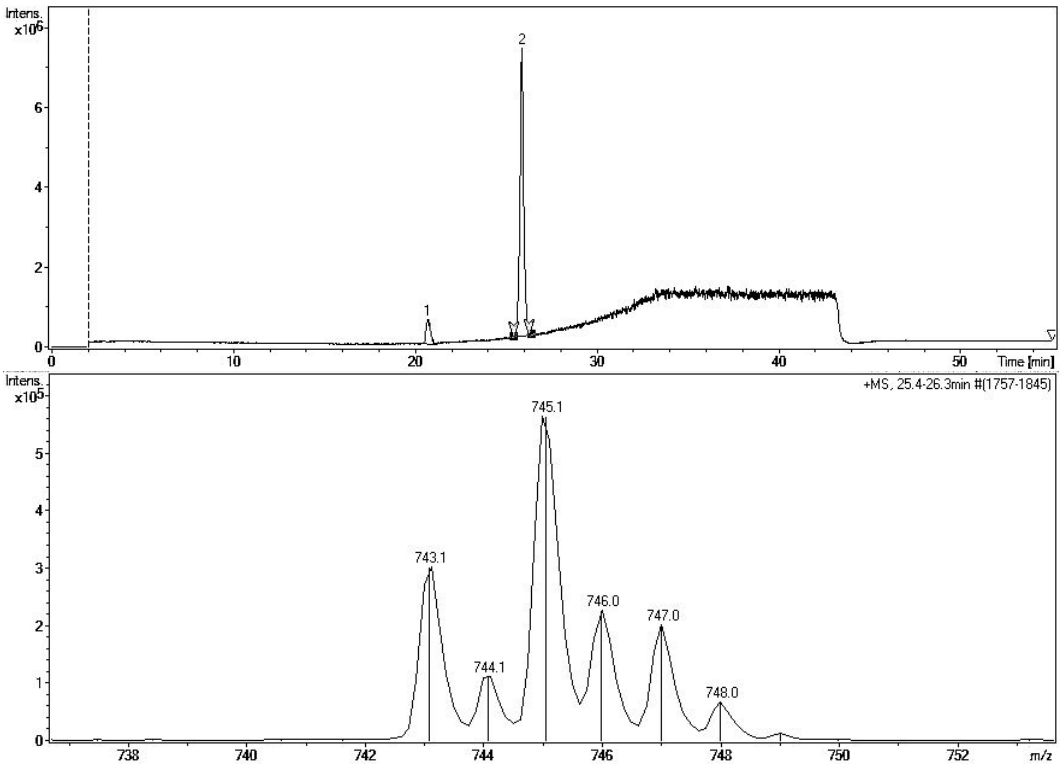

Figure S16: (Top) LC trace of complex **16**. (Bottom) Primary MS fragment of highlighted LC peak.

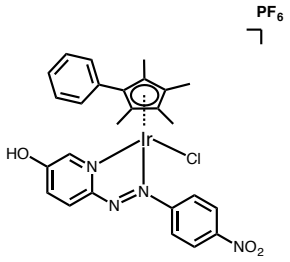

Complex **17**

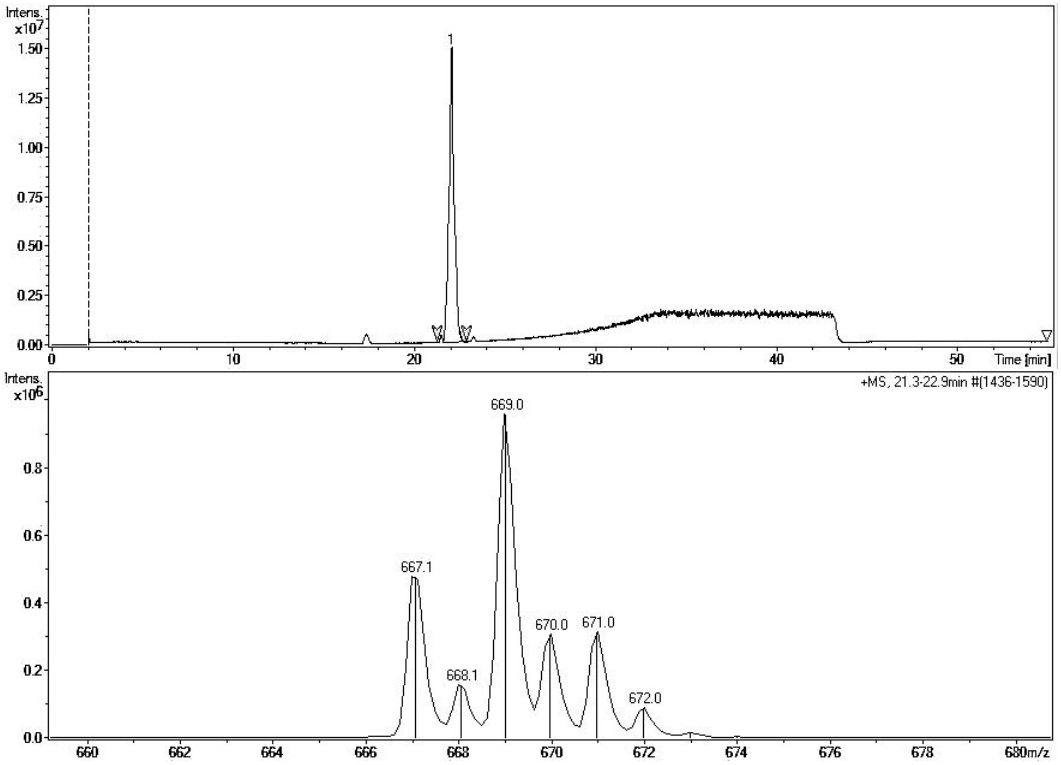

Figure S17: (Top) LC trace of complex **17**. (Bottom) Primary MS fragment of highlighted LC peak.

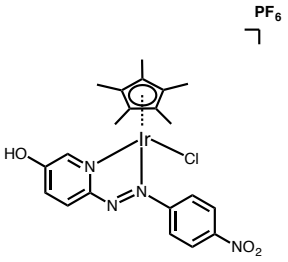

Complex **18**

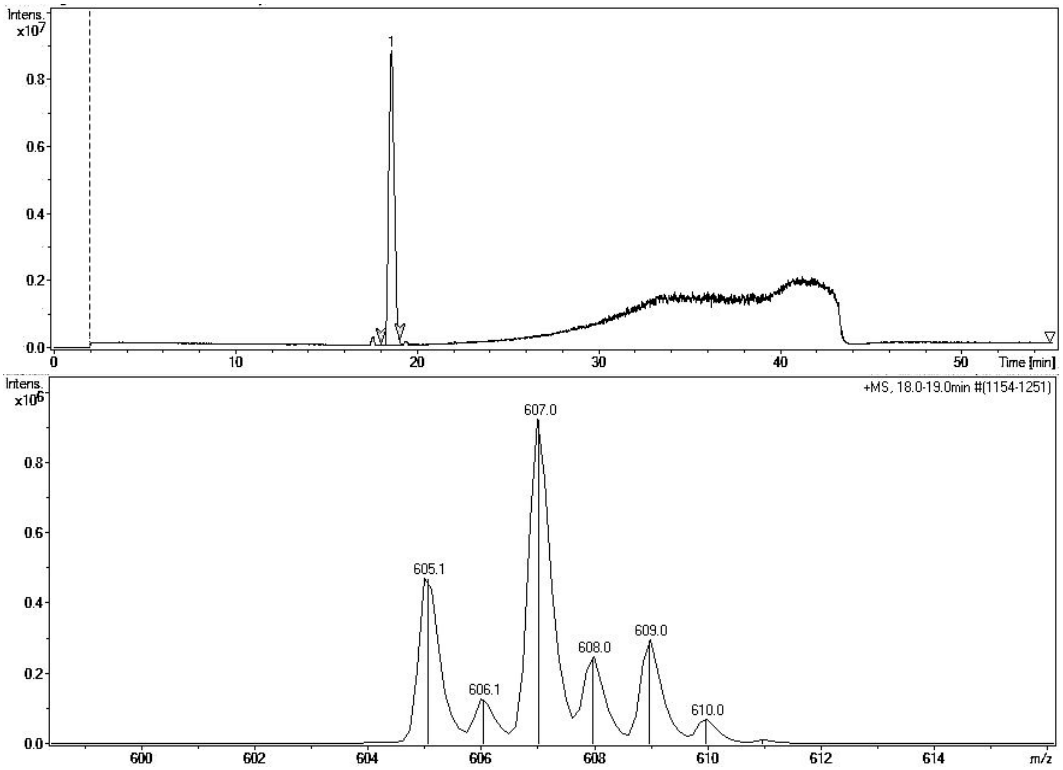

Figure S18: (Top) LC trace of complex **18**. (Bottom) Primary MS fragment of highlighted LC peak.

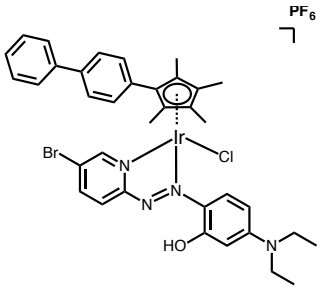

Complex **19**

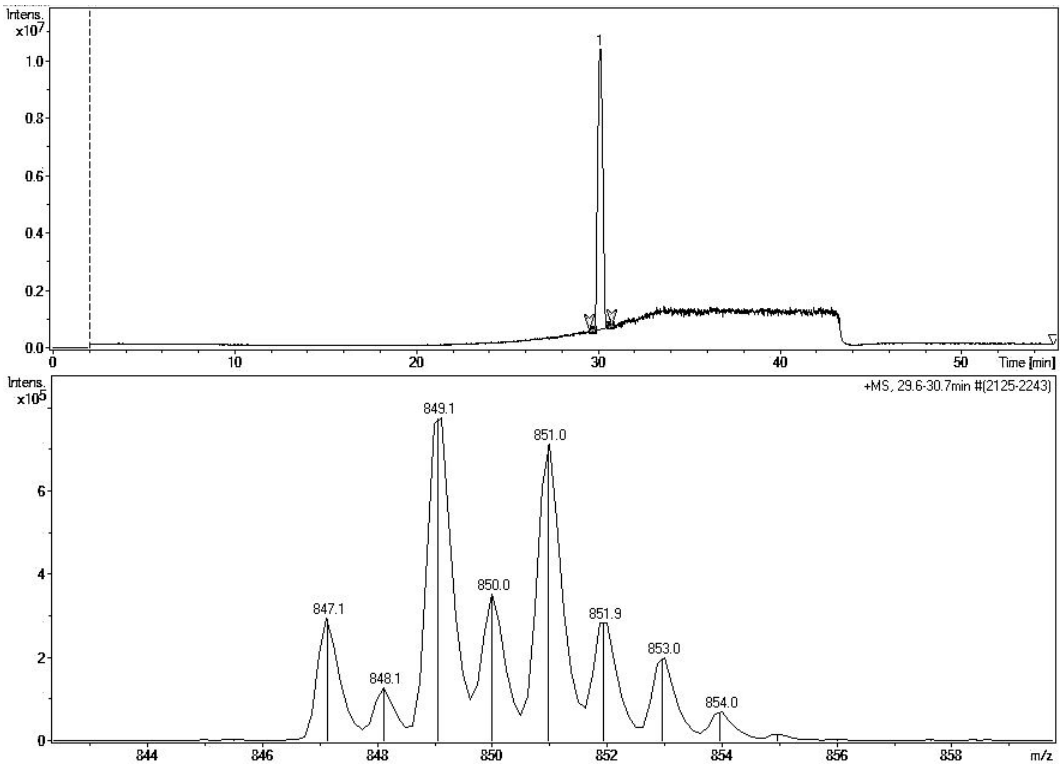

Figure S19: (Top) LC trace of complex **19**. (Bottom) Primary MS fragment of highlighted LC peak.

Peroxide Generation Test

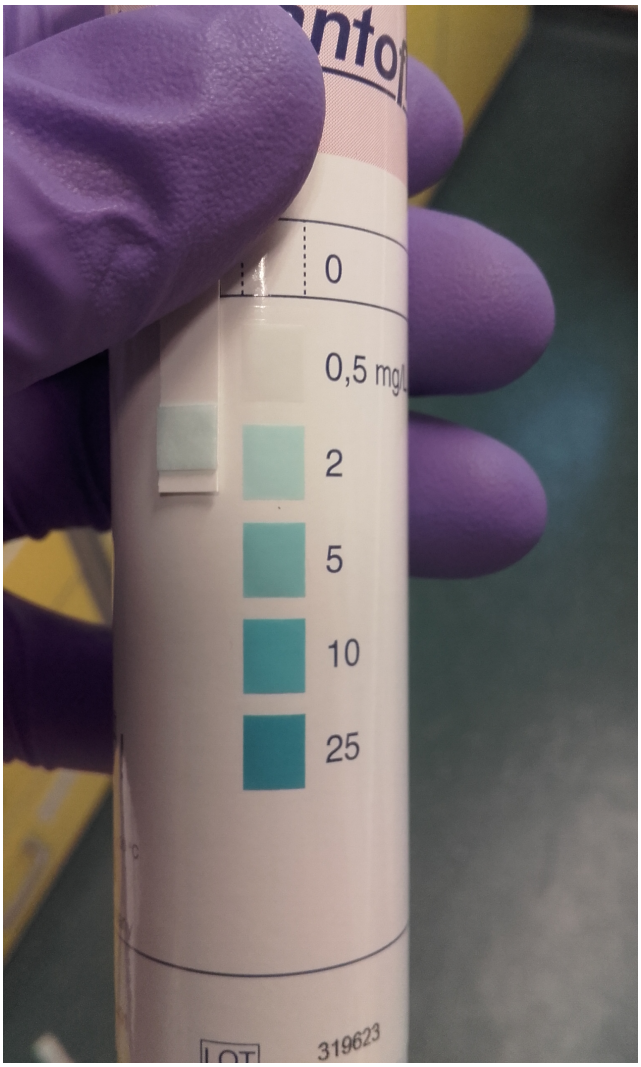

Figure S20: Test for H_2O_2 generation using Quantofix peroxide test sticks on a solution of (2.5 μM) complex **18** incubated with (150 μM) NADH in 0.5% MeOH/99.5% (v/v) 5 mM Na_2HPO_4/NaH_2PO_4 buffer pH 7.4 at 310 K for 24 h.

Stability in DMSO Data

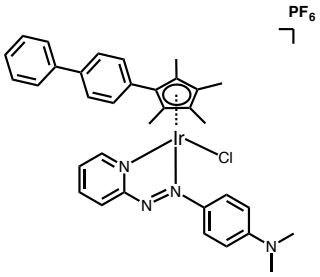

Complex **1**

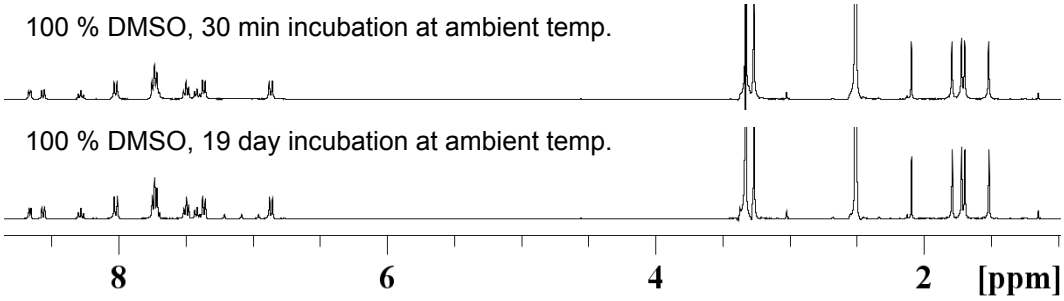

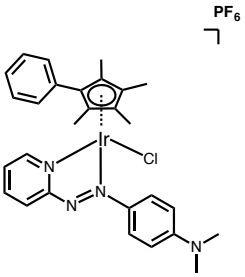

Complex **2**

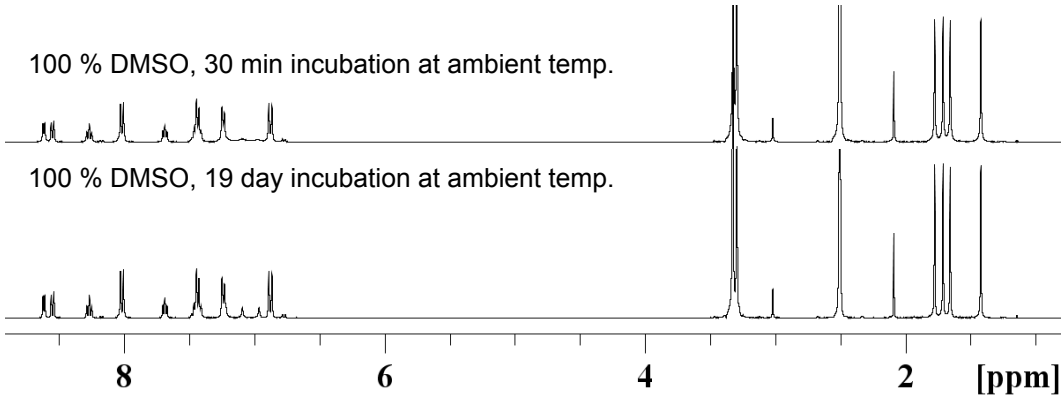

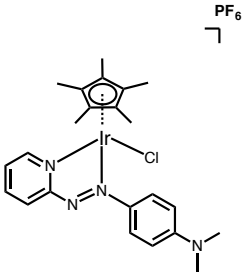

Complex **3**

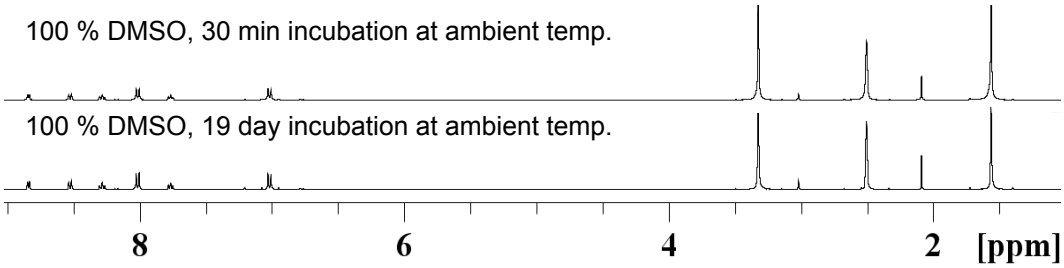

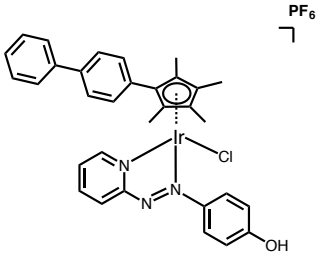

Complex **5**

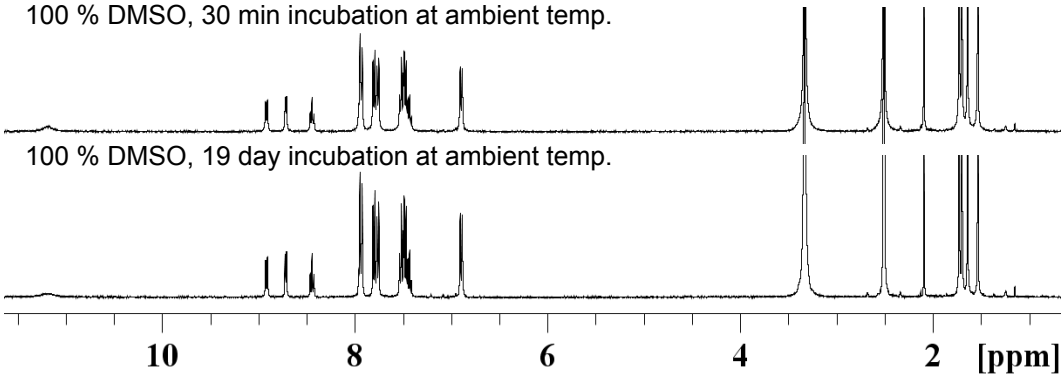

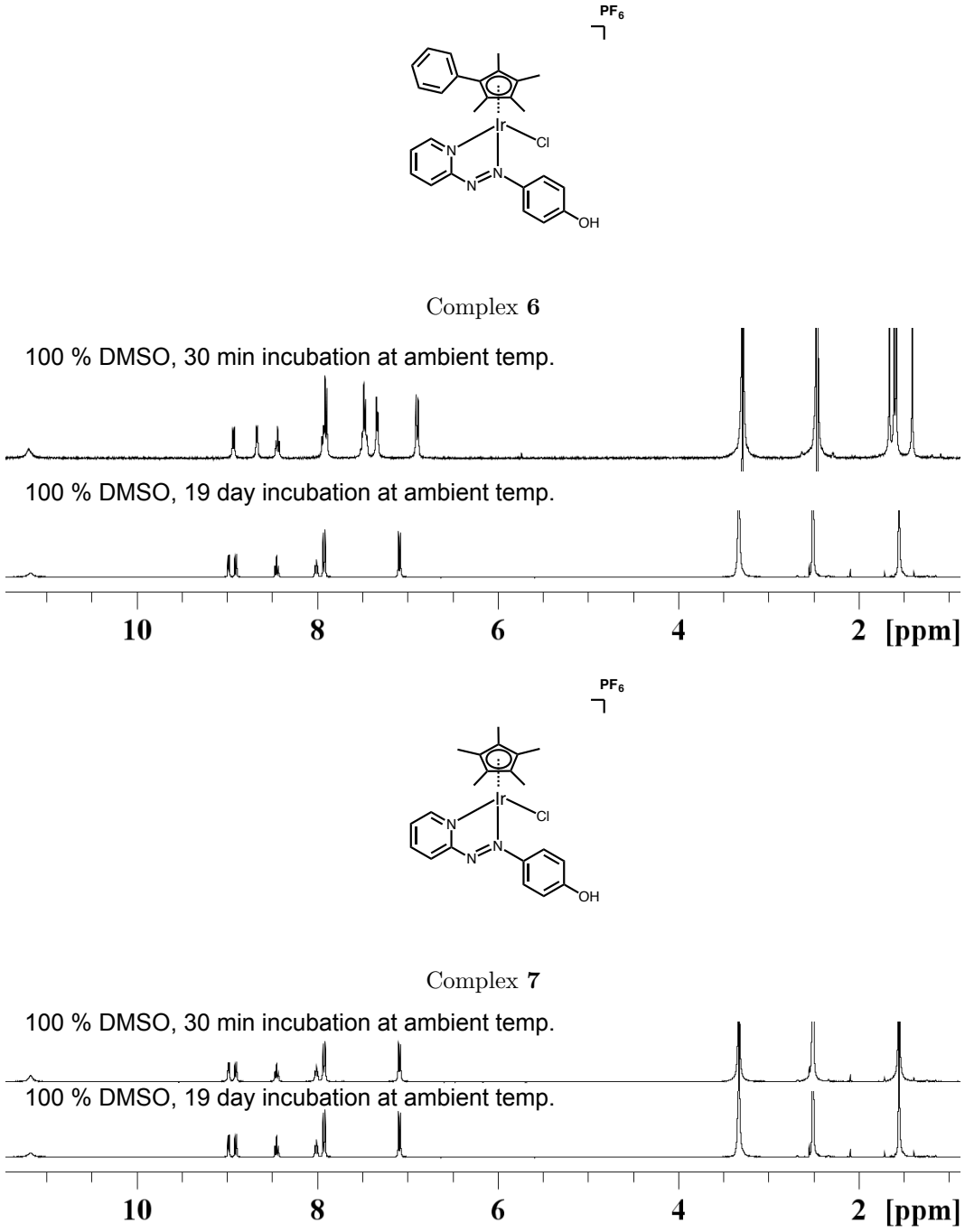

Figure S21: 400 MHz ^{1}H-NMR spectra of a solution of complexes **1** − **6** in 100% d_6-DMSO:D_2O at 298 K incubated for 30 min and 19 days at ambient temperature. No unexpected peaks are observed and differences are visible between the spectra.

LC-MS Nucleotide Binding Data

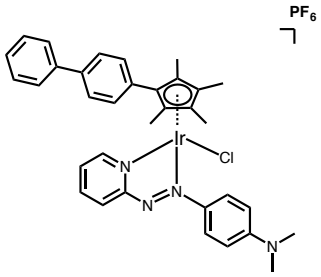

Complex **1**

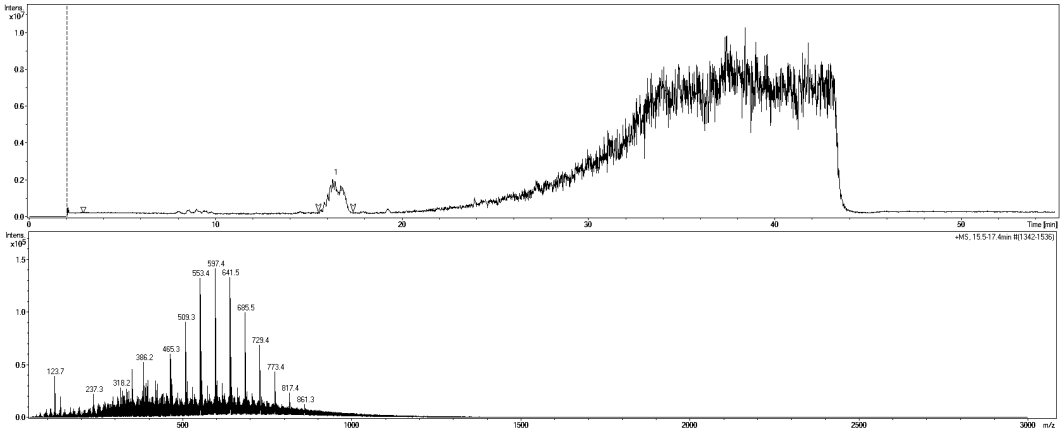

Figure S22: (Top) LC trace of 300 μM of complex **1** incubated with 300 μM of nucleotide 5'-AMP in 50% MeOD:D_2O for 24 h at 310 K. (Bottom) Primary MS fragment of highlighted LC peak 1 of 1.

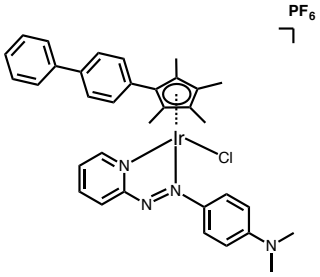

Complex **1**

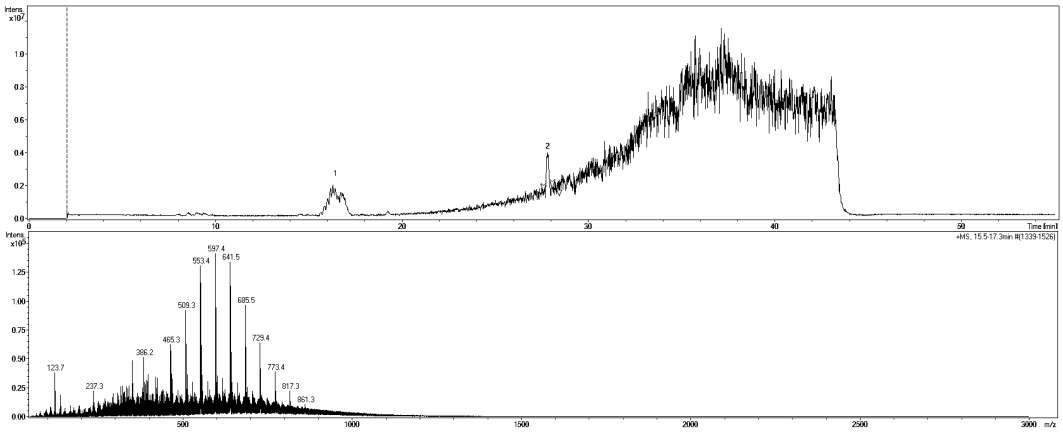

Figure S23: (Top) LC trace of 300 μM of complex **1** incubated with 300 μM of nucleotide 5'-GMP in 50% MeOD:D_2O for 24 h at 310 K. (Bottom) Primary MS fragment of highlighted LC peak 1 of 2.

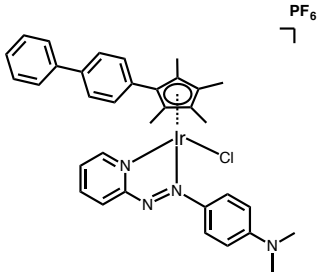

Complex **1**

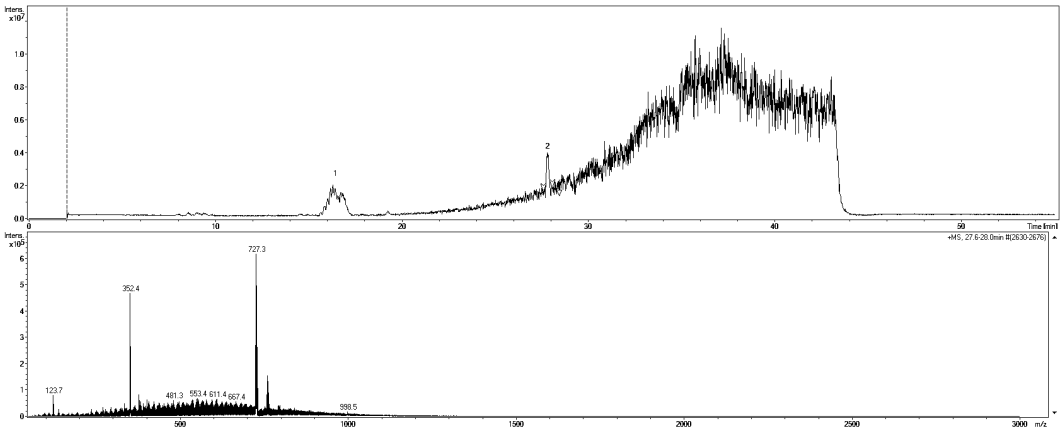

Figure S24: (Top) LC trace of 300 μM of complex **1** incubated with 300 μM of nucleotide 5'-GMP in 50% MeOD:D_2O for 24 h at 310 K. (Bottom) Primary MS fragment of highlighted LC peak 2 of 2.

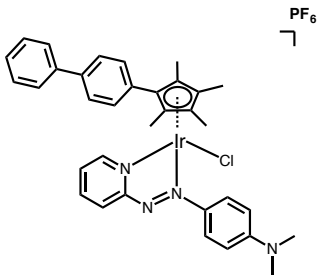

Complex **1**

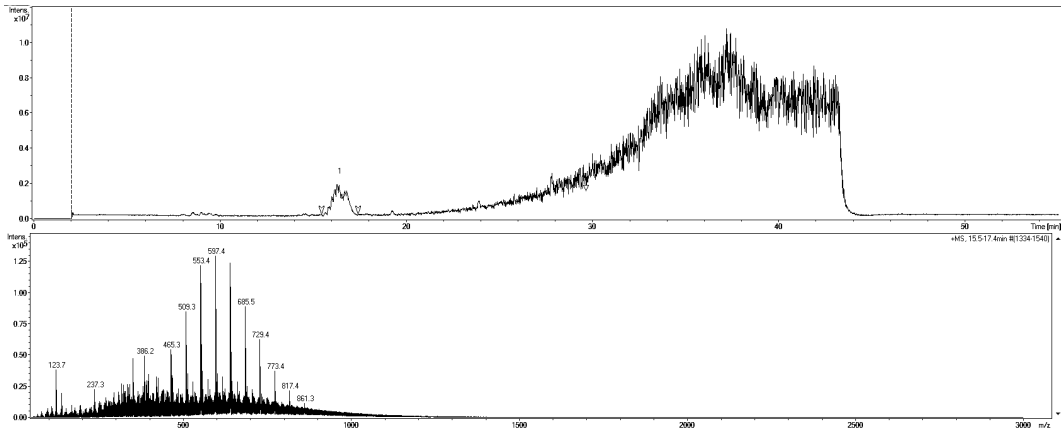

Figure S25: (Top) LC trace of 300 μM of complex **1** incubated with 300 μM of nucleotide 5'-CMP in 50% MeOD:D_2O for 24 h at 310 K. (Bottom) Primary MS fragment of highlighted LC peak 1 of 1.

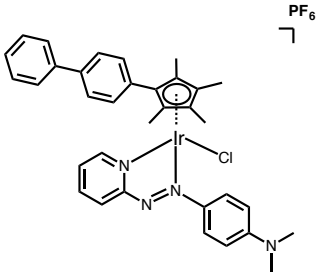

Complex **1**

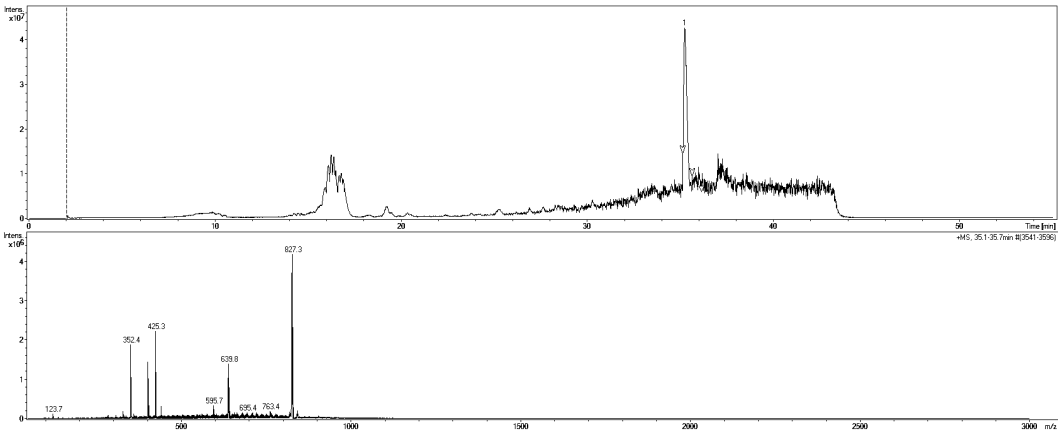

Figure S26: (Top) LC trace of 300 μM of complex **1** incubated with 300 μM of nucleotide 5'-TMP in 50% MeOD:D_2O for 24 h at 310 K. (Bottom) Primary MS fragment of highlighted LC peak 1 of 1.

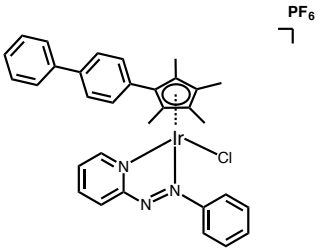

Complex **13**

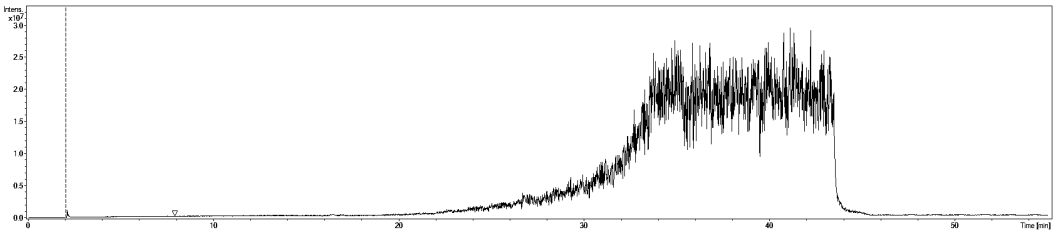

Figure S27: (Top) LC trace of 300 μM of complex **13** incubated with 300 μM of nucleotide 5'-AMP in 50% MeOD:D_2O for 24 h at 310 K.

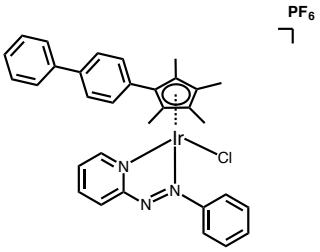

Complex **13**

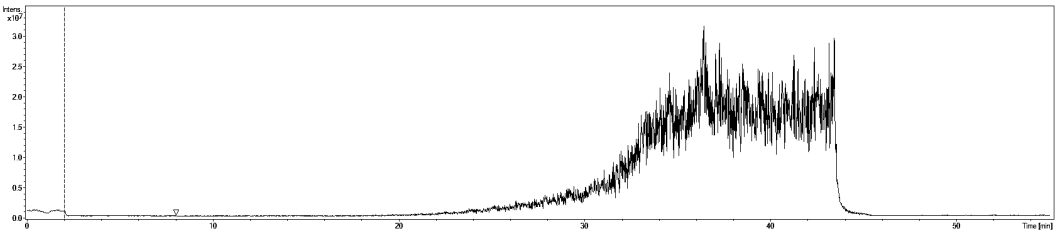

Figure S28: (Top) LC trace of 300 μM of complex **13** incubated with 300 μM of nucleotide 5'-GMP in 50% MeOD:D_2O for 24 h at 310 K.

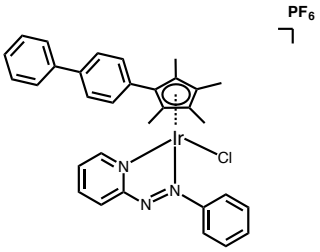

Complex **13**

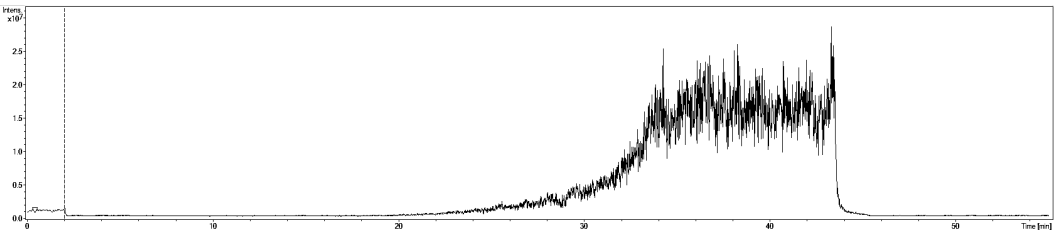

Figure S29: (Top) LC trace of 300 μM of complex **13** incubated with 300 μM of nucleotide 5'-CMP in 50% MeOD:D_2O for 24 h at 310 K.

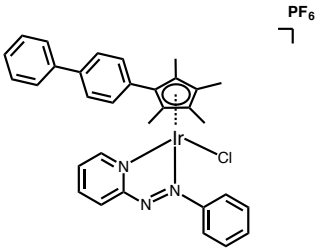

Complex **13**

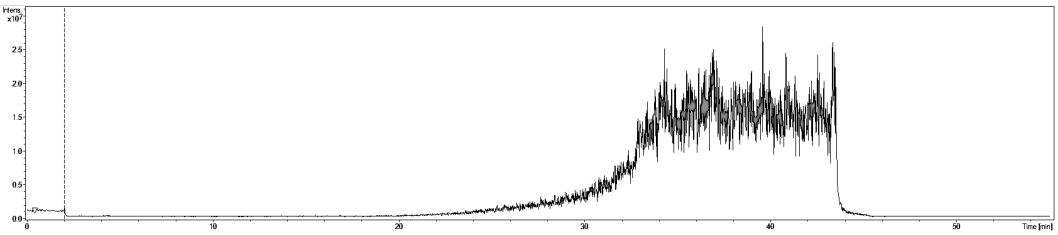

Figure S30: (Top) LC trace of 300 μM of complex **13** incubated with 300 μM of nucleotide 5'-TMP in 50% MeOD:D_2O for 24 h at 310 K.

LC-MS GSH Interaction Data

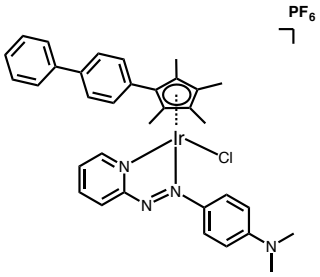

Complex **1**

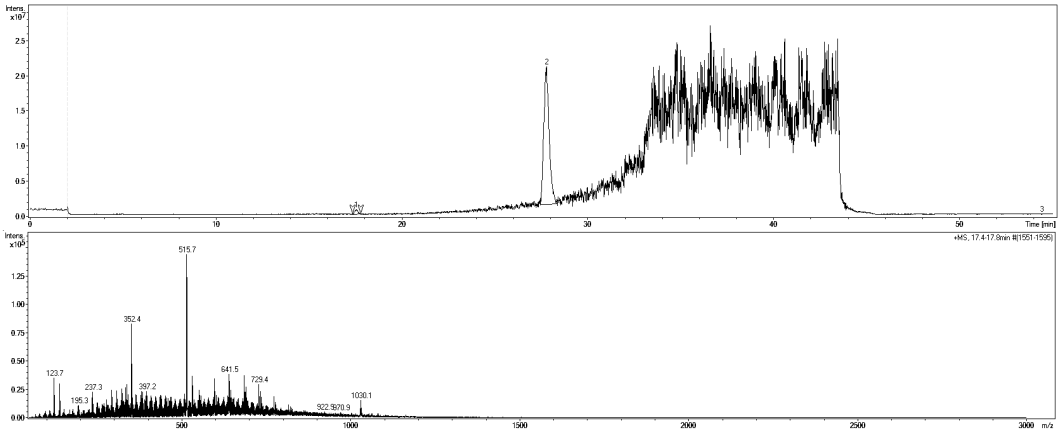

Figure S31: (Top) LC trace of complex **1** incubated with GSH at 310 K for 24 h. (Bottom) Primary MS fragment of highlighted LC peak 1 of 2.

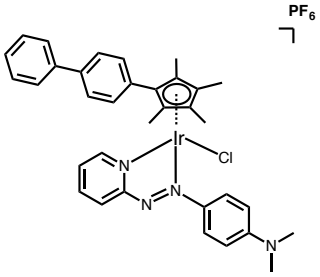

Complex **1**

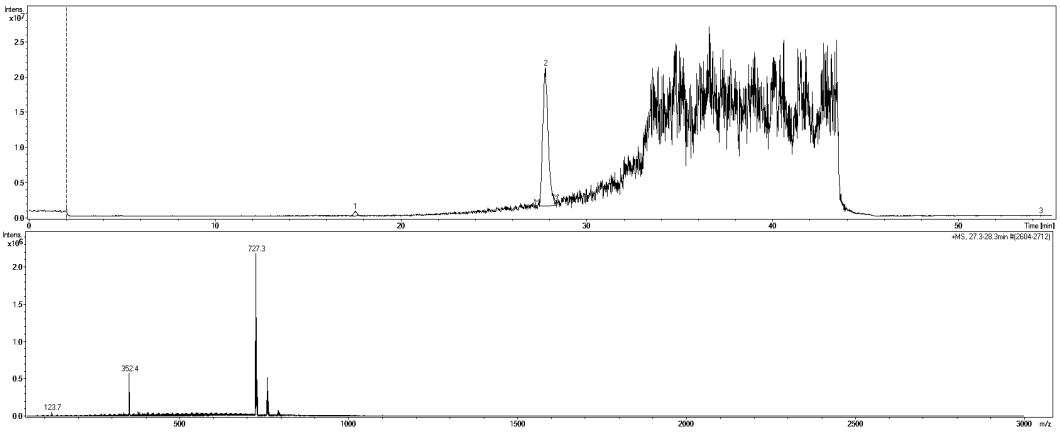

Figure S32: (Top) LC trace of complex **1** incubated with GSH at 310 K for 24 h. (Bottom) Primary MS fragment of highlighted LC peak 2 of 2.

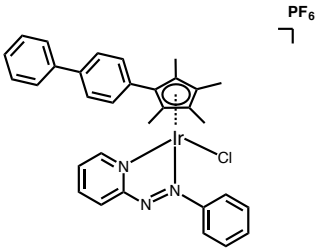

Complex **13**

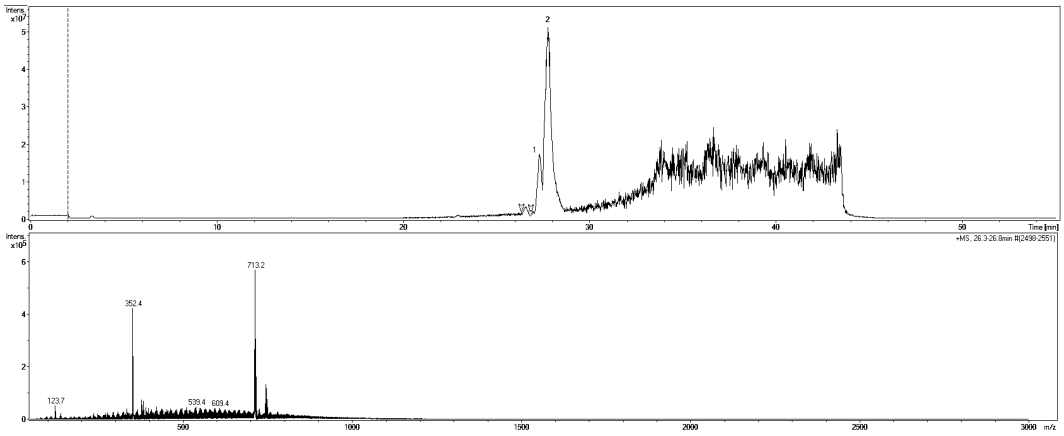

Figure S33: (Top) LC trace of complex **1**. (Bottom) Primary MS fragment of highlighted LC peak 1 of 2.

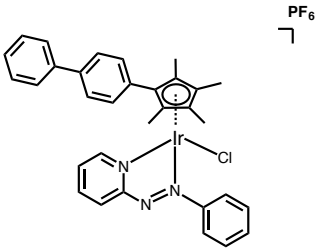

Complex **13**

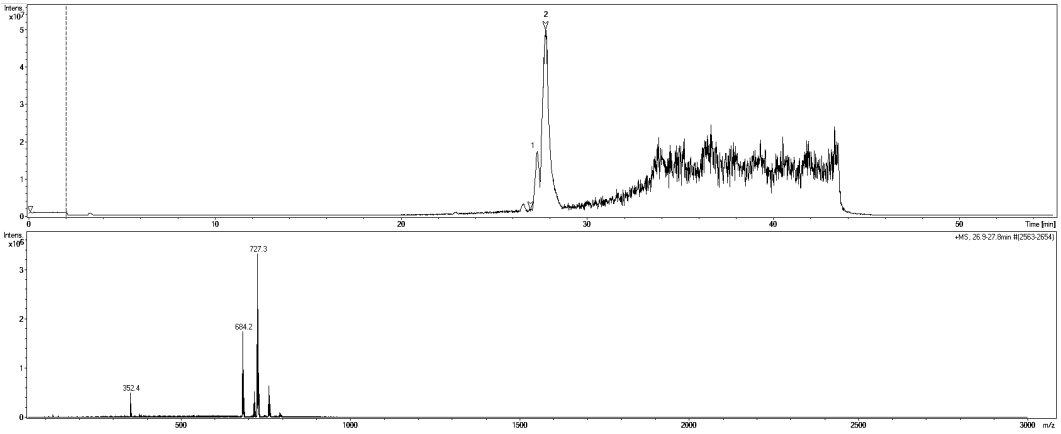

Figure S34: (Top) LC trace of complex **1**. (Bottom) Primary MS fragment of highlighted LC peak 2 of 2.

LC-MS GSSG Interaction Data

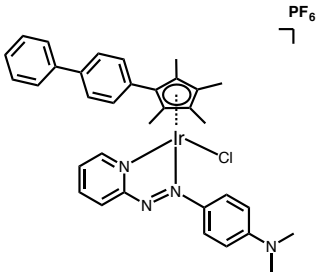

Complex **1**

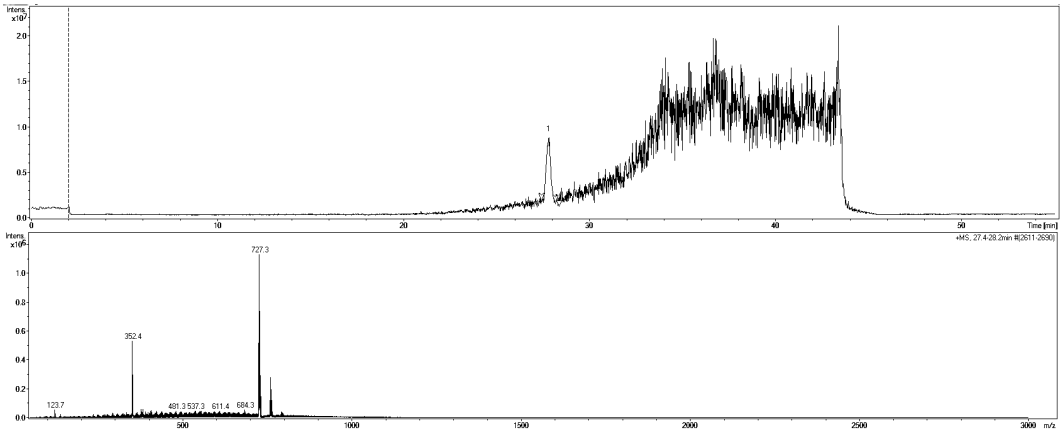

Figure S35: (Top) LC trace of complex **1** incubated with GSSG at 310 K for 24 h. (Bottom) Primary MS fragment of highlighted LC peak 1 of 1.

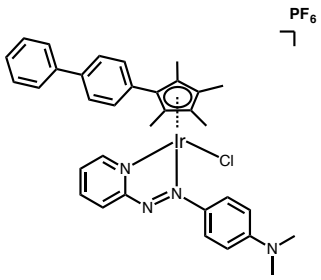

Complex **1**

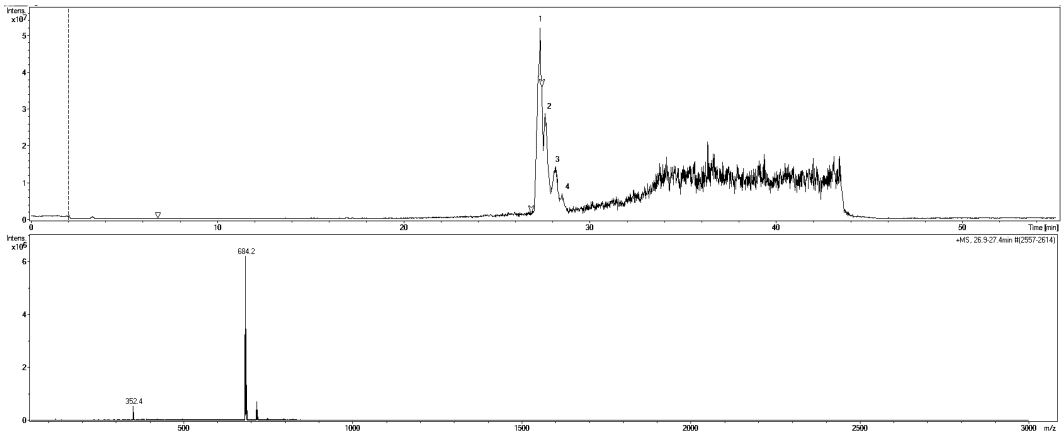

Figure S36: (Top) LC trace of complex **1** incubated with GSSG at 310 K for 24 h. (Bottom) Primary MS fragment of highlighted LC peak 1 of 4.

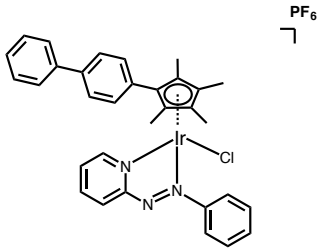

Complex **13**

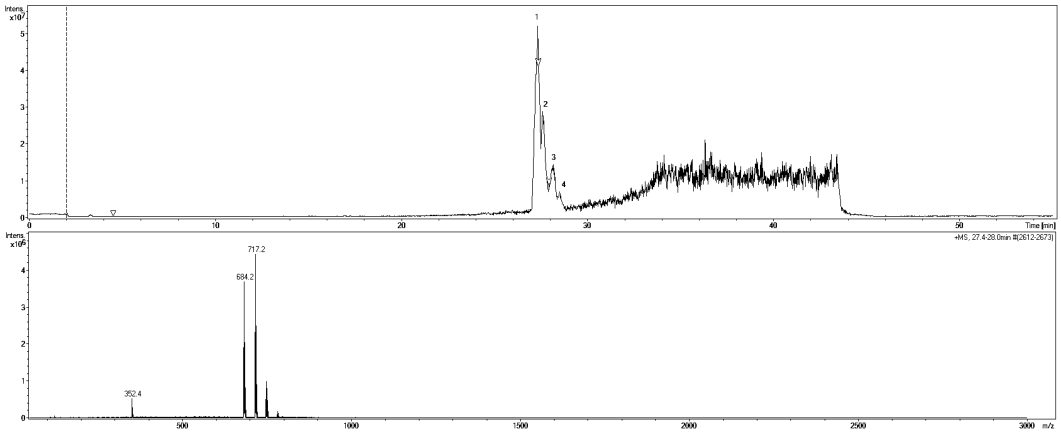

Figure S37: (Top) LC trace of complex **13** incubated with GSSG at 310 K for 24 h. (Bottom) Primary MS fragment of highlighted LC peak 2 of 4.

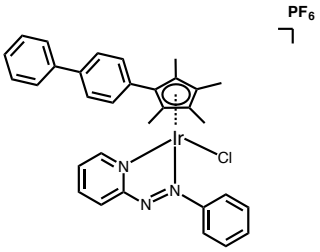

Complex **13**

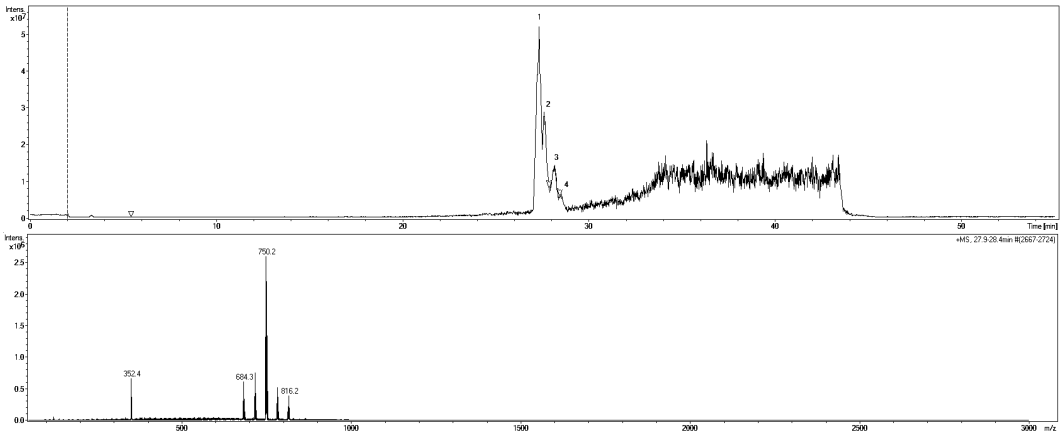

Figure S38: (Top) LC trace of complex **13** incubated with GSSG at 310 K for 24 h. (Bottom) Primary MS fragment of highlighted LC peak 3 of 4.

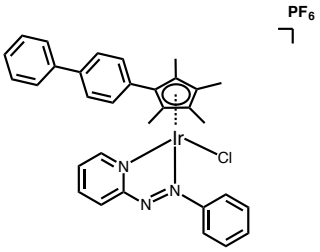

Complex **13**

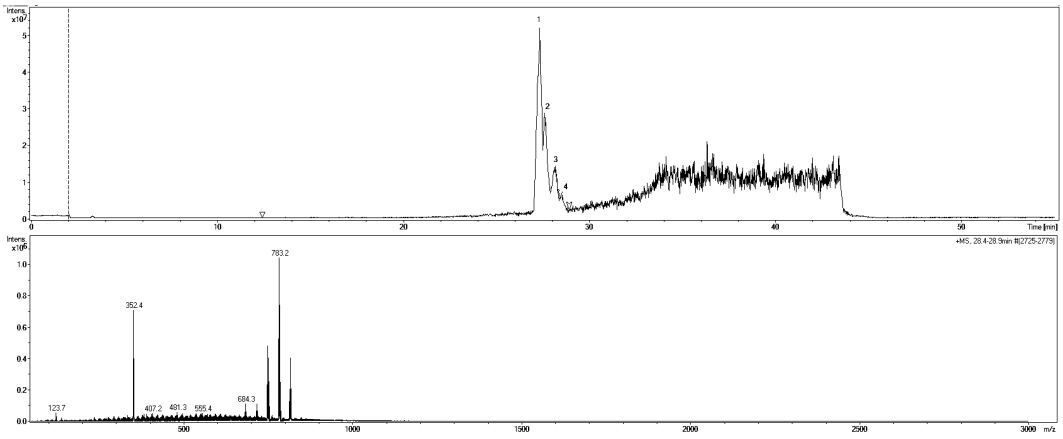

Figure S39: (Top) LC trace of complex **13** incubated with GSSG at 310 K for 24 h. (Bottom) Primary MS fragment of highlighted LC peak 4 of 4.

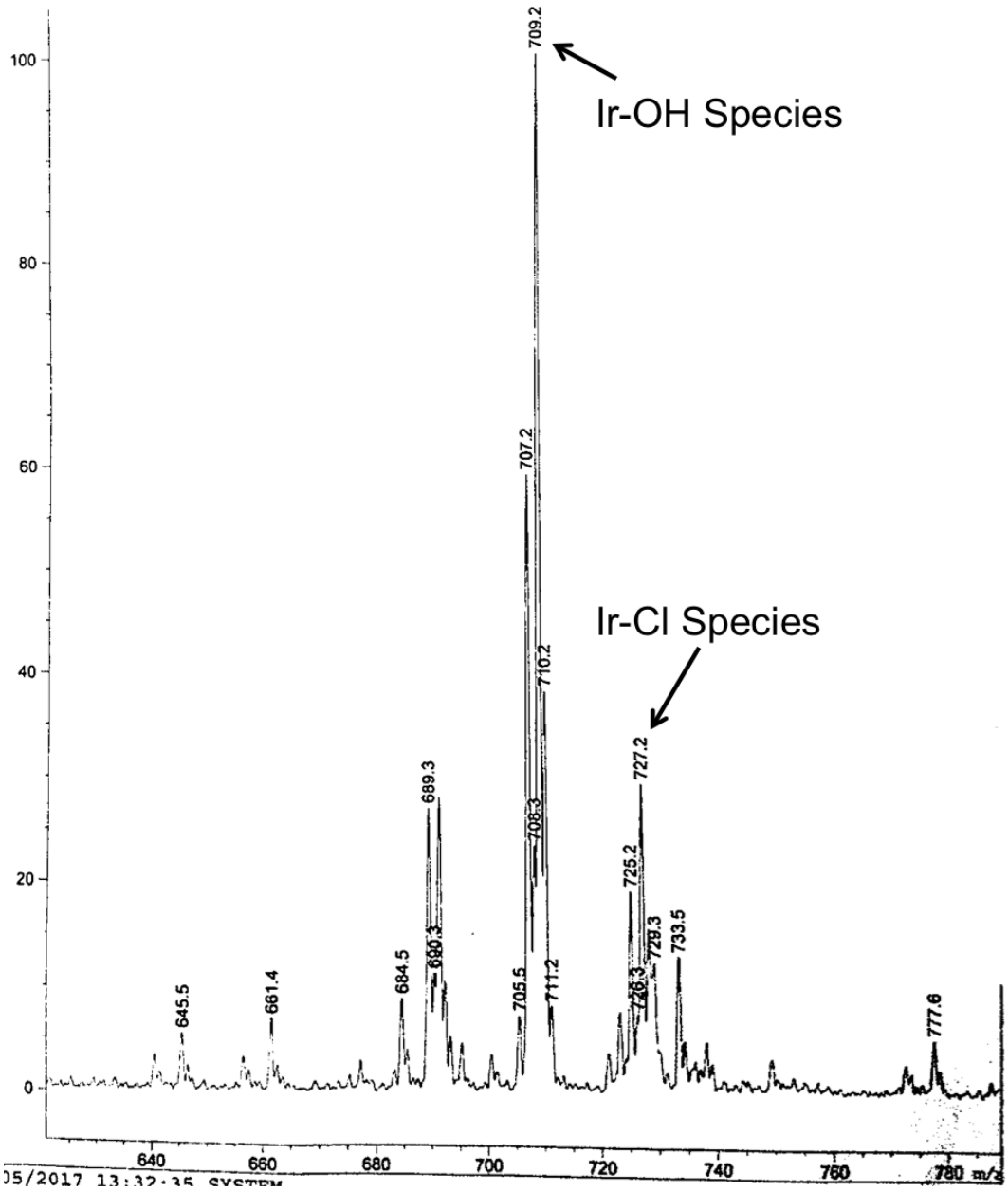

Figure S40: ESI-MS trace of complex **1** incubated in H_2O for 14 days. Only two peaks are prominent most likely corresponding to Ir-Cl and Ir-OH species.